



A University of Sussex PhD thesis

Available online via Sussex Research Online:

<http://sro.sussex.ac.uk/>

This thesis is protected by copyright which belongs to the author.

This thesis cannot be reproduced or quoted extensively from without first obtaining permission in writing from the Author

The content must not be changed in any way or sold commercially in any format or medium without the formal permission of the Author

When referring to this work, full bibliographic details including the author, title, awarding institution and date of the thesis must be given

Please visit Sussex Research Online for more information and further details



University of Sussex

Constraining models of inflation with a
non-trivial field-space by using numerical
calculations of their non-Gaussianities

Sean Butchers

Submitted for the degree of Doctor of Philosophy

University of Sussex

August 2019

Declaration

I hereby declare that this thesis has not been and will not be submitted in whole or in part to another University for the award of any other degree.

The work in this thesis has been completed in collaboration with Dr. David Seery where Chapter 2 of this thesis is based on the following peer-reviewed publication:

- Butchers, S. & Seery, D. (2018). ‘Numerical evaluation of inflationary 3-point functions on curved field space with the transport method & CppTransport’. JCAP, 1807(07), 031. arXiv:1803.10563.

In this work, I calculated the covariantised transport equations including M_{IJ} , u_2 & u_3 , found the covariant versions of the two-point and three-point function initial conditions as well the field-covariant version of the gauge transformation to ζ . Furthermore, I added all the curvature quantities (Γ_{JK}^I , R_{JKL}^I & $R_{JKL;M}^I$) to the CppTransport code, performed every numerical analysis for each model and wrote the paper.

In Chapter 3, I present my work on a cosmological code: CpptSample which we hope to publish soon. In this work, I have written the majority of the CpptSample code and the modifications to CppTransport needed for sampling, completed all of the numerical analysis in the paper and written most of the pre-publication presented here. The code additions to CppTransport that translate a model file for CpptSample were added and written about in the paper by Alessandro Maraiio.

Signature:

Sean Butchers

UNIVERSITY OF SUSSEX

SEAN BUTCHERS, DOCTOR OF PHILOSOPHY

CONSTRAINING MODELS OF INFLATION WITH A NON-TRIVIAL FIELD-SPACE BY
USING NUMERICAL CALCULATIONS OF THEIR NON-GAUSSIANITIESSUMMARY

An era of cosmological inflation is the preferred mechanism for producing primordial fluctuations that are later amplified to become the observed large-scale structure. Unfortunately, constraining inflation is problematic because there are numerous models that reproduce the Gaussian power-spectrum found in the CMB. This problem is further elevated when multi-field models are considered because the kinetic part of their Lagrangian often contains a non-trivial field metric describing a curved geometry in the field-space. Additionally, these models can produce measurable primordial non-Gaussianities which are now constrained in the Planck data. The non-Gaussianities of an inflation model are measured using the bispectrum \mathcal{B} and its amplitude f_{NL} for a specific triangular template and the Gaussian statistics are described using the tensor-to-scalar ratio r and the scalar spectral index n_s .

In the first part of this thesis, we extend the transport method, first introduced by Mulryne, Seery and Wesley, to be able to calculate the power spectrum and the bispectrum and their associated observables from an inflation model with a non-canonical field metric. We implement these in a publicly available code called `CppTransport` to automate the calculation of the statistical properties of the primordial fluctuations. The results of this code are tested using a model that can be described in both canonical and non-canonical field coordinates with excellent agreement. We also demonstrate the code's accuracy by comparing our bispectrum results with a separate numerical implementation of the transport method called `PyTransport 2.0`, again finding good agreement. Lastly, we consider a class of gelaton models that were predicted to produce boosted equilateral configurations of the bispectrum and showed this is difficult to accomplish for models with simple potentials and a hyperbolic field-space.

In the second part of the thesis, we introduce a new code `CpptSample`, which is a CosmoSIS module that adds sampling functionality and Bayesian model selection to `CppTransport`. In this, we build an interface which allows the Monte-Carlo-Markov-Chain (MCMC) samplers in CosmoSIS to provide cosmological and Lagrangian initial conditions to `CppTransport`. The results for the primordial spectra are then passed on to the Boltzmann code `CLASS` to calculate the theoretical CMB power spectrum based on the underlying model and Bayesian evidence is found from the Planck2015 likelihood code. Our implementation of this retains all the extensions needed for models with a non-trivial field-space and does not rely on the slow-roll approximation. We demonstrate this by calculating marginalised statistics for the quadratic, quartic, Gelaton/QSFI and α -attractor models of inflation.

Acknowledgements

First, I must thank my supervisor David Seery for his support and guidance throughout the PhD – I know that I’ve learnt so much from you and I couldn’t have completed this work without your help. I must also thank my second supervisor Christian Byrnes particularly for moral support whilst writing my thesis and whilst doing my corrections. I’m lucky enough to have studied at the University of Sussex for almost 10(!) years and I’ve learnt so much from so many people that it would be impossible to thank everyone but I would like to thank Mark Hindmarsh for being my MPhys project supervisor and introducing me to inflation.

Most of all, I thank my girlfriend Rebecca Clare who has been through every step of the PhD with me throughout all the good and bad parts – in many ways you deserve this just as much as me. I also thank my parents Helen & Simon and my brother Ryan as I know I wouldn’t have ever done cosmology research without your guidance and continued belief in me. My sincerest thanks also go to everyone at Hurstwood park neurological centre for the medical care I received in December 2010 – I’m genuinely lucky to be alive and I wouldn’t have been able to study without the surgery I had there.

I must also mention my athletics club Brighton Phoenix and particularly everyone who trains with me on Monday nights because running not only helped keep me sane whenever I was finding the PhD difficult but somehow I’m now a fairly good runner too! I should also extend this with an apology to everyone who has had to share an office with me: Daniel, Michaela, Pippa and Steven because I would inevitably spend too much time talking about running and especially for treating the cycle ride to university as cross-training.

Finally I would like to thank my examiners Antony Lewis and Sebastien Renaux-Petel for the viva. It may have taken a really long time but I think your comments have improved the thesis.

Contents

List of Tables	ix
List of Figures	xiii
1 Introduction	1
1.1 Preface	1
1.2 Friedmann cosmology	3
1.2.1 FLRW metric	3
1.2.2 Friedmann equations	4
1.2.3 Problems with the hot big-bang model	9
1.3 Inflation	11
1.3.1 Conditions for inflation	11
1.3.2 Scalar fields	13
1.3.3 Slow-roll parameters and the attractor solution	14
1.4 Field perturbations	16
1.4.1 Quantising the perturbations	17
1.4.2 Gauges and super-horizon conservation	19
1.4.3 Tensor perturbations	21
1.4.4 Observables for two-point statistics	22
1.5 Non-Gaussianities	24
1.5.1 The bispectrum and its shapes	25
1.5.2 Separate universes and the δN expansion	29
1.5.3 Calculating the three-point function	33
1.6 Non-canonical fields	35
1.6.1 Field-space covariance	36
1.6.2 The transport method	37
1.7 Connecting inflation to the CMB	38

1.7.1	Temperature spectrum	38
1.7.2	Parameter inference	41
1.8	Summary of the thesis	43
2	Project I – Numerical evaluation of inflationary 3-point functions on curved field space	45
2.1	Abstract	45
2.2	Introduction	45
2.3	Differences from the canonical case	49
2.3.1	Field-covariant formalism	49
2.3.2	Hamiltonian	51
2.3.3	Initial conditions	53
2.3.4	Covariant transport equations	55
2.3.5	Gauge transformation	57
2.4	Numerical results	58
2.4.1	Obtaining the transport codes	60
2.4.2	Cartesian versus polar coordinates	61
2.4.3	Quasi-two-field inflation	64
2.4.4	The gelaton model	67
2.4.5	Isocurvature modes	75
2.5	Conclusions	75
2.6	Appendix: Detailed calculations	77
2.6.1	Perturbed action in curved field space	77
2.6.2	Transport method	83
2.6.3	Initial conditions	87
2.6.4	Gauge transformation to curvature perturbations	94
3	Project II – CpptSample: sampling the primordial perturbation using CppTransport	98
3.1	Abstract	98
3.2	Introduction	98
3.3	The transport method and CppTransport	102
3.4	Code methodology	106
3.4.1	CosmoSIS modules	106
3.4.2	Using CppTSample	108

3.4.3	Full pipeline	116
3.5	Numerical results	117
3.5.1	Quartic inflation	119
3.5.2	Quadratic inflation	122
3.5.3	alpha-attractor inflation	125
3.5.4	Gelaton/QSFI inflation	129
3.6	Conclusions	132
3.7	Appendix: Full covariance plots	134
3.8	Appendix: Convergence plots	138
3.8.1	Quartic model	138
3.8.2	Quadratic model	138
3.8.3	Alpha-attractor model	139
3.8.4	Gelaton/QSFI model	139
4	Conclusions	140
4.1	Summary of the research	140
4.2	Prospects for the future	143
	Bibliography	145

List of Tables

- 1.1 Planck 2018 results taken from [Aghanim et al., 2018] for the present values of the following cosmological parameters: baryon-density, cold dark-matter density (with $h \equiv H_0/100\text{km s}^{-1}\text{Mpc}^{-1}$), Hubble constant, dark-energy density, matter density (baryons + cold dark-matter), curvature density, redshift of radiation-matter equality and radiation density (given from $\Omega_R = \Omega_m/(1 + z_{\text{eq}})$). 7
- 1.2 A table giving the parameters that describe the statistics for the two-point correlation function taken from the Planck 2018 results [Akrami et al., 2018]. Note: $r_{0.002}$ indicates the pivot scale is chosen to be 0.002Mpc^{-1} 24
- 1.3 A table giving different measurements of the reduced bispectrum for the different triangle configurations taken from the Planck 2015 results [Ade et al., 2016a]. Note: ‘68% CL, stat’ indicates there is an additional statistical error from not being able to model all of the bispectrum configurations. 26
- 3.1 Planck 2015 cosmological parameters used for the cold dark matter density, baryon density, the reduced Hubble constant and the optical depth for CppTSample runs with the second column giving the values used when only inflation parameters are varied and the third column giving the uniform priors used for the full MCMC runs. 118
- 3.2 Marginalised 68% limits with best-fit values and Gelman-Rubin values for the quartic model returned by the Metropolis-Hastings sampler on the Planck 2015 TT+TE+EE+lowP likelihood with sampled parameters in bold. 122
- 3.3 Marginalised 68% limits with best-fit values and Gelman-Rubin values for the quadratic model returned by the Metropolis-Hastings sampler on the Planck 2015 TT+TE+EE+lowP likelihood with sampled parameters in bold. 124

3.4	Marginalised 68% limits with best-fit values and Gelman-Rubin values on the parameters in the alpha-attractor model as returned by the Metropolis-Hastings sampler on the Planck 2015 TT+TE+EE+lowP likelihood (sampled parameters in bold).	128
3.5	The start-values and priors used for the Gelaton/QSFI model described in Equations (3.35) & (3.36).	130
3.6	Marginalised 68% limits with best-fit values and Gelman-Rubin values on the parameters in the Gelaton/QSFI model as returned by the Metropolis-Hastings sampler with the Planck 2015 TT+TE+EE+lowP likelihood (sampled parameters in bold).	131

List of Figures

- 1.1 A space-time diagram demonstrating the horizon problem. The two grey triangles indicate photons that have propagated from the big-bang (η_{BB}) up until the CMB at η_{re} . Today at η_0 , we shouldn't see correlated regions for θ larger than 1° because it shouldn't be possible for the grey triangles to be causally connected. 10
- 1.2 A phase-space plot in ϕ and $\dot{\phi}$ showing the inflation trajectories converging to the attractor solutions for the chaotic model of inflation with a potential $V = m^2\phi^2/2$. This is figure 5.3 taken from [Mukhanov, 2005]. 16
- 1.3 Plots of the bispectrum shapes demonstrating the $\alpha\beta$ -parameterisation with the f_{NL} values given as proportions of the maximum value. Left: local bispectrum shape; right: equilateral bispectrum shape. 28
- 1.4 Planck 2018 results for the temperature power spectrum, taken from [Aghanim et al., 2018]. Red dots are the measurements and the blue line is the best-fit Λ CDM model with residuals given in the lower panel. $D_\ell \equiv \ell(\ell + 1)C_\ell/2\pi$ 40
- 2.1 Field plots for the QSFI/Gelaton model (2.35) until end of inflation. Left: time evolution of the canonical fields X and Y . Right: time evolution of the non-canonical fields R and θ 62
- 2.2 QSFI/Gelaton residual plots for the dimensionless power spectrum (left) and bispectrum (right) on equilateral configurations for a k and a k_t mode both leaving the horizon at $N = 8.0$ respectively. 62
- 2.3 QSFI/Gelaton residual plots for the reduced bispectrum on equilateral configurations. Left: time evolution of f_{NL} for a k_t mode leaving the horizon at $N = 8.0$. Right: k_t -dependence of f_{NL} for a range of k_t values leaving between 17.0 and 24.2 e-folds after the initial conditions. 63

2.4	Power spectrum residuals from the quasi-two-field model. Left: residual as a function of time for the k -mode that exits the horizon at 19.0 e-folds from the initial time. Right: residual of $\ln(\mathcal{P}_\zeta)$ as a function of $\ln(k/k_*)$ for a range of k numbers exiting the horizon between 0.0 and 5.2 e-folds after the scale, k_* , which exits at $N_* = 13.5$	64
2.5	Quasi-two-field residual time-plots for three-point functions on equilateral configurations. Left: dimensionless bispectrum, \mathcal{B} , for a k_t value that exits the horizon at $N_{\text{exit}} = 19.9$ plotted against time. Right: reduced bispectrum, f_{NL} , plotted against time for the same k_t and N_{exit} values.	66
2.6	Reduced bispectrum residuals in equilateral k_t space where $k_* = 1$ and $N_{*\text{exit}} = 0.1$. Left: residuals for the reduced bispectrum f_{NL} plotted against a range of k_t values exiting the horizon between 10.9 & 19.9 e-folds after inflation begins. Right: zoom-in of the largest residual at $k_t \approx 2.2 \times 10^8$. . .	67
2.7	Shape plots for the quasi-two-field model. Left: 3D surface plot of the dimensionless bispectrum, $\mathcal{B}(\alpha, \beta)$, taken at $N = 14.232$ e-folds for a range of shapes with $-0.98 \leq \alpha \leq 0.98$ and $0 \leq \beta \leq 0.99$ and a fixed k_t mode with $N_{\text{exit}} = 16.6$ e-folds. Right: 2D contour plot for the same values.	68
2.8	Background fields and power spectrum for the gelaton model. Left: e-fold evolution of fields ϕ and χ with inflation ending at $N = 51$. Right: dimensionless power-spectrum \mathcal{P}_ζ for a k mode exiting the horizon 8.0 e-folds after the initial conditions.	70
2.9	Left: dimensionless bispectrum \mathcal{B} for an equilateral configuration where $k_t = 3$ with each individual k mode exiting the horizon at $N = 8.0$. Right: reduced bispectrum f_{NL} plotted against a range of k values exiting the horizon between 0-46 e-folds after the scale k_* with $N_{*\text{exit}} = 3.0$	70
2.10	Left: gelaton model surface plot showing the shape of the reduced bispectrum, $f_{\text{NL}}(\alpha, \beta)$, taken at a time $N = 25.0$ e-folds for a k_t mode that leaves the horizon 18.9 e-folds after the initial time. Right: contour plot of the data in the left panel.	71
2.11	Left: a plot of the gelaton mass m_{gelaton}^2 and H^2 demonstrating that the constraint $m_{\text{gelaton}}^2 \gg H^2$ is satisfied. Right: a plot showing the departure in the speed of sound, $ c_s - 1 $ is very small due to the constraints described in §2.4.4.	73

2.12	Left: a plot of every dimensionless three-point function from the three fields in the quasi-two-field model given for an equilateral k_t mode exiting the horizon 19.1 e-folds after the initial time. Right: a plot of all of the three-point functions possible for the two fields in the gelaton model which is given for an equilateral k_t mode exiting the horizon 49.2 e-folds after the initial time.	76
3.1	Diagram demonstrating the code pipeline used by <code>CppTSample</code>	117
3.2	Covariance plots of $\log_{10}(\lambda)$, N_{piv} , $\ln(10^{10} A_s)$, $\ln(10^{10} A_t)$, n_s , n_t , r and $f_{\text{NL}}^{\text{eq}}$ for the chaotic quartic inflation model as returned by the apriori sampler on Planck 2015 TT data.	121
3.3	Covariance plots of $\log_{10}(m)$, N_{piv} , $\ln(10^{10} A_s)$, $\ln(10^{10} A_t)$, n_s , n_t , r and $f_{\text{NL}}^{\text{eq}}$ for the chaotic quadratic inflation model returned by the apriori sampler on Planck 2015 TT data.	123
3.4	Covariance plots for the parameters $\log_{10}(V_0)$, A , N_{piv} , $\ln(10^{10} A_s)$, $\ln(10^{10} A_t)$, n_s , n_t , r and $f_{\text{NL}}^{\text{eq}}$ in the alpha-tractor inflation model as returned by the apriori sampler on Planck 2015 TT data.	127
3.5	Two plots showing the bispectrum given by the Gelaton/QSF1 model with parameters set from the values in Table 3.6. Left: dimensionless bispectrum (3.22) and right: reduced bispectrum (3.24) both for an equilateral configuration with $k_t = 3 \times 0.002 \text{ Mpc}^{-1}$	132
3.6	Covariance and distribution plots for the parameters $\log_{10}(\lambda)$, N_{piv} , $\Omega_c h^2$, $\Omega_b h^2$, h_0 , τ , $\ln(10^{10} A_s)$, $\ln(10^{10} A_t)$, n_s , n_t , r & $f_{\text{NL}}^{\text{eq}}$ in the quartic inflation model and based on Planck 2015 TT+TE+EE+lowP data.	134
3.7	Covariance and distribution plots for the parameters $\log_{10}(m)$, N_{piv} , $\Omega_c h^2$, $\Omega_b h^2$, h_0 , τ , $\ln(10^{10} A_s)$, $\ln(10^{10} A_t)$, n_s , n_t , r & $f_{\text{NL}}^{\text{eq}}$ in the quadratic inflation model and based on Planck 2015 TT+TE+EE+lowP data.	135
3.8	Covariance and distribution plots for the parameters $\log_{10}(V_0)$, A , N_{piv} , $\Omega_c h^2$, $\Omega_b h^2$, h_0 , τ , $\ln(10^{10} A_s)$, $\ln(10^{10} A_t)$, n_s , n_t , r & $f_{\text{NL}}^{\text{eq}}$ in the α -tractor model and based on Planck 2015 TT+TE+EE+lowP data.	136
3.9	Covariance and distribution plots for the parameters R_0 , $\log_{10}(V_0)$, η_R , g_R , λ_R , α , $\Omega_c h^2$, $\Omega_b h^2$, h_0 , τ , $\ln(10^{10} A_s)$, $\ln(10^{10} A_t)$, n_s , n_t & r in the Gelaton/QSF1 model and based on Planck 2015 TT+TE+EE+lowP data.	137
3.10	A trace plot of $\ln(\mathcal{L})$ vs. sample number for the 15 chains used in the quartic model MCMC data with the first 4000 samples removed.	138

- 3.11 A trace plot of $\ln(\mathcal{L})$ vs. sample number for the 15 chains used in the quadratic model MCMC data with the first 4000 samples removed. 138
- 3.12 A trace plot of $\ln(\mathcal{L})$ vs. sample number for the 15 chains used in the alpha-attractor model MCMC data with the first 4000 samples removed. . . 139
- 3.13 A trace plot of $\ln(\mathcal{L})$ vs. sample number for the 15 chains used in the Gelaton/QSFI model MCMC data with the first 500 samples removed. . . . 139

Chapter 1

Introduction

1.1 Preface

The previous century saw cosmology develop at a great pace. The observation of the Cosmic Microwave Background (CMB) radiation has meant we can now make precise astrophysical measurements from the earliest measurable time periods. Cosmological models developed from these observations are able to track the evolution of the universe from the first second all the way to the present day. Despite these successes, there remains some unanswered questions. Why do we have such a homogeneous universe after nearly 14 billion years of expansion? Where did the inhomogeneities in the CMB come from? Fortunately, inflation provides a testable framework for answering these questions.

The predictions made by inflation are characterised by the statistics of the primordial curvature perturbation, ζ , which is usually measured using its *power spectrum*. However, there are many inflation models each with similar predictions for the power spectrum. Therefore, measurements of the CMB do not provide enough information about the power spectrum to rule out many of these models which leaves cosmologists with a constraint problem.

Non-Gaussianities based on higher-order statistics measured by a *bispectrum* could provide the answer to the constraint problem because they allow us to demand the CMB measurements are consistent with *both* of the N-point functions. This is of particular interest to the particle physics community because theories such as string theory can produce inflation based on interactions in their complex field-spaces.

In this thesis, I present work that enables us to calculate the bispectrum for these models with a non-trivial field space and then test those predictions using a new cosmological code I have developed.

Synopsis.—In Chapter 1, we give an overview of inflationary theory. This begins in §1.2 where we describe Friedmann cosmology and identify some of the problems with it. In §1.3, we discuss how inflation uses scalar fields to solve the problems with the hot big-bang model. Next in §1.4, we describe how the inflation field is perturbed and show how the power spectrum is calculated from the perturbations. Calculation of the bispectrum and how to adapt this for non-canonical fields is given in §1.5 and §1.6 respectively. Finally in §1.7, we show how these calculations are related to CMB measurements.

In Chapter 2, we present the published work [Butchers & Seery, 2018] where we performed the calculations necessary to calculate the bispectrum for an inflation model with a non-trivial field space. These calculations include perturbing the action to third-order and then finding the transport equations, initial conditions and the gauge transformations to ζ needed for numerical analysis. We then implemented these in the `CppTransport` code and tested the calculations on several models by using residuals between our results and other codes. Finally, we tested the gelaton model to show that it is difficult to produce boosted equilateral modes on the Fourier bispectrum. For hyperbolic field-space manifolds and simple inflationary potentials, we found the enhanced equilateral modes are not currently measurable.

In Chapter 3, we present our work on a cosmological code `CppTSample`, which is designed to add inflation parameter sampling to `CppTransport`. Our implementation uses the samplers provided by `CosmoSIS` [Zuntz et al., 2015] to pass initial conditions to `CppTransport` which then calculates the power spectrum and bispectrum from them. The spectra results are used in the Boltzmann code `CLASS` [Lesgourgues, 2011] that calculates the predicted CMB based on the initial condition sample. The Planck likelihood code is then used to estimate the quality of fit to the data for the samples, and we extract best-fit parameters for several inflation models.

In Chapter 4, we provide a summary of the work completed and explain what has been added to the field of cosmology with our work. In addition, we provide an outlook for the future with upcoming CMB measurements and the potential consequences related to the work presented here.

Units.—We use natural units where the speed of light and Planck’s constant are set to unity as $c = \hbar = 1$. The reduced Planck mass is $M_{\text{p}}^2 = (8\pi G)^{-1}$. We use the metric signature $(-, +, +, +)$. Greek indices (μ, ν, \dots) label space-time indices, whereas lower-case Roman indices from the middle of the alphabet, (i, j, \dots) , label spatial indices. We use an over-dot to indicate a time-derivative such as $\dot{a} \equiv da/dt$ and also use a compact notation

for the covariant derivative where $\nabla_\nu X^\mu \equiv X^\mu_{;\nu}$.

1.2 Friedmann cosmology

Today, modern cosmology theories always begin with the *cosmological principle*, which is the statement that the universe must be both homogeneous and isotropic when viewed on large-enough scales, and the *Copernican principle*, which states that there are no privileged observers in the universe. The evidence for these principles is given from large-scale structure surveys and the CMB where homogeneity is found on scales larger than $\sim 100\text{Mpc}$ [Wu et al., 1999].

1.2.1 FLRW metric

These principles combined with the observations that the universe is expanding in all directions in proportion to its physical distance [Hubble, 1929] led Friedmann, Lemaître, Roberston and Walker to independently find the FLRW metric [Friedmann, 1924] to describe the geometrical and causal structure of the universe as

$$ds^2 = g_{\mu\nu} dx^\mu dx^\nu = -dt^2 + a^2(t) \left(\frac{dr^2}{1 - kr^2} + r^2 (d\theta^2 + \sin^2 \theta + d\phi^2) \right), \quad (1.1)$$

where $g_{\mu\nu}$ is the space-time metric, $a(t)$ is the time-dependent, dimensionless scale factor giving the expansion rate of the universe and is normalised so that the present value is $a_0 = 1$. Finally k is the constant related to the spatial curvature and has dimensions of $[\text{length}]^{-2}$. The scale factor must be independently found from Einstein's field equations which can be derived from the Einstein-Hilbert action [Hilbert, 1915] given as

$$S_{\text{EH}} = \int d^4x \sqrt{-g} \left(\frac{1}{2} M_{\text{P}}^2 R + \mathcal{L}_M - \Lambda \right), \quad (1.2)$$

where the reduced Planck mass is defined $M_{\text{P}}^2 = (8\pi G)^{-1}$ with Newton's gravitational constant equal to $G = 6.67 \times 10^{-11} \text{ m}^3 \text{ kg}^{-1} \text{ s}^{-2}$, $g \equiv \det(g_{\mu\nu})$ is the determinant of the space-time metric in (1.1), \mathcal{L}_M is the Lagrangian term describing any matter fields included in the theory, Λ is the cosmological constant and R is the Ricci scalar. This scalar is found from the Riemann tensor, $R^\rho_{\sigma\mu\nu}$ which is given by

$$R^\rho_{\sigma\mu\nu} = \partial_\mu \Gamma^\rho_{\nu\sigma} - \partial_\nu \Gamma^\rho_{\mu\sigma} + \Gamma^\rho_{\mu\lambda} \Gamma^\lambda_{\nu\sigma} - \Gamma^\rho_{\nu\lambda} \Gamma^\lambda_{\mu\sigma}, \quad (1.3)$$

where $\partial_\mu \equiv \partial/\partial x^\mu$ and $\Gamma^\rho_{\mu\nu}$ is an affine connection on the manifold given by

$$\begin{aligned} \Gamma^\rho_{\mu\nu} &= \frac{1}{2} g^{\rho\sigma} \Gamma_{\sigma\mu\nu} \\ &= \frac{1}{2} g^{\rho\sigma} (\partial_\nu g_{\sigma\mu} + \partial_\mu g_{\sigma\nu} - \partial_\sigma g_{\mu\nu}). \end{aligned} \quad (1.4)$$

From equation (1.4), we may define a covariant derivative that can transform between different tangent spaces using parallel transport as

$$X^\mu_{;\nu} \equiv \partial_\nu X^\mu + \Gamma^\mu_{\nu\rho} X^\rho, \quad (1.5)$$

where X^μ is some arbitrary contravariant vector. The Ricci curvature tensor may be found by performing a contraction over the first and third indices of $R^\sigma_{\mu\rho\nu}$,

$$R_{\mu\nu} = R^\rho_{\mu\rho\nu} = g^{\sigma\rho} R_{\sigma\mu\rho\nu}, \quad (1.6)$$

and the Ricci scalar can be found by contracting indices on the Ricci tensor as

$$R = g^{\mu\nu} R_{\mu\nu} = g^{\sigma\rho} g^{\mu\nu} R_{\sigma\mu\rho\nu}. \quad (1.7)$$

The Einstein field equations [Einstein, 1916] are given in terms of these different quantities by varying (1.2) with respect to the field metric $g_{\mu\nu}$ as

$$R_{\mu\nu} - \frac{1}{2} R g_{\mu\nu} = \frac{1}{M_{\text{P}}^2} (T_{\mu\nu} + \Lambda g_{\mu\nu}), \quad (1.8)$$

where $T_{\mu\nu}$ is the stress-energy tensor and is given by the variation with respect to the matter content as

$$T_{\mu\nu} = -2 \frac{\delta \mathcal{L}_M}{\delta g^{\mu\nu}} + g_{\mu\nu} \mathcal{L}_M. \quad (1.9)$$

If we assume the matter content of the universe behaves as a perfect fluid that is homogeneous and isotropic as described by the FLRW metric then we can write the stress-energy tensor in a simpler form as

$$T_{\mu\nu} = (\rho + P) u_\mu u_\nu + P g_{\mu\nu}, \quad (1.10)$$

where ρ denotes the energy density, P is the pressure and $u_\mu(t, \mathbf{x})$ is the 4-velocity giving the fluid's flow. For a comoving observer, isotropy implies that the spatial components of the 4-velocity must be zero since the energy and momentum should not depend on a direction and homogeneity implies that the stress-energy tensor should only evolve with the time components which means the 4-velocity is given by $u_\mu(t, \mathbf{x}) = (1, 0, 0, 0)$.

1.2.2 Friedmann equations

Equation (1.10) can be used to find conservation laws as the stress-energy tensor is a conserved Noether current which means the covariant derivative must equal zero,

$$T^\mu_{\nu;\mu} = \partial_\mu T^\mu_\nu + \Gamma^\mu_{\mu\lambda} T^\lambda_\nu - \Gamma^\lambda_{\mu\nu} T^\mu_\lambda = 0, \quad (1.11)$$

where the continuity equation is given from the evolution of the energy density ($\nu = 0$) as

$$\dot{\rho} + 3\frac{\dot{a}}{a}(1+w)\rho = 0, \quad (1.12)$$

and the equation of state is given by $w = p/\rho$. This equation can be integrated to give the evolution of the scale factor for each matter component by using each component's dependency on pressure. For non-relativistic matter, the pressure is negligible ($P = 0 \implies w_{\text{mat}} = 0$), so equation (1.12) gives $\rho_{\text{mat}} \propto a^{-3}$. We can define radiation as any relativistic particle having pressure equal to one-third of the energy density ($P = \frac{1}{3}\rho \implies w_{\text{rad}} = \frac{1}{3}$), which gives $\rho_{\text{rad}} \propto a^{-4}$. The dark-energy component associated with the cosmological constant, Λ , has a negative-pressure ($P = -\rho \implies w_{\Lambda} = -1$) which implies the energy-density is constant with $\rho_{\Lambda} \propto a^0$ from equation (1.12). These densities can all be combined by parametrising according to their equation of state as

$$\rho(a) \propto a^{-3(1+w)}. \quad (1.13)$$

Having specified the form of the stress-energy tensor and the metric, we can use the Einstein field equations (1.8) to give the first Friedmann equation [Friedman, 1922] from the time-time component as

$$H^2 \equiv \left(\frac{\dot{a}}{a}\right)^2 = \frac{1}{3M_{\text{P}}^2}\rho - \frac{k}{a^2} + \frac{1}{3}\Lambda, \quad (1.14)$$

where we have given the definition of the Hubble parameter as $H \equiv \dot{a}/a$. The second Friedmann equation is obtained from the trace of the Einstein field equations (1.8) and then using the first Friedmann equation (1.14) to eliminate terms to find

$$\frac{\ddot{a}}{a} = -\frac{1}{6M_{\text{P}}^2}(1+3w)\rho + \frac{\Lambda}{3}, \quad (1.15)$$

where $\ddot{a} \equiv d^2a/dt^2$ and is also known as the acceleration equation. This can also be rewritten in terms of a deceleration parameter q , which has the definition

$$q \equiv -\frac{\ddot{a}a}{\dot{a}^2} = \frac{(1+3w)\rho}{6M_{\text{P}}^2H^2} - \frac{\Lambda}{3H^2}, \quad (1.16)$$

where the sign convention is chosen so that when $q > 0$, the universe is decelerating and when $q < 0$, it is accelerating instead.

Model building.—Cosmologists use these equations to determine how the geometry of the universe depends on the individual matter components discussed previously. This is done using a critical density which is defined from equation (1.14) for a flat universe ($k = 0$) with no contribution from the cosmological constant ($\Lambda = 0$) as

$$\rho_{\text{crit}} = 3H^2M_{\text{P}}^2, \quad (1.17)$$

which can then be used to define dimensionless density parameters

$$\Omega_{i,0} \equiv \frac{\rho_{i,0}}{\rho_{\text{crit},0}}, \quad (1.18)$$

where i is an index specifying each matter component and the label 0 is used to indicate when these are the present-day measured values. This allows the deceleration parameter in equation (1.16) to be written more simply as

$$q = \frac{1}{2}\Omega_{\text{mat}} + \Omega_{\text{rad}} - \Omega_{\Lambda}, \quad (1.19)$$

where we can see that when $(\Omega_{\text{mat}}/2 + \Omega_{\text{rad}}) < \Omega_{\Lambda}$ the universe expansion is accelerating as we measure today.

Equation (1.14) can also be rewritten in terms of these parameters by using each component's dependence on the scale-factor as

$$\frac{H}{H_0} = \sqrt{\Omega_{\text{mat}}a^{-3} + \Omega_{\text{rad}}a^{-4} + \Omega_{\text{k}}a^{-2} + \Omega_{\Lambda}}, \quad (1.20)$$

where the curvature and Λ density parameters are defined slightly differently as $\Omega_{\text{k}} \equiv -k/(a_0H_0)^2$ and $\Omega_{\Lambda} \equiv \Lambda/3H^2$ respectively so that there is no curvature contribution in a flat universe. As equation (1.20) is a differential equation in a and t , we can find how the scale factor for each matter component depends on time by assuming the evolution of the scale factor is dominated by that single component ($\Omega_{i,0} = 1$) and then integrating the equation. During matter-domination, we find $a(t) \propto t^{2/3}$, whereas for radiation-domination, the solution gives $a(t) \propto t^{1/2}$ and for Λ -domination, the scale-factor evolves exponentially as $a(t) \propto e^{Ht}$ which gives the accelerating expansion associated with dark-energy. This can also be done with all the terms with their measured values included and numerically integrated to find the time periods each component was dominant for and when the dominant component changed.

From equation (1.20), we may define the cosmological redshift, z , which is given by

$$a(t) = \frac{a}{a_0} = \frac{1}{(1+z)}, \quad (1.21)$$

where we recall that the scale-factor is normalised so that $a_0 = 1$. This relation can be used to determine the redshift of different epochs in the universe such as when the matter and radiation density contributions are equal (z_{eq}) or the epoch of reionisation (z_{re}). The redshift can also be used to form measures of distance such as the *angular diameter distance* and the *luminosity distance* which are respectively used by observational cosmologists to form *standard rulers* and *standard candles*. These standard measures were used to find the Baryon Acoustic Oscillations (BAOs) peak [Eisenstein et al., 2005] and with type Ia

Parameters	Measurement	68% Confidence region
$\Omega_b h^2$	0.02242	0.00014
$\Omega_c h^2$	0.11933	0.00091
$H_0[\text{km s}^{-1} \text{Mpc}^{-1}]$	67.66	0.42
Ω_Λ	0.6889	0.0056
Ω_m	0.3111	0.0056
Ω_k	0.001	0.002
z_{eq}	3387	21
$\Omega_R[\times 10^{-5}]$	9.182	0.175

Table 1.1: Planck 2018 results taken from [Aghanim et al., 2018] for the present values of the following cosmological parameters: baryon-density, cold dark-matter density (with $h \equiv H_0/100\text{km s}^{-1} \text{Mpc}^{-1}$), Hubble constant, dark-energy density, matter density (baryons + cold dark-matter), curvature density, redshift of radiation-matter equality and radiation density (given from $\Omega_R = \Omega_m/(1 + z_{\text{eq}})$).

supernovae to determine that the expansion of the universe is accelerating [Perlmutter et al., 1999, Riess et al., 1998].

Thermal history & Λ CDM model.— These equations are enough to discuss the dynamics of the early universe and to give a brief overview of the thermal history up until production of the Cosmic Microwave Background (CMB). In this description, the *equilibrium distribution function* for different particle species follow the Fermi-Dirac or Bose-Einstein distributions for fermions and bosons respectively

$$f_i(p, t) = \frac{g_i}{(2\pi)^3} \left[\exp\left(\frac{E_i(p) - \mu}{T}\right) \pm 1 \right]^{-1}, \quad (1.22)$$

where i denotes the specific particle, g_i is the spin degeneracy factor, $E_i(p) = \sqrt{p^2 + m^2}$ is the energy of the particle, μ_i is the chemical potential, T_i is the temperature, the ± 1 is for fermions and bosons respectively and we use natural units where the Boltzmann constant is $k_B = 1$. This distribution function gives the number of particles with a 3-momentum element $d^3\mathbf{p}$ contained in a volume element $d^3\mathbf{x}$. We can integrate equation (1.22) to obtain the number density n , energy density ρ and pressure density P respectively as

$$\begin{aligned} n &= \int f_i(p, t) d^3\mathbf{p}, \\ \rho &= \int E(p) f_i(p, t) d^3\mathbf{p}, \\ P &= \int \frac{p^2}{3E(p)} f_i(p, t) d^3\mathbf{p}. \end{aligned} \quad (1.23)$$

As the universe expands and cools, different particles become Boltzmann suppressed in equation (1.22) when the temperature becomes less than the mass of a given particle and their number density begins to decrease as the universe expands. This is interpreted as the epoch when the universe is no longer hot enough to produce that particle via pair production and the particle becomes non-relativistic so it instead begins to annihilate.

This particle history begins with *baryogenesis* where through a currently-unknown process, an overabundance of matter is produced over antimatter. At a temperature of 100GeV, the *electro weak phase transition* begins where particles began to get their masses via the Higgs mechanism and at $T \sim 150\text{MeV}$, the universe is cool enough for the quarks to form mesons and baryons in the *QCD phase transition*. As the lightest particles in the standard model, the neutrinos were the first particles to decouple from thermal equilibrium at $T \sim 1\text{MeV}$. Next, *electron-positron annihilation* begins at $T \sim 500\text{keV}$ and the annihilation energy is transferred to the photons but not the decoupled neutrinos causing there to be a Cosmic Neutrino Background (C ν B) that is slightly cooler than the CMB.

The production of light elements in *Big-bang Nucleosynthesis* (BBN) is dependent initially on the abundances of protons and neutrons which are controlled in the early universe via the weak interaction mainly in β^\pm decay. This continues in equilibrium until $T \sim 1\text{MeV}$ when the neutrinos decouple but nucleosynthesis cannot begin then because the lightest elements like deuterium (D) have binding energies $E \sim \mathcal{O}(\text{MeV})$ so that any elements formed are immediately broken down via photodissociation. BBN doesn't begin producing a significant amount of deuterium until $T \sim 100\text{keV}$ which is mainly used to produce helium (^4He) with much smaller abundances of beryllium (^7Be) and lithium (^7Li). BBN finishes soon afterwards because the universe isn't hot enough to produce heavier elements due to their Coulomb barriers. However the predicted relative abundances of these elements [Peebles, 1966] is one of the most successful cosmological predictions when compared with measurements.

The universe transitioned from being radiation dominated to matter dominated during the *matter-radiation equality* epoch when the temperature is $T \sim 0.75\text{eV}$. Eventually the universe cools enough for electrons to preferentially combine with protons to form neutral hydrogen in *recombination* at $T \sim 0.3\text{eV}$ where the decrease in the number of free electrons causes Thomson scattering to stop between the electrons and photons. Finally, the photons decouple entirely in *photon decoupling* at a temperature $T \sim 0.25\text{eV}$ and time $t \sim 380,000\text{yrs}$ where the photons can now free-stream in the observed CMB we see today.

The ΛCDM cosmological model describes these processes well using 6 independent

parameters which are determined using measurements of the CMB made from various space telescopes such as **COBE** [Mather et al., 1994], **WMAP** [Hinshaw et al., 2013] and **PLANCK** [Aghanim et al., 2018]. The Planck 2018 results for some of these cosmological parameters (see [Lahav & Liddle, 2014] for a detailed description of both the independent and derived parameters) are summarised in Table 1.1. However, there are some problems with this hot big-bang model description as will be seen in the following sections.

1.2.3 Problems with the hot big-bang model

Despite the many successes of the Λ CDM model for making measurable predictions of the CMB and in giving a time-line of key events in the early universe, there are some problems in the measurements that remain unexplained by this model. In fact, the standard model of cosmology does not predict the observed homogeneities and isotropy we observe despite the use of the FLRW metric given in equation (1.1).

The horizon problem.—If we consider the distance travelled by a photon from the big-bang to recombination when the photon is able to travel freely as the CMB and then to an observer today, we first note that photons follow a null geodesic which means $ds^2 = 0$ in equation (1.1). This implies that

$$dt = a(t)d\chi, \quad (1.24)$$

where χ is the radial part of the FLRW metric and represents the comoving distance travelled by the photon. We may define a conformal time, $d\eta \equiv dt/a$, equal to this comoving distance

$$\chi = \int d\chi = \int_{\eta_i}^{\eta_0} d\eta \equiv \int_{t_i}^{t_0} \frac{dt}{a(t)} = \int_{\ln(a_i)}^{\ln(a_0)} d \ln a \frac{1}{aH}, \quad (1.25)$$

where t_i is the initial time, t_0 is the present time and in the last step we defined the comoving *Hubble radius* $(aH)^{-1}$. We can use equation (1.20) to show that the conformal time for a dominant matter component parametrised via its equation of state is

$$\eta(a, w) = \frac{2}{H_0(1+3w)} a^{\frac{1}{2}(1+3w)} = \frac{2}{H_0(1+3w)} (aH)^{-1}, \quad (1.26)$$

where we see that the conformal time and Hubble radius are almost equal. This conformal time is also known as the comoving particle horizon and is the furthest distance a photon could have travelled in a time t . From equation (1.26), it is simple to see that the scale factor evolves as $a(\eta) \propto \eta^{2/(1+3w)}$ for the different cosmological components.

This can be used in equation (1.25) with t set to be the recombination time ($t_{\text{re}} \sim 370,000$ yrs) to find the comoving distances between the big-bang and recombination and

between recombination and today which are $\chi_{\text{re}} \sim 300\text{Mpc}$ and $\chi_0 \sim 14000\text{Mpc}$ respectively. The ratio of these is $\chi_{\text{re}}/\chi_0 = 300\text{Mpc}/14000\text{Mpc} \sim 1^\circ$ which gives the expected angular size of patches in the CMB that are causally correlated. However, we measure the CMB today to have a temperature $T_0 = (2.72548 \pm 0.00057)\text{K}$ [Fixsen, 2009] with $\Delta T/T \sim 10^{-4}$ which indicates the CMB temperature is strongly correlated across the whole sky on angles much larger than causality predicts. A diagram demonstrating this problem can be seen in Figure 1.1.

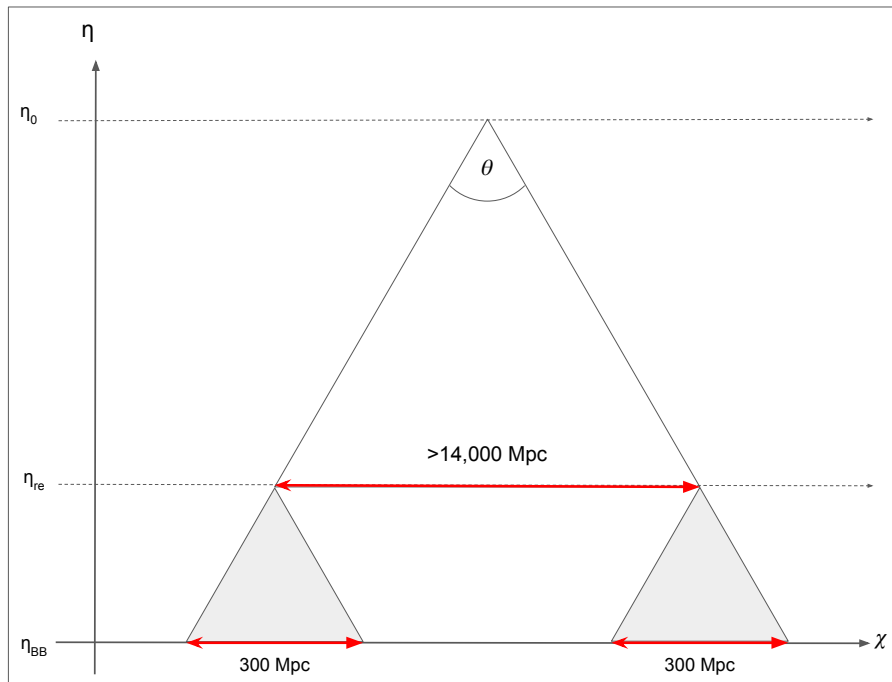


Figure 1.1: A space-time diagram demonstrating the horizon problem. The two grey triangles indicate photons that have propagated from the big-bang (η_{BB}) up until the CMB at η_{re} . Today at η_0 , we shouldn't see correlated regions for θ larger than 1° because it shouldn't be possible for the grey triangles to be causally connected.

The flatness problem.—In the first Friedmann equation (1.14), we saw that the spatial curvature parameter k is related to the energy densities and the Hubble parameter in a FLRW universe. If we consider this equation without a contribution from the Λ term ¹ and use the density's dependence on the scale factor given in equation (1.13), we have

$$|\Omega(t) - 1| = \frac{k}{a^2 H^2} \propto k a^{1+3w}, \quad (1.27)$$

¹The Λ term is excluded here because it gives many of the same dynamics as inflation ie. $\ddot{a} > 0$ and a negative-pressure. Excluding it doesn't make any difference to the outcome because the universe is radiation and matter dominated before the cosmological constant dominates much later.

where we recall that $w_{\text{mat}} = 0$ & $w_{\text{rad}} = \frac{1}{3}$. The right-hand side of this equation must be increasing in size because $|\Omega_{\text{mat}}(t) - 1| \propto t^{2/3}$ and $|\Omega_{\text{rad}}(t) - 1| \propto t$ which all implies the universe is being driven away from spatial flatness as time passes. Back in Table 1.1, we saw that the current measurement of the curvature density parameter is $\Omega_k = (0.001 \pm 0.002)$ or that the universe is spatially flat up to a 0.2% uncertainty. This means that the universe must have been incredibly flat in the early universe to within $\pm 10^{-30}$ during the electro-weak phase transition [Liddle, 1998]. The ‘fine-tuning’ of this parameter is unlikely without some physical process to describe why the early universe was so flat.

The hot-relics problem.—The third and final problem exists because the very early-universe would have been very hot with temperatures well above the Grand Unified Scale (GUT) at 10^{16} GeV. At these temperatures, the three forces in the standard model of particle physics are believed to become equal in strength and unify as one force and the GUT theories from beyond the standard physics (BSM) models predict that heavy ‘relic’ particles were produced and should be observed today. The most commonly discussed of these is the magnetic monopoles [’t Hooft, 1974, Polyakov, 1974] where isolated poles with a magnetic charge are produced due to a broken symmetry. Today, we haven’t found any of these relics which either implies that the GUT and standard cosmology theories are incompatible or that the unification ideas of GUT theories are incorrect.

1.3 Inflation

Cosmological inflation refers to the period of accelerating, quasi-exponential expansion of space occurring from 10^{-36} s to 10^{-32} s after the initial big-bang. It was originally proposed by several authors [Guth, 1981] [Linde, 1982] [Albrecht & Steinhardt, 1982] as a means of resolving the aforementioned problems with the hot big-bang model. As we will later see, it is also a way of producing the quantum fluctuations that later grew to produce the large-scale structure seen in the universe today.

1.3.1 Conditions for inflation

Exponential expansion implies that the scale factor evolves in proportion to the Hubble parameter as $a(t) \propto e^{Ht}$. As this expansion is accelerating, this must mean that $\dot{a} > 0$ and that the condition for inflation is

$$\ddot{a} > 0. \tag{1.28}$$

If we then insert this condition into the second Friedmann equation (1.15), we find a condition on the pressure that is

$$1 + 3w < 0 \iff w = \frac{P}{\rho} < -\frac{1}{3}, \quad (1.29)$$

where we see that inflation requires the cosmological fluid to have a *negative* pressure as the energy density ρ cannot be negative. This is clearly a violation of the strong energy condition (SEC) [Visser & Barcelo, 2000] which states that for normal matter $\rho + 3P > 0$. Next we consider the Hubble radius which is related to \dot{a} as $(aH)^{-1} = (\dot{a})^{-1}$ which we can then take a time-derivative of as

$$\frac{d}{dt} \left(\frac{1}{aH} \right) = \frac{d}{dt} \left(\frac{1}{\dot{a}} \right) = -\frac{\ddot{a}}{\dot{a}^2}, \quad (1.30)$$

where if we use the first inflation condition (1.28) for

$$\ddot{a} > 0 \iff \frac{d}{dt} \left(\frac{1}{aH} \right) < 0, \quad (1.31)$$

which means that during inflation the comoving Hubble radius is *shrinking*. This means the Hubble radius is now distinct from conformal time because in the η solution (1.26) with $a \rightarrow 0$ and $w < -\frac{1}{3}$, we have $\eta \rightarrow -\infty$. We can define the different length scales based on their size relative to the Hubble radius where a comoving distance x will be causally connected in the *sub-horizon* regime if $x < (aH)^{-1}$ and disconnected in the *super-horizon* regime when $x > (aH)^{-1}$. *Horizon-crossing* occurs when $x = (aH)^{-1}$. It is this property in particular that allows the problems with the hot big-bang model to be resolved because the particle horizon continues to *expand* while the Hubble radius *shrinks*.

Resolving the problems.—As we now have a shrinking Hubble radius with an expanding particle horizon, the causality issues in the horizon problem are now solved provided that the currently observable Hubble sphere is smaller than the Hubble radius at the start of inflation. That would mean all observable scales are now causally related on angular sizes with $\theta > 1^\circ$. In addition to this, the flatness problem is solved with $w \leq -1/3$ in equation (1.27) because the scale-factor dependence now gives $|\Omega(t) - 1| \rightarrow 0$ indicating the universe is tending to spatial flatness during inflation. Finally, the hot-relics problem is also solved because the massive expansion caused by inflation now means the abundance of relics should be dilute enough for them to be unobservable today.

The last question remaining is how much inflation is needed to solve these problems? In order to calculate this, we define another measure of time known as *e-foldings*, which is the number of times the universe has expanded by a factor of e

$$N = \ln \left(\frac{a_2}{a_1} \right) = \int_{t_1}^{t_2} H dt. \quad (1.32)$$

As previously mentioned, we have a condition on the Hubble radius to solve the horizon problem

$$a_0 H_0 < a_i H_i, \quad (1.33)$$

where ‘i’ indicates these values are at the start of inflation. In order to estimate the value of $a_i H_i$, we must assume *something* about the post-inflation history. This is usually a period of reheating, evolving like matter, before radiation domination begins up until the epoch of matter-radiation equality where matter becomes dominant until dark energy becomes more significant in the Λ -dominated era. There are various estimates made by different authors [Liddle & Leach, 2003] [Dodelson & Hui, 2003] [Remmen & Carroll, 2014] but typically we need $55 < N < 70$ e-folds to solve the horizon and flatness problems depending on the model of inflation and the assumptions on reheating.

1.3.2 Scalar fields

We will now see how a homogeneous, slowly-rolling scalar field, $\phi(t)$ can satisfy all the conditions set out in §1.3.1. For this scalar field, the Lagrangian term describing it is $\mathcal{L}_M = (\nabla\phi)^2/2 - V(\phi)$ which means the Einstein-Hilbert action (1.2) is

$$S_{\text{EH}} = \frac{1}{2} \int d^4x \sqrt{-g} (M_{\text{P}}^2 R + \partial_\mu \phi \partial^\mu \phi - 2V(\phi)), \quad (1.34)$$

where we have no contribution from the cosmological constant $\Lambda = 0$ as it has a negligible effect on the dynamics in the early-universe. The second term above is the *canonical* kinetic term and we define it as being *non-canonical* whenever it is modified by a term such as the field-space metric G_{IJ} which describes a non-trivial field space. As the field is slowly-rolling, the dynamics are largely determined by the potential energy $V(\phi)$ in the last term. It is usually the potential that determines a particular model of inflation; every unique $V(\phi)$ corresponds with a different model. If we minimise the action with respect to the field, we find the background field equation

$$\ddot{\phi} + 3H\dot{\phi} + V'(\phi) = 0, \quad (1.35)$$

where $V'(\phi) \equiv dV/d\phi$. If the potential term dominates over the $3H\dot{\phi}$ term, the solution for ϕ exponentially decays with the potential value whereas if the potential is subdominant then the solution is a harmonic oscillator solution with a damping term $3H\dot{\phi}$ known as Hubble damping. We can now use \mathcal{L}_M in equation (1.9) to find the stress-energy tensor

$$T_{\mu\nu} = \partial_\mu \phi \partial_\nu \phi - g_{\mu\nu} \left(\frac{1}{2} \partial_\lambda \phi \partial^\lambda \phi - V(\phi) \right). \quad (1.36)$$

If we assume the scalar field is also a perfect fluid, then the energy density is

$$\rho = \frac{1}{2}\dot{\phi}^2 + V(\phi), \quad (1.37)$$

and has a pressure given by

$$P = \frac{1}{2}\dot{\phi}^2 - V(\phi), \quad (1.38)$$

where the field equation (1.35) can also be found by inserting equations (1.37) & (1.38) into the continuity equation (1.12). The equation of state can be calculated for this scalar matter fluid

$$w_\phi = \frac{P}{\rho} = \frac{\frac{1}{2}\dot{\phi}^2 - V(\phi)}{\frac{1}{2}\dot{\phi}^2 + V(\phi)} \simeq -\frac{V(\phi)}{V(\phi)} = -1, \quad (1.39)$$

and we can see the SEC inflation condition (1.29) is satisfied when the potential $V(\phi)$ dominates over the kinetic term $\frac{1}{2}\dot{\phi}^2$. This is further verified when we use the energy density and pressure solutions to write the Friedmann equations for the scalar field as

$$H^2 = \frac{1}{3M_{\text{P}}^2} \left(\frac{1}{2}\dot{\phi}^2 + V(\phi) \right), \quad (1.40a)$$

$$\frac{\ddot{a}}{a} = -\frac{1}{3M_{\text{P}}^2} \left(\dot{\phi}^2 - V(\phi) \right), \quad (1.40b)$$

where we have taken the spatial curvature to be flat with $k = 0$. From the second Friedmann equation (1.40b), we can see that if $V(\phi) \gg \dot{\phi}^2$, then the condition $\ddot{a} > 0$ is satisfied and the scalar field is generating accelerating expansion as we need. As the condition that inflation gives a shrinking Hubble sphere is derived from the condition on \ddot{a} , we find all the requirements needed to solve the big-bang problems are met.

1.3.3 Slow-roll parameters and the attractor solution

The shrinking Hubble radius condition described by equation (1.31) can be used to show that the Hubble parameter is slowly evolving and that the scalar field is slowly rolling. If we perform a time derivative on that condition, we can define a slow-roll parameter ϵ

$$\frac{d}{dt} \left(\frac{1}{aH} \right) = -\frac{\dot{a}H + a\dot{H}}{(aH)^2} = -\frac{1}{a} \left(1 - \frac{\dot{H}}{H^2} \right) < 0 \implies \epsilon \equiv -\frac{\dot{H}}{H^2} < 1, \quad (1.41)$$

where we can immediately see the Hubble parameter must be slowly varying to satisfy this condition on ϵ . We can better define ϵ in terms of the fields by differentiating the Friedmann equation (1.40a) by using the field equation (1.35) to give $\dot{\phi}^2 = -2M_{\text{P}}^2\dot{H}$ and find

$$\epsilon_{\text{H}} \equiv -\frac{\dot{H}}{H^2} = \frac{\dot{\phi}^2}{2M_{\text{P}}^2H^2} \ll 1, \quad (1.42)$$

where inflation is usually defined to continue until $\epsilon_{\text{H}} = 1$ and the sub-script H indicates this parameter is defined in terms of H . In order to solve the horizon problem, we also need ϵ to be evolving slowly to ensure we have enough inflation. This is used to define the second slow-roll parameter η as

$$|\eta_{\text{H}}| \equiv \frac{d \ln \epsilon}{dN} = \frac{\dot{\epsilon}}{H\epsilon} \ll 1, \quad (1.43)$$

where we can see this condition implies $\dot{\epsilon}/\epsilon$ is small compared with the Hubble radius H^{-1} . These parameters can be given in terms of potentials by first using the condition that $\dot{\phi}^2 \ll V(\phi)$ to approximate the field and Friedmann equations respectively as

$$3H\dot{\phi} \approx V'(\phi), \quad (1.44a)$$

$$H^2 \approx \frac{V}{3M_{\text{P}}^2}, \quad (1.44b)$$

where collectively these equations are known as the *slow-roll approximation*. Equations (1.44a) & (1.44b) are used to define the potential slow-roll parameters with ϵ_{V} as

$$\epsilon_{\text{V}} \equiv \frac{M_{\text{P}}^2}{2} \left(\frac{V'(\phi)}{V(\phi)} \right)^2 \ll 1, \quad (1.45)$$

and the parameter η_{V} as

$$\eta_{\text{V}} \equiv M_{\text{P}}^2 \frac{V''(\phi)}{V} \ll 1, \quad (1.46)$$

where these parameters measure the slope and curvature of the potential respectively and in the slow-roll limit they are related to the Hubble parameter definitions as $\epsilon_{\text{H}} \rightarrow \epsilon_{\text{V}}$ and $\eta_{\text{H}} \rightarrow \eta_{\text{V}} - \epsilon_{\text{V}}$. From ϵ_{H} in equation (1.42), we can show that the slow-roll approximation gives an attractor solution where we again use $\dot{\phi}^2 = -2M_{\text{P}}^2 \dot{H}$ to find

$$\dot{\phi} = -2M_{\text{P}}^2 H'(\phi), \quad (1.47)$$

which can be inserted into the first Friedmann equation (1.40a) to give the Hamilton-Jacobi equation [Lyth & Liddle, 2009] as

$$[H'(\phi)]^2 - \frac{3}{2M_{\text{P}}^2} H^2(\phi) = -\frac{1}{2M_{\text{P}}^4} V(\phi). \quad (1.48)$$

This can be shown to have an attractor solution by inserting a linear perturbation in H as $H(\phi) = H_0(\phi) + \delta H(\phi)$ into equation (1.48) to obtain

$$H'_0 \delta H' \simeq \frac{3}{2M_{\text{P}}^2} H_0 \delta H, \quad (1.49)$$

which has the solution

$$\delta H(\phi) = \delta H(\phi_i) \exp \left(\frac{3}{2M_{\text{P}}^2} \int_{\phi_i}^{\phi} \frac{H_0(\phi)}{H'_0(\phi)} d\phi \right) = \delta H(\phi_i) \exp[-3N(\phi)], \quad (1.50)$$

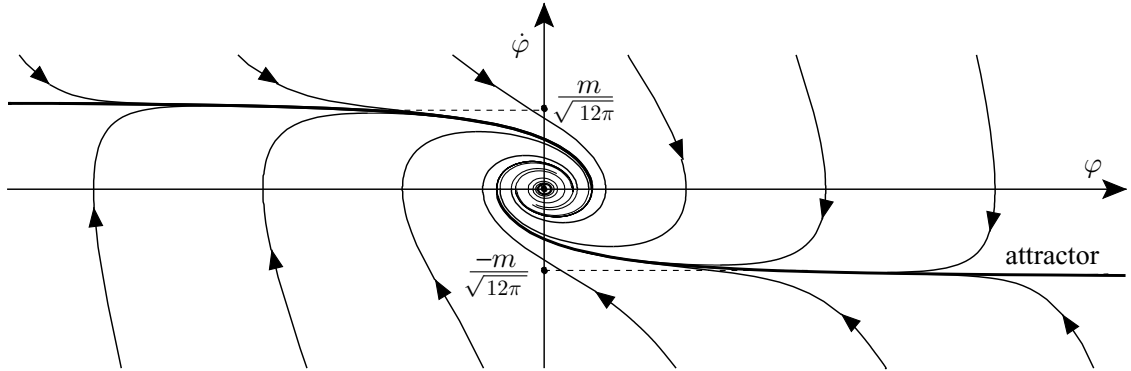


Figure 1.2: A phase-space plot in ϕ and $\dot{\phi}$ showing the inflation trajectories converging to the attractor solutions for the chaotic model of inflation with a potential $V = m^2\phi^2/2$. This is figure 5.3 taken from [Mukhanov, 2005].

where ϕ_i is the initial value of the scalar field at the start of inflation. From equation (1.50), we can see that $\delta H/H_0$ converges quickly to zero when $\epsilon_H \leq 1$ and the *attractor solution* will be reached for most initial values of ϕ_i . This can be seen particularly well in the $\phi - \dot{\phi}$ phase-space for chaotic inflation [Linde, 1983] with a potential $V(\phi) = \frac{1}{2}m^2\phi^2$. This is given in Figure 1.2, where we can see all initial values of ϕ and $\dot{\phi}$ form ‘trajectories’ that converge to the attractor solutions at $\pm m/\sqrt{12\pi}$ and remain together until they reach their final values. As the Hamilton-Jacobi equation (1.48) holds true for *any* slow-roll inflation model with $\epsilon_H < 1$, we can see that most inflation models will have attractor solutions with the incoming inflation trajectories converging to them.

1.4 Field perturbations

So far we have always considered a homogeneous scalar field $\phi(t)$, which only depends on time with no spatial dependence. However, if the scalar field is decomposed into a background component ϕ_0 that only depends on time and a small, spatially dependant perturbation $\delta\phi$ as $\phi(\mathbf{x}, t) = \phi_0(t) + \delta\phi(\mathbf{x}, t)$, then it was shown by various authors [Guth & Pi, 1982] [Bardeen et al., 1983] [Mukhanov, 1985] [Lyth, 1985] [Sasaki, 1986] that these small fluctuations in the field can generate the primordial density perturbations that later formed the large-scale structure in our universe. In this section, we will see how the predictions made from these calculations can later be used to constrain inflation using our measurements of the CMB.

1.4.1 Quantising the perturbations

We begin by considering an action that just contains the Lagrangian for the free-scalar field as

$$S = \frac{1}{2} \int d^4x \sqrt{-g} \{ \partial_\mu \phi \partial^\mu \phi - V(\phi) \}, \quad (1.51)$$

where x is an arbitrary space-time coordinate. In order to apply our perturbation, we take a Taylor expansion up to $\mathcal{O}(\delta\phi^2)$ in the action to obtain

$$S_2 = \frac{1}{2} \int d^4x \sqrt{-g} \{ \partial_\mu(\delta\phi) \partial^\mu(\delta\phi) - V_{,\phi\phi}(\phi) \delta\phi^2 \}, \quad (1.52)$$

where $\delta\phi(\mathbf{x}, t) \equiv \phi(\mathbf{x}, t) - \phi_0(t)$ and $V_{,\phi\phi}(\phi) = d^2V/d\phi^2$. For now, we consider the FLRW metric to be unperturbed and spatially flat which can be expressed using conformal time as

$$ds^2 = a^2(\eta) (-d\eta^2 + \delta_{ij} dx^i dx^j). \quad (1.53)$$

From equation (1.53), we have $\sqrt{-g} = a^4$, which allows us to rewrite equation (1.52) using conformal time as

$$S_2 = \frac{1}{2} \int d\eta d^3x a^2 \{ (\partial_\eta \delta\phi)^2 - (\nabla \delta\phi)^2 - a^2 V_{,\phi\phi}(\delta\phi)^2 \}, \quad (1.54)$$

where the action can be minimised by varying it with respect to the perturbation $\delta\phi$. Next we may define our Fourier convention as

$$f(\eta, \mathbf{x}) = \frac{1}{(2\pi)^3} \int d^3k \hat{f}(\eta, \mathbf{k}) e^{i\mathbf{k}\mathbf{x}}, \quad (1.55)$$

and transform equation (1.54) to obtain

$$(\delta\phi)'' + 2\frac{a'}{a}(\delta\phi)' + |\mathbf{k}|^2(\delta\phi) + a^2 V_{,\phi\phi}(\delta\phi) = 0 \quad (1.56)$$

where k is a comoving wave number defined as $k = 2\pi a/x$ and a prime $'$ denotes a differentiation with respect to η here. The quantisation of this field requires the perturbation is promoted to a quantum operator

$$\hat{\delta\phi}(\eta, \mathbf{x}) = \int \frac{d^3k}{(2\pi)^3} \left\{ \hat{a}(\mathbf{k}) f(\eta, k) + \hat{a}^\dagger(-\mathbf{k}) f^*(\eta, k) \right\} e^{i\mathbf{k}\mathbf{x}}, \quad (1.57)$$

where \hat{a}^\dagger and \hat{a} are creation and annihilation operators respectively, with canonical commutation relations $[\hat{a}, \hat{a}] = [\hat{a}^\dagger, \hat{a}^\dagger] = 0$ and $[\hat{a}(\mathbf{k}), \hat{a}^\dagger(\mathbf{q})] = (2\pi)^3 \delta(\mathbf{k} - \mathbf{q})$. We also need the canonical conjugate momentum which is given by

$$\delta\pi = \frac{dL}{d(\delta\phi)'} = a^2(\delta\phi)', \quad (1.58)$$

which is promoted to a quantum operator

$$\hat{\delta}\pi(\eta, \mathbf{x}) = \int \frac{d^3k}{(2\pi)^3} a^2(\eta) \left\{ \hat{a}(\mathbf{k}) f'(\eta, k) + \hat{a}^\dagger(-\mathbf{k}) f^{*'}(\eta, k) \right\} e^{i\mathbf{k}\mathbf{x}}, \quad (1.59)$$

where $f(\eta, \mathbf{x})$ is a function governing the time evolution that needs to be determined using the commutation relations between $\hat{\delta}\phi$ and $\hat{\delta}\pi$. These relations are given by

$$[\hat{a}(\mathbf{k}), \hat{a}^\dagger(\mathbf{q})] = (2\pi)^3 \delta(\mathbf{k} - \mathbf{q}), \quad (1.60a)$$

$$[\hat{\delta}\phi(\eta, \mathbf{x}), \hat{\delta}\pi(\eta, \mathbf{y})] = i\delta(\mathbf{x} - \mathbf{y}). \quad (1.60b)$$

If we insert equations (1.57) & (1.59) into commutation relation (1.60b) and use the commutation relation (1.60a) for the creation and annihilation operators, we find the *Wronskian condition*

$$a^2(\eta) \left\{ f(\eta, k) f^{*'}(\eta, k) - f^*(\eta, k) f'(\eta, k) \right\} = i. \quad (1.61)$$

Finding $f(\eta, k)$ needs us to use the η -dependence of $a(\eta)$ for de-Sitter space with $a = e^{Ht}$ which gives $\eta = -(aH)^{-1}$ and $a(\eta) = -(H\eta)^{-1}$. The function $f(\eta, k)$ must satisfy the perturbed field equation (1.56)

$$f''(\eta, k) - \frac{2}{\eta} f'(\eta, k) + \{k^2 + a^2 V_{,\phi\phi}\} f(\eta, k) = 0. \quad (1.62)$$

In slow-roll inflation, we can assume $k^2 \gg a^2 V_{,\phi\phi}$ because the slow-roll parameter η_V is proportional to $V_{,\phi\phi}$ and $\eta_V \sim 0$ during inflation. Neglecting the potential term means equation (1.62) is satisfied with

$$f(\eta, k) = |A|(1 - ik\eta)e^{ik\eta}, \quad (1.63)$$

with $|A|$ being a normalisation constant needed to satisfy the Wronskian condition. When applying the Wronskian condition, we find $|A| = H/\sqrt{2k^3}$ which allows us to fully define the field operators [Chernikov & Tagirov, 1968] [Schomblond & Spindel, 1976] [Bunch & Davies, 1978] as

$$\hat{\delta}\phi(\eta, \mathbf{x}) = \int \frac{d^3k}{(2\pi)^3} \left\{ \frac{H}{\sqrt{2k^3}} \left(\hat{a}(\mathbf{k})(1 + ik\eta)e^{-ik\eta} + \hat{a}^\dagger(-\mathbf{k})(1 - ik\eta)e^{ik\eta} \right) \right\} e^{i\mathbf{k}\mathbf{x}}, \quad (1.64)$$

with a momentum operator

$$\hat{\delta}\pi(\eta, \mathbf{x}) = \int \frac{d^3k}{(2\pi)^3} \left\{ \frac{H}{\sqrt{2k^3}} \left(\hat{a}(\mathbf{k})k^2\eta e^{-ik\eta} + \hat{a}^\dagger(-\mathbf{k})k^2\eta e^{ik\eta} \right) \right\} e^{i\mathbf{k}\mathbf{x}}, \quad (1.65)$$

where the annihilation operator \hat{a} now annihilates the vacuum state as $\hat{a}(\mathbf{k})|0\rangle = 0$ for all \mathbf{k} . The creation operator \hat{a}^\dagger creates the particles compatible with the flat-field space state on subhorizon scales. This is the vacuum state seen by an observer who is in free-fall with

the expansion and is following a geodesic path. The two-point correlation function of this vacuum state is given by

$$\langle \hat{\delta}\phi(\eta, \mathbf{k}) \hat{\delta}\phi(\eta, \mathbf{k}') \rangle = (2\pi)^3 \frac{H^2}{2k^3} \left(1 + \frac{k^2}{a^2 H^2} \right) \delta(\mathbf{k} + \mathbf{k}'), \quad (1.66)$$

where we can define a power-spectrum $P_{\delta\phi}(k)$ using the definition $\langle \hat{\delta}\phi(\eta, \mathbf{k}) \hat{\delta}\phi(\eta, \mathbf{k}') \rangle \equiv (2\pi)^3 \delta(\mathbf{k} + \mathbf{k}') P_{\delta\phi}(k)$ to obtain

$$P_{\delta\phi}(k) = \frac{H^2}{2k^3} \left(1 + \frac{k^2}{a^2 H^2} \right). \quad (1.67)$$

The power spectrum measures the scale-dependence for the variation in the fluctuations $\delta\phi$ so that a larger power spectrum value corresponds with a larger variance in $\delta\phi$ for a particular value of k . From equation (1.67), we can see that it has almost no scale-dependence as for super-horizon modes with $k \ll aH$, the second term above doesn't contribute significantly to the power spectrum. In fact, on super-horizon scales with $k\eta \ll 1$, we lose the terms $\propto ik\eta$ in equation (1.64) and the commutator $[\hat{\delta}\phi(\eta, \mathbf{k}), \hat{\delta}\pi(\eta, \mathbf{q})] = 0$ on these scales. This is known as the *quantum-to-classical transition* [Starobinsky, 1982] [Polarski & Starobinsky, 1996] [Lyth & Seery, 2008] where the initial quantum fluctuations in $\delta\phi$ become classical, stochastic perturbations after horizon-crossing. It is through this process that the small-scale structure is amplified into the large-scale structure observed today.

1.4.2 Gauges and super-horizon conservation

At this point, we have only considered scalar perturbations in the field and neglected the scalar perturbations in the metric. However, there is not a unique way to choose the coordinates that define these perturbations so we choose a *gauge* that slices the spacetime onto a particular hypersurface. An observer in these gauge coordinates follows a time-like world line known as a *thread* with a four-velocity $u^\mu = dx^\mu/d\eta$ defining their *frame*. The perturbations in the fields can then be uniquely defined using *gauge-invariant* variables that do not change between different gauge choices. These can be defined using the FLRW metric containing arbitrarily perturbed scalar fields as

$$ds^2 = -(1 + 2A)dt^2 + 2a^2(t)\nabla_i B dx^i dt + a^2(t) [(1 - 2\psi)\gamma_{ij} + 2\nabla_i \nabla_j E] dx^i dx^j, \quad (1.68)$$

where A , B , ψ & E are four independent functions of time and ∇_i represents a covariant derivative with respect to the unperturbed spatial metric γ_{ij} . The quantity ψ can be identified as the gauge-dependant curvature perturbation of a fixed-t hypersurface which

in the gauge $t \rightarrow t + \delta t$ transforms as

$$\psi \rightarrow \psi' = \psi + H\delta t, \quad (1.69)$$

where we have first applied the transformation to $a(t)$ and then applied that to the $(1-2\psi)$ term in equation (1.68) whilst only keeping linear terms. This can be related to the energy density which transforms as

$$\rho \rightarrow \rho' = \delta\rho - \dot{\rho}\delta t. \quad (1.70)$$

If we set equation (1.70) to zero for constant density, we find $\delta t = \delta\rho/\dot{\rho}$ which can be used in equation (1.69) to define the *curvature perturbation on constant-density hypersurfaces* ζ [Bardeen, 1980] as

$$-\zeta = \psi + H\frac{\delta\rho}{\dot{\rho}}. \quad (1.71)$$

This can be related to the *comoving curvature perturbation* \mathcal{R} as the spatially flat Ricci scalar for the metric γ_{ij} for constant conformal time is

$$R^{(3)} = \frac{4}{a^2}\nabla^2\psi, \quad (1.72)$$

which allows us to define \mathcal{R} using $4\nabla^2\mathcal{R} = -a^2R^{(3)}$ and defines \mathcal{R} in terms of ψ too. Under a gauge transformation, ψ transforms as before, but we now define the comoving gauge as the slicing that observes no momentum density with $\delta T_i^0 = -\dot{\phi}\partial_i\delta\phi = 0$ which implies that $\delta\phi \rightarrow \delta\phi - \dot{\phi}\delta t = 0$ to give the definition of \mathcal{R} [Lukash, 1980] [Lyth, 1985] as

$$\mathcal{R} = \psi + H\frac{\delta\phi}{\dot{\phi}}. \quad (1.73)$$

During slow-roll inflation, the energy-density perturbation $\delta\rho$ is dominated by the scalar field perturbation $\delta\phi$ which makes $-\zeta$ and \mathcal{R} equivalent which is also true on super-horizon scales where $-\zeta = \mathcal{R} + \mathcal{O}(k^2)$ [Baumann, 2011].

The curvature perturbations ζ and \mathcal{R} are vital because they are *gauge-invariant* – the coordinate definitions do not change the values of these when using different gauges so that no fictitious perturbations are produced when using them. We would also like these perturbations to be conserved on super-horizon scales so that we can find a transfer function to a given mode when that scale re-enters the horizon after inflation has ended. This function will relate the primordial power spectrum to the temperature fluctuations seen in the CMB today. To prove the conservation on super-horizon scales [Wands et al., 2000], we define a time-like vector orthogonal to the constant-t hypersurface as

$$n^\mu = (1 - A, -\nabla^i B). \quad (1.74)$$

As the energy-momentum tensor is covariantly conserved ($T^\mu{}_{\nu;\mu} = 0$), there is a locally conserved conservation law $n^\nu T^\mu{}_{\nu;\mu} = 0$ for the density perturbation which gives

$$\dot{\delta\rho} = -3H(\delta\rho + \delta P) + (\rho + P) \left[3\dot{\psi} - \nabla^2(\sigma + v + B) \right], \quad (1.75)$$

where $\sigma = \dot{E} - B$ is the shear and v represents the velocity of the fluid. We find $\dot{\zeta}$ by identifying that $\delta\rho = 0$ and $\psi = -\zeta$ whilst neglecting the divergence term, $\nabla^2(\sigma + v + B)$ because on super-horizon scales the Fourier transformation gives $\nabla^2/(aH)^2 = -k^2/(aH)^2 \sim 0$ to find

$$\dot{\zeta} = -\frac{H}{\rho + P} \delta P_{\text{nad}}, \quad (1.76)$$

where δP_{nad} is a non-adiabatic pressure perturbation. Equation (1.76) shows that ζ and therefore \mathcal{R} are conserved on super-horizon scales provided that the divergence term is negligible and that there are no non-adiabatic pressure perturbations – that is perturbations that satisfy

$$\delta P_{\text{nad}} = \delta P - \frac{\dot{P}}{\dot{\rho}} \delta\rho = 0, \quad (1.77)$$

which can be integrated to show that the pressure P must be a unique function of ρ .

1.4.3 Tensor perturbations

Expansion into scalar modes is not the only way to perturb the space-time metric and the corresponding Einstein equations. In fact, the metric can be further decomposed into two divergence-free spatial *vector* perturbations and a traceless, symmetric *tensor* perturbation as well as the four scalar modes discussed previously. This gives ten degrees of freedom in the perturbations because the vectors and tensor both have two independent components. For the vector perturbations, the Einstein equations all give solutions that decay with the expansion of the universe [Bertschinger, 2001] [Mukhanov, 2005] and these perturbations are not generated by inflation so we will not consider them here.

For the tensor modes, the perturbed FLRW line element is

$$ds^2 = a^2(\eta) \left[-d\eta^2 + (\delta_{ij} + 2h_{ij}) dx^i dx^j \right], \quad (1.78)$$

where h_{ij} is the traceless and transverse tensor perturbation. The Einstein field equation (1.8) can be used to find the equation of motion for this field as

$$(h_{\mathbf{k}}^s)'' + 2\frac{a'}{a}(h_{\mathbf{k}}^s)' + k^2(h_{\mathbf{k}}^s) = 0, \quad (1.79)$$

where we have assumed that T_{ij} has zero anisotropic stress like a perfect fluid. Under the Fourier decomposition, the tensor perturbation is now split into two scalar modes s for

each polarisation (+, ×). This means there are two copies of the same field equation found in the scalar mode: one for each polarisation ie. $M_{\text{P}} h_{ij}^s = 2(\delta\phi)$ with a factor of the Planck mass added to make h dimensionless. Therefore, we may use equation (1.66) to write the tensor two-point correlation function for each polarisation as

$$\langle h_{ij}^s(\mathbf{k}), h_{ij}^s(\mathbf{k}') \rangle = \frac{4}{M_{\text{P}}^2} \langle \hat{\delta}\phi(\mathbf{k}) \hat{\delta}\phi(\mathbf{k}') \rangle = (2\pi)^3 \frac{2H^2}{k^3 M_{\text{P}}^2} \delta(\mathbf{k} - \mathbf{k}'), \quad (1.80)$$

where we define the total tensor power-spectrum $P_{h_{ij}}$ as the sum over the two polarisations and use the definition $\langle h_{ij}(\mathbf{k}) h_{ij}(\mathbf{k}') \rangle \equiv (2\pi)^3 \delta(\mathbf{k} + \mathbf{k}') P_{h_{ij}}(k)$ to obtain

$$P_{h_{ij}}(k) = \frac{4H^2}{k^3 M_{\text{P}}^2}. \quad (1.81)$$

It is through this mechanism that inflation generates primordial gravitational waves where the fluctuations in the spatial metric are amplified by inflation. They are often called a “smoking gun” for inflation because a detection of these waves would give strong evidence as it is difficult to generate the tensor fluctuations without inflation. Moreover in the next section, we will see how the tensor power spectrum can be combined with the tensor to scalar ratio to probe the energy scale of inflation and hence the scales of structure for quantum gravity.

1.4.4 Observables for two-point statistics

In summary so far, we have a power spectrum for the scalar fluctuations given by equation (1.67) and a tensor power spectrum given by equation (1.81) as well as some gauge-invariant variables ζ and \mathcal{R} to describe them with. These variables are equivalent and conserved in the super-horizon regime so we can use equation (1.73) in the zero-curvature gauge ($\psi = 0$) to find the dimensionless power spectrum as

$$\mathcal{P}_{\zeta}(k) = \frac{k^3}{2\pi^2} \left(\frac{H}{\dot{\phi}} \right)^2 P_{\delta\phi}(k) \Big|_{k=aH} = \left(\frac{H}{\dot{\phi}} \right)^2 \left(\frac{H}{2\pi} \right)^2 \Big|_{k=aH}, \quad (1.82)$$

where the dimensionless normalisation has been chosen so that $\langle \zeta \zeta \rangle = \int_0^\infty \mathcal{P}_{\zeta}(k) d \ln k$ and the vertical bar indicates these should be evaluated at horizon crossing for the mode k . Similarly for the tensor power spectrum, we have the dimensionless version given by

$$\mathcal{P}_{h_{ij}}(k) = \frac{k^3}{2\pi^2} P_{h_{ij}}(k) \Big|_{k=aH} = \frac{2H^2}{\pi^2 M_{\text{P}}^2} \Big|_{k=aH}. \quad (1.83)$$

The scalar power spectrum can be parametrised in k -space with

$$\mathcal{P}_{\zeta}(k) = \mathcal{A}_s(k_*) \left(\frac{k}{k_*} \right)^{n_s(k_*) - 1}, \quad (1.84)$$

where \mathcal{A}_s gives the scalar spectrum amplitude and k_* is a pivot scale used as a reference. The k -dependence of the power spectrum is given by the *scalar spectral index*

$$n_s - 1 = \frac{d \ln \mathcal{P}_\zeta(k)}{d \ln k}, \quad (1.85)$$

where zero scale dependence is given by $n_s = 1$. This is similarly done for the tensor power spectrum with

$$\mathcal{P}_{h_{ij}}(k) = \mathcal{A}_t(k_*) \left(\frac{k}{k_*} \right)^{n_t(k_*)}, \quad (1.86)$$

and the *tensor spectral index*

$$n_t = \frac{d \ln \mathcal{P}_{h_{ij}}(k)}{d \ln k}, \quad (1.87)$$

with scale-invariance given by $n_t = 0$ instead. We define the *tensor-to-scalar ratio* r as

$$r = \frac{\mathcal{P}_{h_{ij}}(k)}{\mathcal{P}_\zeta(k)} = \frac{8}{M_{\text{P}}^2} \left(\frac{d\phi}{dN} \right)^2 \simeq \frac{\mathcal{A}_t}{\mathcal{A}_s}, \quad (1.88)$$

where we have used $dN = H dt$ to simplify and assumed zero scale dependence for both the scalar and tensor spectra with $n_s \simeq 1$ and $n_t \simeq 0$ in the approximation. As the tensor power spectrum (1.83) depends on both H and M_{P} , we can use this to determine the energy scale of inflation because we have measured the scalar power spectrum amplitude as $\mathcal{A}_s \sim 2 \times 10^{-9}$. If we assume the slow-roll approximation remains valid with $\epsilon \ll 1$, we can insert the tensor power spectrum (1.83) into r (1.88) and use the approximate Friedmann equation (1.44b) to give the potential in terms of r as

$$V^{\frac{1}{4}} \simeq \left(\frac{r}{0.01} \right)^{\frac{1}{4}} \cdot 10^{16} \text{GeV}, \quad (1.89)$$

which implies that a large value of the tensor to scalar ratio $r > 0.01$ corresponds with inflation happening at GUT scale energies. Therefore a measurement of primordial gravitational waves and hence a measurement of r would tell us about the energy scale of inflation *and* the scale of structure for quantum gravity. Moreover, determining the value of H during inflation would allow us to reconstruct and constrain the inflationary potential values *exactly* via ϵ_{H} (1.42) and the Hamilton-Jacobi equation (1.48).

We can also use equation (1.88) to determine the variation of the scalar field ϕ during inflation by rearranging for $d\phi$ and integrating to obtain the *Lyth bound* [Lyth, 1997] [Efstathiou & Mack, 2005] [Easther et al., 2006]

$$\left(\frac{\Delta\phi}{M_{\text{P}}} \right) \gtrsim \left(\frac{r}{0.01} \right)^{\frac{1}{2}}, \quad (1.90)$$

where in his analysis Lyth chose the scales $1 < \ell \lesssim 100$ which exit the horizon over $\Delta N \simeq 4$ and making this a lower limit on the field variation $\Delta\phi$. This assumes that r does

not significantly vary over ΔN and that slow-roll is valid with the first Hubble slow-roll parameter remaining small $\epsilon < 1$. If the scalar field value changes by $\Delta\phi = M_{\text{P}}$ throughout inflation, we have medium-field inflation with $r \sim 0.01$, whereas we have $r \ll 0.01$ and $r \gg 0.01$ for small- and large-field inflation respectively. We can also see from equation (1.89) that an inflation model with $V^{1/4} \sim 10^{16}\text{GeV}$ must have a scalar field variation of at least $1M_{\text{P}}$. The implication of this is that the effective field-theory description of inflation breaks down [Lyth, 1997] for large-field models with $\Delta\phi > M_{\text{P}}$ and we are unlikely to be able to determine the form of the potential even with a measurement of r . Evidently measuring primordial gravitational waves and the tensor to scalar ratio is *critical* for understanding the physics of inflation.

The parameters that describe the two-point statistics for inflation are accurately measured by the Planck 2018 [Akrami et al., 2018] and BICEP2/Keck Array [Ade et al., 2015] collaborations and can be seen in Table 1.2. As we can see, there is only an upper limit on the measurement of r indicating that the primordial gravitational waves have not been detected yet so there are no measurements of \mathcal{A}_t or n_t . Nevertheless, the upper-limit on r suggests that inflation was likely small-field and numerical calculations of \mathcal{A}_s and n_s can be used to constrain inflation by comparing with confidence regions obtained from sampling initial conditions. However as we will now see, the two-point correlation of the inflaton field isn't the *only* way to constrain inflation.

Parameters	Measurement	$\pm 68\%$ Confidence region
$\mathcal{A}_s [\times 10^{-9}]$	2.105	0.030
n_s	0.9649	0.0042
$r_{0.002}$	< 0.064	–

Table 1.2: A table giving the parameters that describe the statistics for the two-point correlation function taken from the Planck 2018 results [Akrami et al., 2018]. Note: $r_{0.002}$ indicates the pivot scale is chosen to be 0.002Mpc^{-1} .

1.5 Non-Gaussianities

At this point, we have seen that single-field inflation sources primordial density perturbations from quantum fluctuations in the scalar field. The density perturbations are found to be Gaussian-correlated since the two-point correlator is proportional to a delta-function which implies statistical homogeneity. Additionally, the perturbations are nearly *scale-invariant* because there is almost no k -dependence in the dimensionless power spectrum of

the field perturbation $\delta\phi$ with a small amount measured by the spectral index. These observations also show that the primordial fields are *adiabatic* which means that the pressure density P is a unique function of ρ for all particle species. However, these observations do not describe all the information in the primordial perturbations because we can measure the small departures from these predictions using *non-Gaussianities*, which come from higher-order correlation functions of the scalar perturbations.

1.5.1 The bispectrum and its shapes

If the primordial scalar fields were purely Gaussian, we would find that all odd- n correlation functions are zero and the even- n correlation functions are all proportional to products of 2-point correlation functions. However, even single-field inflation models predict a small amount of non-Gaussianity [Maldacena, 2003] [Falk et al., 1993] [Creminelli, 2003] and the potential for using measurements of non-Gaussianity to constrain inflation led cosmologists [Allen et al., 1987] [Salopek & Bond, 1990] [Falk et al., 1993] [Gangui et al., 1994] [Bartolo et al., 2004] to calculate the 3-point correlation function and its associated *bispectrum*. The 3-point function is conventionally written in terms of the curvature perturbation [Falk et al., 1993] [Gangui et al., 1994] as

$$\langle \zeta_{\mathbf{k}_1} \zeta_{\mathbf{k}_2} \zeta_{\mathbf{k}_3} \rangle = (2\pi)^3 \delta^3(\mathbf{k}_1 + \mathbf{k}_2 + \mathbf{k}_3) B(\mathbf{k}_1, \mathbf{k}_2, \mathbf{k}_3), \quad (1.91)$$

where B is the bispectrum and the subscripts indicate the momentum associated with each field. The bispectrum is conventionally written in terms of the *reduced bispectrum* f_{NL} as

$$B(\mathbf{k}_1, \mathbf{k}_2, \mathbf{k}_3) = \frac{6}{5} f_{\text{NL}}(k_1, k_2, k_3) [P_\zeta(k_1)P_\zeta(k_2) + \text{cyclic perms}], \quad (1.92)$$

where f_{NL} parametrises the amplitude of the bispectrum and measures the non-linearity of the fields.

The local model of bispectrum non-Gaussianities is defined by decomposing the curvature perturbation into a Gaussian and non-Gaussian part [Komatsu & Spergel, 2001] as

$$\zeta(x) = \zeta_g(x) - \frac{3}{5} f_{\text{NL}}^{\text{LOC}} [\zeta_g^2(x) - \langle \zeta_g^2(x) \rangle], \quad (1.93)$$

where ζ_g is a Gaussian perturbation and $f_{\text{NL}}^{\text{LOC}}$ is a constant parameter in the local model and is *not* the reduced bispectrum. Equations (1.92) & (1.93) can be combined to obtain [Maldacena, 2003] [Vernizzi & Wands, 2006]

$$B_{\text{LOCAL}}(\mathbf{k}_1, \mathbf{k}_2, \mathbf{k}_3) = -\frac{6}{5} f_{\text{NL}} P_\zeta^2 \frac{\sum_i k_i^3}{\prod_i k_i^3}, \quad (1.94)$$

Reduced bispectrum	Measurement	68% CL, stat
$f_{\text{NL}}^{\text{local}}$	0.8	5.0
$f_{\text{NL}}^{\text{equil}}$	-4	43
$f_{\text{NL}}^{\text{ortho}}$	-26	21

Table 1.3: A table giving different measurements of the reduced bispectrum for the different triangle configurations taken from the Planck 2015 results [Ade et al., 2016a]. Note: ‘68% CL, stat’ indicates there is an additional statistical error from not being able to model all of the bispectrum configurations.

where LOCAL indicates this is the most generic form of non-Gaussianity that developed on super-horizon scales and is *local* in real space. The main reason the bispectrum contains more information about the primordial perturbations than the power spectrum is that it is a function of three connected scales each giving different triangular *shapes*. In principle, an inflation model could predict a larger correlation in ζ for a particular triangular shape which allows us to look for the variations produced in the CMB by those scales and shapes to constrain the inflationary potential.

Classifying the triangles

Effectively there is an infinite number of triangular shapes possible to form in the bispectrum but in practice different types of inflation models predict strong correlations only for a particular triangular shape allowing them to be categorised. The first of these is the ‘squeezed’ bispectrum in which $k_3 \rightarrow 0$ and $k_1 \approx k_2$, leaving an isosceles triangle with a long wavelength modulator where the bispectrum has the proportionality

$$B^{(\text{squ})} \propto \frac{1}{k_1^3} \frac{1}{k_3^3}, \quad (1.95)$$

which is also proportional to the long- and short-wavelength power spectra. Multi-field models with detectable levels of squeezed non-Gaussianities typically obtain these via the transfer of superhorizon isocurvature perturbations in the second field to the adiabatic curvature perturbation. As this process is happening on superhorizon scales, we find the squeezed configurations are also well described using the local bispectrum as [Falk et al., 1993] [Gangui et al., 1994]

$$B^{\text{LOC}}(k_1, k_2, k_3) \simeq 2f_{\text{NL}}^{\text{LOC}} \left[\frac{1}{k_1^{4-n_s} k_2^{4-n_s}} + \text{cyclic} \right]. \quad (1.96)$$

For single-field slow-roll models, Maldacena found a relation between the non-linearity parameter and the scalar spectral index for squeezed configurations which is given by

$f_{\text{NL}}^{\text{sq}} \simeq -\frac{5}{12}\mathcal{O}(n_s - 1)$ [Maldacena, 2003] [Creminelli & Zaldarriaga, 2004] [Babich et al., 2004] which implies the level of squeezed non-Gaussianities must be small because slow-roll predicts almost no scale-dependence. This relation is therefore known as the *single-field consistency relation* because a detection of squeezed limit non-Gaussianities would rule out almost all single-field inflation models due to their unmeasurable squeezed bispectrum. Many of the inflation models producing non-Gaussianities in the squeezed configuration by using additional scalar field(s) are summarised in [Byrnes & Choi, 2010]. Alternatively, the curvaton model can also predict a significant amount of squeezed non-Gaussianities [Mollerach, 1990] [Lyth & Wands, 2002].

Single-field models typically produce non-Gaussianities in the “equilateral” configuration where the sides of the triangle are approximately equal $k_1 \approx k_2 \approx k_3$ and are often associated with the inflaton perturbation propagating with a speed of sound c_s smaller than the speed of light [Chen et al., 2007]. Inflation models predicting equilateral non-Gaussianity typically have non-standard kinetic terms with DBI inflation [Silverstein & Tong, 2004] representing a good example of this behaviour. Single-field models with non-canonical kinetic terms also have an “orthogonal” configuration [Senatore et al., 2010] which is an isosceles triangle with $k_3 \neq 0$ and models of inflation exhibiting this include ghost inflation [Arkani-Hamed et al., 2004] and Galileon-like models [Burrage et al., 2011]. There are many other possible configurations in addition to those discussed here with some of these discussed in the latest Planck data releases [Ade et al., 2014c] [Ade et al., 2016a] with the latest measurements of f_{NL} given in Table 1.3.

In order to simplify the parametrisation of the triangular shapes in the bispectrum, Fergusson et al. [Fergusson & Shellard, 2007] introduced two parameters α and β that measure the height and width of a triangle in terms of the total perimeter $k_t \equiv k_1 + k_2 + k_3$ so that each side is given as

$$k_1 = \frac{k_t}{4}(1 + \alpha + \beta), \quad (1.97a)$$

$$k_2 = \frac{k_t}{4}(1 - \alpha + \beta), \quad (1.97b)$$

$$k_3 = \frac{k_t}{2}(1 - \beta), \quad (1.97c)$$

where these parameters have the domains $0 \leq k_t \leq \infty$, $-(1-\beta) \leq \alpha \leq 1-\beta$ and $0 \leq \beta \leq 1$.

These parameters can be used along with the dimensionless bispectrum \mathcal{B} defined as

$$\mathcal{B}(k_1, k_2, k_3) \equiv (k_1 k_2 k_3)^2 B(k_1, k_2, k_3), \quad (1.98)$$

or with the reduced bispectrum magnitude $|f_{\text{NL}}|$ to represent these shapes in plots as demonstrated in Figure 1.3. From this, we can see that the squeezed configurations give

peaks in the corners of the triangle at $(\alpha = \pm 1, \beta = 0)$ & $(\alpha = 0, \beta = 1)$, whereas the equilateral configurations peak in the centre of the triangle at $(\alpha = 0, \beta = 1/3)$. By calculating the bispectrum for a variety of possible shapes, we can find the bispectrum values for particular templates and compare these with the CMB measurements to constrain the model of inflation used.

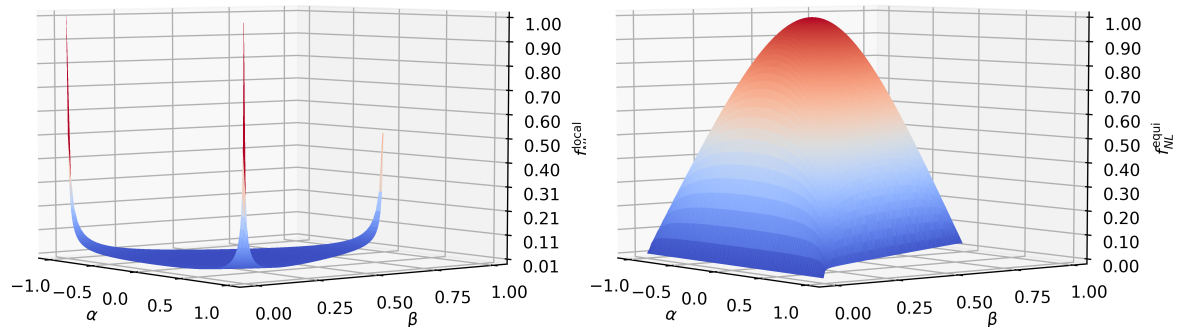


Figure 1.3: Plots of the bispectrum shapes demonstrating the $\alpha\beta$ -parameterisation with the f_{NL} values given as proportions of the maximum value. Left: local bispectrum shape; right: equilateral bispectrum shape.

Isocurvature modes

The potential introduction of fields other than the inflating one means that we must consider *isocurvature* modes coming from the interactions between the different fields which could give non-adiabatic (or entropy) perturbations such as (1.77). These non-adiabatic perturbations can change the curvature perturbations on super-horizon scales either during inflation [Garcia-Bellido & Wands, 1995] [Garcia-Bellido & Wands, 1996] [Tsujiikawa & Yajima, 2000] or after inflation [Kodama & Hamazaki, 1996] [Hamazaki & Kodama, 1996]. Gordon et al. [Gordon et al., 2001] gave a gauge-invariant definition of the total isocurvature perturbation as

$$\mathcal{S} = H \left(\frac{\delta P}{\dot{P}} - \frac{\delta \rho}{\dot{\rho}} \right), \quad (1.99)$$

which is extended to the entropy perturbation between any two quantities x and y with

$$\mathcal{S}_{xy} = H \left(\frac{\delta x}{\dot{x}} - \frac{\delta y}{\dot{y}} \right). \quad (1.100)$$

Multiple-field models of inflation always have isocurvature modes producing non-adiabatic perturbations like equation (1.100) where the different fields replace x and y . It is then possible that these perturbations decay into standard model particles such as neutrinos or a dark matter candidate. In this situation, the inflating adiabatic field is defined parallel to the inflation trajectory and the isocurvature mode(s) are defined orthogonally instead [Gordon et al., 2001], which can then be used to find non-adiabatic modes in the bispectrum

[Seery et al., 2012] [Elliston et al., 2011]. In addition, the adiabatic limits *must* have been reached with the isocurvature modes sufficiently decayed to guarantee that the multi-field model is predictive with a constant power spectrum \mathcal{P}_ζ and stable values of n_s and r [Renaux-Petel & Turzynski, 2015]. It should be noted however that the latest Planck constraints on inflation [Akrami et al., 2018] constrain the non-adiabatic contribution to the CMB to be zero up to approximately 1.5% so an inflation candidate model *must* have smaller isocurvature modes than the adiabatic modes.

1.5.2 Separate universes and the δN expansion

The previous discussion of the non-Gaussianity classifications should make it clear that a framework for calculating the cosmological perturbations for *multiple fields* is needed. This introduces problems because we must be able to accurately track these perturbations on super-horizon scales and also calculate any non-adiabatic modes coming from field interactions orthogonal to the inflaton trajectory.

It is for these reasons we make use of the *separate universe assumption* [Starobinsky, 1982] [Lyth, 1985] [Starobinsky, 1985] with regions smoothed on super-horizon scales ($k \ll aH$) where each ‘universe’ evolves as a homogeneous and isotropic FLRW region *locally* and has *separate* values for density, pressure and the field values. In this scenario, each field’s perturbations are absorbed in to the initial conditions of each patch separately instead of simultaneously solving the Einstein equations for each field. After each universe has been smoothed on a comoving scale k^{-1} , the spatial gradients of order $\mathcal{O}(k/a)$ are negligible because $k^{-1} \gg H^{-1}$ which makes the region homogeneous. The time evolution of the curvature and non-adiabatic perturbations can then be calculated by patching together all the different regions.

This approach was first used by Starobinsky [Starobinsky, 1982] [Starobinsky, 1985] and later by Lyth [Lyth, 1985] to calculate the super-horizon perturbations. The method was later developed to become the δN -expansion [Sasaki & Stewart, 1996] [Lyth et al., 2005] which begins with the ADM formalism of the metric [Arnowitt et al., 2008] given as

$$ds^2 = -N^2 dt^2 + h_{ij} (dx^i + N^i dt) (dx^j + N^j dt), \quad (1.101)$$

where N is the lapse function, N^i is the shift vector and h_{ij} is the spatial metric. The lapse function and the shift vector here are *Lagrange multipliers* because they have no time-dependence and therefore they are *not* dynamical variables. Instead, they determine the particular foliation of the 4D spacetime which is decomposed into 3D space-like

hypersurfaces Σ_t and the vector connecting two hypersurfaces is given by

$$t^\mu = Nn^\mu + N^\mu, \quad (1.102)$$

where the lapse N measures proper time and the shift vector N^i relates the spatial coordinates between the two hypersurfaces respectively. The time-like vector normal to the const- t hypersurface has its components given by $n_\mu = [-N, 0]$ and $n^\mu = [1/N, -N^i/N]$ as well as a spatial metric which is decomposed as

$$h_{ij} = a^2(t)e^{2\psi(t,x^i)}\tilde{h}_{ij}, \quad (1.103)$$

where $a(t)$ is the scale-factor, $\psi(t, x^i)$ is the curvature perturbation and $\det \tilde{h}_{ij} = 1$.

Instead of considering the perturbative expansion in terms of powers of the perturbations, we can use a gradient expansion method instead where at a fixed time each spatial gradient is multiplied by a factor ϵ which is then expanded as a power series. If ϵ is set to be a sufficiently large cosmological scale, we may then state the universe is smooth above this scale giving homogeneity on large scales as expected. If we use the observable scales defined in terms of the Hubble radius, $(aH)^{-1}$, to set ϵ as

$$\epsilon = \frac{k}{aH}, \quad (1.104)$$

we can see that on large scales with $k \rightarrow 0$, we also have $\epsilon \rightarrow 0$ allowing it to be expanded. This also implies that on super-horizon scales with $k \ll aH$, we have $\epsilon \rightarrow 0$ too. Then the *locally measurable* parts of the metric (1.101), with scales smaller than the smoothing scale but larger than the Hubble scale, reduces to the FLRW metric allowing us to use the separate universe approximation. As a result of this, the shift vector N^i must be $\mathcal{O}(\epsilon)$, the time-derivative of \tilde{h}_{ij} must be $\mathcal{O}(\epsilon^2)$ and the ADM metric simplifies to

$$ds^2 = -N^2 dt^2 + 2N_i dx^i dt + h_{ij} dx^i dx^j. \quad (1.105)$$

When using the separate universe assumption, we may assume the stress-energy tensor takes the perfect fluid form given in equation (1.10) as well as having a perfect-fluid 4-velocity. We can use time-like coordinates by using $g_{\mu\nu}u^\mu u^\nu = -1$ and then expand in terms of ϵ to find

$$u^\mu = \left[\frac{1}{\sqrt{N^2 - N_i N^i}}, 0 \right] = \left[\frac{1}{N}, 0 \right] + \mathcal{O}(\epsilon^2), \quad (1.106a)$$

$$u_\mu = \left[-\sqrt{N^2 - N_i N^i}, \frac{N_i}{\sqrt{N^2 - N_i N^i}} \right] = \left[-N, \frac{N_i}{N} \right] + \mathcal{O}(\epsilon^2). \quad (1.106b)$$

The expansion of u^μ up to linear order in these comoving coordinates is defined as

$$\theta \equiv \nabla_\mu u^\mu = \frac{1}{Na^3 e^{3\psi}} \partial_t \left(\frac{Na^3 e^{3\psi}}{N} + \mathcal{O}(\epsilon^2) \right) = \frac{3}{N} \left[\frac{\dot{a}}{a} + \dot{\psi} \right] + \mathcal{O}(\epsilon^2), \quad (1.107)$$

where we have used $\sqrt{-g} = Na^3 e^{3\psi}$ here. The results here are the same if we instead expanded with respect to the hypersurface normal n^μ so that $\theta = \theta_n$ at linear order. This means this result would be true for any gauge that gives $N^i = \mathcal{O}(\epsilon)$ and provided that no component of the fluid exchanges energy with a different component. This means we can define a local Hubble parameter using $3\tilde{H} = \theta_n$ to find

$$\tilde{H} = \frac{1}{N} \left(\frac{\dot{a}}{a} + \dot{\psi} \right) + \mathcal{O}(\epsilon^2). \quad (1.108)$$

This can be related to the curvature perturbation ψ by applying the energy-conservation equation $-u_\mu \nabla_\nu T^{\mu\nu} = 0$ to find

$$\frac{1}{N} \dot{\rho} + 3\tilde{H}(\rho + P) + \mathcal{O}(\epsilon^2) = 0. \quad (1.109)$$

If we insert equation (1.108) into equation (1.109), we find

$$\dot{\psi} = -\frac{\dot{\rho}}{3(\rho + P)} - \frac{\dot{a}}{a}. \quad (1.110)$$

This equation can be integrated to find [Lyth et al., 2005]

$$\begin{aligned} \psi(t_2, x^i) - \psi(t_1, x^i) &= -\frac{1}{3} \int_{t_1}^{t_2} dt \frac{\dot{\rho}}{\rho + P} - \ln \left(\frac{a(t_2)}{a(t_1)} \right) \\ &= N(t_2, t_1; x^i) - N_0(t_2, t_1) \equiv \delta N, \end{aligned} \quad (1.111)$$

where we have identified the number of e-folds associated with moving along the world-line x^i as $N(t_2, t_1; x^i)$ and N_0 as the background change in e-folds. This states that the change in ψ between slicing is given by the background number of e-folds subtracted from the *actual* number of e-folds giving the difference δN . If the pressure is adiabatic, it can be written as a unique function of ρ and the integration variable can be changed to $d\rho$ so that this equation becomes

$$\psi(t_2, x^i) - \psi(t_1, x^i) = -\frac{1}{3} \int_{\rho_1}^{\rho_2} \frac{d\rho}{\rho + P} - \ln \left(\frac{a(t_2)}{a(t_1)} \right), \quad (1.112)$$

which identifies the curvature perturbation on constant-density hypersurfaces ζ as

$$-\zeta \equiv \psi(t, x^i) + \frac{1}{3} \int_{\rho_1}^{\rho_2} \frac{d\rho}{\rho + P}. \quad (1.113)$$

The δN formula can be used to calculate the bispectrum by expanding in terms of e-fold derivatives [Lyth & Rodriguez, 2005] as

$$\zeta(t, \mathbf{x}) \approx \sum_i N_{,i}(t) \delta\phi_i + \frac{1}{2} \sum_{ij} N_{,ij}(t) \delta\phi_i \delta\phi_j + \dots, \quad (1.114)$$

where $N_{,i} = \partial N / \partial \phi^i$ and $N_{,ij} = \partial^2 N / \partial \phi^i \partial \phi^j$. We therefore expect the power spectrum to be written in terms of the first term only because the inner product must be $\mathcal{O}(\delta\phi_i^2)$ in the power spectrum. Similarly, the bispectrum terms of $\mathcal{O}(\delta\phi_i^3)$ are given from combinations of the first and second term as well as those containing the second term only. The power spectrum can be simply written as

$$\mathcal{P}_\zeta = \left(\frac{H}{2\pi} \right)^2 \sum_i N_{,i}^2(t) \Big|_{k=aH}. \quad (1.115)$$

The three-point correlation function is harder to calculate where the function in Fourier space to leading-order contains

$$\begin{aligned} \langle \zeta(\mathbf{k}_1) \zeta(\mathbf{k}_2) \zeta(\mathbf{k}_3) \rangle \supseteq & N_{,i} N_{,k} N_{,m} \langle \delta\phi^i(\mathbf{k}_1) \delta\phi^k(\mathbf{k}_2) \delta\phi^m(\mathbf{k}_3) \rangle + \\ & \frac{1}{2} N_{,i} N_{,k} N_{,mn} \langle \delta\phi^i(\mathbf{k}_1) \delta\phi^k(\mathbf{k}_2) (\delta\phi^m * \delta\phi^n)_{\mathbf{k}_3} \rangle + \text{perms}, \end{aligned} \quad (1.116)$$

where $*$ indicates a convolution and perms indicates permutations in \mathbf{k} . The first term above is the three-point function that was first calculated by Maldacena [Maldacena, 2003] but was neglected in the original δN expansion as it was assumed to be zero because it is an odd- n correlation function. If we only consider leading-order Feynman diagrams in the second term, we find

$$\begin{aligned} \langle \zeta(\mathbf{k}_1) \zeta(\mathbf{k}_2) \zeta(\mathbf{k}_3) \rangle \supseteq & \frac{1}{2} N_{,i} N_{,k} N_{,mn} (2\pi)^3 \delta(\mathbf{k}_1 + \mathbf{k}_2 + \mathbf{k}_3) \cdot \\ & \left[P^{im}(k_1) P^{kn}(k_2) + P^{in}(k_1) P^{km}(k_2) \right], \end{aligned} \quad (1.117)$$

where the momentum vector in the convolution has been integrated out and the combinations of indices are leading-order. If we compare this with the bispectrum (1.91) and use equation (1.115) for the power spectrum, we find

$$B_\zeta(k_1, k_2, k_3) \supseteq N_{,i} N_{,k} N_{,ik} \frac{H^4}{4k_1^3 k_2^3 k_3^3} (k_1^3 + k_2^3 + k_3^3). \quad (1.118)$$

This same procedure can be repeated for the local model and the curvature perturbation defined as $\zeta = \zeta_g - \frac{3}{5} f_{\text{NL}} \zeta_g^2$ to find B^{local} as

$$B^{\text{local}} \supseteq -\frac{6}{5} f_{\text{NL}}^{\text{local}} \left((N_{,i})^2 \frac{H^2}{2} \right)^2 \frac{k_1^3 + k_2^3 + k_3^3}{4k_1^3 k_2^3 k_3^3}. \quad (1.119)$$

As these expressions give the same *local* non-Gaussianities due to the separate universe approximation, they may be equated to find an equation for f_{NL} as

$$-\frac{3}{5} f_{\text{NL}} = \frac{\sum_{ij} N_{,i} N_{,j} N_{,ij}}{2 \left[\sum_i N_{,i}^2 \right]^2} + \text{higher order terms}. \quad (1.120)$$

In principle, equations (1.115), (1.119) & (1.120) can be used to directly calculate the power spectrum, bispectrum and reduced bispectrum respectively. A caveat of this method

however is that one must be able to find the variational derivatives of N which becomes computationally expensive for a large number of fields. In addition, these calculations also assume a super-horizon limit because of the separate universe assumption and would break down if we need to calculate sub-horizon effects.

1.5.3 Calculating the three-point function

In order to find all the quantum effects given in the sub-horizon regime of the bispectrum, the action describing the scalar field matter must be expanded to third-order as we want to calculate correlations of *three* fields. Maldacena [Maldacena, 2003] and later Seery [Seery & Lidsey, 2005a], [Seery & Lidsey, 2005b] were the first to calculate the full three-point function for *canonical* scalar fields which are defined with a Euclidean field-space metric given by $G_{IJ} = \delta_{IJ}$. This calculation begins with the scalar field action (1.34) with N fields denoted using the index I as

$$S = \frac{1}{2} \int d^4x \sqrt{-g} (R + \partial_\mu \phi^I \partial^\mu \phi_I - 2V(\phi)), \quad (1.121)$$

with $M_P = 1$. We use the ADM decomposition (1.101) to write the perturbative expansion of the action in terms of the lapse function and shift vector defined previously enabling us to find the scalar and tensor contributions to the non-Gaussianities. This calculation begins with splitting the kinetic terms into a temporal and spatial part as

$$\partial_\mu \phi^I \partial^\mu \phi_I = -\frac{1}{N^2} (\pi^I \pi_I) + h_{ij} \partial^i \phi^I \partial^j \phi_I, \quad (1.122)$$

where we define $\pi^I \equiv \dot{\phi}^I - N^i \partial_i \phi^I$. In order to find equations of motion for these fields, we must use the Gauss-Codazzi relation defined as

$$R = R^{(3)} - (\text{Tr } K)^2 + \text{Tr}(K^2), \quad (1.123)$$

where $R^{(3)}$ is the spatial Ricci scalar, K is the extrinsic curvature of the hypersurface orthogonal to the normal vector n_μ and the Gibbons-Hawking boundary term [Gibbons & Hawking, 1977] is removed to ensure the equations of motion are second-order. The extrinsic curvature is calculated using $K_{\mu\nu} = \nabla_\mu n_\nu$ to find

$$K_{\mu\nu} = \frac{1}{N} \left(-\frac{1}{2} \dot{h}_{ij} + N_{i|j} \right), \quad (1.124)$$

where the index $i|j$ denotes the covariant derivative compatible with the spatial metric h_{ij} . Equations (1.122), (1.123) & (1.124) can be used to write the action as

$$S = \frac{1}{2} \sqrt{h} \int d^4x \left[N \left(R^{(3)} - h_{ij} \partial^i \phi^I \partial^j \phi_I - 2V \right) + \frac{1}{N} \left(\pi^I \pi_I + E^{ij} E_{ij} - E^2 \right) \right], \quad (1.125)$$

where E_{ij} is the extrinsic curvature defined in (1.124). The constraint equations are found by varying under the lapse and shift which gives

$$R^{(3)} - h_{ij}\partial^i\phi^I\partial^j\phi_I - 2V - \frac{1}{N^2}\{\pi^I\pi_I + E^{ij}E_{ij} - E^2\} = 0, \quad (1.126)$$

from the lapse and

$$\nabla^i\left\{\frac{1}{N}(E_{ij} - h_{ij}E)\right\} = \frac{1}{N}\pi_I\partial_j\phi^I, \quad (1.127)$$

from the shift vector. Equations (1.126) & (1.127) can be solved for N and N^i respectively but we must first expand the spatial Ricci scalar to third-order for the tensor part. Therefore, we write the spatial metric as

$$h_{ij} = a^2 e^{\gamma_{ij}} \iff h^{ij} = \frac{1}{a^2} e^{-\gamma_{ij}}. \quad (1.128)$$

The calculation then uses equation (1.7) to calculate the Ricci scalar from equation (1.128) with a third-order Taylor expansion of the exponential terms (ie. $\exp(\gamma_{ij}) \approx \delta_{ij} + \gamma_{ij} + \frac{1}{2}\gamma_{ik}\gamma_{kj} + \frac{1}{6}\gamma_{ik}\gamma_{kl}\gamma_{lj} + \dots$) to find [Maldacena, 2003] [Dias et al., 2015b]

$$\begin{aligned} R^{(3)} = & -\frac{1}{4a^2}\partial_k\gamma_{ij}\partial_k\gamma_{ij} + \frac{1}{6a^2}\gamma_{ac}\gamma_{fb}(\partial_a\partial_b\gamma_{cf}) + \frac{1}{4a^2}\gamma_{fm}(\partial_m\gamma_{ba})(\partial_f\gamma_{ba}) \\ & - \frac{1}{6a^2}\gamma_{bd}(\partial_b\gamma_{ac})(\partial_a\gamma_{cd}) + \frac{1}{6a^2}\gamma_{an}(\partial_b\gamma_{ma})(\partial_m\gamma_{nb}), \end{aligned} \quad (1.129)$$

which gives an $\mathcal{O}(\gamma^2)$ term and four $\mathcal{O}(\gamma^3)$ terms. Then we define an expansion of the lapse as $N = 1 + \alpha_1 + \alpha_2 + \alpha_3 + \dots$ and a transverse and traceless expansion of the shift vector as $N_i = \partial_i\theta_{(n)} + \beta_{(n)}$ where the numerical and (n) subscripts indicates the order of expansion. These expansions can be used in equation (1.126) to obtain the lapse function [Seery & Lidsey, 2005a]

$$N = 1 + \frac{\dot{\phi}^I\delta\phi_I}{2H}, \quad (1.130)$$

and in equation (1.127) for the shift vector [Seery & Lidsey, 2005a]

$$N_i = -\frac{a^2}{2H}\partial^{-2}\left\{V\dot{\phi}^\alpha\delta\phi_\alpha + V_\alpha\delta\phi^\alpha + \dot{\phi}^\alpha\delta\dot{\phi}_\alpha\right\}, \quad (1.131)$$

where we see that these contain only linear functions of $\delta\phi$ as the second- & third-order expansions of these contribute nothing to the third-order action so they are excluded here. These expansions are inserted into the action (1.125) and simplified using the constraint equations and integration by parts to obtain the second-order action as

$$\begin{aligned} S_2 = \int d^4x a^3 \left\{ \delta\dot{\phi}^I\delta\phi_I - \frac{1}{a^2}\partial_i\delta\phi^I\partial^i\delta\phi_I - m_{IJ}\delta\phi^I\delta\phi^J + \right. \\ \left. \frac{1}{4}\dot{\gamma}_{ij}\dot{\gamma}_{ij} - \frac{1}{4a^2}\partial_k\gamma_{ij}\partial_k\gamma_{ij} \right\}, \end{aligned} \quad (1.132)$$

where the scalar interactions are on the first line with the tensor interactions on the second line and a mass-matrix m_{IJ} defined as

$$m_{IJ} = V_{,IJ} - \frac{1}{a^3} \frac{d}{dt} \left(\frac{a^3 \dot{\phi}_I \dot{\phi}_J}{H} \right). \quad (1.133)$$

This process is repeated for the third-order action, which we split into each type of interaction. The action containing 3 gravitons is given by

$$S_{\gamma\gamma\gamma} = \frac{1}{2} \int d^4x a^3 \left\{ \frac{1}{6a^2} \gamma_{ac} \gamma_{fb} (\partial_a \partial_b \gamma_{cf}) + \frac{1}{4a^2} \gamma_{fm} (\partial_m \gamma_{ba}) (\partial_f \gamma_{ba}) - \frac{1}{6a^2} \gamma_{bd} (\partial_b \gamma_{ac}) (\partial_a \gamma_{cd}) + \frac{1}{6a^2} \gamma_{an} (\partial_b \gamma_{ma}) (\partial_m \gamma_{nb}) \right\}, \quad (1.134)$$

with the action containing 2 gravitons and a scalar given by

$$S_{\gamma\gamma\phi} = \frac{1}{2} \int d^4x a^3 \left\{ -\frac{1}{2a^2} \dot{\gamma}_{ij} \partial_k \gamma_{ij} \partial_k \theta_{(1)} + \alpha_1 \left[-\frac{1}{4a^2} \partial_k \gamma_{ij} \partial_k \gamma_{ij} - \frac{1}{4} \dot{\gamma}_{ij} \dot{\gamma}_{ij} \right] \right\}, \quad (1.135)$$

with the action containing 1 graviton and 2 scalars given as

$$S_{\gamma\phi\phi} = \frac{1}{2} \int d^4x a^3 \left\{ \frac{1}{a^2} \gamma_{ij} \partial^i \delta\phi^I \partial^j \delta\phi_I - \frac{1}{a^4} \gamma_{ij} \partial^2 \theta_{(1)} \partial^i \partial^j \theta_{(1)} - \frac{1}{a^4} \gamma_{ij} \partial_k \theta_{(1)} \partial^i \partial^j \partial^k \theta_{(1)} + \frac{\alpha_1}{a^2} \dot{\gamma}_{ij} \partial^i \partial^j \theta_{(1)} \right\}, \quad (1.136)$$

and the action containing 3 scalars given as

$$S_{\phi\phi\phi} = \frac{1}{2} \int d^4x a^3 \left\{ -\frac{1}{3} V_{IJK} \delta\phi^I \delta\phi^J \delta\phi^K - \frac{2\delta\phi^I}{a^2} \partial_j \theta_{(1)} \partial^j \delta\phi_I + \alpha_1 \left[-\frac{1}{a^2} \partial_i \delta\phi^I \partial^i \delta\phi_I - V_{IJ} \delta\phi^I \delta\phi^J - \delta\dot{\phi}^I \delta\dot{\phi}_I - \frac{1}{a^4} \partial_i \partial_j \theta_{(1)} \partial_i \partial_j \theta_{(1)} + \frac{1}{a^4} \partial^2 \theta_{(1)} \partial^2 \theta_{(1)} + \alpha_1 \left(2\dot{\phi}^I \delta\dot{\phi}_I + \alpha_1 \left(6H^2 - \dot{\phi}^I \dot{\phi}_I \right) \right) \right] \right\}, \quad (1.137)$$

where we have written the action here in terms of α_1 and $\theta_{(1)}$ for brevity here. We will later see how these can be used with the transport method to compute evolution equations for the power spectrum and bispectrum during sub- and super-horizon regimes with all tree-level quantum effects included. Before this however, we must see how this calculation can be extended to include non-canonical fields.

1.6 Non-canonical fields

Thus far, the calculations for the bispectrum have all assumed a trivial relationship between the participating fields in which the field metric defining the field-space geometry is a Kronecker delta function. The motivation for the inclusion of these non-canonical fields

largely comes from the supergravity community in which the field-space metric is given by the Kähler potential and the scalar part of the superpotential is used as the inflating potential [Baumann & McAllister, 2015] [Roest et al., 2013]. Other sources of a non-trivial field-space include quasi-single-field inflation (QSFI) [Chen & Wang, 2010] and more recently the α -attractor models [Kallosh et al., 2013] [Ferrara et al., 2013] [Kallosh & Linde, 2013a].

The critical problem with introducing a non-trivial field-space is that each scalar field becomes an additional coordinate in the theory with each field having a dependence on the space-time coordinates as well as the field-space. Therefore, our gauge-invariant variables introduced previously may no longer be invariant after performing the perturbative expansion up to third-order. We will now see how this problem can be resolved by introducing a systematic approach first used by Gong & Tanaka [Gong & Tanaka, 2011] to make the field coordinates invariant similarly to the space-time coordinates.

1.6.1 Field-space covariance

If we now recall our field perturbation definition as $\delta\phi^I(\mathbf{x}, t) \equiv \phi^I(\mathbf{x}, t) - \phi_0^I(t)$, we realise the perturbation in the field $\delta\phi^I$ is given by the difference between the actual field ϕ^I and the background field ϕ_0^I . Provided this difference is sufficiently small, it should be possible to define a unique geodesic between these two points that comes from the field-space metric G_{IJ} . This geodesic requires an initial point given by ϕ_0^I and the initial velocity Q^I which is initially on the tangent-space of ϕ_0^I and is parametrised along the geodesic trajectory with $\lambda = 0$ at ϕ_0^I and $\lambda = \epsilon$ at ϕ^I . The field-space invariant geodesic equation is then

$$D_\lambda^2 \phi^I = \frac{d^2 \phi^I}{d\lambda^2} + \Gamma^I_{JK} \frac{d\phi^J}{d\lambda} \frac{d\phi^K}{d\lambda} = 0, \quad (1.138)$$

with the initial conditions

$$\phi^I|_{\lambda=0} = \phi_0^I, \quad (1.139)$$

$$D_\lambda \phi^I|_{\lambda=0} = \left. \frac{d\phi^I}{d\lambda} \right|_{\lambda=0} \equiv Q^I, \quad (1.140)$$

where Γ^I_{JK} is the field-space affine connection compatible with parallel transport between the vectors. If we expand ϕ^I as a power series around ϵ and use the geodesic equation to simplify second- and third-order derivatives, we get

$$\phi^I = \phi_0^I + Q^I \epsilon - \frac{1}{2} \Gamma^I_{JK} Q^J Q^K \epsilon^2 + \frac{1}{6} (\Gamma^I_{LM} \Gamma^M_{JK} - \Gamma^I_{JK;L}) Q^J Q^K Q^L \epsilon^3 + \dots, \quad (1.141)$$

where we can subtract ϕ_0^I and set $\epsilon = 1$ to obtain $\delta\phi^I$ as

$$\delta\phi^I = Q^I - \frac{1}{2} \Gamma^I_{JK} Q^J Q^K + \frac{1}{6} (\Gamma^I_{LM} \Gamma^M_{JK} - \Gamma^I_{JK;L}) Q^J Q^K Q^L + \dots. \quad (1.142)$$

This implies that we may write the field perturbation $\delta\phi^I$ in terms of Q^I at linear order and use that instead to write the action in a form that is both spacetime covariant and field-space covariant. The only part still needed is the covariant λ derivative of $\partial_\mu\phi^I$ which is

$$D_\lambda\partial_\mu\phi^I = \partial_\mu\frac{d\phi^I}{d\lambda} + \Gamma^I_{JK}\partial_\mu\phi^J\frac{d\phi^K}{d\lambda} = D_\mu Q^I. \quad (1.143)$$

The only question that remains is how does this change the perturbative expansion of the scalar field action (1.121)? Elliston et al. [Elliston et al., 2012] were the first to compute this before we later repeated the calculation [Butchers & Seery, 2018]. Under repeated λ -derivatives, the kinetic term $G_{IJ}\partial_\mu\phi^I\partial^\mu\phi^J$ needs commutation relations between the derivatives D_μ and D_λ which will become Riemann curvature tensor terms in the form $[\nabla_\lambda, \nabla_\mu]V^I = R^I_{JKL}V^JQ^K\partial_\mu\phi^L$ where V^I is an arbitrary vector. The potential $V(\phi^I)$ transforms as a scalar under a coordinate-change and the Ricci scalar R contains no information about the field indices, *all* of the extra terms needed for non-canonical terms are Riemann curvature tensors and the action is otherwise equivalent to a naïve covariantisation of equations (1.132)-(1.137). More details of this are found throughout the paper in Chapter 2 and particularly in the appendix 2.6 where the fully perturbed action is given in equations (2.88)-(2.93), the transport equations are given in equations (2.106a) & (2.106b) with the u-tensors given in equations (2.117a) & (2.117b), the 2-point and 3-point initial conditions are given in equations (2.128)-(2.129c) & (2.143)-(2.146) and the gauge transformations to ζ are given in (2.161a) & (2.161b).

1.6.2 The transport method

Having found the third-order action for the non-canonical scalar fields, we now need to discuss how to compute the bispectrum from it. In principle, this could be done using traditional methods where Feynman diagrams are found for the scalar-field action and then wave-functions and vertex integrals are calculated from them but this is complicated for an action with many terms such as (1.137). Consequently the *moment transport method* was first developed in [Mulryne et al., 2010] and [Mulryne et al., 2011] where the *transport equations* are differential equations that evolve *statistical moments* like an N-point correlation function of $\delta\phi$. Then a gauge transformation is used to find the ζ perturbations during the super-horizon epochs needed for computing observables like the power spectrum. This method was later extended to compute the spectral index in [Dias & Seery, 2012], before in [Seery et al., 2012] it was shown that raytracing techniques can be applied to compute the ODEs and the gauge transformation. The method was first applied to

find the bispectrum on curved field-space in [Elliston et al., 2012] and for the trispectrum² in [Anderson et al., 2012]. An important advantage of using the transport method was demonstrated in [Mulryne, 2013] where it was shown that the method can also be extended to compute inflationary perturbations on the quantum sub-horizon scales. Computing the bispectrum meant that a second-order gauge transformation to ζ needed to be found in [Dias et al., 2015a]. Finally, the method was deployed in several codes: `mTransport` [Dias et al., 2015b] for the two-point function with non-canonical fields, then `PyTransport` [Mulryne & Ronayne, 2016] and `CppTransport` [Dias et al., 2016] [Seery, 2016] initially for computing the bispectrum with canonical fields. `PyTransport` was extended to compute the bispectrum for non-trivial fields in [Ronayne & Mulryne, 2017] and in chapter 2, we present our work from [Butchers & Seery, 2018] where `CppTransport` was extended to use a curved field space.

1.7 Connecting inflation to the CMB

Inflation provides a framework for calculating numerous observable quantities that are different for each model analysed. However, these quantities are, at best, calculated at the end of inflation which is approximately 380,000 years before the CMB photons can free-stream after recombination. Therefore, further calculations are needed to relate the observed temperature anisotropies seen in the CMB with the calculated anisotropies predicted by a model of inflation and hence constrain the parameters of that model.

1.7.1 Temperature spectrum

The observed temperature fluctuations $\Delta T/T$ are seen as incoming photons streaming in a direction \mathbf{n} from the inside part of a sphere at a position \mathbf{x} and at a time t_0 . We therefore define the temperature fluctuations in terms of spherical harmonics, $Y_{\ell,m}(\mathbf{n})$, where statistical homogeneity implies these must only depend on the direction of the incoming photon, \mathbf{n} . Hence, the multipole expansion of the temperature fluctuations [Durrer, 2008] [Lyth & Liddle, 2009] is given in terms of the expansion coefficients, $a_{\ell m}$, as

$$\frac{\Delta T(\mathbf{n})}{T} = \sum_{\ell,m} a_{\ell m} Y_{\ell m}(\mathbf{n}), \quad (1.144)$$

²The trispectrum comes from a 4-point correlation function such as $\langle \zeta(\mathbf{k}_1)\zeta(\mathbf{k}_2)\zeta(\mathbf{k}_3)\zeta(\mathbf{k}_4) \rangle$ and is measured by non-linearity parameters g_{NL} & τ_{NL} . It won't be further discussed in the thesis but for a review, see [Byrnes & Choi, 2010] or [Sasaki et al., 2006] [Byrnes et al., 2006] [Seery et al., 2007] for calculations.

where statistical homogeneity and isotropy implies the ensemble average of the multipoles contains no diagonal components as

$$\langle a_{\ell m} a_{\ell' m'}^* \rangle = \delta_{\ell\ell'} \delta_{mm'} C_\ell, \quad (1.145)$$

where C_ℓ is the power spectrum of the CMB anisotropies. These can be found directly from the temperature power spectrum using the equation

$$\left\langle \frac{\Delta T(\mathbf{n})}{T} \frac{\Delta T(\mathbf{n}')}{T} \right\rangle = \sum_\ell \frac{2\ell + 1}{4\pi} C_\ell P_\ell(\cos \theta), \quad (1.146)$$

where P_ℓ gives the Legendre polynomials and θ is the angle between \mathbf{n} and \mathbf{n}' . The temperature fluctuations must be related to the Fourier modes of the incoming photons which can be represented using the Rayleigh plane-wave expansion [Hu & Sugiyama, 1995a] [Hu & Sugiyama, 1995b] [Hu & Sugiyama, 1996]. The primordial curvature perturbations, $\zeta(\mathbf{k})$, are then related to the CMB anisotropies using *transfer functions* $\Delta_\ell(k)$ which allow the harmonic components of $\Delta T/T$ to be read from equation (1.144) as

$$a_{\ell m} = 4\pi i^\ell \int \frac{d^3\mathbf{k}}{(2\pi)^3} \Delta_\ell(k) \zeta(\mathbf{k}) Y_{\ell m}(\hat{\mathbf{k}}). \quad (1.147)$$

The key CMB physics in equation (1.147) is contained in the transfer function $\Delta_\ell(k)$ which relates the curvature perturbation given at the end of inflation to the surface of last scattering at recombination. They must describe how the matter perturbations evolve throughout this period including all the cosmological events described in Section 1.2.2. This is achieved using cosmological perturbation theory where the stress-energy tensor in the Einstein equation is expanded in terms of perturbations in the energy density $\delta\rho$ and the pressure density δP . The solutions of these equations have different effects on the CMB power spectrum.

The first of these are the *acoustic oscillations* [Peebles & Yu, 1970] [Sunyaev & Zel'dovich, 1970] which originate from when the baryons were tightly coupled to the photons during the radiation-dominated era. Initially, the perturbations in the gravitational potential cause a gravitational collapse which is stopped by the photon's high pressure component. This process of collapsing and expanding repeated until the photons decoupled leaving peaks in the range $100 \leq \ell \leq 1000$ on the CMB. There is also the *Sachs-Wolfe effect* [Sachs & Wolfe, 1967] which is caused by the photons being gravitationally redshifted by varying amounts due to differences in the gravitational potential sourced from the primordial fluctuations. Additionally, there is the *Integrated Sachs-Wolfe effect* [Rees & Sciama, 1968] which is associated with the photons having to 'climb' out of potential wells on the path between the last scattering surface and our observations. These effects both

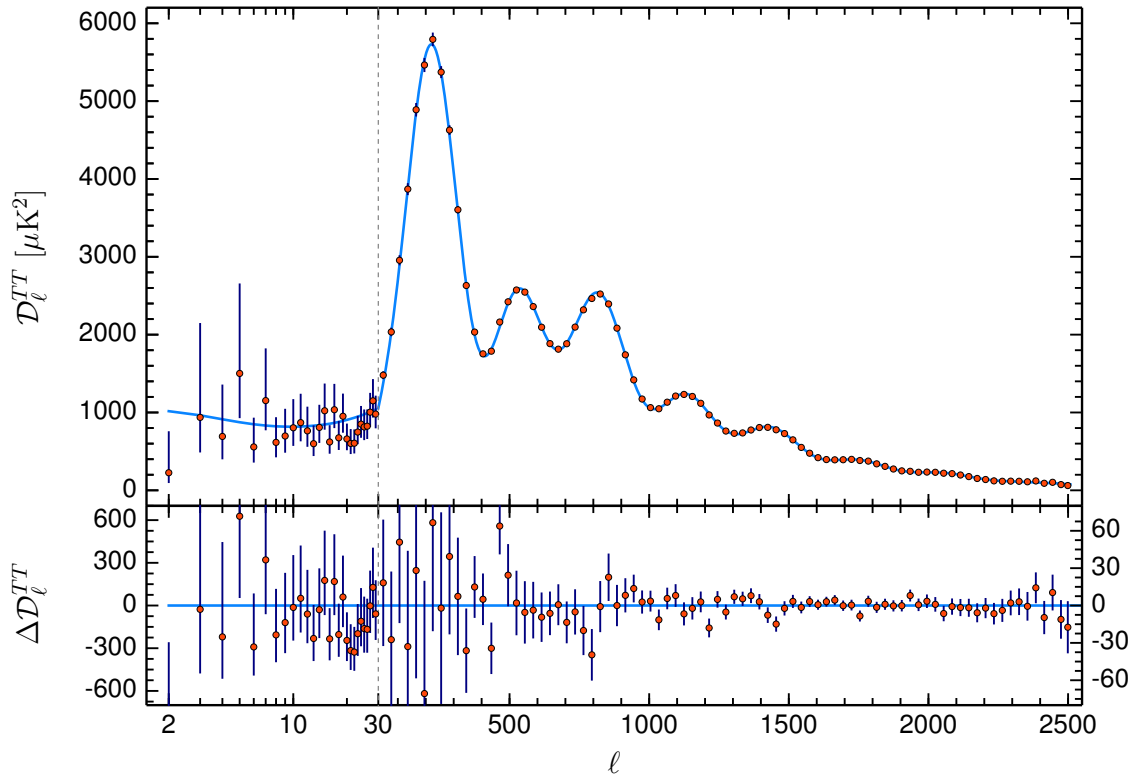


Figure 1.4: Planck 2018 results for the temperature power spectrum, taken from [Aghanim et al., 2018]. Red dots are the measurements and the blue line is the best-fit ΛCDM model with residuals given in the lower panel. $D_\ell \equiv \ell(\ell + 1)C_\ell/2\pi$.

cause the C_ℓ values to be increased on multipoles with $\ell \leq 90$. Finally on the smallest scales with $\ell \geq 1000$, the CMB power spectrum is *Silk damped* [Silk, 1968] because the recombination is not instantaneous so there is diffusion between the baryons and photons with damped oscillations.

The transfer functions that describe these physical effects are calculated by Boltzmann codes such as CAMB [Lewis et al., 2000] or CLASS [Lesgourgues, 2011] [Blas et al., 2011] which take an input of a primordial spectrum and cosmological parameters to predict the CMB power spectrum which can then be compared with observations. The results of these codes for the ΛCDM model can be seen plotted alongside the CMB power spectrum in Figure 1.4. We see all of the physical effects described in the previous paragraph and observe that ΛCDM gives an excellent fit apart from $\ell \leq 30$ where cosmic variance dominates the uncertainties.

1.7.2 Parameter inference

In principle, inflation should provide the initial conditions for the Boltzmann codes described previously because the values of the power spectrum and bispectrum can be found at the end of inflation which sets the initial values needed by the codes. The implication of this is that an inflation model with a particular set of initial conditions predicts a unique imprint on the CMB based on that model's perturbations. Therefore, we can discriminate between inflationary models by evaluating how well the model's predicted CMB matches the measurements. In addition, if we sample the underlying distributions for the parameters then we can estimate constraints on the inflation parameters using the quality of fit to the data. The *Bayesian framework* is ideal for achieving this goal because it allows us to update the probability of an event as we collect more data about the event. It relies on Bayes' theorem which is given as

$$P(\theta|\mathbf{X}, \alpha) = \frac{P(\mathbf{X}|\theta, \alpha) \cdot P(\theta|\alpha)}{P(\mathbf{X}|\alpha)}, \quad (1.148)$$

where θ is a vector containing the parameters of the model, \mathbf{X} is the observed sample of n data points for and α is any hyperparameter needed to describe the distribution function of θ . The term $P(\mathbf{X}|\theta, \alpha)$ is known as the *likelihood* and measures the probability of obtaining the data given the model $\mathcal{M}(\theta, \alpha)$. The term $P(\theta|\alpha)$ is known as the *prior* probability distribution function which measures the distribution of parameters before obtaining the data and represents our underlying 'beliefs' about the model. The $P(\mathbf{X}|\alpha)$ term is known as the *evidence* which is the probability of obtaining the data from the model with the uncertainty in the parameters marginalised out. The combination of these in equation (1.148) give the *posterior* probability distribution functions, $P(\theta|\mathbf{X}, \alpha)$, for any parameter in the model which collectively can be used to estimate the ideal parameters for obtaining the data.

The evidence is often difficult to calculate so typically the posterior distribution is calculated using only the numerator as

$$P(\theta|\mathbf{X}, \alpha) \propto P(\mathbf{X}|\theta, \alpha) \cdot P(\theta|\alpha), \quad (1.149)$$

which is justified because the evidence effectively normalises the posterior to account for all possible values of θ and is a constant when extracting parameters from the CMB. Priors are much harder to choose since the posterior could be preferentially influenced by the prior instead of the data. This is critical for a CMB analysis based on inflation parameters because the only information we have on these parameters comes from what is physically allowed by the theory. Hence, the priors on inflation parameters should be

weakly informative and assign equal probabilities to physically allowed values in the theory. The likelihood, \mathcal{L} , is much easier to obtain since the Planck collaboration provide codes [Aghanim et al., 2016] for computing it based on C_ℓ values from a predicted CMB spectrum. For data-points that are Gaussian distributed, the likelihood is given by

$$\mathcal{L} = \prod_i \frac{1}{\sqrt{2\pi\sigma_i^2}} \exp\left(-\frac{(y_i - \bar{y}_i)^2}{2\sigma_i^2}\right) \propto \exp\left(-\frac{\chi^2}{2}\right), \quad (1.150)$$

where y_i is the data, \bar{y}_i is the mean value, σ_i is the standard deviation and χ^2 is the chi-squared value for the data. When discriminating between models, the convention is often to give the log likelihood value as

$$-2\ln(\mathcal{L}_{\text{ML}}) \approx \chi^2, \quad (1.151)$$

where \mathcal{L}_{ML} is the maximum likelihood which corresponds with the minimum χ^2 value so that a model giving a better fit has a *smaller* value.

The last tool needed to extract the posterior probability distributions for the inflation parameters is a sampling method that fairly converges to the desired distribution. For cosmological parameter extraction, we use Markov chain Monte Carlo (MCMC) samplers [Christensen & Meyer, 2000] [Christensen et al., 2001] [Knox et al., 2001] [Kosowsky et al., 2002] [Lewis & Bridle, 2002] to fairly sample a distribution function. In this method, samples of a parameter θ are drawn randomly (Monte Carlo). For each successive sample, we propose moving to a new position based only on the previous sample (Markov chain) and accept the move based on the value's agreement with the likelihood and prior distributions. Most of the parameter values in the chain will converge to the most probable posterior distribution apart from those at the start of the chain which are in a region of low probability. The low-probability part of the chain is referred to as the *burn-in phase* and the parameter values here are removed to ensure the sampled posterior is representative of the actual population distribution.

After sampling, the best-fit parameter values can be extracted by making a histogram of the values in the chain where the mean of each distribution corresponds with the ideal value. Uncertainties can be estimated by measuring the proportion of values lying in *confidence regions* which are usually set to 68% and 95%. We perform this type of analysis in Chapter 3 for several inflation models including an α -attractor model which was only possible because of our work discussed in Chapter 2 based on a non-trivial field space.

1.8 Summary of the thesis

After the review of inflationary theory and how it is connected to observations made from the CMB, it is clear that the inflationary framework should be extended to include a non-trivial field-space and applied in a numerical code. This work is presented in Chapter 2 where the major achievements are listed below.

- We found a field-covariant Hamiltonian with perturbations up to third-order. Furthermore, we showed that this covariantises naïvely apart from several new Riemann curvature terms appearing in the action.
- We found the initial conditions and gauge transformations to ζ also covariantise simply by tracking the field-index position.
- We found the transport equations needed for the non-canonical fields and add extensions to `CppTransport` which enable numerical computations of the bispectrum for these models.
- We tested the new additions to the code by using the Gelaton/QSFI model which can be written using both canonical and non-canonical coordinates and found excellent agreement to within $10^{-3}\%$.
- We compared our results for the Quasi-two-field model with results from the `PyTransport` and `mTransport` codes where agreement was typically within 0.1% for most cases.
- We showed that the gelaton model of inflation only produces a limited boost to the bispectrum amplitude on equilateral configurations.
- Moreover, we showed why the boost is limited by using constraints given from the speed of sound for the perturbations and the gelaton mass requirements.

Furthermore, it is clear that in order to find constraints on the parameters in non-trivial models of inflation, we should add sampling and Bayesian model selection functionalities to `CppTransport`. This work is presented in Chapter 3 where the major achievements are listed below.

- We built a cosmological code `CppTSample` which is a `CosmoSIS` module that allows for all of the `CosmoSIS` MCMC samplers to provide initial conditions for the inflation parameters describing a model in `CppTransport`.

- Furthermore, this can be used with the CosmoSIS likelihood modules for Planck and WMAP data which enables us to find the likelihood of obtaining CMB data given a non-trivial model.
- Additionally, the CppTSample module could be used to give initial conditions for other modules that perform late-time cosmological calculations such as the galaxy power spectrum.
- We tested our module with the single-field quadratic and quartic models of inflation and showed that our results are consistent with slow-roll predictions and that they are both ruled out based on CMB observations as expected.
- We found constraints that are consistent with the universality predictions in the power spectrum and the bispectrum for an α -attractor model which wouldn't have been possible without our non-trivial field calculations seen in Chapter 2.
- We found constraints on the Gelaton/QSFI model of inflation which also has a non-canonical field metric and despite its long integration time we showed it can give values for n_s and r that are within their Planck constraints.

Chapter 2

Project I – Numerical evaluation of inflationary 3-point functions on curved field space

2.1 Abstract

We extend the public `CppTransport` code to calculate the statistical properties of fluctuations in multiple-field inflationary models with curved field space. Our implementation accounts for all physical effects at tree-level in the ‘in–in’ diagrammatic expansion. This includes particle production due to time-varying masses, but excludes scenarios where the curvature perturbation is generated by averaging over the decay of more than one particle. We test our implementation by comparing results in Cartesian and polar field-space coordinates, showing excellent numerical agreement and only minor degradation in compute time. We compare our results with the `PyTransport 2.0` code, which uses the same computational approach but a different numerical implementation, finding good agreement. Finally, we use our tools to study a class of gelaton-like models which could produce an enhanced non-Gaussian signal on equilateral configurations of the Fourier bispectrum. We show this is difficult to achieve using hyperbolic field-space manifolds and simple inflationary potentials.

2.2 Introduction

Inflation [Guth, 1981, Linde, 1982, Albrecht & Steinhardt, 1982] has become established as a preferred framework in which to describe the early universe. In inflation, primor-

dial quantum fluctuations are amplified, giving large-scale variations in energy density that are inherited by later structure. Recent ideas from theories of beyond-the-Standard-Model physics have introduced multiple-field models yielding 2-point statistics consistent with measurement, but which may be theoretically preferable because their field values remain sub-Planckian. In such theories the kinetic term $X = -G_{IJ}\partial^a\phi^I\partial_a\phi^J/2$ is often non-canonical and is expressed in terms of a kinetic matrix $G_{IJ}(\phi)$. (We define our notation more carefully below. Here, upper-case Latin indices label the different species of scalar fields, and lower-case indices label spacetime dimensions.) The matrix G_{IJ} is real, symmetric, and transforms as a covariant 2-tensor under field redefinitions, so it may be interpreted as a metric. The resulting ‘covariant’ formalism constrains the ways in which G_{IJ} can appear in observable quantities and offers a convenient computational framework with the usual advantages of tensor calculus.

Examples in this class include models descending from string theory or supergravity where the kinetic matrix is inherited from a Kähler potential $K(\phi^I, \phi^{I*})$ [Lyth & Riotto, 1999, Baumann & McAllister, 2015]. The α -attractor scenario suggested by Kallosh & Linde is of this type [Kallosh & Linde, 2013b, Ferrara et al., 2013, Kallosh et al., 2013], including its multiple-field variants [Achúcarro et al., 2017]. Also, a full description of the interesting Higgs inflation model, including Goldstone modes, requires a noncanonical metric that derives from the Goldstone sigma model [Greenwood et al., 2013]. Alternatively, the freedom to choose non-Cartesian coordinates on field space may simply provide a more convenient option, as with the ‘gelaton’ and ‘quasi-single field inflation’ scenarios [Tolley & Wyman, 2010, Chen & Wang, 2010].

Numerical tools.—Whatever the origin of the noncanonical kinetic structure, to constrain such models using modern datasets we require precise numerical predictions. Numerical tools for performing inflationary calculations have existed for some time, but their capabilities have been limited. Ringeval et al. provided the early code `FieldInf`, which is capable of computing 2-point functions with an arbitrary choice of metric G_{IJ} [Ringeval et al., 2006, Martin & Ringeval, 2006, Ringeval, 2008], but many other tools restrict to the canonical case $G_{IJ} = \delta_{IJ}$. Major examples include `ModeCode/MultiModeCode` [Mortonson et al., 2011, Easter & Peiris, 2012, Norena et al., 2012, Price et al., 2015], `PyFlation` [Huston & Malik, 2009, Huston & Malik, 2011, Huston & Christopherson, 2012] and `BINGO` [Hazra et al., 2013, Sreenath et al., 2015]. `ModeCode/MultiModeCode` and `PyFlation` are 2-point function solvers for canonical multiple-field models, and `BINGO` is a 2- and 3-point function solver for single-field models.

All these are traditional codes that require customization by the user for each model of interest. Recent developments in inflationary perturbation theory [Mulryne et al., 2010, Mulryne et al., 2011, Seery et al., 2012, Mulryne, 2013] have allowed the construction of *automated* tools [Dias et al., 2015b, Dias et al., 2016, Ronayne & Mulryne, 2017]. These accept the specification of an inflationary model by its Lagrangian and leverage symbolic algebra methods to produce custom code that solves for the inflationary n -point functions. We collectively refer to these as the *transport tools* (transportmethod.com). The suite contains three tools, all of which apply to multiple-field models:

- **mTransport** [Dias et al., 2015b] is a 2-point function solver implemented in *Mathematica*. It allows a nontrivial kinetic matrix and is suited to interactive model exploration.
- **PyTransport** [Mulryne & Ronayne, 2016, Ronayne & Mulryne, 2017] is a 2- and 3-point function solver implemented in Python. Version 1 (September 2016) restricted to canonical kinetic terms. Version 2 (September 2017) introduced support for an arbitrary kinetic matrix. Because it is implemented as a Python library it is well-suited to scripting or inclusion in other codes.
- **CppTransport** [Seery, 2016] is a 2- and 3-point function solver implemented in C++. It has built-in functionality to parallelize computations and can postprocess correlation functions to produce inflationary observables. It manages storage of its data products as SQL databases. It is well-suited to larger calculations that benefit from its auto-parallelization or which produce significant data volumes, and performs well with ‘feature’ models containing steps or kinks where its library of sophisticated steppers offers assistance. It is less easy (but still possible) to incorporate within larger codes than PyTransport. The original release 2016.3 restricted to canonical kinetic terms.

In this paper we describe a new release of CppTransport (2018.1) that extends its functionality to nontrivial kinetic matrices. We apply these new tools to a class of gelaton-like scenarios and show that (at least in the scenarios we study) the parameter space available to generate enhanced equilateral correlations is very small. We compare our numerical results with the independent mTransport and PyTransport implementations, finding excellent agreement.¹

Synopsis.—The necessary equations for computation of the inflationary two-point function

¹Although the transport tools all use the same computational framework, their numerical implementations vary considerably in detail and therefore this constitutes a nontrivial check on numerical correctness.

were given by Mulryne [Mulryne, 2013] and extended to a non-Euclidean field space by Dias et al. [Dias et al., 2015b]. We have nothing novel to say about this part of the analysis. The extension to three-point correlations was given in Ref. [Dias et al., 2016], but this was limited to models with canonical kinetic terms.

This paper is divided into three principal parts. First, in §2.3, we highlight the key modifications required to adapt the analysis of Ref. [Dias et al., 2016] for a nontrivial field-space metric. A similar discussion has already been given by Ronayne et al. [Ronayne & Mulryne, 2017]. We briefly review the field-space covariant formulation of inflationary perturbations in §2.3.1, and use this to derive the covariant cubic Hamiltonian in §2.3.2. In §2.3.3 we discuss the computation of initial conditions for each correlation function. We formulate the covariant transport hierarchy in §2.3.4 and explain how to relate covariant correlation functions to the curvature perturbation in §2.3.5.

Second, in §2.4 we present a selection of numerical results. For those wishing to replicate our numerics, we explain how to obtain `CppTransport` in §2.4.1. In §§2.4.2–2.4.3 we validate our numerical implementation by comparing results computed using polar field-space coordinates with known results in Cartesian coordinates. In §2.4.4 we apply our method to the ‘gelaton’ model proposed by Tolley & Wyman [Tolley & Wyman, 2010]. In this scenario a light degree of freedom is ‘dressed’ by the interactions of a noncanonical heavy mode, obtaining a subluminal phase velocity and potentially enhanced correlations on equilateral Fourier configurations. Our numerical tools successfully reproduce the features of the scenario, but we show that (at least for the range of potentials we consider) it is difficult to find suitable parameters that allow both sufficient inflation *and* large enhancement of the equilateral modes. We conclude in §2.5.

Third, we include a large amount of supplementary information in Appendix 2.6. This includes more detailed computations of the transport hierarchy given in §2.3, together with a selection of intermediate results not discussed in the main text.

Obtaining `CppTransport`.—The latest builds of `CppTransport` and `PyTransport` are available from the website transportmethod.com. Alternatively, both `CppTransport` and `PyTransport` are permanently deposited at zenodo.org; at the time of writing, the current releases are 2018.1 for `CppTransport` and 2.0 for `PyTransport`.

Notation.—We use natural units where $c = \hbar = 1$. The reduced Planck mass is $M_{\text{P}}^2 = (8\pi G)^{-1}$. We use the metric signature $(-, +, +, +)$. Greek indices (μ, ν, \dots) label space-time indices, whereas lower-case Roman indices from the middle of the alphabet, (i, j, \dots) , label spatial indices. Upper-case Roman indices (I, J, \dots) label field-space coordinates. We

employ a compressed Fourier notation defined in Eq. (2.4) in which these labels appear in a bold, sans-serif font: $(\mathbf{I}, \mathbf{J}, \dots)$. For phase-space coordinates, we use Roman letters from the start of the alphabet, (a, b, \dots) .

2.3 Differences from the canonical case

To accommodate a non-Euclidean field-space metric we require a covariantization (with respect to the metric G_{IJ}) of the formalism developed in Ref. [Dias et al., 2016] for the Euclidean case. The advantage of a covariant formalism is that it naturally packages additional terms arising from the metric as Christoffel and Riemann contributions in the same way as spacetime covariance. Its construction entails the replacement of ordinary derivatives by covariant derivatives and contraction of all indices with G_{IJ} . However, detailed computations show that Riemann terms also appear, meaning that the resulting formalism is not ‘minimally coupled’ to the field-space curvature. The details of this covariantization were given in Gong & Tanaka [Gong & Tanaka, 2011] and Elliston et al. [Elliston et al., 2012].

Dias et al. [Dias et al., 2015b] applied these ideas to find a covariant formulation of the transport equations for the two-point function. In this section we briefly review this construction and extend it to the three-point function. A more detailed discussion is given in Appendices 2.6.1–2.6.4.

2.3.1 Field-covariant formalism

Perturbation series.—In a covariant formalism our aim is to construct correlation functions that transform tensorially under field redefinitions. These are coordinate transformations in field space. Correlation functions of the field perturbations $\delta\phi^I \equiv \phi^I(\mathbf{x}, t) - \phi^I(t)$ do *not* have this property, because the coordinates ϕ^I do not themselves transform tensorially (despite the species label ‘ I ’).

A suitable alternative was given by Gong & Tanaka [Gong & Tanaka, 2011], who observed that in a normal neighbourhood of $\phi^I(t)$ we can associate $\phi^I(\mathbf{x}, t)$ with the geodesic that connects it to $\phi^I(t)$. The geodesic is uniquely determined by its tangent vector Q^I at $\phi^I(t)$. By construction Q^I is field-space covariant and is defined in the unperturbed spacetime. It is therefore a candidate to appear in correlation functions of the form $\langle Q^I \rangle$, $\langle Q^I Q^J \rangle$, \dots , $\langle Q^I Q^J \dots Q^K \rangle$, each of which will inherit a tensorial transformation law from Q^I . See Refs. [Gong & Tanaka, 2011, Elliston et al., 2012, Dias et al., 2015b] for further

details.

Correlation functions.—After quantization, our intention is to compute 2- and 3-point correlation functions of the Heisenberg-picture fields Q^I together with their canonical momenta $P^J \equiv D_t Q^J$, where $D_t \equiv \dot{\phi}^I \nabla_I$ is the covariant time derivative and $\dot{\phi}^I = d\phi^I/dt$. As usual, in order to use time-dependent perturbation theory, we split the Hamiltonian into free and interacting parts corresponding to the quadratic and cubic (or higher) terms [Dias et al., 2016]. Notice that, with this definition, all mass terms are included in the free Hamiltonian. Finally, we define interaction-picture fields q^I and p^J that are related to the Heisenberg-picture fields by a similarity transformation $q^I = F^\dagger Q^I F$, $p^J = F^\dagger P^J F$, where F is the unitary operator

$$F = \bar{\text{T}} \exp \left(i \int_{-\infty^+}^t H_{\text{int}}(t') dt' \right), \quad (2.1)$$

and $\bar{\text{T}}$ is the anti-time ordering operator that arranges the fields in its argument in order of increasing time. The interacting part of the Hamiltonian is H_{int} . The notation ‘ $-\infty^+$ ’ indicates that the integral is to be performed over a contour deformed away from the real axis into the positive complex plane in the distant past, with analytic continuation used to define the integrand. This can be regarded as the theorem of Gell-Mann & Low in the present context [Gell-Mann & Low, 1951, Weinberg, 2005].

We frequently collect the phase-space coordinates Q^I , P^I into a single vector $X^a = (Q^I, P^J)$, and likewise for the interaction picture fields $x^a = (q^I, p^J)$. Latin indices a, b, \dots , from the early part of the alphabet run over the dimensions of phase space, on which the metric should be taken to have block-diagonal form

$$G_{ab} = \begin{pmatrix} G_{IJ} & 0 \\ 0 & G_{KL} \end{pmatrix}. \quad (2.2)$$

The vacuum expectation value of any (possibly composite) Heisenberg-picture operator $\mathcal{O}(X)$ can be written in terms of F , F^\dagger and the interaction picture fields using

$$\begin{aligned} \langle \mathcal{O}(X) \rangle &= \left\langle 0 \left| F \mathcal{O}(x) F^\dagger \right| 0 \right\rangle \\ &= \left\langle 0 \left| \bar{\text{T}} \exp \left(i \int_{-\infty^+}^t H_{\text{int}}(t') dt' \right) \mathcal{O}(x) \text{T} \exp \left(-i \int_{-\infty^-}^t H_{\text{int}}(t'') dt'' \right) \right| 0 \right\rangle, \end{aligned} \quad (2.3)$$

where $|0\rangle$ is the vacuum of the free Hamiltonian. We describe Eq. (2.3) as the ‘in-in’ formula, and use it to compute all correlation functions of cosmological perturbations in our field-covariant formalism. For further details, see Appendix 2.6.1 for the definition of the covariant variable Q^I , and Appendix 2.6.2 for the definition of correlation functions.

2.3.2 Hamiltonian

In addition to the change from $\delta\phi^I$ to Q^I , the Hamiltonian acquires new terms generated by derivatives of the metric. The procedure to calculate these follows Maldacena [Maldacena, 2003, Seery & Lidsey, 2005b, Seery & Lidsey, 2005a]. We minimally couple N fields to gravity, allowing a nontrivial kinetic matrix and a potential V , and use the ADM decomposition to integrate out the Hamiltonian and momentum constraints. Finally the result is expanded to the desired order in perturbations. The computation to third order in Q^I was done by Elliston et al. [Elliston et al., 2012], or see Appendix 2.6.1 for further details.

Summation convention.—To write the results, we use a compact notation in which repeated index labels imply both summation over species labels and integration over Fourier wavenumbers. We indicate that this convention is in use by writing the species indices in bold sans-serif. Specifically, such contractions should be interpreted to mean

$$A_{\mathbf{I}}B^{\mathbf{I}} = \sum_{\mathbf{I}} \int \frac{d^3k_{\mathbf{I}}}{(2\pi)^3} A_{\mathbf{I}}(\mathbf{k}_{\mathbf{I}}) B^{\mathbf{I}}(\mathbf{k}_{\mathbf{I}}), \quad (2.4)$$

where, as always, the field metric G_{IJ} is used to raise and lower indices. In some manipulations a δ -function can be produced that changes the sign of a momentum label. We indicate this by placing a bar on each index for which the sign of the momentum should be reversed, eg.,

$$A_{\mathbf{I}}B^{\bar{\mathbf{I}}} = \sum_{\mathbf{I}} \int \frac{d^3k_{\mathbf{I}}}{(2\pi)^3} A_{\mathbf{I}}(\mathbf{k}_{\mathbf{I}}) B^{\mathbf{I}}(-\mathbf{k}_{\mathbf{I}}). \quad (2.5)$$

Second- and third-order kernels.—To third order, the result can be written

$$S_{\phi} = \frac{1}{2} \int dt a^3 \left\{ G_{\mathbf{I}\mathbf{J}} D_t Q^{\mathbf{I}} D_t Q^{\mathbf{J}} + M_{\mathbf{I}\mathbf{J}} Q^{\mathbf{I}} Q^{\mathbf{J}} + A_{\mathbf{I}\mathbf{J}\mathbf{K}} Q^{\mathbf{I}} Q^{\mathbf{J}} Q^{\mathbf{K}} + B_{\mathbf{I}\mathbf{J}\mathbf{K}} Q^{\mathbf{I}} Q^{\mathbf{J}} D_t Q^{\mathbf{K}} + C_{\mathbf{I}\mathbf{J}\mathbf{K}} D_t Q^{\mathbf{I}} D_t Q^{\mathbf{J}} Q^{\mathbf{K}} \right\}, \quad (2.6)$$

where the second-order kernels $G_{\mathbf{I}\mathbf{J}}$ and $M_{\mathbf{I}\mathbf{J}}$ are defined as

$$\begin{aligned} G_{\mathbf{I}\mathbf{J}} &\equiv (2\pi)^3 G_{IJ} \delta(\mathbf{k}_1 + \mathbf{k}_2), \\ M_{\mathbf{I}\mathbf{J}} &\equiv (2\pi)^3 \delta(\mathbf{k}_1 + \mathbf{k}_2) \left(\frac{\mathbf{k}_1 \cdot \mathbf{k}_2}{a^2} G_{IJ} - m_{IJ} \right), \end{aligned} \quad (2.7)$$

and the mass-matrix m_{IJ} satisfies

$$m_{IJ} \equiv V_{;IJ} - R_{KIJL} \dot{\phi}^K \dot{\phi}^L - \frac{1}{a^3 M_{\text{P}}^2} D_t \left(\frac{a^3 \dot{\phi}_I \dot{\phi}_J}{H} \right). \quad (2.8)$$

Then the third-order kernels $A_{\mathbf{IJK}}$, $B_{\mathbf{IJK}}$ and $C_{\mathbf{IJK}}$ are given by

$$A_{\mathbf{IJK}} \equiv (2\pi)^3 \delta(\mathbf{k}_1 + \mathbf{k}_2 + \mathbf{k}_3) A_{IJK}, \quad (2.9a)$$

$$B_{\mathbf{IJK}} \equiv (2\pi)^3 \delta(\mathbf{k}_1 + \mathbf{k}_2 + \mathbf{k}_3) B_{IJK}, \quad (2.9b)$$

$$C_{\mathbf{IJK}} \equiv (2\pi)^3 \delta(\mathbf{k}_1 + \mathbf{k}_2 + \mathbf{k}_3) C_{IJK}, \quad (2.9c)$$

and the corresponding ‘species tensors’ are

$$\begin{aligned} A_{IJK} \equiv & -\frac{1}{3} V_{;IJK} - \frac{\dot{\phi}_I \dot{V}_{;JK}}{2HM_P^2} + \frac{\dot{\phi}_I \dot{\phi}_J Z_K}{4H^2 M_P^4} + \frac{\dot{\phi}_I Z_J Z_K}{8H^3 M_P^4} \left(1 - \frac{(\mathbf{k}_2 \cdot \mathbf{k}_3)^2}{k_2^2 k_3^2} \right) \\ & + \frac{\dot{\phi}_I \dot{\phi}_J \dot{\phi}_K}{8H^3 M_P^6} (6H^2 M_P^2 - \dot{\phi}^2) - \frac{\dot{\phi}_K \dot{\phi}^L \dot{\phi}^M}{2HM_P^2} R_{L(IJ)M} + \frac{1}{3} R_{(I|LM|J;K)} \dot{\phi}^L \dot{\phi}^M \\ & + \frac{\dot{\phi}_I G_{JK} \mathbf{k}_2 \cdot \mathbf{k}_3}{2HM_P^2 a^2}, \end{aligned} \quad (2.10a)$$

$$B_{IJK} \equiv \frac{4}{3} R_{K(IJ)L} \dot{\phi}^L - \frac{\dot{\phi}_I Z_J \dot{\phi}_K}{4H^3 M_P^4} \left(1 - \frac{(\mathbf{k}_2 \cdot \mathbf{k}_3)^2}{k_2^2 k_3^2} \right) + \frac{\dot{\phi}_I \dot{\phi}_J \dot{\phi}_K}{4H^2 M_P^4} - \frac{Z_I G_{JK} \mathbf{k}_1 \cdot \mathbf{k}_2}{HM_P^2 k_1^2}, \quad (2.10b)$$

$$C_{IJK} \equiv -\frac{G_{IJ} \dot{\phi}_K}{2HM_P^2} + \frac{\dot{\phi}_I \dot{\phi}_J \dot{\phi}_K}{8H^3 M_P^4} \left(1 - \frac{(\mathbf{k}_1 \cdot \mathbf{k}_2)^2}{k_1^2 k_2^2} \right) + \frac{\dot{\phi}_I G_{JK} \mathbf{k}_1 \cdot \mathbf{k}_3}{HM_P^2 k_1^2}. \quad (2.10c)$$

The brackets surrounding indices in the Riemann terms indicate that the enclosed indices should be symmetrized with weight unity, except for indices between vertical bars | which are excluded. Further, note that the tensor A_{IJK} should be symmetrized over all three indices IJK with weight unity, and B_{IJK} , C_{IJK} should be symmetrized over IJ with weight unity. The numbered-indices on the momentum labels \mathbf{k}_1 , \mathbf{k}_2 , \mathbf{k}_3 are mapped to the field-space labels as $1 \rightarrow I$, $2 \rightarrow J$ and $3 \rightarrow K$ (e.g. the momentum \mathbf{k}_2 comes from a Fourier-transformed spatial-derivative of a J field-coordinate like $\partial_i Q^J$), and should be permuted during symmetrization. The quantity Z_I is defined by

$$Z_I \equiv D_t \dot{\phi}_I + \frac{\dot{\phi}_I \dot{\phi}_J \dot{\phi}^J}{2HM_P^2}. \quad (2.11)$$

From these expressions it is simple to calculate the Hamiltonian using a Legendre transformation. We define the canonical momentum $P_{\mathbf{I}}$ to satisfy

$$P_{\mathbf{I}}(t) \equiv \frac{\delta S_\phi}{\delta(D_t Q^{\mathbf{I}})}, \quad (2.12)$$

where the variational derivative can be computed using the rule

$$\frac{\delta[Q^{\mathbf{I}}(\mathbf{k}_I, t)]}{\delta[Q^{\mathbf{J}}(\mathbf{k}_J, t')]} = \delta_J^I (2\pi)^3 \delta(t - t') \delta(\mathbf{k}_I + \mathbf{k}_J) = \delta_{\mathbf{J}}^{\mathbf{I}} \delta(t - t'). \quad (2.13)$$

To compute the Hamiltonian we require the relation $H = \int dt [P^{\mathbf{I}}(D_t Q_{\mathbf{I}}) - L]$ which should be regarded as a function of $Q^{\mathbf{I}}$ and $P^{\mathbf{I}}$. Finally, for convenience, we rescale the momentum

by a factor a^3 , viz. $P_I \rightarrow a^3 P_I$, to obtain the final third-order Hamiltonian,

$$H = \frac{1}{2} \int dt a^3 \left(G_{IJ} P^I P^J - M_{IJ} Q^I Q^J - \right. \\ \left. A_{IJK} Q^I Q^J Q^K - B_{IJK} Q^I Q^J P^K - C_{IJK} P^I P^J Q^K \right). \quad (2.14)$$

The second-order terms on the first line represent the free part of the Hamiltonian H_0 , and the third-order terms on the second line represent the interacting part of the Hamiltonian H_{int} . The new contributions introduced by derivatives of the nontrivial field-space metric are given by the Riemann terms found in the M_{IJ} , A_{IJK} and B_{IJK} tensors.

2.3.3 Initial conditions

We will require suitable initial conditions for each correlation function on subhorizon scales. To compute these we use Eq. (2.3) to compute each correlation function at sufficiently early times—normally between four and ten e-folds inside the horizon, although the precise numbers are model-dependent; see Ref. [Dias et al., 2015b]—that all species can be approximated as massless. Such a time can normally be found, provided all masses remain bounded, because the physical wavenumber k/a corresponding to a fixed comoving wavenumber k is pushed into the ultraviolet at early times, making each mode kinetically dominated for sufficiently small a . The outcome is that we can compute *universal* initial conditions applicable to any model, no matter what mass spectrum or interactions it contains, provided the computation of its correlation functions begins sufficiently far inside the horizon [Dias et al., 2015b, Dias et al., 2016]. For more details see §3 of Ref. [Dias et al., 2015b] and §6 of Ref. [Dias et al., 2016].

Two-point function.—A suitable initial condition for the covariant equal-time 2-point function was computed by Dias et al. [Dias et al., 2015b], following Elliston et al. [Elliston et al., 2012]. In our notation their results can be written

$$\langle Q^I(\mathbf{k}_1) Q^J(\mathbf{k}_2) \rangle_{\text{init}} = (2\pi)^3 \delta(\mathbf{k}_1 + \mathbf{k}_2) G^{IJ} \left(\frac{1}{2ka^2} + \frac{H^2}{2k^3} \right), \quad (2.15a)$$

$$\langle Q^I(\mathbf{k}_1) P^J(\mathbf{k}_2) \rangle_{\text{init}} = (2\pi)^3 \delta(\mathbf{k}_1 + \mathbf{k}_2) G^{IJ} \left(-\frac{H}{2ka^2} + \frac{i}{2a^3} \right), \quad (2.15b)$$

$$\langle P^I(\mathbf{k}_1) Q^J(\mathbf{k}_2) \rangle_{\text{init}} = (2\pi)^3 \delta(\mathbf{k}_1 + \mathbf{k}_2) G^{IJ} \left(-\frac{H}{2ka^2} - \frac{i}{2a^3} \right), \quad (2.15c)$$

$$\langle P^I(\mathbf{k}_1) P^J(\mathbf{k}_2) \rangle_{\text{init}} = (2\pi)^3 \delta(\mathbf{k}_1 + \mathbf{k}_2) G^{IJ} \left(\frac{k}{2a^4} \right), \quad (2.15d)$$

where the time-dependent quantities H , a and G_{IJ} appearing on the right-hand sides should be evaluated at the initial time t_{init} , indicated by the subscript ‘init’ attached to each correlation function.

Eqs. (2.15a)–(2.15d) are effectively the same as those found in the canonical case [Dias et al., 2016] except that the Euclidean kinetic matrix δ^{IJ} is replaced by the metric G^{IJ} . For further details of the computation see Appendix 2.6.3.

Three-point function.—Initial conditions for the 3-point functions require the in–in formula (2.3). The lowest-order nonzero contribution to each correlator is given by

$$\begin{aligned} \langle X^I X^J X^K \rangle \subseteq i \int_{-\infty^+}^{\eta} d\tau H_{\mathbf{LMN}} \int \left(\prod_{n=1}^3 \frac{d^3 q_n}{(2\pi)^3} \right) (2\pi)^3 \delta \left(\sum_{i=1}^3 \mathbf{q}_i \right) \\ \times \left\{ \langle X_{q_1}^{\mathbf{L}} X_{k_1}^I \rangle \langle X_{q_2}^{\mathbf{M}} X_{k_2}^J \rangle \langle X_{q_3}^{\mathbf{N}} X_{k_3}^K \rangle + \text{perms} \right\} + \text{c.c.}, \end{aligned} \quad (2.16)$$

where ‘perms’ indicates a sum over permutations of the pairing between ‘external’ indices IJK and the ‘internal’ indices \mathbf{LMN} , ‘c.c.’ indicates the complex conjugate of the preceding term, and $H_{\mathbf{LMN}}$ contains all the cubic terms found in Eq. (2.14). For further details we refer to Appendix 2.6.3.

To express the results we require some extra notation. First, we divide A_{IJK} into ‘fast’ terms, which involve the scale factor a and evolve exponentially fast in e-folds, and ‘slow’ terms, which evolve on slow-roll timescales,

$$A^{IJK} \equiv A_{\text{slow}}^{IJK} + A_{\text{fast}}^{IJK} = A_{\text{slow}}^{IJK} + \frac{\dot{\phi}^I G^{JK} \mathbf{k}_2 \cdot \mathbf{k}_3}{2HM_{\text{P}}^2 a^2} \quad (2.17)$$

The fast term grows rapidly on subhorizon scales and is always relevant when computing initial conditions. In Ref. [Dias et al., 2016] it was explained that the slow terms can also be relevant in scenarios with enhanced three-body interactions such as a QSFI model.

Second, we introduce the quantities $\mathbf{k}_{\text{tot}} \equiv \mathbf{k}_1 + \mathbf{k}_2 + \mathbf{k}_3$, $k_t \equiv k_1 + k_2 + k_3$ and $K \equiv k_1 k_2 + k_1 k_3 + k_2 k_3$. The results for each correlation function are²

$$\begin{aligned} \langle Q^I Q^J Q^K \rangle_{\text{init}} = \frac{(2\pi)^3 \delta(\mathbf{k}_{\text{tot}})}{4a^4 k_1 k_2 k_3 k_t} \left\{ \frac{\dot{\phi}^I G^{JK}}{4HM_{\text{P}}^2} \mathbf{k}_2 \cdot \mathbf{k}_3 + \frac{a^2}{2} A_{\text{slow}}^{IJK} - C^{IJK} \frac{k_1 k_2}{2} \right. \\ \left. + \frac{a^2 H}{2} B^{IJK} \left[\frac{(k_1 + k_2) k_3}{k_1 k_2} - \frac{K^2}{k_1 k_2} \right] + 5 \text{ perms} \right\}, \end{aligned} \quad (2.18a)$$

$$\begin{aligned} \langle P^I Q^J Q^K \rangle_{\text{init}} = \frac{(2\pi)^3 \delta(\mathbf{k}_{\text{tot}})}{4a^4 (k_1 k_2 k_3)^2 k_t} \\ \times \left\{ k_1^2 (k_2 + k_3) \left[\frac{\dot{\phi}^I G^{JK}}{4HM_{\text{P}}^2} \mathbf{k}_2 \cdot \mathbf{k}_3 + \frac{a^2}{2} A_{\text{slow}}^{IJK} - C^{IJK} \frac{k_1 k_2}{2} + 5 \text{ perms} \right] \right. \\ \left. + k_1 \left[-\frac{\dot{\phi}^I G^{JK}}{4HM_{\text{P}}^2} \mathbf{k}_2 \cdot \mathbf{k}_3 \left(K^2 + \frac{k_1 k_2 k_3}{k_t} \right) - \frac{a^2}{2} A_{\text{slow}}^{IJK} \left(K^2 - \frac{k_1 k_2 k_3}{k_t} \right) \right. \right. \\ \left. \left. + B^{IJK} \frac{k_1 k_2 k_3^2}{2H} + C^{IJK} \frac{k_1^2 k_2^2}{2} \left(1 + \frac{k_3}{k_t} \right) + 5 \text{ perms} \right] \right\}, \end{aligned} \quad (2.18b)$$

²Eq. (2.18d) corrects a minor typo in v1 and v2 of the arXiv version of Ref. [Dias et al., 2016]. This typo was corrected in the arXiv v3.

$$\begin{aligned}
\langle P^I P^J Q^K \rangle_{\text{init}} &= \frac{(2\pi)^3 \delta(\mathbf{k}_{\text{tot}})}{4a^6 H^2 (k_1 k_2 k_3)^2 k_t} \\
&\times \left\{ k_1^2 k_2^2 k_3 \left[-\frac{\phi^I G^{JK}}{4HM_{\text{P}}^2} \mathbf{k}_2 \cdot \mathbf{k}_3 - \frac{a^2}{2} A_{\text{slow}}^{IJK} + C^{IJK} \frac{k_1 k_2}{2} - \frac{a^2 H}{2} B^{IJK} \frac{(k_1 + k_2) k_3}{k_1 k_2} \right. \right. \\
&\quad \left. \left. + 5 \text{ perms} \right] + k_1^2 k_2^2 \left[\frac{a^2 H}{2} B^{IJK} k_3 + 5 \text{ perms} \right] \right\},
\end{aligned} \tag{2.18c}$$

$$\begin{aligned}
\langle P^I P^J P^K \rangle_{\text{init}} &= \frac{(2\pi)^3 \delta(\mathbf{k}_{\text{tot}})}{4a^6 H^2 k_1 k_2 k_3 k_t} \left\{ \frac{\phi^I G^{JK}}{4HM_{\text{P}}^2} \mathbf{k}_2 \cdot \mathbf{k}_3 \left(K^2 + \frac{k_1 k_2 k_3}{k_t} \right) + \frac{a^2}{2} A_{\text{slow}}^{IJK} \left(K^2 - \frac{k_1 k_2 k_3}{k_t} \right) \right. \\
&\quad \left. - B^{IJK} \frac{k_1 k_2 k_3^2}{2H} - C^{IJK} \frac{k_1^2 k_2^2}{2} \left(1 + \frac{k_3}{k_t} \right) + 5 \text{ perms} \right\}.
\end{aligned} \tag{2.18d}$$

All time-dependent quantities on the right-hand side are to be evaluated at the initial time t_{init} , and the tangent-space indices I, J, K, \dots , live in the tangent space associated with this time.

Where permutations are specified, they should be carried out *only within the bracket* in which the instruction to sum over permutations is given. (Notice that these means some momentum factors, such as those multiplying the square-bracket terms in Eqs. (2.18b) and (2.18c), are not symmetrized. This is correct because these momentum factors arise from wavefunctions associated with the external fields, and these are not symmetric.) Each permutation should be formed by simultaneous exchange of the species labels I, J, K and their partner momenta $\mathbf{k}_1, \mathbf{k}_2, \mathbf{k}_3$.

The form of these equations matches the canonical case [Dias et al., 2016], except for the Riemann terms embedded in A_{slow}^{IJK} and B^{IJK} . For further details of the calculation, see Appendix 2.6.3.

2.3.4 Covariant transport equations

Next, we require differential equations to evolve each correlation function from its initial value to any time of interest. These equations were derived in the superhorizon limit by Mulryne et al. [Mulryne et al., 2010, Mulryne et al., 2011, Elliston et al., 2012] and later extended to cover the subhorizon era [Mulryne, 2013, Dias et al., 2015b].

The procedure to derive these evolution equations matches that of Dias et al. [Dias et al., 2016]. We begin from the Hamiltonian (2.14), which can be written in the generic form

$$H = \frac{1}{2!} H_{\mathbf{ab}} X^{\mathbf{a}} X^{\mathbf{b}} + \frac{1}{3!} H_{\mathbf{abc}} X^{\mathbf{a}} X^{\mathbf{b}} X^{\mathbf{c}} + \dots \tag{2.19}$$

The corresponding covariant evolution equation is

$$D_t X^{\mathbf{a}} = u^{\mathbf{a}}_{\mathbf{b}} X^{\mathbf{b}} + \frac{1}{2!} u^{\mathbf{a}}_{\mathbf{bc}} X^{\mathbf{b}} X^{\mathbf{c}} + \dots, \quad (2.20)$$

where $u^{\mathbf{a}}_{\mathbf{b}}$ and $u^{\mathbf{a}}_{\mathbf{bc}}$ are phase-space tensors that can be expressed in terms of $H_{\mathbf{ab}}$ and $H_{\mathbf{abc}}$ [Dias et al., 2016]. The derivative D_t should be taken to act in phase space with a block-diagonal connexion. For example, acting on contra- and covariant indices this produces

$$D_t X^a{}_b = \frac{d}{dt} X^a{}_b + \Gamma_c^a X^c{}_b - \Gamma_b^c X^a{}_c, \quad (2.21)$$

where Γ_b^a is the block matrix

$$\Gamma_b^a = \begin{pmatrix} \dot{\phi}^K \Gamma_{JK}^I & 0 \\ 0 & \dot{\phi}^K \Gamma_{JK}^I \end{pmatrix}. \quad (2.22)$$

In each block I represents the species label associated with the phase-space label a , and J represents the species label associated with b .

A similar equation can be found for the fields in the interaction picture. Using Eq. (2.3) to deduce tree-level expressions for the 2- and 3-point functions in terms of interaction-picture fields, it follows that evolution equations can be derived by direct differentiation and use of the interaction-picture equations of motion to rewrite time derivatives. The results are

$$D_t \Sigma^{ab} = u^a{}_c \Sigma^{cb} + u^b{}_c \Sigma^{ac}, \quad (2.23a)$$

$$D_t \alpha^{abc} = u^a{}_d \alpha^{dbc} + u^a{}_{de} \Sigma^{db} \Sigma^{ec} + 2 \text{ cyclic } (a \rightarrow b \rightarrow c), \quad (2.23b)$$

where we have written the phase-space 2- and 3-point functions as

$$\langle X^{\mathbf{a}} X^{\mathbf{b}} \rangle \equiv (2\pi)^3 \delta(\mathbf{k}_a + \mathbf{k}_b) \Sigma^{ab}, \quad (2.24a)$$

$$\langle X^{\mathbf{a}} X^{\mathbf{b}} X^{\mathbf{c}} \rangle \equiv (2\pi)^3 \delta(\mathbf{k}_a + \mathbf{k}_b + \mathbf{k}_c) \alpha^{abc}. \quad (2.24b)$$

These equations match those in the canonical case except that the time derivative $D_t \equiv \dot{\phi}^I \nabla_I$ is now covariant and will introduce terms involving the connexion components. A more detailed derivation of these equations can be found in Appendix 2.6.2.

For practical calculations we need explicit expressions for the u -tensors. They are [Dias

et al., 2016]

$$u^a_b = \begin{pmatrix} 0 & \delta^I_J \\ M^I_J & -3H\delta^I_J \end{pmatrix}, \quad (2.25a)$$

$$u^a_{bc} = \left\{ \begin{array}{l} \begin{pmatrix} -B_{JK}^I & -C^I_{JK} \\ 3A^I_{JK} & B^I_{KJ} \end{pmatrix} \\ \begin{pmatrix} -C^I_{KJ} & 0 \\ B^I_{JK} & C_{KJ}^I \end{pmatrix} \end{array} \right\}, \quad (2.25b)$$

in which the index a labels rows of the top-level matrix. For u^a_b , the index b labels the remaining columns; for u^a_{bc} , the indices bc label rows and columns of each submatrix. As above, the field-space labels I, J, K represent the species associated with the phase-space labels a, b and c .

Further details of the calculation, including the Heisenberg equations of motion for Q^I and P^I , can be found in Appendix 2.6.2.

2.3.5 Gauge transformation

Although the formalism of covariant correlation functions is computationally convenient, the covariant perturbations Q^I and their statistical properties are not directly measurable. The final step is therefore to express correlation functions of measurable quantities such as the curvature perturbation ζ in terms of the covariant correlation functions. This is a covariantization of the gauge transformation from the spatially flat gauge to the uniform density gauge [Dias et al., 2015a, Dias et al., 2015b, Dias et al., 2016].

Using the methods of Ref. [Dias et al., 2015a] we find that the density fluctuation on spatially flat slices can be written in terms of the covariant perturbations Q^I ,

$$\begin{aligned} \delta\rho = & \dot{\phi}^I D_t Q_I + V_I Q^I + \frac{1}{2} (3\alpha_1^2 - 2\alpha_2 - 2\alpha_1) \dot{\phi}^I \dot{\phi}_I \\ & + \frac{1}{2} V_{IJ} Q^I Q^J + \frac{1}{2} D_t Q^I D_t Q_I - 2\alpha_1 \dot{\phi}^I D_t Q_I + \frac{1}{2} R_{IJKL} Q^I \dot{\phi}^J \dot{\phi}^K Q^L, \end{aligned} \quad (2.26)$$

where α_1 and α_2 , respectively, are the first- and second-order perturbations to the lapse. We have neglected spatial gradients that become negligible on superhorizon scales.

Eq. (2.26) is superficially different to the canonical case due to the final term involving the Riemann tensor. However, the same term appears in the Hamiltonian constraint (see Eq. (2.85)), and after using this constraint to simplify (2.26) the result matches the naïve covariantization of the canonical formula [Dias et al., 2015a].

Using the results of Dias et al. [Dias et al., 2015a] to express ζ in terms of $\delta\rho$, it follows that the curvature perturbation can be written in the form

$$\zeta(\mathbf{k}) = N_{\mathbf{a}} X^{\mathbf{a}} + \frac{1}{2} N_{\mathbf{ab}} X^{\mathbf{a}} X^{\mathbf{b}}. \quad (2.27)$$

The coefficient matrices N_a and N_{ab} are given by

$$N_a = -\frac{\dot{\phi}_I}{2HM_{\text{P}}^2\epsilon} \begin{pmatrix} 1 \\ 0 \end{pmatrix}, \quad (2.28a)$$

$$N_{ab} = \frac{1}{3H^2M_{\text{P}}^2\epsilon} \begin{pmatrix} \frac{\dot{\phi}_I\dot{\phi}_J}{M_{\text{P}}^2} \left[-\frac{3}{2} + \frac{9}{2\epsilon} + \frac{3}{4\epsilon^2} \frac{V_K\pi^K}{H^3M_{\text{P}}^2} \right] & \frac{3}{H\epsilon} \frac{\dot{\phi}_I\dot{\phi}_J}{M_{\text{P}}^2} - \frac{3H}{k^2} [\mathbf{k}_a \cdot \mathbf{k}_b + k_a^2] G_{IJ} \\ \frac{3}{H\epsilon} \frac{\dot{\phi}_I\dot{\phi}_J}{M_{\text{P}}^2} - \frac{3H}{k^2} [\mathbf{k}_a \cdot \mathbf{k}_b + k_b^2] G_{IJ} & 0 \end{pmatrix}. \quad (2.28b)$$

2.4 Numerical results

We are now able to solve the equations obtained in §2.3 and use them to compute the observable 2- and 3-point functions of an arbitrary model with user-defined kinetic mixing matrix.

Overview.—In summary, this involves obtaining numerical solutions to the 2- and 3-point function transport equations (2.23a)–(2.23b), using the u -tensors specified in (2.25a)–(2.25b). In turn, these depend on the kinetic matrix G_{IJ} and the ‘species tensors’ m_{IJ} , A_{IJK} , B_{IJK} and C_{IJK} that specify the Hamiltonian (cf. Eq. (2.14)). They must be determined for each model from the general formulae (2.7) and (2.10a)–(2.10c). The initial conditions are given by Eqs. (2.18a)–(2.18d), provided a suitable initial time can be found at which the massless approximation is valid for all species. These initial conditions also depend on G_{IJ} , m_{IJ} , A_{IJK} , B_{IJK} and C_{IJK} . Finally, Eqs. (2.28a) and (2.28b) are used to construct the correlation functions of ζ .

Each of the transport tools `mTransport`, `CppTransport` and `PyTransport` uses symbolic algebra to automate the calculation of M_{IJ} , A_{IJK} , B_{IJK} and C_{IJK} from a specification of the kinetic matrix G_{IJ} and the potential V . With explicit expressions for each tensor, it is possible to set up the transport equations and compute suitable initial conditions. Additionally, both `CppTransport` and `PyTransport` automate the task of finding a suitable

initial time at which the massless approximation is valid; in `mTransport` this currently has to be done by hand, or a suitable initial time estimated.

Notation.—When discussing concrete models we generally use the dimensionless power spectrum $\mathcal{P}(k)$, defined in terms of the ordinary power spectrum $P(k)$ (see Eq. (2.163)) using

$$\mathcal{P}(k) \equiv \frac{k^3}{2\pi} P(k), \quad (2.29)$$

The analogous quantity for the three-point function is the ‘dimensionless bispectrum’, defined by

$$\mathcal{B}(k_1, k_2, k_3) \equiv (k_1 k_2 k_3)^2 B(k_1, k_2, k_3). \quad (2.30)$$

We also use the reduced bispectrum, conventionally written $f_{\text{NL}}(k_1, k_2, k_3)$, which is defined to satisfy

$$\frac{6}{5} f_{\text{NL}}(k_1, k_2, k_3) \equiv \frac{B(k_1, k_2, k_3)}{P(k_1)P(k_2) + P(k_1)P(k_3) + P(k_2)P(k_3)}. \quad (2.31)$$

Notice that this is *not* the same as the parameter $f_{\text{NL}}^{\text{local}}$ measured by CMB experiments, although in models where the bispectrum is dominantly of the ‘local’ type it is closely related to it.

To specify the configuration of Fourier wavenumbers that characterize the bispectrum we use the parametrization suggested by Fergusson & Shellard [Fergusson & Shellard, 2007],

$$k_1 \equiv \frac{k_t}{4} (1 + \alpha + \beta), \quad (2.32a)$$

$$k_2 \equiv \frac{k_t}{4} (1 - \alpha + \beta), \quad (2.32b)$$

$$k_3 \equiv \frac{k_t}{2} (1 - \beta). \quad (2.32c)$$

The overall scale of the momentum triangle is measured by its perimeter $k_t \equiv k_1 + k_2 + k_3$, and its shape is measured by α and β . The allowed ranges are $-1 \leq \alpha \leq 1$ and $0 \leq \beta \leq 1$.

By default, `CppTransport` uses its own ‘internal normalization’ in which a distinguished e-fold number N_* is user-chosen and the wavenumber k_* is set to exit the horizon at this time by making $k_* = aH$ which gives k in units of energy internally. In this normalization, other wavenumbers are measured relative to k_* by giving the ratios k/k_* or k_t/k_* respectively. This convention means that all wavenumbers quoted in this section are dimensionless. In each case we quote the corresponding value of N_* . Where other horizon exit times are given, these are measured relative to the initial conditions at $N = 0$.

2.4.1 Obtaining the transport codes

All tools (mTransport, CppTransport and PyTransport) can be downloaded from the website transportmethod.com. At the time of writing the current version of PyTransport is v2.0 and the current version of CppTransport is 2018.1. Alternatively, development versions of CppTransport and PyTransport can be downloaded from their respective GitHub repositories. In this paper we focus on the new features in CppTransport that support an arbitrary metric G_{IJ} .

An introduction to CppTransport was given in §8 of Dias et al. [Dias et al., 2016] and a comprehensive user guide is available on the arXiv [Seery, 2016]. When making use of the new features available in 2018.1 most steps remain the same, with only minor variations:

- To use a nontrivial metric G_{IJ} it is first necessary to specify that the model is non-canonical by including the directive

```
lagrangian = nontrivial_metric;
```

in the `model` block of the input file. Having done so the metric can be specified along with the potential as a list of components surrounded by square brackets `[...]`. For example, the metric on a flat two-dimensional field-space in polar coordinates would be written

```
metric = [ R, R = 1; theta, theta = R^2; ];
```

Off-diagonal elements need be specified only for the upper or lower triangle, and entries that are not given are assumed to be zero. Elements can make use of subexpressions declared elsewhere in the model file.

- A suitable set of templates must be chosen for the core and implementation files that use correct index placement and employ the covariantized formulae given in §2.3. An extra set of templates with these properties is bundled with 2018.1. To use them, the `template` block of the model file should read

```
templates
{ core          = "nontrivial_metric_core";
  implementation = "nontrivial_metric_mpi";
};
```

All Riemann terms will be correctly included in the u -tensors and initial conditions, and the transport equations will include correct connexion components.

2.4.2 Cartesian versus polar coordinates

We begin by reproducing results for the gelaton-like scenario [Tolley & Wyman, 2010] studied in Dias et al. [Dias et al., 2016]. This is an ‘adiabatic-like’ model in which a continuously-turning light field is dressed by the fluctuations of a transverse heavy field, and has similarities to the scenario of quasi-single field inflation [Chen & Wang, 2010]. Because the heavy field tracks the minimum of the effective potential, slightly displaced due to the radial motion of the light field, the model behaves as if it has a single collective degree of freedom.

The model is most conveniently expressed in polar field-space coordinates R and θ , and therefore Ref. [Dias et al., 2016] performed a coordinate transformation to Cartesian fields $X = R \cos \theta$, $Y = R \sin \theta$ to produce a Euclidean kinetic matrix. In this section we study the model in its original polar formulation, finding excellent agreement. The Lagrangian is

$$S = \frac{1}{2} \int d^4x \sqrt{-g} [(\partial R)^2 + R^2(\partial\theta)^2 + 2V(R, \theta)], \quad (2.33)$$

where R is the heavy field and θ is the light field. The field-space metric is

$$G_{IJ} = \begin{pmatrix} 1 & 0 \\ 0 & R^2 \end{pmatrix}. \quad (2.34)$$

In Ref. [Dias et al., 2016] the potential was chosen so that it represents a circular valley at fixed R . The angular velocity $\omega = \dot{\theta}/H$ was chosen so that a rotation through π occurred over approximately 30 e-folds. A suitable choice is

$$V = V_0 \left(1 + \frac{29\pi}{120} \theta + \frac{1}{2} \frac{\eta_R}{M_{\text{P}}^2} (R - R_0)^2 + \frac{1}{3!} \frac{g_R}{M_{\text{P}}^3} (R - R_0)^3 + \frac{1}{4!} \frac{\lambda_R}{M_{\text{P}}^4} (R - R_0)^4 \right), \quad (2.35)$$

with the parameters $V_0 = 10^{-10} M_{\text{P}}^4$, $\eta_R = 1/\sqrt{3}$, $g_R = M_{\text{P}}^2 V_0^{-1/2}$, $\lambda_R = 0.5 M_{\text{P}}^3 \omega^{-1/2} V_0^{-3/4}$ and $R_0 = (30 M_{\text{P}}^2 / \pi^2)^{1/2}$.

Ref. [Dias et al., 2016] used initial conditions corresponding to

$$X_{\text{init}} = -R_0, \quad (2.36a)$$

$$Y_{\text{init}} = 10^{-2} R_0. \quad (2.36b)$$

In polar coordinates these become

$$R_{\text{init}} = \sqrt{X_{\text{init}}^2 + Y_{\text{init}}^2}, \quad (2.37a)$$

$$\theta_{\text{init}} = \tan^{-1} \left(\frac{Y_{\text{init}}}{X_{\text{init}}} \right). \quad (2.37b)$$

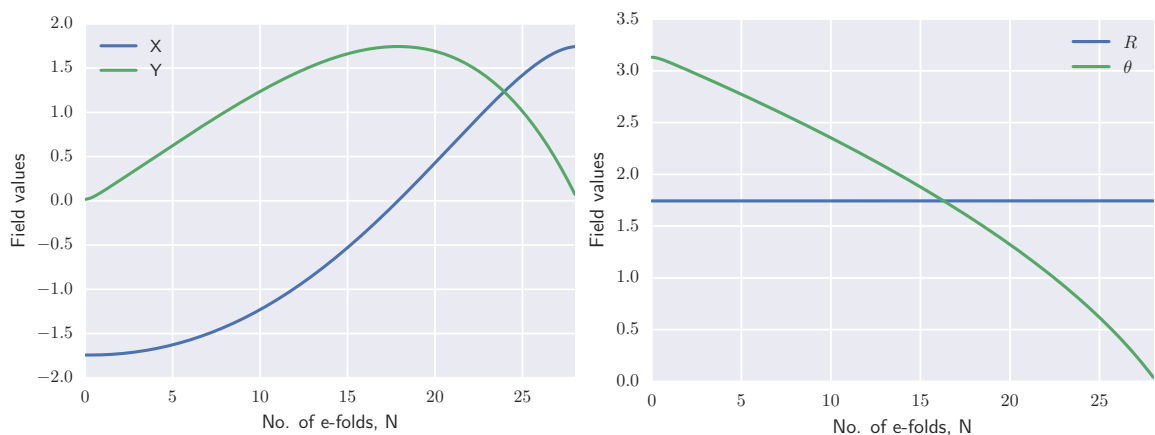


Figure 2.1: Field plots for the QSFI/Gelaton model (2.35) until end of inflation. Left: time evolution of the canonical fields X and Y . Right: time evolution of the non-canonical fields R and θ .

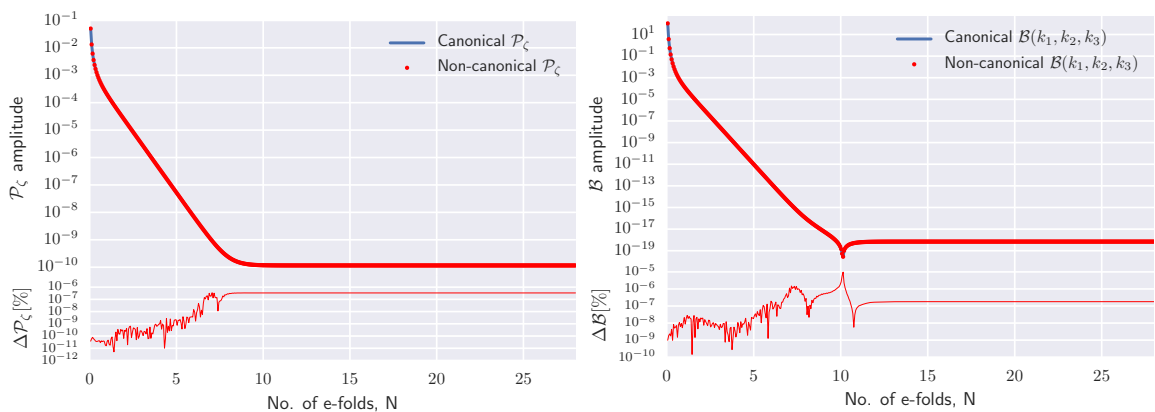


Figure 2.2: QSFI/Gelaton residual plots for the dimensionless power spectrum (left) and bispectrum (right) on equilateral configurations for a k and a k_t mode both leaving the horizon at $N = 8.0$ respectively.

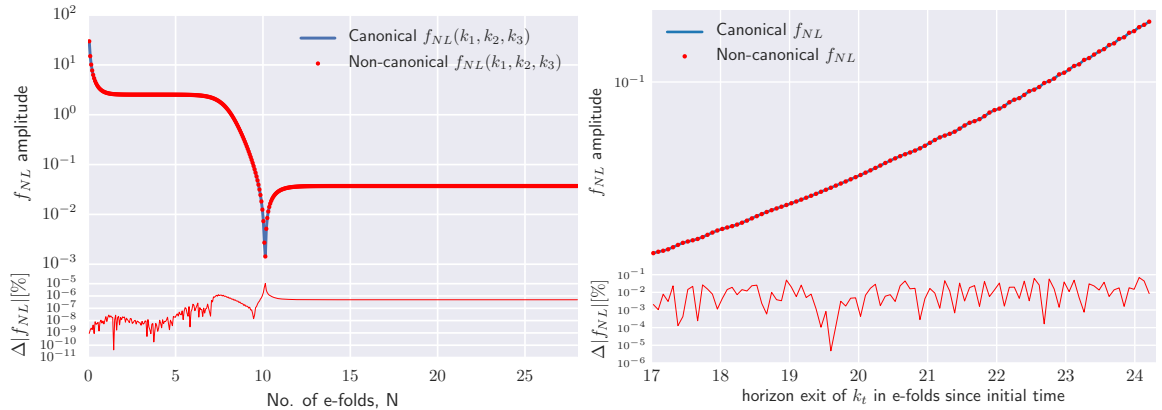


Figure 2.3: QSFI/Gelaton residual plots for the reduced bispectrum on equilateral configurations. Left: time evolution of f_{NL} for a k_t mode leaving the horizon at $N = 8.0$. Right: k_t -dependence of f_{NL} for a range of k_t values leaving between 17.0 and 24.2 e-folds after the initial conditions.

The background evolution is plotted in Fig. 2.1. Inflation lasts for 28 e-folds, and the field evolutions match to high accuracy.

In the left panel of Fig. 2.2 we plot the dimensionless power spectrum of ζ together with its residual, defined by $\Delta\mathcal{P} = |\mathcal{P}_{\text{n.can}} - \mathcal{P}_{\text{can}}|/\mathcal{P}_{\text{can}}$. The results agree to better than $10^{-6}\%$. The right panel gives a similar comparison for the dimensionless bispectrum, showing agreement to better than $10^{-5}\%$.

In Fig. 2.3 we compare the predicted value of the reduced bispectrum f_{NL} . The left-hand panel shows its time evolution for a single Fourier configuration that exits the horizon at 8.0 e-folds. The results agree to within $10^{-5}\%$, where the largest residual is given during the rapid evolution of f_{NL} during horizon crossing.

The right panel of Fig. 2.3 shows the values measured at the end of inflation as a function of wavenumbers that exit the horizon between 17.0 and 24.2 e-folds after the initial conditions are set. Here the residuals are typically at the $10^{-2}\%$ level with the maximum residual at 0.07%. These are different from the left panel due to the k_t values exiting much later, at a time closer to the end of inflation at 28.0 e-folds where the bispectrum has rapid small-amplitude oscillations.

Despite the f_{NL} vs. k_t plot having larger residuals, these results indicate that the non-canonical transport formalism agrees with its canonical counterpart to within at least 0.1% when applied to this model.

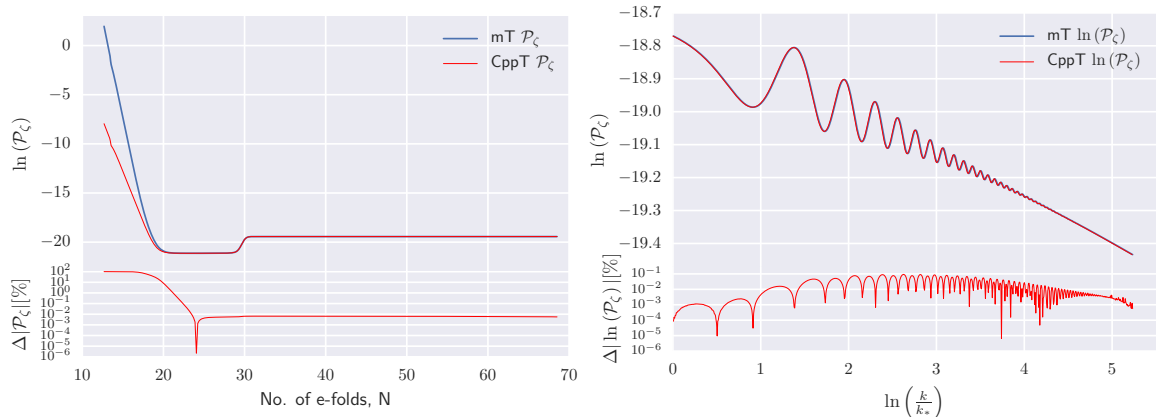


Figure 2.4: Power spectrum residuals from the quasi-two-field model. Left: residual as a function of time for the k -mode that exits the horizon at 19.0 e-folds from the initial time. Right: residual of $\ln(\mathcal{P}_\zeta)$ as a function of $\ln(k/k_*)$ for a range of k numbers exiting the horizon between 0.0 and 5.2 e-folds after the scale, k_* , which exits at $N_* = 13.5$.

2.4.3 Quasi-two-field inflation

Dias et al. [Dias et al., 2015b] introduced a ‘quasi-two-field’ model in which two light scalars drive inflation. One of these fields excites a heavy third field via a noncanonical kinetic coupling, giving rise to oscillatory features in the power spectrum. This is an extension of a simpler two-field model suggested by Achúcarro et al. [Achúcarro et al., 2011]. Such oscillatory features have been well-studied in the literature [Gao et al., 2012, Achúcarro et al., 2011, Achúcarro et al., 2014, Adshead et al., 2013, Flauger et al., 2017]. The power spectrum was computed using `mTransport` by Dias et al. [Dias et al., 2015b], and the bispectrum was computed using `PyTransport` by Ronayne et al. [Ronayne & Mulryne, 2017], giving us an opportunity to benchmark `CppTransport` against the other transport tools. Note that this is *not* an empty comparison, because although all the transport tools use the same underlying framework they make very different numerical choices in implementation.

The three fields in the model are labelled ϕ_1 , ϕ_2 and ϕ_3 , and the field-space metric is

$$G_{IJ} = \begin{pmatrix} 1 & \Gamma(\phi_1) & 0 \\ \Gamma(\phi_1) & 1 & 0 \\ 0 & 0 & 1 \end{pmatrix}, \quad (2.38)$$

where $\Gamma(\phi_1)$ is defined to equal [Achúcarro et al., 2011]

$$\Gamma(\phi_1) = \frac{\Gamma_0}{\cosh^2 \frac{2(\phi_1 - \phi_{1(0)})}{\Delta\phi_1}}, \quad (2.39)$$

where $\Gamma_0 = 0.9$ is the maximum value of $\Gamma(\phi_1)$, $\phi_{1(0)} = 7M_{\text{P}}$ is the value of ϕ_1 at the apex of the turn and $\Delta\phi_1 = 0.12M_{\text{P}}$ is the range of ϕ_1 during the turn. The potential is

$$V = \frac{1}{2}g_1m^2\phi_1^2 + \frac{1}{2}g_2m^2\phi_2^2 + \frac{1}{2}g_3m^2\phi_3^2, \quad (2.40)$$

with parameters $g_1 = 30$, $g_2 = 300$, $g_3 = 30/81$, $m = 10^{-6}$. The initial conditions are

$$\phi_1^{\text{init}} = 10.0M_{\text{P}}, \quad (2.41a)$$

$$\phi_2^{\text{init}} = 0.01M_{\text{P}}, \quad (2.41b)$$

$$\phi_3^{\text{init}} = 13.0M_{\text{P}}. \quad (2.41c)$$

Two-point function.—In this section, we define the residual between the `mTransport` and `CppTransport` power spectrum as

$$|\Delta\mathcal{P}| = \frac{|\mathcal{P}_{\text{CppT}} - \mathcal{P}_{\text{mT}}|}{\mathcal{P}_{\text{mT}}}. \quad (2.42)$$

In the left panel of Fig. 2.4 we plot the residual as a function of time for the k -mode that exits the horizon $N = 19.0$ e-folds from the initial time. During the superhorizon phase the agreement is typically at 0.01% or better, except at a small number of points where the evolution is particularly rapid.

Note that the solutions diverge on *subhorizon* scales. As explained in Ref. [Dias et al., 2015a], the curvature perturbation ζ does not have a unique definition on subhorizon scales, and the precise value we assign depends which k -dependent terms are kept. `mTransport` uses the ‘local’ form of ζ defined in Ref. [Dias et al., 2015a], whereas `CppTransport` and `PyTransport` uses the ‘simple’ form (which agrees with Eqs. (2.28a)–(2.28b)). At linear level these are [Dias et al., 2015a]

$$\zeta_{\text{local}} = \frac{1}{2H^2M_{\text{P}}^2\epsilon(3-\epsilon)}(\dot{\phi}_I\dot{Q}^I + V_I Q^I) \quad (2.43a)$$

$$\zeta_{\text{simple}} = -\frac{\dot{\phi}_I Q^I}{2HM_{\text{P}}^2\epsilon}. \quad (2.43b)$$

The ‘local’ form mixes Q^I and \dot{Q}^I whereas the ‘simple’ form involves only Q^I . Correlation functions involving \dot{Q}^I increase on subhorizon scales more rapidly than correlation functions of Q^I alone, which accounts for the different time-dependence visible in Fig. 2.4 on subhorizon scales. The discrepancy is harmless. On superhorizon scales the two forms agree to high accuracy, as they should.

Although this difference means that the ζ correlation functions cannot be compared directly on subhorizon scales, we have verified that the field correlation functions (which are unambiguous) agree to 5 significant figures.

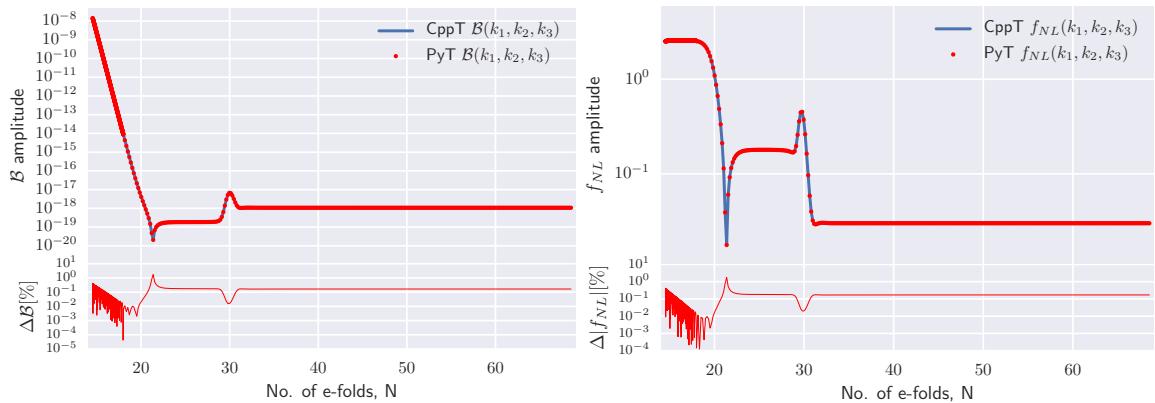


Figure 2.5: Quasi-two-field residual time-plots for three-point functions on equilateral configurations. Left: dimensionless bispectrum, \mathcal{B} , for a k_t value that exits the horizon at $N_{\text{exit}} = 19.9$ plotted against time. Right: reduced bispectrum, f_{NL} , plotted against time for the same k_t and N_{exit} values.

In the right panel of Fig. 2.4 we plot the residuals as a function of scale for a range of k -modes exiting the horizon up to 5.3 e-folds from the pivot scale. The residuals remain below 0.1% over the whole range. This shows excellent agreement between `mTransport` and `CppTransport` despite the rapid oscillations visible in the power spectrum.

Three-point function.—To compare 3-point functions we use the latest version of `PyTransport` [Ronayne & Mulryne, 2017]. For each measure X of 3-point correlations we define the residual $|\Delta X| = |X_{\text{CppT}} - X_{\text{PyT}}|/X_{\text{CppT}}$.

In the left-hand panel of Fig. 2.5 we plot the residual of the dimensionless bispectrum as a function of time for an equilateral configuration where k_t exits the horizon roughly 20 e-folds after the initial time. Our results agree at roughly 0.3% through most of the evolution, with short-lived excursions to larger values at times of rapid evolution. In the right-hand panel we give an equivalent plot for the reduced bispectrum f_{NL} . We conclude that the variation in numerical results between any two of the transport tools is negligible in comparison with current experimental errors.

The left panel of Fig. 2.6 shows the residual of the reduced bispectrum as a function of k_t for scales exiting the horizon between 10.9 and 19.9 e-folds after the initial time. Agreement between `CppTransport` and `PyTransport` is at the level $\leq 1\%$ over almost the entire range of k_t , despite the extremely rapid oscillations visible in the range $10^7 \lesssim k_t \lesssim 10^8$. In the right panel we show a zoomed-in section highlighting the region of most significant disagreement. The cause of the discrepancy is currently under investigation. This is the only model we have encountered in which our codes show a small disagreement of this kind.

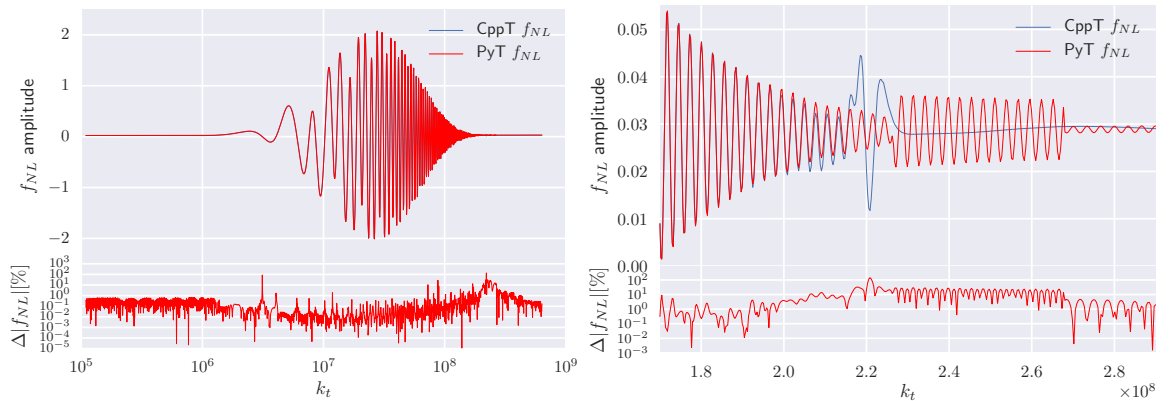


Figure 2.6: Reduced bispectrum residuals in equilateral k_t space where $k_* = 1$ and $N_{*exit} = 0.1$. Left: residuals for the reduced bispectrum f_{NL} plotted against a range of k_t values exiting the horizon between 10.9 & 19.9 e-folds after inflation begins. Right: zoom-in of the largest residual at $k_t \approx 2.2 \times 10^8$.

Shape plots.—Up to this point we have focused on the bispectrum amplitude as a function of time or scale, but important information is also encoded in the shape regarding the type of interactions that appear in the Lagrangian. In Fig. 2.7 we show the dimensionless bispectrum as a function of α and β at fixed k_t , rescaled to have unit amplitude on the equilateral configuration [Fergusson & Shellard, 2007]. We choose k_t so that the wavenumber characterizing this configuration exits the horizon 16.6 e-folds after the initial conditions, and the plots depict the shape given 14.232 e-folds after the initial conditions. In the left panel we show the amplitude as a surface plot with the z -height representing the (rescaled) bispectrum amplitude, and in the right panel we give a corresponding contour plot.

At the time given in Fig. 2.7, the shape shows 15 separate peaks that have evolved from an equilaterally-dominated bispectrum with a single maximum at the equilateral configuration. During the subhorizon phase of inflation, each region of the shape continuously subdivides, generating further peaks. The subdivision continues until horizon-crossing at $N \approx 17$, after which 8 peaks have formed along each side of the shape plot. The bispectrum shape is briefly re-excited during the turn at $N = 30$ e-folds before settling to a constant value until the end of inflation. This behaviour is best seen in our video of the surface plot evolution available on Vimeo.

2.4.4 The gelaton model

We now apply our tools to a new example: the gelaton model introduced by Tolley & Wyman [Tolley & Wyman, 2010]. In this model a heavy gelaton field, with a mass $m \gtrsim H$,

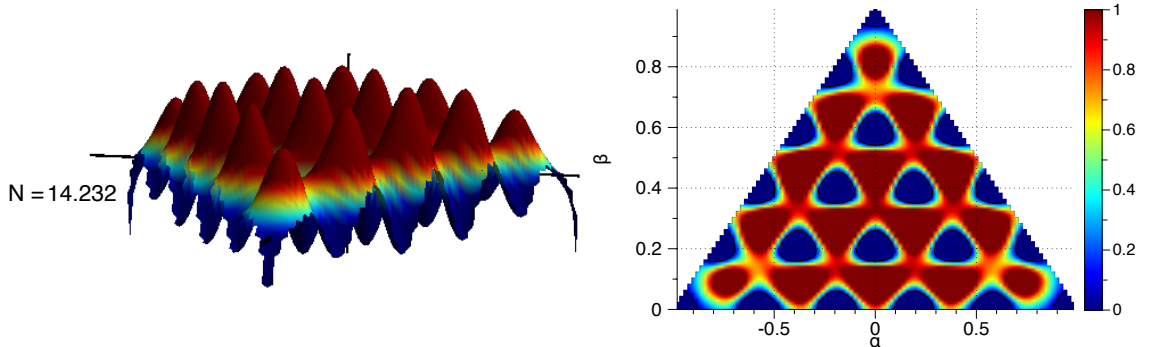


Figure 2.7: Shape plots for the quasi-two-field model. Left: 3D surface plot of the dimensionless bispectrum, $\mathcal{B}(\alpha, \beta)$, taken at $N = 14.232$ e-folds for a range of shapes with $-0.98 \leq \alpha \leq 0.98$ and $0 \leq \beta \leq 0.99$ and a fixed k_t mode with $N_{\text{exit}} = 16.6$ e-folds. Right: 2D contour plot for the same values.

is strongly coupled to a light field and dresses its excitations. This causes the light field's dynamics to be modified. Tolley & Wyman modelled this behaviour using an action with nontrivial kinetic mixing,

$$S = \frac{1}{2} \int d^4x \sqrt{-g} \left[M_{\text{P}}^2 R - \partial_\mu \phi \partial^\mu \phi - e^{2b(\phi)} \partial_\mu \chi \partial^\mu \chi - V(\phi, \chi) \right]. \quad (2.44)$$

Here ϕ is the gelaton, χ is the inflaton, and we can see that the field-space metric is given by:

$$G_{IJ} = \begin{pmatrix} 1 & 0 \\ 0 & e^{2b(\phi)} \end{pmatrix}. \quad (2.45)$$

The function $b(\phi)$ is chosen so that the effective mass of the gelaton is much larger than H , ensuring that it remains at the minimum of its effective potential. This is displaced from the minimum of the bare potential $V(\phi, \chi)$ due to the kinetic coupling. We label the true minimum ϕ_0 , which should be determined by the condition that the ϕ field is in static equilibrium,

$$V_{,\phi}(\phi_0, \chi) - 2b_{,\phi}(\phi_0) e^{2b(\phi_0)} X = 0, \quad (2.46)$$

where $X = -\frac{1}{2}(\partial\chi)^2$ is the kinetic energy of χ . After integrating out ϕ from the action (2.44) it can be shown that the resulting low-energy theory is equivalent to a $P(X, \chi)$ model [Tolley & Wyman, 2010] in which the action is an arbitrary function of X and χ . Expanding the low-energy action to second order shows that the dressed χ fluctuations propagate with phase velocity

$$c_s^2 = \left(1 + \frac{4e^{2b} (b_{,\phi})^2 \dot{\chi}^2}{m_{\text{gelaton}}^2} \right)^{-1}, \quad (2.47)$$

where m_{gelaton} is the effective gelaton mass. It is known that $P(X, \chi)$ models in which the speed of sound is significantly different from unity give enhanced three-point correlations on equilateral configurations [Seery & Lidsey, 2005b, Chen et al., 2007, Silverstein & Tong, 2004, Alishahiha et al., 2004]. The gelaton model will exhibit such a phenomenology if the speed of sound can be depressed significantly below unity, $c_s \ll 1$, while keeping the gelaton mass large, $m_{\text{gelaton}} \gtrsim H$.

DBI potential.—We now specialize to the ‘hyperbolic manifold’ scenario suggested by Tolley & Wyman in which $b(\phi) = g\phi/M_{\text{P}}$. With this choice, the dynamics of DBI inflation can be replicated by adopting the following potential

$$V_{\text{DBI}}(\phi, \chi) = T(\chi) \cosh\left(\frac{2g\phi}{M_{\text{P}}}\right) - T(\chi) + W(\chi), \quad (2.48)$$

where $g = 0.43$ is a free parameter used to adjust the gelaton mass, $T(\chi)$ is the brane tension in the DBI interpretation, and $W(\chi)$ is a potential representing interactions between the brane and other degrees of freedom in the geometry. The gelaton mass is

$$m_{\text{gelaton}}^2 = 4g^2 M_{\text{P}}^{-2} T(\chi) \exp\left(-\frac{2g\phi}{M_{\text{P}}}\right). \quad (2.49)$$

To fix the model we must specify $T(\chi)$ and $W(\chi)$. We adopt

$$T(\chi) = \frac{1}{2}\lambda^2\chi^2, \quad (2.50a)$$

$$W(\chi) = \Lambda^4 - \frac{1}{2}m^2\chi^2, \quad (2.50b)$$

where $\lambda = 0.001M_{\text{P}}$, $\Lambda = 0.005M_{\text{P}}$, and $m = 10^{-5}M_{\text{P}}$. The potential $W(\chi)$ is chosen to keep the expectation value of χ sub-Planckian. It can be assumed to be representative of any hilltop potential provided χ does not become too large.

The initial conditions for the two fields are $\phi_{\text{init}} = 1 \times 10^{-3}M_{\text{P}}$ and $\chi_{\text{init}} = 1 \times 10^{-4}M_{\text{P}}$ respectively.

Results.—We perform numerical computations with the full two-field model, to determine whether the low-energy effective description containing only the dressed light fluctuation is an accurate representation of the dynamics. We find very good agreement between our numerical results and the predictions of the low-energy effective theory.

In the left panel of Fig. 2.8 we plot the evolution of the background fields from their initial values at $N = 0$ until the end of inflation at $N_{\text{end}} = 51$. At early times the evolution of χ is dominated by its kinetic coupling. The ϕ field is driven by the cosh term in V_{DBI} . In the right panel we show the evolution of the power spectrum for a single k -mode leaving the horizon at $N = 8.0$. It exhibits smooth decay inside the horizon and asymptotes to a constant value on superhorizon scales, as it should for an effectively single-field model.

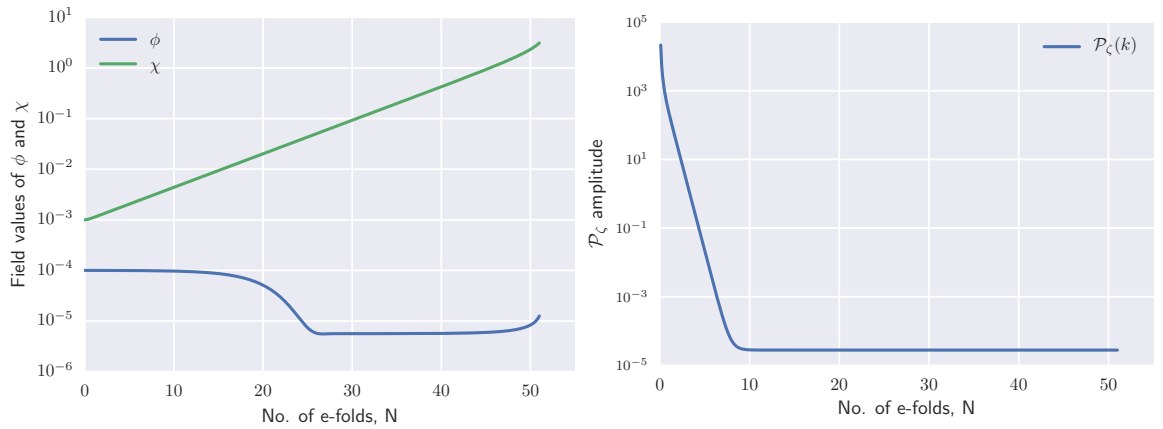


Figure 2.8: Background fields and power spectrum for the gelaton model. Left: e-fold evolution of fields ϕ and χ with inflation ending at $N = 51$. Right: dimensionless power-spectrum \mathcal{P}_ζ for a k mode exiting the horizon 8.0 e-folds after the initial conditions.

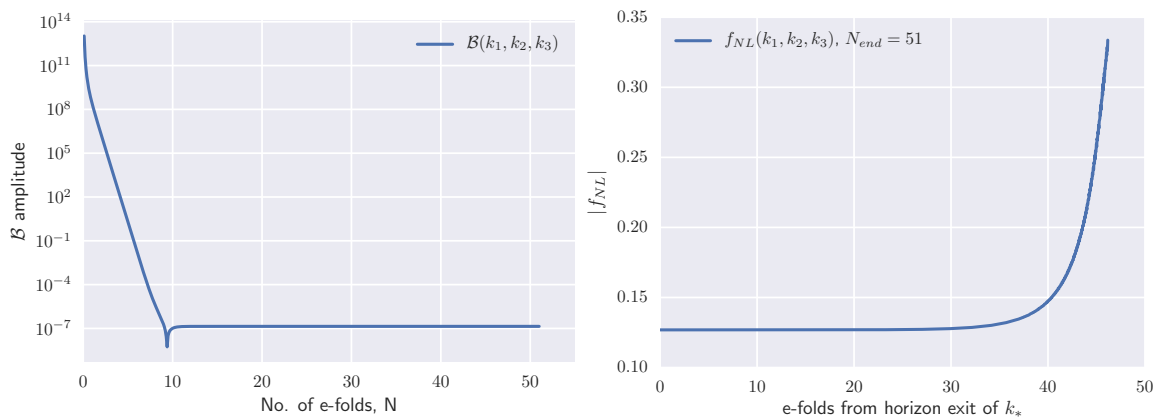


Figure 2.9: Left: dimensionless bispectrum \mathcal{B} for an equilateral configuration where $k_t = 3$ with each individual k mode exiting the horizon at $N = 8.0$. Right: reduced bispectrum f_{NL} plotted against a range of k values exiting the horizon between 0-46 e-folds after the scale k_* with $N_{*exit} = 3.0$.

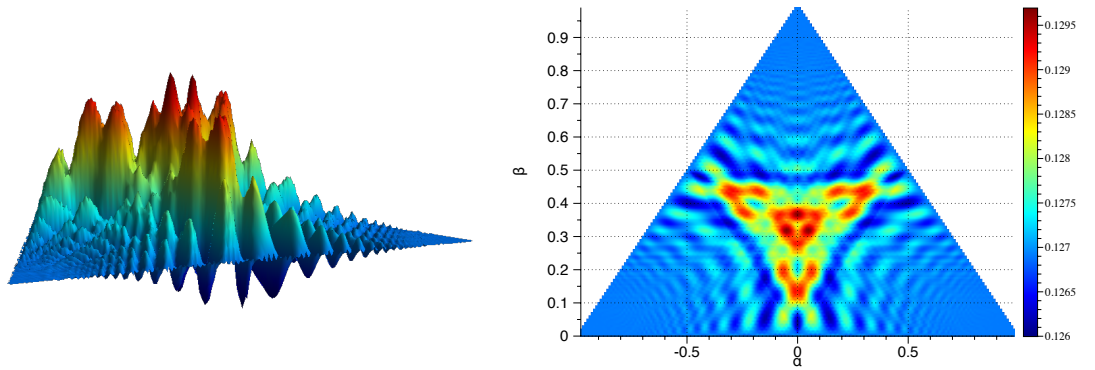


Figure 2.10: Left: gelaton model surface plot showing the shape of the reduced bispectrum, $f_{\text{NL}}(\alpha, \beta)$, taken at a time $N = 25.0$ e-folds for a k_t mode that leaves the horizon 18.9 e-folds after the initial time. Right: contour plot of the data in the left panel.

In the left panel of Fig. 2.9 we plot the evolution of the dimensionless bispectrum for an equilateral configuration with fixed k_t corresponding to horizon exit at a time $N_{\text{exit}} = 8$. In the right panel we show the reduced bispectrum f_{NL} evaluated on equilateral configurations as a function of scale, for a range of k_t exiting the horizon between $N = 0$ and $N = 46$ e-folds after the scale k_* which exits 3.0 e-folds after the initial time. We see that, with this choice of parameters, the enhancement of equilateral configurations is only modest, yielding $|f_{\text{NL}}| \approx 0.13$ for a large range of k before the end of inflation causes $|f_{\text{NL}}|$ to grow slightly as ϵ increases.

In Fig. 2.10 we plot the shape of the reduced bispectrum $f_{\text{NL}}(\alpha, \beta)$ for a single k_t -value that exits the horizon 18.9 e-folds after the initial conditions. As before, the left panel shows a three-dimensional surface plot and the right panel shows the corresponding contour plot. Both are evaluated at time $N = 25.0$, when the time dependence has settled down to become constant. At peak, $|f_{\text{NL}}| \approx 0.1297$ in agreement with the values plotted in Fig. 2.9 (for a different value of k_t), which is still some way from the smallest observable value $|f_{\text{NL}}| \approx 10$. The shape plot shows that the detailed structure of the bispectrum is somewhat complicated, although it resembles the equilateral template in its overall structure.

In the next section we will show that an observationally-relevant amplification of the bispectrum is difficult to achieve for a gelaton model of this type, because consistency constraints give very little parameter space to depress the speed of sound.

Gelaton model parameter constraints

The effective single-field description of the gelaton model is applicable only when the gelaton mass m_{gelaton} is significantly larger than H . For smaller masses we must revert to the full two-field description. We now argue that the modest amplitude of f_{NL} seen in Figs. 2.9 and 2.10 is a consequence of simultaneously satisfying this and other consistency conditions.

Gelaton mass.—First, we require $m_{\text{gelaton}}^2 \gg H^2$. With our choice of tension $T(\chi)$, Eq. (2.49) shows that

$$m_{\text{gelaton}}^2 = 2g^2 M_{\text{P}}^{-2} \lambda^2 \chi^2 \exp\left(-\frac{2g\phi}{M_{\text{P}}}\right). \quad (2.51)$$

Evidently, if the argument of the exponential term is large then the gelaton mass will be exponentially suppressed. Therefore we suppose $|2g\phi/M_{\text{P}}| \lesssim 1$, allowing a Taylor expansion of m_{gelaton} . The leading term is

$$m_{\text{gelaton}}^2 \approx 2g^2 M_{\text{P}}^{-2} \lambda^2 \chi^2 + \dots. \quad (2.52)$$

To estimate the Hubble parameter we assume that the slow-roll approximation applies, making the kinetic terms are sub-dominant to the potential. Under these circumstances a reasonable approximation to H^2 will be

$$H^2 \approx \frac{V_{\text{DBI}}}{3M_{\text{P}}^2} = \frac{1}{6} \frac{\lambda^2}{M_{\text{P}}^2} \chi^2 \left(\cosh \frac{2g\phi}{M_{\text{P}}} - 1 \right) + \frac{1}{3M_{\text{P}}^2} \left(\Lambda^4 - \frac{1}{2} m^2 \chi^2 \right), \quad (2.53)$$

where V_{DBI} from Eq. (2.48) has been inserted assuming our choices for $T(\chi)$ and $W(\chi)$.

Our assumption that the exponential in Eq. (2.51) is not significantly suppressed makes the cosh term in (2.53) negligible. Therefore the most significant contribution to H will come from the potential $W(\chi)$. Meanwhile, to prevent higher order terms become relevant we must constrain the negative term $m^2 \chi^2/2$ to be significantly smaller than the hilltop amplitude Λ^4 . This yields

$$\chi^2 \ll \frac{2\Lambda^4}{m^2}. \quad (2.54)$$

In this regime the dominant contribution to the Hubble rate will come from the hilltop,

$$H^2 \approx \frac{\Lambda^4}{3}. \quad (2.55)$$

Eqs. (2.52) and (2.55) can be used together with the consistency condition $m_{\text{gelaton}}^2 \gg H^2$ to yield a *minimum* value of the χ expectation value,

$$\chi^2 \gg \frac{\Lambda^4}{6g^2 \lambda^2}. \quad (2.56)$$

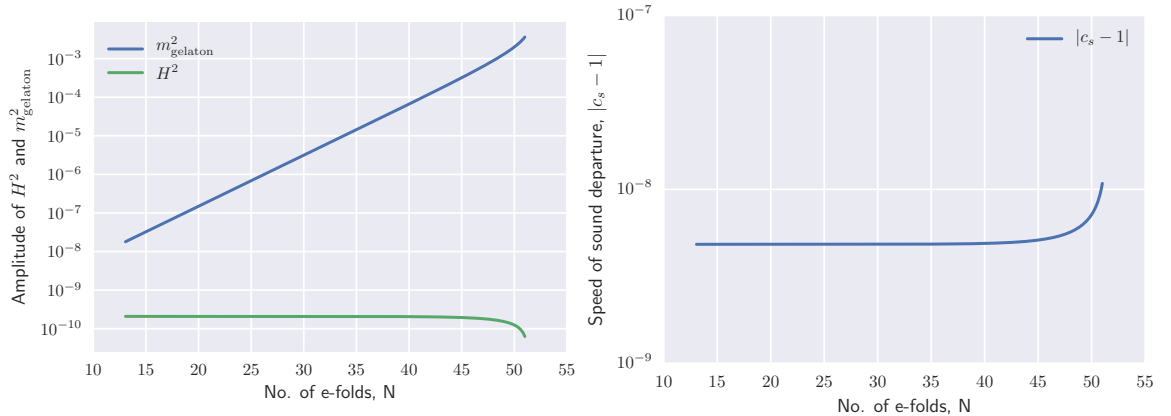


Figure 2.11: Left: a plot of the gelaton mass m_{gelaton}^2 and H^2 demonstrating that the constraint $m_{\text{gelaton}}^2 \gg H^2$ is satisfied. Right: a plot showing the departure in the speed of sound, $|c_s - 1|$ is very small due to the constraints described in §2.4.4.

Consistency of Eqs. (2.54) and (2.56) yields a constraint on the mass m^2 ,

$$m^2 \ll 12g^2\lambda^2. \quad (2.57)$$

Speed of sound.—Second, to give at least modest suppression of the sound speed we suppose $c_s^2 \ll 10/11 \approx 0.9$. Eq. (2.47) then requires

$$\frac{1}{c_s^2} = 1 + \frac{2}{\lambda^2} \left(\frac{\dot{\chi}}{\chi} \right)^2 \gg \frac{11}{10}, \quad (2.58)$$

where, as before, we have performed a Taylor expansion in exponentials of ϕ . The slow-roll approximation can be used to estimate $\dot{\chi}$,

$$\dot{\chi}^2 = \frac{m^4\chi^2}{9H^2} = \frac{m^4\chi^2}{3\Lambda^4}. \quad (2.59)$$

Combining Eq. (2.59) and (2.58) now yields a lower bound for m^2 ,

$$m^2 \gg \sqrt{\frac{3\lambda^2\Lambda^4}{20}}. \quad (2.60)$$

The constraint is the principal obstruction to finding parameter combinations that would yield significant amplification of the equilateral correlations. Most obviously, Eq. (2.60) creates a tension with the upper bound (2.57) causing the available parameter window for m to be rather narrow. The lower limit scales parametrically with λ whereas the upper limit scales with λ^2 , and therefore one strategy to increase the size of the window is to increase λ . Unfortunately, Eq. (2.58) shows that increasing λ will typically force the speed of sound towards unity unless $\dot{\chi}/\chi$ can be changed to compensate. This cannot happen in the slow-roll regime because (2.59) shows that $\dot{\chi}/\chi$ is independent of λ .

For example, with the above choices of g , λ and Λ , the window for m is $0.00139M_{\text{P}} \ll m \ll 0.00145M_{\text{P}}$. This is so narrow that it is not really possible to have the strong ‘ \ll ’ inequality satisfied on either side. As we will see below, our choice $m = 10^{-5}M_{\text{P}}$ amply satisfies the upper bound (2.57) and is sufficient to guarantee $m_{\text{gelaton}} \gg H^2$, but it violates the lower bound and therefore does not yield a suppressed speed of sound.

The limits on the χ expectation value (2.54) and (2.56) give another constraint. Both limits scale with Λ^4 and therefore the relative size of the window does not change with scaling Λ . Instead, we must rely on changing the parameters m or $g\lambda$ that appear in the denominators of (2.54) and (2.56) respectively. We have already seen that m is tightly constrained, making the upper limit practically fixed once Λ is prescribed. Also, if m is not too close to its lower limit then it will also scale roughly with λ . Therefore parametrically widening the available window for the χ expectation value depends on increasing g to decrease the lower limit relative to the upper one. Unfortunately g must be fairly small in order to keep $e^{2g\phi/M_{\text{P}}}$ reasonable small. If the exponential becomes too large then ϵ typically grows also, causing inflation to end exponentially quickly. Therefore, in addition to the small range of m , there is a very small range of χ values that satisfy the constraints for a suppressed speed of sound. In our example the range is roughly $0.0237M_{\text{P}} \ll \chi \ll 0.0254M_{\text{P}}$. This means that it is typically not possible to sustain enhanced three-point correlations for a significant number of e-folds.

We have not succeeded in finding parameter combinations that give a significant enhancement to equilateral correlations while respecting the consistency conditions of the theory. This does not rule out the possibility that the gelaton model can do so, but it would require a different functional form for the potential or the brane tension. We have verified that similar constraints operate for the simplest monomial chaotic models $W(\chi) \propto \chi^n$ for integer n , and that these constraints likewise lead to very narrow windows for m and χ . A modification to the brane tension is possible, but any exotic form would need careful microphysical justification.

Numerical comparison.—In the left panel of Fig. 2.11 we plot the gelaton mass, m_{gelaton}^2 , together with the Hubble rate, H^2 . We demonstrate that $m_{\text{gelaton}}^2 \gg H^2$ so that it is consistent to integrate out the gelaton. Comparison of our numerical results and the analytic estimates given in this section shows that our approximations for m_{gelaton} , c_s , H and $\dot{\chi}$ are each accurate to within an order of magnitude. In the right panel we plot the departure of the speed of sound from unity, $|c_s - 1|$. This is very small, with approximate value $|c_s - 1| \approx 10^{-8}$ using our parameter choices.

Together, the constraints on the gelaton model with a hilltop potential mean that it is possible to get an inflating solution lasting for approximately 50 e-folds, but only without significant amplification of equilateral non-Gaussianities. A similar conclusion applies if we replace the hilltop potential by a monomial large-field model. This does not rule out the possibility that a different gelaton model could achieve significant enhancement, but the resulting model is likely to be more complex than the one considered here.

2.4.5 Isocurvature modes

Throughout this paper, we have always given results for the power spectrum and the bispectrum of the comoving curvature perturbation ζ , because it is only the adiabatic perturbations that are required by observations. However in multi-field models of inflation, there are always isocurvature modes that can give non-adiabatic perturbations which could decay into standard model particles (ν, B, γ) or in to a dark matter candidate such as an axion. Calculating these non-adiabatic perturbations require that the fields are decomposed into an adiabatic perturbation parallel to the background inflation trajectory and non-adiabatic perturbations that are orthogonal to it [Garcia-Bellido & Wands, 1996, Gordon et al., 2001, Lyth & Wands, 2003]. This decomposition was later used with the phase-space description of inflation to find non-adiabatic effects on the bispectrum in Refs. [Elliston et al., 2011, Seery et al., 2012].

`CppTransport` can be used to give all of the n -point functions with mixed fields all written in the flat-space gauge either in a plot or a data table. This feature is demonstrated in Fig. 2.12 above where the left panel gives all of the unique three-point correlation functions from the quasi-two-field model and the right panel gives all of these for the gelaton model. In principle, it would be simple to use the phase-space methods given in Refs. [Elliston et al., 2011, Seery et al., 2012] to calculate the non-adiabatic perturbations for these models or any other inflation model candidate. This could later be used to identify a field decaying into dark matter or another exotic particle.

2.5 Conclusions

We have applied the transport method to calculate the primordial bispectrum produced by inflationary models containing non-canonical kinetic terms. To do so we leverage the formalism of covariant perturbations suggested by Gong & Tanaka [Gong & Tanaka, 2011] to obtain a covariant Hamiltonian up to third order (§§2.3.1–2.3.2). In agreement with other analyses, we show that up to a small number of Riemann terms appearing in M_{IJ} ,

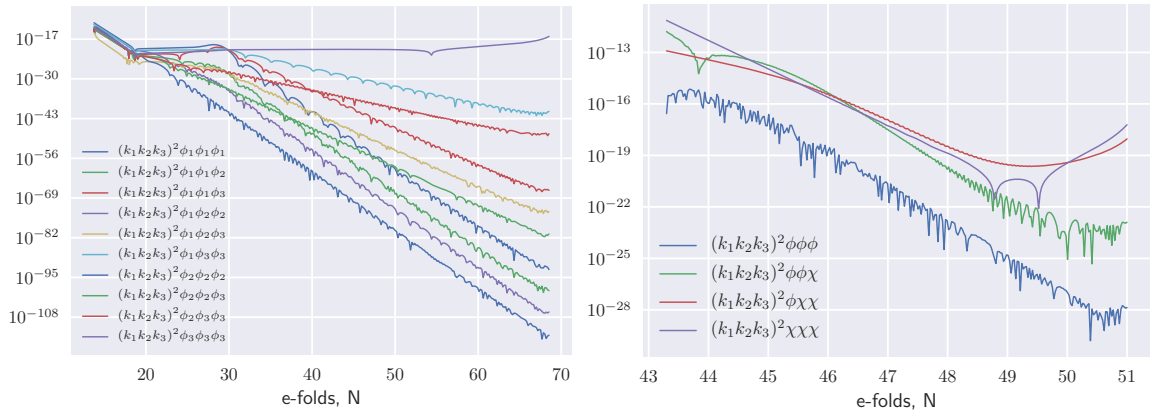


Figure 2.12: Left: a plot of every dimensionless three-point function from the three fields in the quasi-two-field model given for an equilateral k_t mode exiting the horizon 19.1 e-folds after the initial time. Right: a plot of all of the three-point functions possible for the two fields in the gelaton model which is given for an equilateral k_t mode exiting the horizon 49.2 e-folds after the initial time.

A_{IJK} and B_{IJK} , the formalism covariantizes naïvely. Moreover, the initial conditions and gauge transformation to ζ also covariantize naïvely provided index positioning is respected (§§2.3.3–2.3.5). In §2.3.4 we demonstrate how to obtain a covariant hierarchy of transport equations.

We have implemented these equations in a new version of the `CppTransport` tool, which is now capable of handling models with an arbitrary kinetic mixing matrix. At this time, all three transport tools (`mTransport`, `CppTransport` and `PyTransport`) support models of this kind and we can perform a meaningful comparison between them. We find excellent agreement between the different codes (§2.4.3), with differences typically less than 1%. We also find excellent agreement for the same model written in different field-space coordinates (§2.4.2) for which differences typically manifest at less than 0.1%.

In §2.4.4 we used `CppTransport` to obtain numerical predictions for a concrete implementation of the gelaton model. We find good agreement between our numerical results (which capture the full dynamics of the two-field model) and the predictions of the single-field effective description in which the gelaton dresses the light fluctuations, giving them a suppressed speed of sound. We find a small boost in the equilateral bispectrum at the level $|f_{\text{NL}}(k_1, k_2, k_3)| \approx 0.1$ on equilateral configurations. We give an analytic argument that it is not possible to achieve more dramatic enhancements, at least with the potential V_{DBI} designed to reproduce the dynamic of the Dirac–Born–Infeld model, without considering more exotic forms for the potential or brane tension.

To summarise, we have extended the automated numerical framework presented by

Dias et al. [Dias et al., 2016] to include more complex models with a non-trivial kinetic term $G_{IJ}(\phi)\partial_\mu\phi^I\partial^\mu\phi^J$. As before, this allows numerical calculation of all tree-level contributions to the bispectrum and includes physical effects both before and after horizon-crossing. Practically, this means that observable statistics can be found for inflationary models containing a non-trivial kinetic sector, which can include supergravity theories (eg. Refs. [Kallosh & Linde, 2013b, Kallosh et al., 2013]) or models motivated by string-theory (eg. Refs. [Ibanez et al., 2015, Bielleman et al., 2016]). In future we plan to extend CppTransport to allow sampling over the prior probabilities for initial conditions or Lagrangian parameters, enabling estimates of the important observable parameters such as n_s or r in multiple-field models [Mortonson et al., 2011, Easther & Peiris, 2012, Norena et al., 2012, Price et al., 2015].

Acknowledgements The work reported in this paper has been supported by the European Research Council under the European Union’s Seventh Framework Agreement (FP7/2007–2013) and ERC Grant Agreement No. 308082. We would like to thank David Mulryne and John Ronayne for helpful conversations.

2.6 Appendix: Detailed calculations

2.6.1 Perturbed action in curved field space

We begin with an action coupled to N scalar fields ϕ^I , minimally coupled to gravity with a self-interaction potential V ,

$$S \supseteq \frac{1}{2} \int d^4x \sqrt{-g} [R - G_{IJ}g^{\mu\nu}\partial_\mu\phi^I\partial_\nu\phi^J - 2V], \quad (2.61)$$

where R is the Ricci scalar, $g \equiv \det g$ and we use Greek indices and upper case Roman indices for the space-time and field-space coordinates respectively. The kinetic mixing matrix G_{IJ} is symmetric and positive definite, and can be regarded as a metric on field-space. The case of canonical kinetic terms $G_{IJ} = \delta_{IJ}$ corresponds to a flat, Euclidean metric.

In this section we simplify calculations by setting the Planck mass to unity, $M_{\text{P}} = 1$.

Field-covariant perturbations

For a bispectrum calculation we require an expansion in the field perturbations up to third order, where each fluctuation is given by a coordinate displacement $\delta\phi^I = \phi^I(\mathbf{x}, t) - \phi^I(t)$. Here, $\phi^I(t)$ is the background field and $\phi^I(\mathbf{x}, t)$ is the perturbed field. Unfortunately this

expression is not covariant under a change of field coordinates. To obtain a covariant formulation we follow the treatment of Gong & Tanaka [Gong & Tanaka, 2011], who focused on the unique geodesic connecting the field-space coordinates of the perturbed and unperturbed fields. We take this geodesic to be labelled by an affine parameter λ , with normalization adjusted so that $\lambda = 0$ at the unperturbed coordinate and $\lambda = 1$ at the perturbed coordinate. The initial tangent vector to the geodesic is then defined by

$$Q^I \equiv \left. \frac{d\phi^I}{d\lambda} \right|_{\lambda=0}. \quad (2.62)$$

We can then assume parallel transport for our affine parameter λ and write the geodesic equation as

$$D_\lambda^2 \phi^I = \frac{d^2 \phi^I}{d\lambda^2} + \Gamma_{JK}^I Q^J Q^K = 0, \quad (2.63)$$

where D_λ denotes a covariant derivative $Q^I \nabla_I$ and Γ_{JK}^I is a field-space Christoffel symbol. We can then introduce a covariant Taylor expansion of the perturbation, $\delta\phi^I$,

$$\delta\phi^I = \frac{d\phi^I}{d\lambda} + \frac{1}{2!} \frac{d^2 \phi^I}{d\lambda^2} + \dots. \quad (2.64)$$

(Note that the appearance of this equation depends on our normalization convention for λ , but its physical content is independent of it.) Equations (2.62) & (2.63) can then be inserted into Eq. (2.64) to obtain

$$\delta\phi^I = Q^I - \frac{1}{2!} \Gamma_{JK}^I Q^J Q^K + \dots, \quad (2.65)$$

where ‘ \dots ’ denotes terms cubic and higher in Q^I that we have neglected. When applying these perturbations to the action in Eq. (2.61), we will only need to use this formalism for the kinetic part in the second and third terms as the Ricci scalar is zero in the spatially flat gauge. Before doing this however, we will need the field-covariant background equations which can be found [Lee et al., 2005] similarly

$$D_t \dot{\phi}^I + 3H \dot{\phi}^I + G^{IJ} V_{,J} = 0, \quad (2.66)$$

$$3H^2 = \rho = \frac{1}{2} G_{IJ} \partial_\mu \phi^I \partial^\mu \phi^J + V(\phi), \quad (2.67)$$

$$\epsilon \equiv -\frac{\dot{H}}{H^2} = \frac{G_{IJ} \dot{\phi}^I \dot{\phi}^J}{2H^2}, \quad (2.68)$$

which are the field-covariant Klein-Gordon equation, Friedman equation and the inflation condition respectively. The covariant time-derivative in Eq. (2.66) appears frequently in expressions and is defined by

$$D_t Q^I = \dot{Q}^I + \dot{\phi}^J \Gamma_{JK}^I Q^K. \quad (2.69)$$

Next we define $X = -G_{IJ}g^{\mu\nu}\partial_\mu\phi^I\partial_\nu\phi^J - 2V$ and apply λ derivatives up to third order which will add new terms to our perturbed action. However we first need the field-covariant derivative of $\partial_\mu\phi^I$ which is given by

$$D_\lambda\partial_\mu\phi^I = \partial_\mu Q^I + \Gamma_{JK}^I\partial_\mu\phi^J Q^K \equiv D_\mu Q^I. \quad (2.70)$$

Then Eq. (2.70) is used to give the first λ derivative on X ,

$$D_\lambda X|_{\lambda=0} = -g^{\mu\nu}\partial_\mu\phi_I D_\nu Q^I - V_{;I}Q^I, \quad (2.71)$$

which gives no new terms. The second derivative yields

$$D_\lambda^2 X|_{\lambda=0} = -g^{\mu\nu} \{R_{IJKL}\partial_\mu\phi^I\partial_\nu\phi^L Q^J Q^K + D_\mu Q_I D_\nu Q^I\} - V_{;IJ}Q^I Q^J, \quad (2.72)$$

where we see that working with a non-canonical field metric has introduced a curvature term over the field coordinates. Finally the third derivative gives

$$D_\lambda^3 X|_{\lambda=0} = -g^{\mu\nu} \{R_{MJKL;I}\partial_\mu\phi^M\partial_\nu\phi^L Q^I Q^J Q^K + 4R_{IJKL}\partial_\nu\phi^L D_\mu Q^I Q^J Q^K\} - V_{;IJK}Q^I Q^J Q^K, \quad (2.73)$$

where we have a Riemann tensor term as before as well as a covariant derivative of the curvature term. Equations (2.71)–(2.73) will be inserted into the action in Eq. (2.61) along with the metric perturbations to find the perturbed action later.

ADM decomposition and metric perturbations

We will follow the treatment of Maldacena [Maldacena, 2003, Seery & Lidsey, 2005a, Seery & Lidsey, 2005b] and use the (3+1) ADM decomposition [Arnowitt et al., 2008] of the metric which is given by

$$ds^2 = -N^2 dt^2 + h_{ij} (dx^i + N^i dt) (dx^j + N^j dt), \quad (2.74)$$

where N is the lapse function, N^i is the shift vector, and h_{ij} is the spatial metric. With this decomposition, the action in (2.61) can now be rewritten using the Gauss–Codazzi relation to remove the Gibbons–Hawking–York boundary term [York, 1972, Gibbons & Hawking, 1977]

$$S = \frac{1}{2}\sqrt{h} \int d^4x \left\{ N \left(R^{(3)} - G_{IJ}h^{ij}\partial_i\phi^I\partial_j\phi^J - 2V \right) + \frac{1}{N} (\pi^I\pi_I + E^{ij}E_{ij} - E^2) \right\}, \quad (2.75)$$

where $R^{(3)}$ is the Ricci scalar built from the spatial metric and E_{ij} is related to the extrinsic curvature of constant slices,

$$E_{ij} = \frac{1}{2} \left(\dot{h}_{ij} - N_{i|j} - N_{j|i} \right), \quad (2.76)$$

where the vertical bar index denotes a covariant derivative compatible with h_{ij} and we have made the definition

$$\pi^I \equiv \dot{\phi}^I - N^j \phi_{|j}^I. \quad (2.77)$$

We will later expand the lapse function and shift vector in terms of scalar perturbations in our field perturbations for the spatially flat gauge with $h_{ij} = a^2 \delta_{ij}$,

$$N = 1 + \alpha_1 + \alpha_2 + \dots \quad (2.78a)$$

$$N^i = \theta_1^i + \theta_2^i + \dots, \quad (2.78b)$$

where the subscripts 1, 2, ... indicate the order of expansion and α is a perturbation in the lapse function with θ being an expansion in the shift vector.

Perturbing the action

We must now insert the expressions for the kinetic term, $X = -G_{IJ} g^{\mu\nu} \partial_\mu \phi^I \partial_\nu \phi^J - 2V$, found in equations (2.71)–(2.73) as well as the metric perturbations found in equations (2.75) and (2.78) into our action found in Eq. (2.61) which gives the results found by Elliston et al. [Elliston et al., 2012]

$$\begin{aligned} S_2 = \frac{1}{2} \int d^4x a^3 \left\{ \alpha_1 \left[-6H^2 \alpha_1 + \dot{\phi}_I \dot{\phi}^I \alpha_1 - 2\dot{\phi} D_t Q^I - 2V_{,I} Q^I \right] \right. \\ \left. - \frac{2}{a^2} \partial^2 \theta_1 \left[2H \alpha_1 - \dot{\phi}_I Q^I \right] \right. \\ \left. + R_{KIJL} \dot{\phi}^K \dot{\phi}^L Q^I Q^J + D_t Q_I D_t Q^I - \partial_i Q_I \partial^i Q^I - V_{,IJ} Q^I Q^J \right\} \end{aligned} \quad (2.79)$$

and

$$\begin{aligned} S_3 = \frac{1}{2} \int d^4x a^3 \left\{ 6H^2 \alpha_1^3 + \frac{4H}{a^2} \alpha_1^2 \partial^2 \theta_1 - \frac{\alpha_1}{a^4} (\partial_i \partial_j \theta_1 \partial_i \partial_j \theta_1 - \partial^2 \theta_1 \partial^2 \theta_1) \right. \\ \left. - \alpha_1^3 \dot{\phi}_I \dot{\phi}^I + 2\alpha_1^2 \dot{\phi}_I D_t Q^I + \frac{2}{a^2} \alpha_1 \dot{\phi}_I \partial_i \theta_1 \partial_i Q^I - \alpha_1 R_{K(IJ)L} \dot{\phi}^K \dot{\phi}^L Q^I Q^J \right. \\ \left. - \alpha_1 \left(D_t Q_I D_t Q^I + \frac{1}{a^2} D_i Q_I D_i Q^I \right) - \frac{2}{a^2} \partial_i \theta_1 D_t Q_I \partial_i Q^I + \frac{4}{3} R_{I(JK)L} \dot{\phi}^L D_t Q^I Q^J Q^K \right. \\ \left. + \frac{1}{3} R_{(I|LM|J;K)} \dot{\phi}^M \dot{\phi}^L Q^I Q^J Q^K - \alpha_1 V_{;(IJ)} Q^I Q^J - \frac{1}{3} V_{;(IJK)} Q^I Q^J Q^K \right\}, \end{aligned} \quad (2.80)$$

at second and third order respectively where brackets around indices indicate that they can be cyclically permuted and vertical bars exclude indices from that symmetrisation. It should be noted that neither of these actions contain second order terms in the lapse and shift just like the canonical case but we will need them regardless because they are used in the gauge transformation calculation.

Applying constraints for Fourier-space action

We may now vary the second-order action in Eq. (2.79) with respect to the lapse and shift to find expressions for α_1 and θ_1 in terms of the perturbed fields Q^I which are

$$\alpha_1 = \frac{\dot{\phi}_I Q^I}{2H}, \quad (2.81)$$

and

$$\theta_1 = \frac{a^2}{2H} \partial^{-2} \left(-V_{,I} Q^I - \dot{\phi}_I D_t Q^I + 2\alpha_1 \left[-3H^2 + \frac{1}{2} \dot{\phi}_I \dot{\phi}^I \right] \right). \quad (2.82)$$

Here ∂^{-2} denotes the inverse Laplacian operator over spatial coordinates and Eq. (2.82) may be further simplified using the background Eq. (2.66) and Eq. (2.81) for an expression in terms of fields only. As mentioned previously, we also need second-order expressions for the lapse and shift which are found by varying Eq. (2.75) with respect to N and N^i and then expanding perturbatively to find

$$\alpha_2 = \frac{\alpha_1^2}{2} + \frac{1}{2H} \partial^{-2} \left\{ \partial_i (D_t Q^I) \partial^i Q_I + D_t Q^I D_t Q_I + \frac{1}{a^2} (\partial^2 \alpha_1 \partial^2 \theta_1 - \partial_i \partial_j \alpha_1 \partial_i \partial_j \theta_1) \right\}, \quad (2.83)$$

and

$$\begin{aligned} \theta_2 = \frac{a^2}{4H} \partial^{-2} \left\{ 2\alpha_1 \left(\frac{4H}{a^2} \partial^2 \theta_1 + 2\dot{\phi}^I D_t Q_I \right) - V_{IJ} Q^I Q^J - D_t Q^I D_t Q_I \right. \\ \left. + \frac{1}{a^2} \left(2\dot{\phi}^I \partial_i \theta_1 \partial_i Q_I - \partial_i Q^I \partial_i Q_I + \frac{1}{a^2} (\partial^2 \theta_1 \partial^2 \theta_1 - \partial_i \partial_j \theta_1 \partial_i \partial_j \theta_1) \right) \right. \\ \left. + 2H^2 (2\alpha_2 - 3\alpha_1^2) (\epsilon - 3) - R_{IJKL} Q^I \dot{\phi}^J \dot{\phi}^K Q^L \right\}. \end{aligned} \quad (2.84)$$

Equations (2.82) and (2.84) can then be used to give the Hamiltonian constraint for a non-trivial metric on super-horizon scales,

$$\begin{aligned} 0 = V_I Q^I + \frac{1}{2} V_{IJ} Q^I Q^J + \dot{\phi}^I D_t Q_I + \frac{1}{2} D_t Q_I D_t Q^I + \frac{1}{2} R_{IJKL} Q^I \dot{\phi}^J \dot{\phi}^K Q^L \\ + H^2 (2\alpha_1 + 2\alpha_2 - 3\alpha_1^2) (3 - \epsilon) - 2\alpha_1 \dot{\phi}^I D_t Q_I, \end{aligned} \quad (2.85)$$

where the spatial derivatives have been omitted due to them decaying on super-horizon scales. Equations (2.81) and (2.82) can be used to rewrite the second- and third-order actions in terms of only background fields and their perturbations. We would also like to write these in terms of the Fourier modes instead of spatial coordinates so we must adopt a convention and notation to express this. Therefore we use bold sans-serif indices to indicate an integration over Fourier modes for an index contraction such as

$$A_{\mathbf{I}} B^{\mathbf{I}} = \sum_{\mathbf{I}} \int \frac{d^3 k_{\mathbf{I}}}{(2\pi)^3} A_{\mathbf{I}}(\mathbf{k}_{\mathbf{I}}) B^{\mathbf{I}}(\mathbf{k}_{\mathbf{I}}), \quad (2.86)$$

where the indices on the right-hand side represent phase-space coordinate labels and indices may be changed to be co- or contravariant using the field-space metric G_{IJ} . This can be

a problem if the δ -function $G_{\mathbf{I}\mathbf{J}} = (2\pi)^3 G_{IJ} \delta(\mathbf{k}_I + \mathbf{k}_J)$ is produced, because this reverses the sign of a momentum label; we use a prime on the index to indicate this,

$$A_{\mathbf{I}} B^{\bar{\mathbf{I}}} = \sum_I \int \frac{d^3 k_I}{(2\pi)^3} A_I(\mathbf{k}_I) B^I(-\mathbf{k}_I). \quad (2.87)$$

Using these conventions and by substituting equations (2.81) and (2.82) into the second- and third-order actions in equations (2.79) and (2.80), we find

$$S_\phi = \frac{1}{2} \int dt a^3 \left\{ G_{\mathbf{I}\mathbf{J}} D_t Q^{\mathbf{I}} D_t Q^{\mathbf{J}} + M_{\mathbf{I}\mathbf{J}} Q^{\mathbf{I}} Q^{\mathbf{J}} + \right. \\ \left. A_{\mathbf{I}\mathbf{J}\mathbf{K}} Q^{\mathbf{I}} Q^{\mathbf{J}} Q^{\mathbf{K}} + B_{\mathbf{I}\mathbf{J}\mathbf{K}} Q^{\mathbf{I}} Q^{\mathbf{J}} D_t Q^{\mathbf{K}} + C_{\mathbf{I}\mathbf{J}\mathbf{K}} D_t Q^{\mathbf{I}} D_t Q^{\mathbf{J}} Q^{\mathbf{K}} \right\}, \quad (2.88)$$

where the second-order and third-order parts of the action are written on the first and second lines respectively. The second order kernels are given by

$$G_{\mathbf{I}\mathbf{J}} = (2\pi)^3 G_{IJ} \delta(\mathbf{k}_1 + \mathbf{k}_2), \\ M_{\mathbf{I}\mathbf{J}} = (2\pi)^3 \delta(\mathbf{k}_1 + \mathbf{k}_2) \left(\frac{\mathbf{k}_1 \cdot \mathbf{k}_2}{a^2} G_{IJ} - m_{IJ} \right), \quad (2.89)$$

where m_{IJ} satisfies

$$m_{IJ} = V_{;IJ} - R_{KIJL} \dot{\phi}^K \dot{\phi}^L - \frac{1}{a^3} D_t \left(\frac{a^3 \dot{\phi}_I \dot{\phi}_J}{H} \right). \quad (2.90)$$

Then the third-order kernels are given by

$$A_{\mathbf{I}\mathbf{J}\mathbf{K}} = (2\pi)^3 \delta(\mathbf{k}_1 + \mathbf{k}_2 + \mathbf{k}_3) A_{IJK}, \quad (2.91a)$$

$$B_{\mathbf{I}\mathbf{J}\mathbf{K}} = (2\pi)^3 \delta(\mathbf{k}_1 + \mathbf{k}_2 + \mathbf{k}_3) B_{IJK}, \quad (2.91b)$$

$$C_{\mathbf{I}\mathbf{J}\mathbf{K}} = (2\pi)^3 \delta(\mathbf{k}_1 + \mathbf{k}_2 + \mathbf{k}_3) C_{IJK}, \quad (2.91c)$$

with

$$A_{IJK} = -\frac{1}{3} V_{;IJK} - \frac{\dot{\phi}_I V_{;JK}}{2H} + \frac{\dot{\phi}_I \dot{\phi}_J Z_K}{4H^2} + \frac{\dot{\phi}_I Z_J Z_K}{8H^3} \left(1 - \frac{(\mathbf{k}_2 \cdot \mathbf{k}_3)^2}{k_2^2 k_3^2} \right) \\ + \frac{\dot{\phi}_I \dot{\phi}_J \dot{\phi}_K}{8H^3} (6H^2 - \dot{\phi}^2) - \frac{\dot{\phi}_K \dot{\phi}^L \dot{\phi}^M}{2H} R_{L(IJ)M} + \frac{1}{3} R_{(I|LM|J;K)} \dot{\phi}^L \dot{\phi}^M \\ + \frac{\dot{\phi}_I G_{JK} \mathbf{k}_2 \cdot \mathbf{k}_3}{2H a^2}, \quad (2.92a)$$

$$B_{IJK} = \frac{4}{3} R_{I(JK)L} - \frac{\dot{\phi}_I Z_J \dot{\phi}_K}{4H^3} \left(1 - \frac{(\mathbf{k}_2 \cdot \mathbf{k}_3)^2}{k_2^2 k_3^2} \right) + \frac{\dot{\phi}_I \dot{\phi}_J \dot{\phi}_K}{4H^2} - \frac{Z_I G_{JK} \mathbf{k}_1 \cdot \mathbf{k}_2}{H k_1^2}, \quad (2.92b)$$

$$C_{IJK} = \frac{G_{IJ} \dot{\phi}_K}{2H} + \frac{\dot{\phi}_I \dot{\phi}_J \dot{\phi}_K}{8H^3} \left(1 - \frac{(\mathbf{k}_1 \cdot \mathbf{k}_2)^2}{k_1^2 k_2^2} \right) + \frac{\dot{\phi}_I G_{JK} \mathbf{k}_1 \cdot \mathbf{k}_3}{H k_1^2}, \quad (2.92c)$$

and where Z_I is given by

$$Z_I = D_t \dot{\phi}^I + \frac{\dot{\phi}_I \dot{\phi}_J \dot{\phi}^J}{2H}. \quad (2.93)$$

Expression (2.92a) should be symmetrised over all three indices and expressions (2.92b) and (2.92c) should be symmetrised over the first two indices where an exchange of indices corresponds with a matching change of \mathbf{k} vectors. The results for these kernels are identical to those found for the canonical case in [Dias et al., 2016] apart from the addition of Riemann terms appearing on the second line of A_{IJK} above and in the first term of B_{IJK} . We also note that the last term in A_{IJK} is proportional to $(k/a)^2$ so will grow exponentially on sub-horizon scales which we will later need to treat separately when computing initial conditions.

2.6.2 Transport method

We want to use the action we have found in the previous section to find evolution equations for our correlation functions and therefore compute the 2- and 3-point functions on sub- and super-horizon scales. For this we can use the transport method as first detailed in [Mulryne et al., 2010, Mulryne et al., 2011, Seery et al., 2012, Mulryne, 2013], which relates correlation functions of Heisenberg picture operators to those in the interaction picture where the Heisenberg equations of motion can be used to give evolution equations of interaction-picture fields.

Correlation functions

We begin by defining Heisenberg fields and their momenta as Q^I and P^I respectively, which we then can use to write a Hamiltonian split into free and interacting parts,

$$H(Q, P) = H_0(Q, P) + H_{\text{int}}(Q, P), \quad (2.94)$$

where the index 0 denotes the free part and *int* gives the interacting part. Next we must define our new interaction-picture operators using some unitary operator, F , as

$$\begin{aligned} q^I &= F^\dagger Q^I F, \\ p_J &= F^\dagger P_J F, \end{aligned} \quad (2.95)$$

where q^I and p_J are in the interaction picture. From these relations, it is simple to rewrite a vacuum expectation value of Heisenberg picture operators, $\mathcal{O}(Q, P)$, in terms of interaction picture operators,

$$\langle \text{vac} | \mathcal{O}(Q, P) | \text{vac} \rangle = \langle \text{vac} | F \mathcal{O}(q, p) F^\dagger | \text{vac} \rangle, \quad (2.96)$$

where $\langle \text{vac} | \cdots | \text{vac} \rangle$ denotes an expectation value in the Minkowski vacuum. We can use the Heisenberg equation of motion, $dQ/dt = -i[Q, H(Q, P)]$, to show that the differential

equation needed to find the unitary operator F is

$$\frac{dF}{dt} = iF H_{\text{int}}(q, p), \quad (2.97)$$

where the equation for F^\dagger is found by taking the complex conjugate. These differential equations can be solved using a power-series method to give the solution

$$F = \bar{\mathbb{T}} \exp \left(i \int^t H_{\text{int}}(t') dt' \right) \quad (2.98)$$

where $\bar{\mathbb{T}}$ is the anti-time ordering operator which orders its argument in terms of increasing time. We can set the lower limits of these integrals by using a theory by Gell-Mann and Low [Gell-Mann & Low, 1951] which states that the vacuum state of an interacting theory can be related to the ground state of a non-interacting theory with an adiabatic ‘switch on’ of the interacting theory. Then the integrals are performed over contours deformed into the complex plane in the distant past with analytic continuation used to define the fields for each ladder operator. These results are used in Eq. (2.96), yielding

$$\langle \text{vac} | \mathcal{O}(X) | \text{vac} \rangle = \left\langle 0 \left| \bar{\mathbb{T}} \exp \left(i \int_{-\infty^+}^t H_{\text{int}}(t') dt' \right) \mathcal{O}(x) \mathbb{T} \exp \left(-i \int_{-\infty^-}^t H_{\text{int}}(t'') dt'' \right) \right| 0 \right\rangle, \quad (2.99)$$

where $-\infty^+$ and $-\infty^-$ show that the integration contour should be deformed into the positive and negative imaginary half-planes respectively with $X^a = (Q^I, P^J)$ and $x^a = (q^I, p^J)$ defined as phase-space vectors containing fields and momenta in the Heisenberg and interaction picture respectively. This is known as the ‘in-in’ formalism [Adshad et al., 2009] used for computing correlation functions and is a sum over all possible ‘out’ states for the theory.

Evolution equations

We can now use these relations between Heisenberg and interaction picture fields along with our Fourier convention found in equations (2.86) and (2.87) to write the Hamiltonian as

$$H = \frac{1}{2!} H_{\mathbf{ab}} X^{\mathbf{a}} X^{\mathbf{b}} + \frac{1}{3!} H_{\mathbf{abc}} X^{\mathbf{a}} X^{\mathbf{b}} X^{\mathbf{c}} + \dots, \quad (2.100)$$

where all fields are in the Heisenberg picture and ‘ \dots ’ denotes higher-order terms. This allows the Heisenberg equations of motion to be written

$$D_t X^{\mathbf{a}} = u^{\mathbf{a}}_{\mathbf{b}} X^{\mathbf{b}} + \frac{1}{2!} u^{\mathbf{a}}_{\mathbf{bc}} X^{\mathbf{b}} X^{\mathbf{c}} + \dots, \quad (2.101)$$

which gives definitions for the ‘ u -tensors’, $u^{\mathbf{a}}_{\mathbf{b}}$ and $u^{\mathbf{a}}_{\mathbf{bc}}$. There is also a Christoffel symbol appearing on the left hand side of (2.101) because of the field-covariant time derivative

defined in Eq. (2.69). For our action in Eq. (2.88), we choose the free part of the Hamiltonian to be the quadratic terms in perturbations and the interacting part is given by the cubic terms. The time evolution of an interaction-picture field is

$$D_t x^{\mathbf{a}} = u^{\mathbf{a}}_{\mathbf{b}} x^{\mathbf{b}}. \quad (2.102)$$

This allows us to use equations (2.99) and (2.100) to give tree-level two- and three-point correlation functions

$$\langle X^{\mathbf{a}} X^{\mathbf{b}} \rangle = \langle 0 | x^{\mathbf{a}} x^{\mathbf{b}} | 0 \rangle, \quad (2.103a)$$

$$\langle X^{\mathbf{a}} X^{\mathbf{b}} X^{\mathbf{c}} \rangle = \langle 0 | \left[\frac{i}{3!} \int^t H_{\text{def}} x^{\mathbf{d}} x^{\mathbf{e}} x^{\mathbf{f}} dt', x^{\mathbf{a}} x^{\mathbf{b}} x^{\mathbf{c}} \right] | 0 \rangle. \quad (2.103b)$$

Evolution equations can now be found for the two-point function first by differentiating Eq. (2.103a) with respect to time and using Eq. (2.102) to simplify the result. We find

$$D_t \langle X^{\mathbf{a}} X^{\mathbf{b}} \rangle = u^{\mathbf{a}}_{\mathbf{c}} \langle X^{\mathbf{c}} X^{\mathbf{b}} \rangle + u^{\mathbf{b}}_{\mathbf{c}} \langle X^{\mathbf{a}} X^{\mathbf{c}} \rangle, \quad (2.104)$$

where $u^{\mathbf{a}}_{\mathbf{b}}$ can be found by finding the Hamiltonian from our action and then using the Heisenberg equations from it to compare with Eq. (2.101) above. The evolution equation for the 3-point correlation function is slightly harder to calculate than the 2-point function because it requires rewriting some of the commutation relations found after differentiating Eq. (2.103b) as seen in Ref. [Dias et al., 2016]. The result is

$$D_t \langle X^{\mathbf{a}} X^{\mathbf{b}} X^{\mathbf{c}} \rangle = u^{\mathbf{a}}_{\mathbf{d}} \langle X^{\mathbf{d}} X^{\mathbf{b}} X^{\mathbf{c}} \rangle + u^{\mathbf{a}}_{\mathbf{de}} \langle X^{\mathbf{d}} X^{\mathbf{b}} \rangle \langle X^{\mathbf{e}} X^{\mathbf{c}} \rangle + 2 \text{ perms}, \quad (2.105)$$

where there are contributions from both of the u -tensors defined in Eq. (2.100) above and the permutations preserve the ordering of indices. Equations (2.104) and (2.105) both contain a Christoffel symbol term for each of the phase-space indices appearing on the left hand side of each equation. These equations may be further simplified by defining $\langle X^{\mathbf{a}} X^{\mathbf{b}} \rangle \equiv (2\pi)^3 \delta(\mathbf{k}_a + \mathbf{k}_b) \Sigma^{ab}$ and $\langle X^{\mathbf{a}} X^{\mathbf{b}} X^{\mathbf{c}} \rangle \equiv (2\pi)^3 \delta(\mathbf{k}_a + \mathbf{k}_b + \mathbf{k}_c) \alpha^{abc}$ as the two- and three-point functions to obtain

$$D_t \Sigma^{ab} = u^a_c \Sigma^{cb} + u^b_c \Sigma^{ac}, \quad (2.106a)$$

$$D_t \alpha^{abc} = u^a_d \alpha^{dbc} + u^a_{de} \Sigma^{db} \Sigma^{ec} + 2 \text{ cyclic } (a \rightarrow b \rightarrow c), \quad (2.106b)$$

The two differential equations found in equations (2.106a) and (2.106b) can both be solved numerically to find a power spectrum or bispectrum for an inflation theory and only require calculation of the u -tensors and initial conditions.

Calculating the u -tensors

As mentioned previously, we must find the Hamiltonian from our action in Eq. (2.88) so we begin by defining the momentum canonically conjugate to the field perturbations Q^I ,

$$P_I(t) = \frac{\delta S_\phi}{\delta(D_t Q^I)}, \quad (2.107)$$

with a variational derivative defined by

$$\frac{\delta[Q^I(\mathbf{k}_I, t)]}{\delta[Q^J(\mathbf{k}_J, t')]} = \delta_J^I (2\pi)^3 \delta(t - t') \delta(\mathbf{k}_I + \mathbf{k}_J) = \delta_J^I \delta(t - t'). \quad (2.108)$$

Equations (2.107) and (2.108) can then be used on Eq. (2.88) to obtain the momentum,

$$P_I = a^3 \left\{ D_t Q_I + \frac{1}{2} B_{\mathbf{J}\mathbf{K}\bar{\mathbf{I}}} Q^{\mathbf{J}} Q^{\mathbf{K}} + C_{\bar{\mathbf{I}}\mathbf{J}\mathbf{K}} P^{\mathbf{J}} Q^{\mathbf{K}} \right\}, \quad (2.109)$$

where a prime on an index indicates a sign reversal of momentum. From Eq. (2.109), it is simple to rearrange for $D_t Q_I$,

$$D_t Q_I = \frac{P_I}{a^3} - \frac{1}{2} B_{\mathbf{J}\mathbf{K}\bar{\mathbf{I}}} Q^{\mathbf{J}} Q^{\mathbf{K}} - C_{\bar{\mathbf{I}}\mathbf{J}\mathbf{K}} P^{\mathbf{J}} Q^{\mathbf{K}}. \quad (2.110)$$

Then we may use the relation $H = \int dt [P^I(D_t Q_I) - L]$ and rescale the momentum by a factor of a^3 as $P_I \rightarrow a^3 P_I$ to obtain the Hamiltonian

$$H = \frac{1}{2} \int dt a^3 \left(G_{\mathbf{I}\mathbf{J}} P^{\mathbf{I}} P^{\mathbf{J}} - M_{\mathbf{I}\mathbf{J}} Q^{\mathbf{I}} Q^{\mathbf{J}} - \right. \\ \left. A_{\mathbf{I}\mathbf{J}\mathbf{K}} Q^{\mathbf{I}} Q^{\mathbf{J}} Q^{\mathbf{K}} - B_{\mathbf{I}\mathbf{J}\mathbf{K}} Q^{\mathbf{I}} Q^{\mathbf{J}} P^{\mathbf{K}} - C_{\mathbf{I}\mathbf{J}\mathbf{K}} P^{\mathbf{I}} P^{\mathbf{J}} Q^{\mathbf{K}} \right), \quad (2.111)$$

where the terms on the first line are quadratic in perturbations and the terms on the second line are cubic in perturbations which represent H_0 and H_{int} in Eq. (2.94) respectively. Next we must find the Heisenberg equations for the fields Q^I and P^I , which are given by

$$D_t Q^I = -i[Q^I, H], \quad (2.112a)$$

$$D_t P^I = -i[P^I, H] - 3H P^I, \quad (2.112b)$$

where Eq. (2.112b) is slightly different from the typical canonical relation because of the rescaled momentum. If the Hamiltonian in Eq. (2.111) is inserted into equations (2.112a) and (2.112b), then we find

$$D_t Q^I = \delta_J^I P^{\mathbf{J}} - \frac{1}{2} B_{\mathbf{J}\mathbf{K}}^{\bar{\mathbf{I}}} Q^{\mathbf{J}} Q^{\mathbf{K}} - C_{\bar{\mathbf{I}}\mathbf{J}\mathbf{K}} P^{\mathbf{J}} Q^{\mathbf{K}}, \quad (2.113)$$

and

$$D_t P^I = -3H \delta_J^I P^{\mathbf{J}} + M_{\bar{\mathbf{I}}\mathbf{J}} Q^{\mathbf{J}} + \frac{3}{2} A_{\bar{\mathbf{I}}\mathbf{J}\mathbf{K}} Q^{\mathbf{J}} Q^{\mathbf{K}} + B_{\bar{\mathbf{I}}\mathbf{J}\mathbf{K}} Q^{\mathbf{J}} P^{\mathbf{K}} + \frac{1}{2} C_{\mathbf{J}\mathbf{K}}^{\bar{\mathbf{I}}} P^{\mathbf{J}} P^{\mathbf{K}}. \quad (2.114)$$

By comparing the linear terms in equations (2.113) and (2.114) with Eq. (2.101), we first find the $u^{\mathbf{a}}_{\mathbf{b}}$ tensor to be

$$u^{\mathbf{a}}_{\mathbf{b}} = \begin{pmatrix} 0 & \delta_{\mathbf{J}}^{\bar{\mathbf{I}}} \\ M^{\bar{\mathbf{I}}}_{\mathbf{J}} & -3H\delta_{\mathbf{J}}^{\bar{\mathbf{I}}} \end{pmatrix}, \quad (2.115)$$

where we identify each row with terms coming from the evolution equation for Q and P respectively and each column as having terms proportional to Q and P respectively. Similarly, we find the $u^{\mathbf{a}}_{\mathbf{bc}}$ tensor to be

$$u^{\mathbf{a}}_{\mathbf{bc}} = \left\{ \begin{array}{l} \begin{pmatrix} -B_{\mathbf{JK}}^{\bar{\mathbf{I}}} & -C^{\bar{\mathbf{I}}}_{\mathbf{JK}} \\ 3A^{\bar{\mathbf{I}}}_{\mathbf{JK}} & B^{\bar{\mathbf{I}}}_{\mathbf{KJ}} \end{pmatrix} \\ \begin{pmatrix} -C^{\bar{\mathbf{I}}}_{\mathbf{KJ}} & 0 \\ B^{\bar{\mathbf{I}}}_{\mathbf{JK}} & C_{\mathbf{KJ}}^{\bar{\mathbf{I}}} \end{pmatrix} \end{array} \right\}, \quad (2.116)$$

where the rules are the same as before for each 2-by-2 matrix and the extra index \mathbf{c} identifies which 2-by-2 matrix is being referred to. There are also further simplifications to be made regarding the primed indices in (2.115) and (2.116). For both of the equations above, it is the index \mathbf{I} that has a prime which corresponds with a sign reversal of all momenta in equations (2.89) and (2.92a)–(2.92c). However because the k terms in these equations always appear as an inner product of pairs of momenta, then all of the sign reversal will be cancelled out. This means our u -tensors can be written with plain phase-space indices,

$$u^a_b = \begin{pmatrix} 0 & \delta^I_J \\ M^I_J & -3H\delta^I_J \end{pmatrix}, \quad (2.117a)$$

$$u^a_{bc} = \left\{ \begin{array}{l} \begin{pmatrix} -B_{JK}^I & -C^I_{JK} \\ 3A^I_{JK} & B^I_{KJ} \end{pmatrix} \\ \begin{pmatrix} -C^I_{KJ} & 0 \\ B^I_{JK} & C_{KJ}^I \end{pmatrix} \end{array} \right\}. \quad (2.117b)$$

It should be noted that all of the extra terms added by the non-canonical field metric here are contained within the kernels introduced earlier and the only other differences are caused by Christoffel symbols in field coordinate space coming from covariant derivatives.

2.6.3 Initial conditions

Having found the differential equations needed to be solved for a numerical implementation, the next task is to use the formalism developed in section 2.6.2 to find appropriate initial

conditions for the equations giving both the 2- and 3-point correlation functions. We will again need to be careful to ensure that our expressions are kept field-covariant and to find any new field curvature times arising from the inclusion of a non-canonical field metric.

2-point correlation functions

We begin by writing the second-order action in terms of our perturbed fields,

$$S_{(2)} = \frac{1}{2} \int dt a^3 \left\{ -G_{IJ} \partial_\mu Q^I \partial^\mu Q^J - \mathcal{M}_{IJ} Q^I Q^J \right\}, \quad (2.118)$$

where \mathcal{M}_{IJ} is a mass-term encompassing all terms involving potentials and other non-kinetic terms. This calculation is done using the path-integral formalism so we integrate by parts whilst assuming boundary terms vanish at infinity and change the time variable to conformal time, defined by $dt = a d\eta$. We find

$$\begin{aligned} S_{(2)} &= -\frac{1}{2} \int d\eta d^3x a^2 Q^I \left[G_{IJ} \left(\mathcal{D}_\eta^2 + 2\frac{a'}{a} \mathcal{D}_\eta - \partial_i \partial_i \right) + a^2 \mathcal{M}_{IJ} \right] Q^J \\ &= -\frac{1}{2} \int d\eta d^3x \left\{ a^2 Q^I \Delta_{IJ} Q^J \right\}, \end{aligned} \quad (2.119)$$

where we have written a covariant derivative over conformal time as \mathcal{D}_η and use a prime (') to indicate a derivative $d/d\eta$ and defined the quantity Δ_{IJ} as the differential operator in brackets (\dots) above. We now seek to use Eq. (2.99) to find the two-point correlation function but we must distinguish between fields on the left anti-time-ordered product and the right time-ordered product which we do using a Q_+ and Q_- field respectively. Therefore, there are four separate two-point functions for the correlations between ‘++’, ‘+-’, ‘-+’ and ‘--’ fields which need to be calculated with the ‘in-in’ formalism.

It can be shown [Weinberg, 2005] that Eq. (2.99) is written in the path integral formalism with the action above as

$$Z = \int [DQ_+^I DQ_-^I] \exp \left\{ -\frac{i}{2} \int_{\tau_0}^{\tau} d\eta d^3x a^2 \bar{Q}^I \begin{pmatrix} \Delta & \\ & -\Delta \end{pmatrix}_{IJ} Q^J \right\}, \quad (2.120)$$

where $Q^I = (Q_+^I, Q_-^I)$ and \bar{Q}^I denotes the transpose matrix with τ_0 being a time well before horizon-crossing and τ being the time we’re seeking initial conditions for. We define the two point function with a time-ordered product of fields to be

$$D_{++}^{JK'}(\eta, \mathbf{x}; \sigma, \mathbf{y}) = \langle T Q_+^J(\eta, \mathbf{x}) Q_+^{K'}(\sigma, \mathbf{y}) \rangle, \quad (2.121)$$

with similar definitions for the other products of fields and unprimed indices label tangent spaces at η and primed ones label tangent spaces at σ . Using the rules of Gaussian integration for a matrix with vectors that are transpose to one another and by making a

Fourier transform on $D_{\pm\pm}$ to diagonalise the dependence on \mathbf{x} and \mathbf{y} , we can calculate D_{++} using the following differential equation

$$G_{IJ} (\mathcal{D}_\eta^2 + 2\mathcal{H}\mathcal{D}_\eta + k^2) D_{++}^{JK'}(\mathbf{k}) = -\frac{i}{a^2} G_I^{K'} \delta(\eta - \sigma), \quad (2.122)$$

where we have set $\mathcal{H} \equiv a'/a$ as the conformal Hubble constant and we're now ignoring the M_{IJ} term but *only* for the initial conditions in the early, sub-horizon times where they will make a small contribution. We would now like to factorise the tensor structure so we introduce a bi-tensor $\Pi^{JK'}$ which must solve $\mathcal{D}_\eta \Pi^{JK'} = 0$ and a bi-scalar $\Delta_{\pm\pm}(\eta, \sigma, \mathbf{k})$ that contains all of the dimensionful quantities. This means we can now write the 2-point function as

$$D_{++}^{JK'}(\eta, \sigma, \mathbf{k}) = \Pi^{JK'} \Delta_{++}(\eta, \sigma, \mathbf{k}) \quad \text{with} \quad \frac{D}{d\eta} \Pi^{JK'} = 0. \quad (2.123)$$

We are now able to make this substitution into Eq. (2.122) where the bi-tensor can now be factorised out,

$$G_{IJ} \Pi^{JK'} (\Delta_{++}'' + 2\mathcal{H}\Delta_{++}' + k^2 \Delta_{++}) = -\frac{i}{a^2} G_I^{K'} \delta(\eta - \sigma). \quad (2.124)$$

The evolution equation for $\Pi^{JK'}$ can be solved using

$$\begin{aligned} \mathcal{D}_\eta \Pi^{JK'} &= \frac{d\Pi^{JK'}}{d\eta} + \Gamma_{LM}^J \frac{d\phi^L}{d\eta} \Pi^{MK'} = 0 \\ \implies \Pi^{JK'} &= \hat{P} \exp \left(- \int_\sigma^\eta d\tau \Gamma_{L''M''}^{J''} \frac{d\phi^{L''}}{d\tau} \right) G^{M'K'}, \end{aligned} \quad (2.125)$$

where \hat{P} indicates the exponential is path-ordered and double primed indices label tangent spaces evaluated at τ . This bi-tensor is known as the ‘trajectory propagator’ which is the parallel propagator evaluated along the inflationary trajectory with the boundary condition chosen so that when $\sigma \rightarrow \eta$, we have $\Pi^{JK'} \rightarrow G^{JK'}$. This means that field metric dependence is removed from Eq. (2.124) and Δ_{++} satisfies

$$(\mathcal{D}_\eta^2 + 2\mathcal{H}\mathcal{D}_\eta + k^2) \Delta_{++} = -\frac{i}{a^2} \delta(\eta - \sigma). \quad (2.126)$$

This equation is identical to the canonical field-space solution and we see that the complexity introduced by the field-space metric is captured by the trajectory propagator and the use of the in-in formalism. Now we only need to identify each of the different field combinations mentioned earlier. From the boundary conditions in Eq. (2.120) it can be seen [Weinberg, 2005, Elliston et al., 2012] that ‘++’ and ‘--’ as well as ‘+-’ and ‘-+’ field combinations are Hermitian conjugates of one another. This yields the following solutions

for the 2-point correlation function,

$$D_{++}^{IJ'} = (2\pi)^3 \delta(\mathbf{k}_1 + \mathbf{k}_2) \Pi^{IJ'} \frac{H_*^2}{2k^3} (1 + ik\eta)(1 - ik\sigma) e^{ik(\sigma - \eta)}, \quad (2.127a)$$

$$D_{+-}^{IJ'} = (2\pi)^3 \delta(\mathbf{k}_1 + \mathbf{k}_2) \Pi^{IJ'} \frac{H_*^2}{2k^3} (1 + ik\eta)(1 - ik\sigma) e^{ik(\sigma - \eta)} \quad (2.127b)$$

with $D_{--}^{IJ'}$ and $D_{+-}^{IJ'}$ being given by the complex conjugates of equations (2.127a) and (2.127b) respectively with H_* denoting the Hubble parameter taken at horizon crossing. At equal-time with $\sigma = \eta$, these all give the same solution so that the field-field initial condition is

$$\langle Q^I(\mathbf{k}_1) Q^J(\mathbf{k}_2) \rangle_{\text{init}} = (2\pi)^3 \delta(\mathbf{k}_1 + \mathbf{k}_2) G^{IJ} \left(\frac{1}{2ka^2} + \frac{H^2}{2k^3} \right), \quad (2.128)$$

where we have used $\eta = -1/aH$ to remove time dependence. Similarly for field-momentum, momentum-field and momentum-momentum correlations, we have

$$\langle Q^I(\mathbf{k}_1) P^J(\mathbf{k}_2) \rangle_{\text{init}} = (2\pi)^3 \delta(\mathbf{k}_1 + \mathbf{k}_2) G^{IJ} \left(-\frac{H}{2ka^2} + \frac{i}{2a^3} \right), \quad (2.129a)$$

$$\langle P^I(\mathbf{k}_1) Q^J(\mathbf{k}_2) \rangle_{\text{init}} = (2\pi)^3 \delta(\mathbf{k}_1 + \mathbf{k}_2) G^{IJ} \left(-\frac{H}{2ka^2} - \frac{i}{2a^3} \right), \quad (2.129b)$$

$$\langle P^I(\mathbf{k}_1) P^J(\mathbf{k}_2) \rangle_{\text{init}} = (2\pi)^3 \delta(\mathbf{k}_1 + \mathbf{k}_2) G^{IJ} \left(\frac{k}{2a^4} \right). \quad (2.129c)$$

In summary, the introduction of the trajectory propagator, $\Pi^{IJ'}$, has ensured we are tracking all of the fields correctly on sub-horizon scales before becoming G^{IJ} on equal time correlations.

3-point correlation functions

For calculation of the 3-point correlation function initial conditions, it is more convenient to use the operator formalism as used in Eq. (2.99). Each of the exponential functions are expanded using the in-in formalism and the leading-order, non-vanishing terms are given by

$$\langle X^I X^J X^K \rangle \subseteq \left\langle 0 \left| i \int_{-\infty}^{\eta} d\tau [H_{\text{int}}, X^I(\eta, \mathbf{k}_1) X^J(\eta, \mathbf{k}_2) X^K(\eta, \mathbf{k}_3)] \right| 0 \right\rangle, \quad (2.130)$$

where $H_{\text{int}} \equiv H_{\mathbf{LMN}} X^{\mathbf{L}} X^{\mathbf{M}} X^{\mathbf{N}}$ which comes from the cubic terms in the action in Eq. (2.88) along with the kernels defined in equations (2.91a)–(2.92c). If we perform a Fourier transform on the X terms in H_{int} , the first term from the commutator is

$$\langle X^I X^J X^K \rangle \subseteq i \int_{-\infty}^{\eta} d\tau H_{\mathbf{LMN}} \int \frac{\Pi_n d^3 q_n}{(2\pi)^9} (2\pi)^3 \delta(\Sigma \mathbf{q}_i) \left\langle 0 \left| X_{q_1}^{\mathbf{L}} X_{q_2}^{\mathbf{M}} X_{q_3}^{\mathbf{N}} X_{k_1}^I X_{k_2}^J X_{k_3}^K \right| 0 \right\rangle, \quad (2.131)$$

where we have compacted our notation for each Q 's dependence on wave number by placing it as a subscript. Now we can Wick-contract between different fields to rewrite this in terms of 2-point functions as

$$\langle X^I X^J X^K \rangle \subseteq i \int_{-\infty}^{\eta} d\tau H_{\mathbf{LMN}} \int \frac{\Pi_n d^3 q_n}{(2\pi)^9} (2\pi)^3 \delta(\Sigma \mathbf{q}_i) \left\{ \langle X_{q_1}^{\mathbf{L}} X_{k_1}^I \rangle \langle X_{q_2}^{\mathbf{M}} X_{k_2}^J \rangle \langle X_{q_3}^{\mathbf{N}} X_{k_3}^K \rangle + \text{cyclic} \right\}, \quad (2.132)$$

where ‘cyclic’ indicates there are extra terms omitted that are permutations of the field labels on the inner products. Now we can use this to find $\langle Q^I Q^J Q^K \rangle$ whilst just using the A_{LMN} term from H_{int} as an example to evaluate the Fourier integral using Eq. (2.128) as

$$\begin{aligned} \langle Q^I Q^J Q^K \rangle \subseteq i (2\pi)^3 \delta(\Sigma \mathbf{k}_i) \frac{H_*^6}{8(\prod_i k_i^3)} \Pi^{IL} \Pi^{JM} \Pi^{KN} (1 + ik_1 \eta) (1 + ik_2 \eta) (1 + ik_3 \eta) e^{-k_t \eta} \\ \times \int_{-\infty}^{\eta} d\tau \left\{ (1 - ik_1 \tau) (1 - ik_2 \tau) (1 - ik_3 \tau) e^{ik_t \tau} A_{LMN}(\tau) \right\}, \end{aligned} \quad (2.133)$$

where we have defined $k_t = k_1 + k_2 + k_3$ and $\prod_i k_i^3$ indicates a product of k^3 terms. We would like to remove the A_{LMN} term from the τ integral which can be done using a Taylor series at time N_* and using some more trajectory propagators between times η and N_* as

$$A_{LMN} \approx \Pi_L^i \Pi_M^j \Pi_N^k \left\{ A_{ijk}|_* + (N - N_*) \frac{d}{dN} A^{ijk} \Big|_* + \dots \right\}, \quad (2.134)$$

where we use lower-case indices here to indicate that we’re in the N_* tangent space. Indices between trajectory propagators contract in the normal way (ie. $\Pi_L^i \Pi^{LL} = \Pi^{Li}$) so that when we insert this approximation into Eq. (2.133) whilst keeping the lowest order terms and multiplying by 2 for the complex conjugate of a *real* observable, we find that the 3-point function is given by

$$\begin{aligned} \langle Q^I Q^J Q^K \rangle \subseteq \Pi^{Li} \Pi^{Jj} \Pi^{Kk} \cdot i (2\pi)^3 \delta(\Sigma \mathbf{k}_i) \frac{H_*^6 A_{ijk}^*}{4(\prod_i k_i^3)} \\ \times (1 + ik_1 \eta) (1 + ik_2 \eta) (1 + ik_3 \eta) e^{-k_t \eta} \\ \times \int_{-\infty}^{\eta} d\tau \left\{ (1 - ik_1 \tau) (1 - ik_2 \tau) (1 - ik_3 \tau) e^{ik_t \tau} \right\}, \end{aligned} \quad (2.135)$$

where we have placed ‘constant’ terms on the first line, the second line is the ‘external polynomial’ and the third line is the ‘internal polynomial’. While all the ‘constants’ on the first line are not constant, the same terms do appear for every 3-point correlation possible. The external polynomial is determined by the particular interaction chosen on the left hand side of Eq. (2.132) so could be $Q^I Q^J Q^K$, $P^I Q^J Q^K$, $P^I P^J Q^K$ or $P^I P^J P^K$ where $P^I \equiv dQ^I/dt$ which are easy to handle because they are effective constants in the calculation. The internal polynomials however come from the particular cubic Hamiltonian

term chosen in Eq. (2.111) and must be carefully integrated to keep leading-order, real and imaginary terms to ensure the result of Eq. (2.135) is *real* with its factor of i .

External polynomials.— There are 4 different types of external polynomials from each of the possible 3-point interactions that need to be computed. From Eq. (2.135) above, we can see that Q^I contributes the following polynomial,

$$Q^I(\eta) \approx (1 + ik\eta) e^{-ik\eta}. \quad (2.136)$$

It is then simple to take a derivative with respect to η to find

$$P^I(\eta) \approx -ik(1 + ik\eta) e^{-ik\eta} + ik e^{-ik\eta} = k^2 \eta e^{-ik\eta}. \quad (2.137)$$

Using these relations, we can find each of the possible polynomials as

$$\langle Q^I Q^J Q^K \rangle = (1 + ik_t \eta - K^2 \eta^2 - ik_1 k_2 k_3 \eta^3) e^{-ik_t \eta}, \quad (2.138a)$$

$$\langle P^I Q^J Q^K \rangle = (k_1^2 \eta + ik_1^2 (k_2 + k_3) \eta^2 - k_1^2 k_2 k_3 \eta^3) e^{-ik_t \eta}, \quad (2.138b)$$

$$\langle P^I P^J Q^K \rangle = (k_1^2 k_2^2 \eta^2 + ik_1^2 k_2^2 k_3 \eta^3) e^{-ik_t \eta}, \quad (2.138c)$$

$$\langle P^I P^J P^K \rangle = (k_1^2 k_2^2 k_3^2) e^{-ik_t \eta}, \quad (2.138d)$$

where we have defined $K^2 \equiv k_1 k_2 + k_1 k_3 + k_2 k_3$ in (2.138a).

Internal polynomials.— From Eq. (2.141) above, we have 4 different vertex integrals to perform where we keep the highest-order terms in η to ensure we have the correct initial conditions on sub-horizon scales. From Eq. (2.135), we see that $Q(\tau)$ is given by

$$Q(\tau) = (1 - ik\tau) e^{ik\tau}, \quad (2.139)$$

which we can differentiate to obtain $P(\tau)$ as:

$$P(\tau) = \frac{dQ(\tau)}{dt} = \frac{k^2 \tau}{a} e^{ik\tau}. \quad (2.140)$$

As mentioned at the end of section 2.6.1, the A_{IJK} kernel contains a ‘fast’ term that grows exponentially on sub-horizon scales whereas all of the other terms are ‘slow’ and do not grow quickly. In order to numerically model inflationary paradigms that exhibit one or both of these behaviours, we split up the third-order action as follows

$$S_\phi^{(3)} = \int d\tau \frac{a^4}{2} \left\{ \left(\frac{\dot{\phi}^I G^{JK} \mathbf{k}_2 \cdot \mathbf{k}_3}{2H a^2} + A_{\text{slow}}^{IJK} \right) Q_I Q_J Q_K + \frac{1}{a} B_{IJK} Q^I Q^J P^K + \frac{1}{a^2} C_{IJK} P^I P^J Q^K \right\}, \quad (2.141)$$

where A_{slow}^{IJK} denotes the ‘slow’ term which is A^{IJK} with the first term above removed. We can then insert equations (2.139) and (2.140) into Eq. (2.141) and use $\tau = -1/aH$ to

obtain the internal polynomials,

$$A_{\text{fast}}^{IJK} = \frac{\dot{\phi}^I G^{JK}(\mathbf{k}_2 \cdot \mathbf{k}_3)}{4H^3} \left\{ \frac{k_1 k_2 k_3}{k_t} \eta + \frac{i}{k_t} \left(K^2 + \frac{k_1 k_2 k_3}{k_t} \right) + \mathcal{O}(\eta^{-1}) \right\} e^{ik_t \eta} + \text{perms.}, \quad (2.142a)$$

$$A_{\text{slow}}^{IJK} = \frac{A_{\text{slow}}^{IJK}}{2H^3} \left\{ \frac{k_1 k_2 k_3}{k_t} \frac{1}{\eta} + \frac{i}{k_t \eta^2} \left(K^2 - \frac{k_1 k_2 k_3}{k_t} \right) + \mathcal{O}(\eta^{-3}) \right\} e^{ik_t \eta} + \text{perms.}, \quad (2.142b)$$

$$B^{IJK} = -\frac{B^{IJK}}{2H^3} \left\{ i \frac{k_1 k_2 k_3^2}{k_t} - \frac{(k_1 + k_2) k_3^2}{k_t} \frac{1}{\eta} + \mathcal{O}(\eta^{-2}) \right\} e^{ik_t \eta} + \text{perms.}, \quad (2.142c)$$

$$C^{IJK} = \frac{C^{IJK}}{2H^2} \left\{ -\frac{k_1^2 k_2^2 k_3}{k_t} - i \frac{k_1^2 k_2^2}{k_t} \left(1 + \frac{k_3}{k_t} \right) \right\} e^{ik_t \eta} + \text{perms.} \quad (2.142d)$$

3-point initial conditions.— Now we use the external polynomials in equations (2.138a)–(2.138d) with the internal polynomials in equations (2.142a)–(2.142d) with the ‘constant’ terms found in Eq. (2.135) to obtain the initial conditions for a correlation of 3 fields,

$$\begin{aligned} \langle Q^I Q^J Q^K \rangle_{\text{init}} = \frac{(2\pi)^3 \delta(\mathbf{k}_{\text{tot}})}{4a^4 k_1 k_2 k_3 k_t} \left\{ \frac{\dot{\phi}^I G^{JK}}{4HM_{\text{P}}^2} \mathbf{k}_2 \cdot \mathbf{k}_3 + \frac{a^2}{2} A_{\text{slow}}^{IJK} - C^{IJK} \frac{k_1 k_2}{2} \right. \\ \left. + \frac{a^2 H}{2} B^{IJK} \left[\frac{(k_1 + k_2) k_3}{k_1 k_2} - \frac{K^2}{k_1 k_2} \right] + 5 \text{ perms} \right\}, \end{aligned} \quad (2.143)$$

with a correlation of 1 momentum and 2 fields,

$$\begin{aligned} \langle P^I Q^J Q^K \rangle_{\text{init}} = \frac{(2\pi)^3 \delta(\mathbf{k}_{\text{tot}})}{4a^4 (k_1 k_2 k_3)^2 k_t} \\ \times \left\{ k_1^2 (k_2 + k_3) \left[\frac{\dot{\phi}^I G^{JK}}{4HM_{\text{P}}^2} \mathbf{k}_2 \cdot \mathbf{k}_3 + \frac{a^2}{2} A_{\text{slow}}^{IJK} - C^{IJK} \frac{k_1 k_2}{2} + 5 \text{ perms} \right] \right. \\ \left. + k_1 \left[-\frac{\dot{\phi}^I G^{JK}}{4HM_{\text{P}}^2} \mathbf{k}_2 \cdot \mathbf{k}_3 \left(K^2 + \frac{k_1 k_2 k_3}{k_t} \right) - \frac{a^2}{2} A_{\text{slow}}^{IJK} \left(K^2 - \frac{k_1 k_2 k_3}{k_t} \right) \right. \right. \\ \left. \left. + B^{IJK} \frac{k_1 k_2 k_3^2}{2H} + C^{IJK} \frac{k_1^2 k_2^2}{2} \left(1 + \frac{k_3}{k_t} \right) + 5 \text{ perms} \right] \right\}, \end{aligned} \quad (2.144)$$

with a correlation of 2 momenta and a field,

$$\begin{aligned} \langle P^I P^J Q^K \rangle_{\text{init}} = \frac{(2\pi)^3 \delta(\mathbf{k}_{\text{tot}})}{4a^6 H^2 (k_1 k_2 k_3)^2 k_t} \\ \times \left\{ k_1^2 k_2^2 k_3 \left[-\frac{\dot{\phi}^I G^{JK}}{4HM_{\text{P}}^2} \mathbf{k}_2 \cdot \mathbf{k}_3 - \frac{a^2}{2} A_{\text{slow}}^{IJK} + C^{IJK} \frac{k_1 k_2}{2} - \frac{a^2 H}{2} B^{IJK} \frac{(k_1 + k_2) k_3}{k_1 k_2} \right. \right. \\ \left. \left. + 5 \text{ perms} \right] + k_1^2 k_2^2 \left[\frac{a^2 H}{2} B^{IJK} k_3 + 5 \text{ perms} \right] \right\}, \end{aligned} \quad (2.145)$$

and a correlation of 3 momenta,

$$\begin{aligned} \langle P^I P^J P^K \rangle_{\text{init}} = \frac{(2\pi)^3 \delta(\mathbf{k}_{\text{tot}})}{4a^6 H^2 k_1 k_2 k_3 k_t} \left\{ \frac{\dot{\phi}^I G^{JK}}{4HM_{\text{P}}^2} \mathbf{k}_2 \cdot \mathbf{k}_3 \left(K^2 + \frac{k_1 k_2 k_3}{k_t} \right) + \frac{a^2}{2} A_{\text{slow}}^{IJK} \left(K^2 - \frac{k_1 k_2 k_3}{k_t} \right) \right. \\ \left. - B^{IJK} \frac{k_1 k_2 k_3^2}{2H} - C^{IJK} \frac{k_1^2 k_2^2}{2} \left(1 + \frac{k_3}{k_t} \right) + 5 \text{ perms} \right\}. \end{aligned} \quad (2.146)$$

where ‘perms.’ indicates there are terms omitted which are cyclic permutations of the indices but *only within the surrounding brackets* of where the permutation instruction is given.

2.6.4 Gauge transformation to curvature perturbations

The final calculation needed before finding numerical results for inflationary models that use a non-trivial metric is a gauge transformation that translates our correlations functions in phase-space (eg. $\langle Q^I Q^J P^K \rangle$) into correlation functions of the curvature perturbation, ζ . We follow much of the same treatment as in [Dias et al., 2015a] and use some of their results that still apply with a non-trivial field metric in order to find the gauge transformations used in our code.

Calculating ζ

We would like to switch from the spatially-flat gauge used in our calculations so far to the uniform density gauge mainly because ζ is a quantity that is conserved to all orders in perturbation theory [Lyth et al., 2005, Malik & Wands, 2004] and can then be used to calculate the power spectrum and bispectrum for an inflation model. As in [Dias et al., 2015a], we use an exponential mapping of the Lie derivative that is used to change gauges,

$$x^\mu(p) \rightarrow x^\mu(p') = \exp(\mathcal{L}_\xi) x^\mu(p). \quad (2.147)$$

The Lie derivative is performed along a vector, ξ , which is given by

$$\mathcal{L}_\xi \implies \xi = \xi^0 \frac{\partial}{\partial f} + \xi^i \frac{\partial}{\partial x^i}, \quad (2.148)$$

where f here is a label for a time on the flat hypersurface. This exponential mapping is then used with a Taylor expansion on fields and their derivatives to find equations that translate fields in one gauge to another. These expressions can then be applied to the $h_{ij} dx^i dx^j$ part of the ADM decomposition found in Eq. (2.74) to rewrite it in terms of uniform density quantities. Finally, the ADM expression for the curvature perturbation, $\zeta = \det(h_{ij})/a^6$, is used to find

$$\zeta = H\xi^0 + \frac{H}{4} \frac{\partial(\xi^0)^2}{\partial f} + \frac{\dot{H}}{2} (\xi^0)^2, \quad (2.149)$$

where we have chosen to write the gauge transformation only in terms of ξ^0 and we have neglected spatial gradients due to them vanishing on the super-horizon scales we are interested in. We can also use the above expression to find the density perturbation in the

uniform-density gauge, $\delta\rho(u)$, by employing the δN formula [Lyth et al., 2005] to identify ζ with $\delta\rho(u)$ and substitute $\dot{\rho} \rightarrow \dot{N} = H$ with $\ddot{\rho} \rightarrow \ddot{N} = \dot{H}$ to give

$$\delta\rho(u) = \delta\rho + \dot{\rho}\xi^0 + \delta\dot{\rho}\xi^0 + \frac{\dot{\rho}}{2}\xi^0\xi^0 + \frac{\ddot{\rho}}{2}(\xi^0)^2, \quad (2.150)$$

where spatial gradients have been dropped. Equations (2.147)–(2.150) were first found in [Dias et al., 2015a] and still apply in the non-trivial field space used in our calculations. Eq. (2.150) can be used with $\delta\rho(u) = 0$ to find first- and second-order expressions for ξ^0 which are then substituted into Eq. (2.149),

$$\zeta = -H\frac{\delta\rho}{\dot{\rho}} + H\frac{\delta\rho}{\dot{\rho}}\frac{\delta\dot{\rho}}{\dot{\rho}} - \frac{H}{2}\frac{\ddot{\rho}}{\dot{\rho}}\left(\frac{\delta\rho}{\dot{\rho}}\right)^2 + \frac{\dot{H}}{2}\left(\frac{\delta\rho}{\dot{\rho}}\right)^2. \quad (2.151)$$

An expression for ρ is now needed specifically for our matter theory. We may assume that the perfect fluid equations apply, in which case the stress-energy tensor satisfies

$$T^a_b = \partial^a\phi^I\partial_b\phi_I - \delta^a_b\left(\frac{1}{2}\partial_c\phi^I\partial^c\phi_I + V\right). \quad (2.152)$$

The energy density is then related to the T^0_0 component where spatial gradients are neglected and the inverse ADM metric is used to find the second order density ,

$$\rho = -T^0_0 = \frac{1}{2N^2}\dot{\phi}^I\dot{\phi}_I + V, \quad (2.153)$$

where at zeroth order, $\rho = \frac{1}{2}\dot{\phi}^I\dot{\phi}_I + V$, as expected. Eqs. (2.71), (2.72) and (2.78) are then used to perturb Eq. (2.153) to second-order and find the density perturbation, $\delta\rho$,

$$\begin{aligned} \delta\rho = & \dot{\phi}^I D_t Q_I + V_I Q^I + \frac{1}{2}(3\alpha_1^2 - 2\alpha_2 - 2\alpha_1)\dot{\phi}^I\dot{\phi}_I \\ & + \frac{1}{2}V_{IJ}Q^I Q^J + \frac{1}{2}D_t Q^I D_t Q_I - 2\alpha_1\dot{\phi}^I D_t Q_I + \frac{1}{2}R_{IJKL}Q^I\dot{\phi}^J\dot{\phi}^K Q^L. \end{aligned} \quad (2.154)$$

The Hamiltonian constraint given in Eq. (2.85) can then be used to reduce this expression to

$$\delta\rho = 3H^2(3\alpha_1^2 - 2\alpha_2 - 2\alpha_1) \quad (2.155)$$

Then the lapse perturbations given in equations (2.81) & (2.83) can be used to find the density perturbation in terms of fields only,

$$\begin{aligned} \delta\rho = & -3H\dot{\phi}^I Q_I \\ & + \frac{3}{2}\dot{\phi}^I\dot{\phi}^J Q_I Q_J - 3H\partial^{-2}[\partial_i D_t Q^I \partial_i Q_I + D_t Q^I \partial^2 Q_I], \end{aligned} \quad (2.156)$$

where the first- and second-order terms are on the first and second lines respectively and the spatial derivatives have been neglected for the large scales we're interested in. Eq. (2.153)

can be used to find $\dot{\rho}$ and $\ddot{\rho}$ and those results can be used with Eq. (2.156) in Eq. (2.151) to find the uniform-density curvature perturbation, ζ ,

$$\zeta_1 = -\frac{\dot{\phi}^I Q_I}{2H\epsilon}, \quad (2.157)$$

and

$$\zeta_2 = \frac{1}{6H^2\epsilon} \left\{ \dot{\phi}_I \dot{\phi}_J \left(-\frac{3}{2} + \frac{9}{2\epsilon} + \frac{3}{4\epsilon^2} \frac{\dot{\phi}^K V_K}{H^3} \right) Q^I Q^J + \frac{3}{\epsilon H} \dot{\phi}_I \dot{\phi}_J Q^I D_t Q^J - 3H\partial^{-2} (\partial_i D_t Q^I \partial_i Q_I + D_t Q^I \partial^2 Q_I) \right\}, \quad (2.158)$$

where ζ_1 and ζ_2 are the first- and second-order terms respectively. These results are identical to the canonical case as given in [Dias et al., 2015a] but it was important to check no curvature terms were introduced for the non-canonical field space here.

Power spectra and N tensors

We now need to use equations (2.157) & (2.158) to find the statistics of ζ in order to find the power spectrum and bispectrum for a multi-field inflation theory. For this we write ζ in Fourier space,

$$\zeta(\mathbf{k}) = N_{\mathbf{a}} X^{\mathbf{a}} + \frac{1}{2} N_{\mathbf{ab}} X^{\mathbf{a}} X^{\mathbf{b}}, \quad (2.159)$$

where the N tensors are

$$N_{\mathbf{a}}(\mathbf{k}) = (2\pi)^3 \delta(\mathbf{k} - \mathbf{k}_a) N_a, \quad (2.160a)$$

$$N_{\mathbf{ab}}(\mathbf{k}) = (2\pi)^3 \delta(\mathbf{k} - \mathbf{k}_a - \mathbf{k}_b) N_{ab}, \quad (2.160b)$$

and $X^{\mathbf{a}} = (Q^I, P^J)$. We can now Fourier transform equations (2.157) & (2.158) to see that the coefficient matrices N_a and N_{ab} are

$$N_a = -\frac{\dot{\phi}_I}{2H\epsilon} \begin{pmatrix} 1 \\ 0 \end{pmatrix}, \quad (2.161a)$$

$$N_{ab} = \frac{1}{3H^2\epsilon} \begin{pmatrix} \dot{\phi}_I \dot{\phi}_J \left[-\frac{3}{2} + \frac{9}{2\epsilon} + \frac{3}{4\epsilon^2} \frac{V_{\gamma\pi\gamma}}{H^3} \right] & \frac{3}{H\epsilon} \dot{\phi}_I \dot{\phi}_J - \frac{3H}{k^2} [\mathbf{k}_a \cdot \mathbf{k}_b + k_a^2] G_{IJ} \\ \frac{3}{H\epsilon} \dot{\phi}_I \dot{\phi}_J - \frac{3H}{k^2} [\mathbf{k}_a \cdot \mathbf{k}_b + k_b^2] G_{IJ} & 0 \end{pmatrix}. \quad (2.161b)$$

The spectrum and bispectrum are given from the two and three point correlations of ζ . They are defined by

$$\langle \zeta(\mathbf{k}_1) \zeta(\mathbf{k}_2) \rangle = (2\pi)^3 \delta(\mathbf{k}_1 + \mathbf{k}_2) P(k) \quad (2.162a)$$

$$\langle \zeta(\mathbf{k}_1) \zeta(\mathbf{k}_2) \zeta(\mathbf{k}_3) \rangle = (2\pi)^3 \delta(\mathbf{k}_1 + \mathbf{k}_2 + \mathbf{k}_3) B(k_1, k_2, k_3), \quad (2.162b)$$

with the power spectrum, $P(k)$, given by

$$P(k) = N_a N_b \langle X^a(k_a) X^b(k_b) \rangle, \quad (2.163)$$

and the bispectrum $B(k_1, k_2, k_3)$ given by

$$B(k_1, k_2, k_3) = N_a N_b N_c \langle X^a(k_a) X^b(k_b) X^c(k_c) \rangle + \quad (2.164)$$

$$(N_a N_b N_{cd} \langle X^a(k_a) X^c(k_c) \rangle \langle X^b(k_b) X^d(k_d) \rangle + 2 \text{ cyclic}),$$

where ‘2 cyclic’ indicates that there are 2 extra terms that are cyclic permutations of the indices.

Chapter 3

Project II – CpptSample: sampling the primordial perturbation using CppTransport

3.1 Abstract

We introduce a new cosmological code, `CppTSample` – a module for the `CosmoSIS` parameter estimation framework which enables the `CppTransport` tool for computing inflationary correlation functions to provide initial conditions for the `CLASS` Boltzmann code. Our code can then interface with any of the samplers provided by `CosmoSIS` allowing for a large number of parameter samples for an inflation model to be efficiently obtained. The implementation also includes all of the 3-point function and non-trivial field space capabilities of `CppTransport` allowing for bispectrum constraints to be evaluated for non-canonical models. For computing CMB likelihoods, we pass the numerical form of the power spectrum into `CLASS` to ensure all features in the power spectrum are accounted for in the Bayesian analysis. We then demonstrate the module by reproducing results for several well-known models, including estimations of their equilateral bispectrum values. Next, we analyse the multi-field α -attractor and Gelaton/QSFI models which both rely on the non-trivial field space additions recently made to `CppTransport`.

3.2 Introduction

Inflation [Guth, 1981, Linde, 1982, Albrecht & Steinhardt, 1982] has largely been accepted by cosmologists as the primordial mechanism that produced the observed scale-invariant

power spectrum as well as being the source of quantum fluctuations that later grew to become large-scale structure (LSS). For simple inflation models, this prediction is constrained simply using the scalar power spectrum amplitude A_s and the scalar spectral index n_s which are both accurately calculated using their slow-roll predictions. Additionally, we also constrain inflation using the tensor power spectrum with an amplitude A_t , which defines the tensor to scalar ratio $r \equiv A_t/A_s$. These inflation models are accurately constrained by calculating the observables n_s and r with the slow-roll estimators before comparing them with the values inferred from cosmic microwave background (CMB) measurements given from experiments such as the WMAP [Larson et al., 2011, Komatsu et al., 2011, Dunkley et al., 2005, Hinshaw et al., 2013] or Planck [Adam et al., 2016, Ade et al., 2016b, Aghanim et al., 2018, Akrami et al., 2018] telescopes.

Applying constraints rapidly becomes more complicated for inflation models that are either multi-field or do not fulfil all the slow-roll approximations. Typically these models are multi-field with a non-canonical kinetic term defined using a field-space matrix $G_{IJ}(\phi)$ with examples including gelaton inflation [Tolley & Wyman, 2010] or quasi-single field inflation [Chen & Wang, 2010]. In particular, there are many beyond the Standard Model models based on string theory where the field metric is given by the Kähler potential $K(\phi^I, \phi^{I*})$ [Lyth & Riotto, 1999, Baumann & McAllister, 2015] and can include many fields. These models can produce large non-Gaussianities measured using the various reduced bispectrum shape configurations (e.g. $f_{\text{NL}}^{\text{squeezed}}$ or $f_{\text{NL}}^{\text{equilateral}}$) which are constrained to be small by Planck [Ade et al., 2016a]. Additionally, multi-field inflation models can give significant isocurvature perturbations which are also constrained by Planck to be small [Ade et al., 2016a].

Clearly, accurate calculations of the predictions made by these complex models are needed because they allow for some of the most novel physics theories to be tested and constraints on non-Gaussianities provide an additional test on *all* inflation models regardless of their complexity. Therefore the ‘transport method’ was developed [Mulryne et al., 2010, Mulryne et al., 2011, Seery et al., 2012] to calculate the power spectrum and bispectrum using inflationary perturbation theory before applying the method in several automated numerical codes: `mTransport` [Dias et al., 2015b], `CppTransport` [Dias et al., 2016, Seery, 2016] and `PyTransport` [Mulryne & Ronayne, 2016]. Recently, we have extended `CppTransport` and `PyTransport` to calculate the bispectrum for models with the aforementioned non-canonical field space [Ronayne & Mulryne, 2017, Butchers & Seery, 2018].

Bayesian evidence for models.—The problem with this approach to constraining an inflation model is there are many models with parameter combinations that produce observables that are compatible with the current measurements. An inflation model with a wide parameter-space giving ‘successful’ inflation would not be preferentially chosen over a model with a smaller parameter-space compatible with observations as expected based on the ‘fine-tuning’ of the model parameters. Instead the method has been to apply Markov Chain Monte Carlo (MCMC) analysis [Christensen & Meyer, 2000, Christensen et al., 2001, Knox et al., 2001, Kosowsky et al., 2002, Lewis & Bridle, 2002, Verde et al., 2003, Dunkley et al., 2005] to estimate both the cosmological and inflation parameters for a model and then use Bayesian model selection [Hobson et al., 2010, Parkinson et al., 2006, Bridges et al., 2007, Liddle et al., 2006, Gordon & Trotta, 2007] to discriminate between each model’s ability to describe the data.

Bayesian inference has already been successfully applied in several cosmological codes. The Planck collaboration [Akrami et al., 2018] used the ASPIC code [Martin et al., 2014] to compute the observables n_s and r with MCMC samples coming from CosmoMC [Lewis & Bridle, 2002] and MontePython [Audren et al., 2013] or nested samples coming from programs such as MultiNest [Feroz et al., 2009, Feroz et al., 2013]. PolyChord [Handley et al., 2015] is then used to interface with the Boltzmann codes CAMB [Lewis et al., 2000] or CLASS [Lesgourgues, 2011, Blas et al., 2011] for computing the CMB observables before calculating the Bayesian evidence for the given model. Alternatively in [Mortonson et al., 2011, Easther & Peiris, 2012, Norena et al., 2012], ModeCode/MultiModeCode [Price et al., 2015] is used to compute the scalar, tensor and isocurvature power spectra by applying the δN formalism [Sasaki & Stewart, 1996, Wands et al., 2000] with samples obtained from MultiNest for the Bayesian analysis. However, none of these analyses can compute the bispectrum for the previously discussed models that have a non-canonical field-space.

Therefore, we introduce CppTSample, a CosmoSIS module [Zuntz et al., 2015] that is designed to provide samples of the inflationary and cosmological parameters to CppTransport before using a modified CLASS module to find the CMB spectra (TT, EE, TE, and BB) from the model’s power spectrum. Finally, it passes the CMB spectra to the CosmoSIS modules for the Planck2015 [Aghanim et al., 2016] and WMAP5 likelihoods [Dunkley et al., 2009, Hinshaw et al., 2013] to compare with observational data. This approach allows for both the power spectrum and bispectrum to be sampled, with weights assigned by how well the two-point function fits the CMB data. CppTransport does not make use of the slow-roll approximation and therefore can be used to analyse the sophisticated models

previously mentioned. In future, the modular structure of `CosmoSIS` allows for late-time observables like the matter power spectrum to be found from the inflation model and then used to compute other observables such as the galaxy power spectrum and other measures of large-scale structure¹.

Synopsis.—This paper is split into four key parts. Initially, we give a brief overview of the transport method and describe the different observables that can be computed by `CppTransport` in section 3.3. In Section 3.4, we first discuss the modular structure of `CosmoSIS` and give examples of modules to use with our code. Then we explain the numerical methods used to pass information between the different `CosmoSIS` modules, and how we use `CppTSample` to extract the inflationary observables from `CppTransport` in a MCMC sample run.

In Section 3.5, we present some numerical results obtained from our code. We begin by reproducing well-known results for the quartic inflation model in section 3.5.1 and for the quadratic model in section 3.5.2. Next in section 3.5.3, we analyse an α -attractor model which has a non-trivial field metric and use the results to show the ‘universality’ [Achúcarro et al., 2017] of these models. In section 3.5.4, we show how `CppTSample` can be used on the Gelaton/QSFI model. This is numerically expensive but demonstrates how `CppTransport` can be used separately with the best-fit parameters to measure the bispectrum. We conclude in Section 3.6.

Obtaining `CppTSample` and requirements.—`CppTSample` can be downloaded as part of the `CppTransport` platform available from the main GitHub repository. Installation instructions and necessary dependencies² are given in the user guide [Seery, 2016]. Examples of all models discussed in this paper are provided as example `.model` files in this repository. `CosmoSIS` needs to be installed separately to interact with the samplers, with download and installation instructions available from the `CosmoSIS` Wiki. Additionally, both `CppTransport` and `CosmoSIS` must be installed with the same version of the GNU compiler for the shared libraries to be read correctly. Alternatively, the Docker images of `CppTransport` & `CosmoSIS` can be used instead.

Notation.—We use natural units where $c = \hbar = 1$. The reduced Planck mass is $M_{\text{P}}^2 = (8\pi G)^{-1}$. We use the metric signature $(-, +, +, +)$. Greek indices (μ, ν, \dots) label space-time indices, whereas lower-case Roman indices from the middle of the alphabet, (i, j, \dots) ,

¹See [de la Bella et al., 2018] for an example of a `CosmoSIS` module that calculates the halo power spectrum.

²These are CMake, OpenMPI, Boost, GiNaC and OpenSSL.

label spatial indices. Upper-case Roman indices (I, J, \dots) label field-space coordinates. For phase-space coordinates, we use Roman letters from the start of the alphabet, (a, b, \dots). An index with a comma denotes a field derivative ($V_{,I} \equiv \partial V / \partial \phi^I$) and an index with a semi-colon indicating a covariant derivative ($V_{;J}^I \equiv D_J V^I$) where the covariant derivative is

$$D_J V^I \equiv \frac{\partial V^I}{\partial \phi^J} + \Gamma_{JK}^I V^K. \quad (3.1)$$

We also use a compressed Fourier notation where the index labels indicate both a summation over the fields and integration over the Fourier wavenumbers. They appear in a bold, san-serif font: ($\mathbf{I}, \mathbf{J}, \dots$), which is defined using the equation

$$A_{\mathbf{I}} B^{\mathbf{I}} = \sum_I \int \frac{d^3 k_I}{(2\pi)^3} A_I(\mathbf{k}_I) B^I(\mathbf{k}_I), \quad (3.2)$$

where indices are always raised and lowered using the field-metric G_{IJ} .

3.3 The transport method and CppTransport

CppTransport makes use of the transport method [Mulryne et al., 2010, Mulryne et al., 2011, Seery et al., 2012, Dias et al., 2015b, Dias et al., 2016, Ronayne & Mulryne, 2017, Butchers & Seery, 2018] in which the code reads in a model file defining a Lagrangian which gives definitions of the potential $V(\phi^I)$ and the field-space metric G_{IJ} for the case of a non-trivial model. Initially the background field equation is solved

$$D_t \dot{\phi}^I + 3H \dot{\phi}^I + G^{IJ} V_{,J} = 0, \quad (3.3)$$

with the dynamics of H determined using

$$3H^2 = \rho = \frac{1}{2} G_{IJ} \partial_\mu \phi^I \partial^\mu \phi^J + V(\phi), \quad (3.4a)$$

$$\epsilon \equiv -\frac{\dot{H}}{H^2} = \frac{G_{IJ} \dot{\phi}^I \dot{\phi}^J}{2H^2}, \quad (3.4b)$$

which are the covariant field equation, Friedman equation and Hubble slow-roll parameter respectively. We define our perturbed coordinate Q^I using the method given by Gong and Tanaka [Gong & Tanaka, 2011] where Q^I is defined on the tangent-space of $\phi^I(t)$ so that it forms a geodesic connected to $\phi^I(\mathbf{x}, t)$ and can therefore be related to $\delta\phi^I$. The action is symbolically expanded to third-order [Elliston et al., 2012, Dias et al., 2016, Ronayne & Mulryne, 2017, Butchers & Seery, 2018] to obtain

$$S_\phi = \frac{1}{2} \int dt a^3 \left\{ G_{\mathbf{I}\mathbf{J}} D_t Q^{\mathbf{I}} D_t Q^{\mathbf{J}} + M_{\mathbf{I}\mathbf{J}} Q^{\mathbf{I}} Q^{\mathbf{J}} + \right. \\ \left. + A_{\mathbf{I}\mathbf{J}\mathbf{K}} Q^{\mathbf{I}} Q^{\mathbf{J}} Q^{\mathbf{K}} + B_{\mathbf{I}\mathbf{J}\mathbf{K}} Q^{\mathbf{I}} Q^{\mathbf{J}} D_t Q^{\mathbf{K}} + C_{\mathbf{I}\mathbf{J}\mathbf{K}} D_t Q^{\mathbf{I}} D_t Q^{\mathbf{J}} Q^{\mathbf{K}} \right\}, \quad (3.5)$$

where the second-order kernels $G_{\mathbf{IJ}}$ and $M_{\mathbf{IJ}}$ are defined as

$$\begin{aligned} G_{\mathbf{IJ}} &\equiv (2\pi)^3 G_{IJ} \delta(\mathbf{k}_1 + \mathbf{k}_2), \\ M_{\mathbf{IJ}} &\equiv (2\pi)^3 \delta(\mathbf{k}_1 + \mathbf{k}_2) \left(\frac{\mathbf{k}_1 \cdot \mathbf{k}_2}{a^2} G_{IJ} - m_{IJ} \right), \end{aligned} \quad (3.6)$$

with the mass-matrix defined by

$$m_{IJ} \equiv V_{;IJ} - R_{KIJL} \dot{\phi}^K \dot{\phi}^L - \frac{1}{a^3 M_{\text{P}}^2} D_t \left(\frac{a^3 \dot{\phi}_I \dot{\phi}_J}{H} \right). \quad (3.7)$$

The third-order kernels $A_{\mathbf{IJK}}$, $B_{\mathbf{IJK}}$ and $C_{\mathbf{IJK}}$ are [Butchers & Seery, 2018]

$$A_{\mathbf{IJK}} \equiv (2\pi)^3 \delta(\mathbf{k}_1 + \mathbf{k}_2 + \mathbf{k}_3) A_{IJK}, \quad (3.8a)$$

$$B_{\mathbf{IJK}} \equiv (2\pi)^3 \delta(\mathbf{k}_1 + \mathbf{k}_2 + \mathbf{k}_3) B_{IJK}, \quad (3.8b)$$

$$C_{\mathbf{IJK}} \equiv (2\pi)^3 \delta(\mathbf{k}_1 + \mathbf{k}_2 + \mathbf{k}_3) C_{IJK}, \quad (3.8c)$$

while the tensors A_{IJK} , B_{IJK} and C_{IJK} are [Butchers & Seery, 2018]

$$\begin{aligned} A_{IJK} &\equiv -\frac{1}{3} V_{;IJK} - \frac{\dot{\phi}_I V_{;JK}}{2HM_{\text{P}}^2} + \frac{\dot{\phi}_I \dot{\phi}_J Z_K}{4H^2 M_{\text{P}}^4} + \frac{\dot{\phi}_I Z_J Z_K}{8H^3 M_{\text{P}}^4} \left(1 - \frac{(\mathbf{k}_2 \cdot \mathbf{k}_3)^2}{k_2^2 k_3^2} \right) \\ &\quad + \frac{\dot{\phi}_I \dot{\phi}_J \dot{\phi}_K}{8H^3 M_{\text{P}}^6} (6H^2 M_{\text{P}}^2 - \dot{\phi}^2) - \frac{\dot{\phi}_K \dot{\phi}^L \dot{\phi}^M}{2HM_{\text{P}}^2} R_{L(IJ)M} + \frac{1}{3} R_{(I|LM|J;K)} \dot{\phi}^L \dot{\phi}^M \\ &\quad + \frac{\dot{\phi}_I G_{JK} \mathbf{k}_2 \cdot \mathbf{k}_3}{2HM_{\text{P}}^2 a^2}, \end{aligned} \quad (3.9a)$$

$$B_{IJK} \equiv \frac{4}{3} R_{K(IJ)L} \dot{\phi}^L - \frac{\dot{\phi}_I Z_J \dot{\phi}_K}{4H^3 M_{\text{P}}^4} \left(1 - \frac{(\mathbf{k}_2 \cdot \mathbf{k}_3)^2}{k_2^2 k_3^2} \right) + \frac{\dot{\phi}_I \dot{\phi}_J \dot{\phi}_K}{4H^2 M_{\text{P}}^4} - \frac{Z_I G_{JK} \mathbf{k}_1 \cdot \mathbf{k}_2}{HM_{\text{P}}^2 k_1^2}, \quad (3.9b)$$

$$C_{IJK} \equiv -\frac{G_{IJ} \dot{\phi}_K}{2HM_{\text{P}}^2} + \frac{\dot{\phi}_I \dot{\phi}_J \dot{\phi}_K}{8H^3 M_{\text{P}}^4} \left(1 - \frac{(\mathbf{k}_1 \cdot \mathbf{k}_2)^2}{k_1^2 k_2^2} \right) + \frac{\dot{\phi}_I G_{JK} \mathbf{k}_1 \cdot \mathbf{k}_3}{HM_{\text{P}}^2 k_1^2}, \quad (3.9c)$$

where brackets around field-space indices indicates symmetrisation with weight unity and vertical bars indicates indices that are excluded. In this form, the numbered indices on the momentum vectors map to field space indices as $1 \rightarrow I$, $2 \rightarrow J$ and $3 \rightarrow K$ respectively.

Finally, Z_I is given by

$$Z_I \equiv D_t \dot{\phi}_I + \frac{\dot{\phi}_I \dot{\phi}_J \dot{\phi}^J}{2HM_{\text{P}}^2}. \quad (3.10)$$

These expressions are all given for the case of a non-trivial field metric. For the canonical case, all Riemann terms should be removed, the field-metric replaced with $G_{IJ} = \delta_{IJ}$ and the covariant time derivatives replaced with partial time derivatives (cf. Dias et al. [Dias et al., 2016]). Next the *transport equations* are found by first applying a Legendre transformation with the momentum identified as $P^I = D_t Q^I$ to find the Hamiltonian H before using it to calculate the Heisenberg equations of motion, which have the form

$$D_t \Sigma^{ab} = u^a{}_c \Sigma^{cb} + u^b{}_c \Sigma^{ac}, \quad (3.11a)$$

$$D_t \alpha^{abc} = u^a{}_d \alpha^{dbc} + u^a{}_{de} \Sigma^{db} \Sigma^{ec} + g2 \text{ cyclic } (a \rightarrow b \rightarrow c), \quad (3.11b)$$

where we define a phase-space $X^a = (Q^I, P^J)$ with the 2- and 3-point functions given as

$$\langle X^{\mathbf{a}} X^{\mathbf{b}} \rangle \equiv (2\pi)^3 \delta(\mathbf{k}_a + \mathbf{k}_b) \Sigma^{ab}, \quad (3.12a)$$

$$\langle X^{\mathbf{a}} X^{\mathbf{b}} X^{\mathbf{c}} \rangle \equiv (2\pi)^3 \delta(\mathbf{k}_a + \mathbf{k}_b + \mathbf{k}_c) \alpha^{abc}, \quad (3.12b)$$

The ‘u-tensors’ are given by

$$u^a_b = \begin{pmatrix} 0 & \delta^I_J \\ M^I_J & -3H\delta^I_J \end{pmatrix}, \quad (3.13)$$

with a giving the row and b giving the column in u^a_b and

$$u^a_{bc} = \left\{ \begin{array}{l} \left(\begin{array}{cc} -B_{JK}^I & -C^I_{JK} \\ 3A^I_{JK} & B^I_{KJ} \end{array} \right) \\ \left(\begin{array}{cc} -C^I_{KJ} & 0 \\ B^I_{JK} & C_{KJ}^I \end{array} \right) \end{array} \right\}, \quad (3.14)$$

where a identifies the 2×2 matrix with b and c giving the row and column respectively for the 2×2 matrix. The equations of motion for these correlation functions require initial conditions for a numerical solution which are given in Dias et al. [Dias et al., 2016] for the canonical case and originally by Elliston et al. [Elliston et al., 2012, Butchers & Seery, 2018] for the non-canonical case. A similar procedure is needed to compute the transport equations for the tensor perturbations γ_{ij} with the details given in [Dias et al., 2015b, Dias et al., 2016].

Finally, a second-order gauge transformation [Dias et al., 2015a] is needed to convert the flat-space field perturbations $X^{\mathbf{a}}$ to the conserved curvature perturbation ζ . This allows it to be compared with the CMB spectrum and is given as

$$\zeta(\mathbf{k}) = N_{\mathbf{a}} X^{\mathbf{a}} + \frac{1}{2} N_{\mathbf{ab}} X^{\mathbf{a}} X^{\mathbf{b}}, \quad (3.15)$$

with the coefficient matrices N_a and N_{ab} first given in Dias et al. [Dias et al., 2015a] as

$$N_a = -\frac{\dot{\phi}_I}{2HM_{\text{P}}^2\epsilon} \begin{pmatrix} 1 \\ 0 \end{pmatrix}, \quad (3.16a)$$

$$N_{ab} = \frac{1}{3H^2M_{\text{P}}^2\epsilon} \begin{pmatrix} \frac{\dot{\phi}_I\dot{\phi}_J}{M_{\text{P}}^2} \left[-\frac{3}{2} + \frac{9}{2\epsilon} + \frac{3}{4\epsilon^2} \frac{V_K\pi^K}{H^3M_{\text{P}}^2} \right] & \frac{3}{H\epsilon} \frac{\dot{\phi}_I\dot{\phi}_J}{M_{\text{P}}^2} - \frac{3H}{k^2} [\mathbf{k}_a \cdot \mathbf{k}_b + k_a^2] G_{IJ} \\ \frac{3}{H\epsilon} \frac{\dot{\phi}_I\dot{\phi}_J}{M_{\text{P}}^2} - \frac{3H}{k^2} [\mathbf{k}_a \cdot \mathbf{k}_b + k_b^2] G_{IJ} & 0 \end{pmatrix}. \quad (3.16b)$$

Observables.—The dimensionless power spectrum $\mathcal{P}(k)$ can be written as

$$\mathcal{P}(k) = \frac{k^3}{2\pi} P_\zeta(k), \quad (3.17)$$

where the power spectrum $P_\zeta(k)$ is defined by

$$\langle \zeta(\mathbf{k}_1) \zeta(\mathbf{k}_2) \rangle = (2\pi)^3 \delta(\mathbf{k}_1 + \mathbf{k}_2) P_\zeta(k). \quad (3.18)$$

Similarly for the tensor power spectrum, we have

$$\langle \gamma_{ij}(\mathbf{k}_1) \gamma^{ij}(\mathbf{k}_2) \rangle = (2\pi)^3 \delta(\mathbf{k}_1 + \mathbf{k}_2) P_t(k), \quad (3.19)$$

where the tensor field is defined as $\gamma_{ij} \equiv \sqrt{2} M_{\text{P}} h_{ij}$ and h_{ij} is the spatial part of the metric. The scale-dependence for the two-point statistics is measured using the scalar and tensor spectral indices n_s and n_t which are given by

$$n_s - 1 \equiv \frac{d \ln A_s}{d \ln k}, \quad (3.20)$$

$$n_t \equiv \frac{d \ln A_t}{d \ln k}. \quad (3.21)$$

where A_s and A_t are the amplitudes of the scalar and tensor power spectra respectively.

The dimensionless bispectrum $\mathcal{B}(k_1, k_2, k_3)$ is defined to be

$$\mathcal{B}(k_1, k_2, k_3) = (k_1 k_2 k_3)^2 B(k_1, k_2, k_3), \quad (3.22)$$

where the bispectrum $B(k_1, k_2, k_3)$ satisfies

$$\langle \zeta(\mathbf{k}_1) \zeta(\mathbf{k}_2) \zeta(\mathbf{k}_3) \rangle = (2\pi)^3 \delta^3(\mathbf{k}_1 + \mathbf{k}_2 + \mathbf{k}_3) B(k_1, k_2, k_3). \quad (3.23)$$

The reduced bispectrum $f_{\text{NL}}(k_1, k_2, k_3)$ is defined in terms of the bispectrum and the power spectra as

$$\frac{6}{5} f_{\text{NL}}(k_1, k_2, k_3) = \frac{B(k_1, k_2, k_3)}{P(k_1)P(k_2) + P(k_1)P(k_3) + P(k_2)P(k_3)}. \quad (3.24)$$

The triangles formed by the three Fourier wavenumbers are then categorised based on their shapes where an equilateral configuration has all three sides equal in size ($k_1 = k_2 = k_3$), whereas a squeezed configuration has one side much smaller than the others as ($k_1 \simeq k_2 \gg k_3$) and a folded configuration has one side that is much larger than the others ($k_1 \simeq k_2 \ll k_3$). These shapes are parameterised using k_t , α and β as introduced by Fergusson & Shellard [Fergusson & Shellard, 2007]

$$k_1 \equiv \frac{k_t}{4} (1 + \alpha + \beta), \quad (3.25a)$$

$$k_2 \equiv \frac{k_t}{4} (1 - \alpha + \beta), \quad (3.25b)$$

$$k_3 \equiv \frac{k_t}{2} (1 - \beta), \quad (3.25c)$$

where $k_t = k_1 + k_2 + k_3$ is the perimeter of the triangle, with α and β having the ranges $-1 \leq \alpha \leq 1$ and $0 \leq \beta \leq 1$, respectively. An equilateral configuration can be achieved by setting $\alpha = 0$ and $\beta = \frac{1}{3}$, we define a squeezed configuration as having the parameters $\alpha = 0$ and $\beta = 0.98$, and a folded configuration as having the parameters $\alpha = 0$ and $\beta = 0.005$.

3.4 Code methodology

Here we describe each code used in the sampling pipeline and give the details of the calculations performed by each of them. Initially, we will describe the modular structure of `CosmoSIS` and how data is passed between the modules using a *datablock*. This will focus on the different modules available for our MCMC analysis. We will then discuss how to adapt existing `CppTransport` model files to include sampling functionality and how the physical wavenumbers are found from the matching equation to create different integration tasks. We will then discuss how we use `CppTSample` to extract observables and how to produce parameter estimation and covariance plot generation using the existing `GetDist` MCMC analysis framework. Finally, the whole `CppTSample` analysis pipeline will be summarised in a diagram.

3.4.1 CosmoSIS modules

`CosmoSIS` [Zuntz et al., 2015] provides a modular environment for performing its cosmological calculations where each step of the computation is split into a separate module, sharing a common data member known as a *datablock*. This modularity means the problem of creating a pipeline of codependent numerical calculations is reduced to just making sure they can all receive inputs and write outputs to the datablock. Installation instructions with documentation on all of the different modules is available on the `CosmoSIS` Wiki. For our numerical implementation, we make use of the samplers, a Boltzmann code and the likelihood modules in `CosmoSIS`. Throughout this section, the specific module names are referred to in this font.

Sampler modules.—`CosmoSIS` provides a variety of samplers that fulfil different purposes depending on the requirements for the user’s parameter estimation task. Initially for testing, the test sampler will analyse a single parameter set which can be used to find appropriate initial conditions for successful inflation. A simple exploration of the parameter-space can be done by taking N points between two limits for each parameter in the grid and

snake samplers. Alternatively, the maximum likelihood samplers (maxlike, minuit & gridmax) can be used with a likelihood module to find the inflationary initial conditions that give the best fit to data (e.g Planck or WMAP). After finding the best-fit to CMB data, there are several classic MCMC samplers including a Metropolis-Hastings sampler [Metropolis et al., 1953] (metropolis), an importance sampler (importance) and a Fisher matrix sampler (fisher). Additionally, there are more advanced ensemble algorithms available such as the emcee sampler [Foreman-Mackey et al., 2013] as well as the multineest sampler [Feroz et al., 2009, Feroz et al., 2013].

CLASS module.—CosmoSIS also provides modules for several Boltzmann codes including both CAMB [Lewis et al., 2000] and CLASS [Lesgourgues, 2011, Blas et al., 2011]. In addition to these, there are modules for computing the non-linear matter power spectrum using halofit [Smith et al., 2003, Takahashi et al., 2012] or for studying modified gravity with mgcamb [Hojjati et al., 2011, Zhao et al., 2009]. When computing the predicted CMB power spectrum in our numerical implementation, we use a slightly modified version of the CLASS module that uses the `external_Pk` [Achúcarro et al., 2014, Achúcarro et al., 2014] feature instead of specifying the primordial power spectrum by only using A_s and n_s . With this modification, we use `CppTransport` to write a data table of power spectrum values for a range of scales which is passed on to the CLASS module. The resulting CMB power spectrum predictions are based on the primordial power spectrum produced by the inflation model instead of setting priors on the cosmological parameters A_s and n_s . This set-up ensures any features in the primordial power spectrum are taken into account when calculating the CMB power spectrum and hence will affect the likelihoods calculated from CMB data. This modified CLASS code is distributed within the `CppTSample` platform.

Likelihoods and other calculations.—There are numerous likelihood codes implemented as modules in CosmoSIS. For the CMB predictions, there is the WMAP7 [Larson et al., 2011, Komatsu et al., 2011] and WMAP9 [Hinshaw et al., 2013] data accessed via the `wmap` module, with BICEP2 data [Ade et al., 2014a, Ade et al., 2014b] given in the `bicep2` module, and Planck 2015 data [Ade et al., 2016b, Aghanim et al., 2016] given in the `planck` module. In addition to these, there are likelihood modules available for BAO data [Chuang et al., 2013, Kazin et al., 2014] and supernovae data [Riess et al., 2011] too. We make use of some of the MCMC samplers discussed previously to determine the underlying probability distribution for the inflation observables and then use the Planck data for the likelihoods. While we only use the CMB data for our analyses a user could, in principle, use our module to compute the CMB power spectrum which can be used to study LSS by using the galaxy

bias and likelihood modules available in CosmoSIS.

3.4.2 Using CppTSample

Now we have samplers and likelihood codes accessible via the CosmoSIS datablock, we will describe how CppTSample obtains its initial conditions and constructs integration tasks for CppTransport.

Initial conditions.—The crux of sampling a model is determining what values and priors parameters in a model will be sampled over. CosmoSIS provides three default priors: uniform prior taking lower and upper values, Gaussian prior taking the mean and standard deviation, and an exponential prior $P(x) \propto \exp(x/\beta)$ with only one parameter β . Priors can be set for parameters as well as both field initial values and the derivative of the field initial value. This allows for an in-depth analysis of the inflationary dynamics of a model with varying parameters. A prior doesn't need to be specified for either a field or parameter, where instead it is set to a fixed value. This allows for some numbers to be held constant, while other parameters are being sampled over. Values and priors are both specified in the CppTransport model file as described below.

Updated model file.—The basis of the CppTransport platform is the use of a model file which describes the fields and parameters of an inflationary model that form the model's potential and a metric when using a non-canonical field-space. CppTSample extends the use of the model files by allowing users to specify priors and values directly in the model file, ensuring that all information about a model is in the same location. To enable auto-generation of the CosmoSIS files needed for sampling, the following line needs to be added anywhere to the model file.

```
1 sampling { generate_sampling = "True"; };
```

This will then trigger the CppTransport translator to generate the additional files needed for sampling. Adding priors and values to parameters and fields is very simple through the use of `prior` and `value` commands and for fields also setting conditions on the initial field derivative through `deriv_prior` and `deriv_value`. These values get written out to CosmoSIS `.ini` files which means that the entire information about a model and the sampling strategy is held within the model file. This also ensures that only one file needs to be viewed and changed – making the CppTSample platform very easy to customise.

An example model file with values and priors for the double quadratic model with potential $V(\phi, \chi) = \frac{1}{2}M_\phi^2\phi^2 + \frac{1}{2}M_\chi^2\chi^2$ is given below. See the existing CppTransport user-guide

[Seery, 2016] for a more detailed explanation on how to write a model file, or browse some provided examples in the CppTransport GitHub repository and adapt them as necessary.

```

1  sampling { generate_sampling = "True"; };
2
3  field phi
4  {
5      latex = "\phi";
6      value = "9.0 10.0 11.0";
7      prior = "uniform 9.0 11.0";
8      deriv_value = "0.0";
9  };
10
11 field chi
12 {
13     latex = "\chi";
14     value = "5.0 12.9 15.0";
15     prior = "gaussian 13.0 1.5";
16     deriv_value = "-1.0 0.0 1.0";
17     deriv_prior = "exponential 0.05"
18 };
19
20 parameter Mphi
21 {
22     latex = "M_\phi";
23     value = "8E-5 9E-5 1E-4";
24     prior = "gaussian 9E-5 1E-6";
25 };
26
27 parameter Mchi
28 {
29     latex = "M_\chi";
30     value = "1E-5";
31 };
32 cd
33 potential = Mphi^2 * phi^2 / 2 + Mchi^2 * chi^2 / 2;

```

When using a prior for a parameter or field, three values can be given in the `value` property. The first is the lower-bound, the second is the optional starting value, and the third is the upper-bound. The starting value is used by many MCMC samplers (e.g. Metropolis-Hastings) and is where the MCMC chain will start from. The starting point allows us to verify whether the MCMC chain has converged on the maximum-likelihood point and the lower- and upper-bounds allow for further constraints to be placed on a parameter in addition to the prior such as ensuring that a parameter is positive-definite or below a certain value.

We can also construct a log-uniform prior for parameters that span several orders of magnitude by rewriting the parameter p as an exponent with base b in the potential and/or metric as $\exp(\ln(b) \cdot p)^3$. As an example, we can sample the parameter m appearing in the potential $V = \frac{1}{2}m^2\phi^2$ uniformly between 10^{-7} and 10^{-5} , we write the model file as follows.

```

1  parameter m
2  {
3      latex = "m";
4      value = "-7 -5";
5      prior = "uniform -7 -5";
6  };
7  potential = (1/2) * ( exp(m * log(10.0)) )^2 * phi^2;
```

With the translator successfully installed (see `CppTransport` user-guide [Seery, 2016]), we can generate the sampling output files for a model file named ‘MODEL.model’ via the following command.

```
CppTransport --verbose --generate-cmake MODEL.model
```

We have added the optional argument `--generate-cmake` which automatically produces a `CMakeLists.txt` file for use with the CMake build system utilised by `CppTransport`. The `CppTransport` command translates the `MODEL.model` file into the C++ header files needed by `CppTSample` and places them in the `build/` directory as well as the `CosmoSIS MODEL_mcmc.ini`, `MODEL_values.ini` and `MODEL_priors.ini` files in the `MODEL_mcmc/` directory. The build environment is configured for `CppTSample` by navigating into the `build/` directory and issuing the following CMake command

```

cmake .. -DCMAKE_BUILD_TYPE=Release
↪ -DCMAKE_INSTALL_PREFIX=/path/to/CppTransport/installation/location
↪ -DCOSMOSIS_SRC_DIR=$COSMOSIS_SRC_DIR
```

where the `$COSMOSIS_SRC_DIR` environment variable is set when installing `CosmoSIS`, and `/path/to/CppTransport/installation/location` is the location of the run-time header files when installing `CppTransport`. If CMake ran successfully, we can now build the `CppTSample` shared library by issuing the following build command

³Having to use `exp` is an unfortunate caveat of the `CppTransport` translator because it can’t differentiate an exponent with an arbitrary base but can differentiate `exp`.

```
make MODEL_sampling
```

If compiling was successful, we can now start sampling the model by using the following CosmoSIS command in the model’s root directory.

```
cosmosis MODEL_mcmc/MODEL_mcmc.ini
```

By default, this will use the Metropolis-Hastings sampler to sample over 25 000 points. It will write to an output file located at `MODEL_mcmc/mcmc_output.txt`. Many different customisation options can be used in CosmoSIS where the CosmoSIS wiki provides instructions to use different samplers or including additional likelihood modules.

Customising sampling runs.—When a model is first analysed, baseline performance of the sampler is normally assessed and likelihoods of the samples is checked so initially the sampling should happen quickly. Therefore, by default the CosmoSIS `MODEL_mcmc.ini` file does not have any of the three-point function analysis turned on. Since evaluating the three-point function takes significantly longer than the two-point function, this causes unnecessary time usage when simply evaluating the performance of the model. The three-point function analysis can be freely turned on and off by adjusting the relevant section in the `MODEL_mcmc.ini` file. This is in the `[cppt_sample]` block, which is generated as:

```
[cppt_sample]
file = ${PWD}/build/libMODEL_sampling.so
M_P = 1.0
k_samples = 400
k_pivot = 0.002
Debug = F
ThreepfEqui = F
ThreepfSqueeze = F
ThreepfFold = F
MassEigenSquare = F
```

The options `ThreepfEqui`, `ThreepfSqueeze` and `ThreepfFold` govern running the equilateral, squeezed and folded three-point function configurations. Setting any of these to true, represented by ‘T’, will trigger `CppTSample` to include the respective three-point function calculation when sampling. Performance is generally good for the equilateral and folded configurations, with squeezed triangles taking longer – however this is very model specific.

We can also customise how the mass-matrix eigenvalues are reported from `CppTSample`. `CppTSample` returns the normalised eigenvalues of the mass matrix (m_i/H) at four points in the fields evolution: 55 e -folds before the end of inflation – which is roughly at horizon

crossing – and 2.5, 1 and 0 e -folds before the end of inflation. This allows the rough evolution of the mass matrix to be determined, and specifically allows us to check whether a sample has reached an adiabatic limit at the end of inflation [Elliston et al., 2011]. `CppTSample` can instead return the squares of the eigenvalues of the mass matrix by setting the `MassEigenSquare` option to true. This could be desired if using the squared values makes comparisons between `CppTSample` and existing data easier.⁴

The value for k_{pivot} is also changed here by changing the `k_pivot` variable. The default value is 0.002 Mpc^{-1} for comparison with the Planck measurements, but 0.05 Mpc^{-1} can be chosen for comparison with WMAP results.

If for any reason sampling runs are not successfully completing or taking a long time to complete, the `Debug` flag can be turned to true which automatically prints debugging information about how `CppTSample` is progressing through each sample which can help determine where errors are occurring in the pipeline.

GetDist integration.—`CppTSample` provides native integration to the `GetDist` MCMC analysis framework, which is included as part of `CosmoMC` [Lewis & Bridle, 2002, Lewis, 2013], through the use of an automatically generated Python file. This reads in the `CosmoSIS` output file containing the sampled parameters, output files and likelihood for each sample and formats it in a way that `GetDist` is able to understand. It then calls `GetDist` to produce parameter estimation tables at both the 68 % and 95 % confidence level, saving the outputs as \LaTeX tables and printing them to the terminal as well as producing a triangle covariance plot for the sampled and output parameters. Examples of these parameter tables and triangle plots can be seen in our numerical results in Section 3.5.

The Python file also utilises the `Seaborn` plotting package to produce histograms for the main cosmological parameters of interest (n_s , n_t , A_s , A_t , r , f_{NL} , ends of inflation, and mass matrix eigenvalues) from the `CosmoSIS` output file. This allows for detailed, high-quality figures for publication to be automatically produced without any extra files. The automatically generated file requires the Python `GetDist`, `Matplotlib`, `NumPy`, `Pandas` and `Seaborn` libraries are installed which are easily available via `pip` or `conda` and the plots are produced by running `python MODEL_GetDist.py` from the terminal. All plots are written using standard `Matplotlib` code so they can easily be customised by the user.

Matching equation for physical scales.—In order to connect the observed scales in the

⁴`CppTSample` is sign-aware when returning the mass-matrix eigenvalues, and so irrespective of if asked for m_i/H or m_i^2/H^2 , the negative values are preserved so it is easy to identify any tachyons in the mass spectrum.

CMB with the wavenumbers used in `CppTransport`, we need the matching equation [Liddle & Leach, 2003, Adshead et al., 2011, Mortonson et al., 2011] which gives the number of e -folds between the horizon exit time of the pivot scale $k_* [\text{Mpc}^{-1}]$ and the epoch of recombination when the CMB is produced. If we assume the universe instantaneously reheats to an energy density $\rho = \sigma T_{\text{reheat}}^4 = 10^{16} \text{ GeV}$, the matching equation is

$$N^{\text{IRH}}(k) = \ln\left(\frac{a_{\text{end}}}{a_k}\right) = 55.75 - \ln\left(\frac{k}{k_*}\right) - \ln\left(\frac{10^{16} \text{ GeV}}{V_k^{1/4}}\right) + \ln\left(\frac{V_k^{1/4}}{V_{\text{end}}^{1/4}}\right), \quad (3.26)$$

where k is some scale given in units of $[\text{Mpc}^{-1}]$, V_k is the value of the potential at the horizon-exit time of k and V_{end} is the potential value at the end of inflation. In Equation (3.26), the slow-roll approximation has been used to re-write factors of the Hubble parameter H in terms of the potential V using the equation $H^2 \approx V/3M_{\text{P}}^2$ which is an accurate estimation for single-field models. However for multi-field models, this approximation can become less accurate if any of the fields have a sufficiently large kinetic term with $G_{IJ}\partial_\mu\phi^I\partial^\mu\phi^J \approx V(\phi^I)$.

Therefore in our module, we use `CppTransport` to return the Hubble values during inflation and replace factors of $V^{1/4}$ with $(3H^2)^{1/4}$ to include all parts of the kinetic sector for these non-trivial models. We use $M_{\text{P}} = 1$ in the numerical implementation so that the reheating energy density is rewritten as $10^{16} \text{ GeV}/M_{\text{P}} = (2.435 \times 10^2)^{-1}$ which gives

$$\ln\left(\frac{k}{k_*}\right) = 55.75 - N^{\text{IRH}}(k) + \ln\left(243.5 \cdot 3^{1/4} H_k^{1/2}\right) + \ln\left(\frac{H_k^{1/2}}{H_{\text{end}}^{1/2}}\right), \quad (3.27)$$

where all quantities are evaluated in units where $M_{\text{P}} = 1$.

In `CppTSample`, the background solution for H is used in Equation (3.27) to find the physical scales corresponding with different exit times. `CppTransport` requires that the wavenumbers are written in terms of $a_k H_k$ for its own normalisation where all scales are divided by a scale k_{pre} exiting at a user-set time N_{pre} . We therefore exponentiate Equation (3.27) to find

$$k_{\text{phys}} = \left(\frac{3^{1/4} \cdot 243.5 k_* e^{55.75}}{a_{\text{end}} H_{\text{end}}^{1/2}}\right) a_k H_k, \quad (3.28)$$

where we can see that $k_{\text{phys}} \propto a_k H_k$ which implies there is a relation $k_{\text{phys}} = \gamma k_{\text{cppt}}$ with the constant set using the physical scale exiting at N_{pre} as $\gamma = k_{\text{phys}}[N_{\text{pre}}]$ when the `CppTransport` wavenumber is normalised to be $k_{\text{cppt}} = 1$. This method is used to calculate all the wavenumbers for each sample; we have checked this linear relationship matches the results of Equation (3.28). The exit-time of a physical scale is found using the `compute_Nexit_for_physical_k` function which uses bisection to return the number

of e -folds left until the end of inflation and is used to return the exit-time of the pivot scale N_{pivot} .

General reheating.—There is also an inherent uncertainty in $N(k)$ because the matching between physical scales depends on the post-inflationary reheating between the end of inflation and reheating when the inflaton field decays into standard model particles and the universe is rethermalised. The typical assumption [Adshead et al., 2011] [Mortonson et al., 2011] is that the universe evolves like matter until it reaches the reheating temperature T_{rh} where it becomes radiation-dominated until the epoch of matter-radiation equality. However the equation of state and the mechanism for the transfer of energy from the inflaton to the reheating energy density ρ_{rh} are unknown which corresponds to a shift ΔN relative to the instantaneous reheating pivot exit-time in equation (3.26). We account for this by using an additional MCMC sample parameter `Nsamples` which is added to the matching equation by setting it in the `[inflation_parameters]` section of the value and prior CosmoSIS files as follows

```
[inflation_parameters]
Nsamples = uniform 0 10
```

where the above example sets a uniform prior on N_{samples} between 0 and 10. Positive values⁵ should be chosen for N_{samples} to ensure the pivot scale exits the horizon *after* the instant reheating time with $N(k) < N^{\text{IRH}}$.

Integration tasks.—The first integration task constructed and executed by the `CppTSample` module is the two-point function pivot task, `tk2_piv`. This task contains 15 wavenumbers centred on the chosen k_{pivot} value in a log-spaced range $(1 - 0.007)k_{\text{pivot}} \leq k \leq (1 + 0.007)k_{\text{pivot}}$. This task is used to extract the observable A_s, A_t, r values at the pivot scale allowing for comparison between experimentally measured values.

Next, `CppTSample` constructs and integrates a much broader two-point function task `tk2`. As mentioned previously in Section 3.4.1, we are using a modified version of the CosmoSIS CLASS module that predicts the CMB spectrum based on a table of power spectrum values corresponding to different physical scales. `CppTSample` produces the requested physical scales with the number of points corresponding to the `k_samples` variables in the `[cppt_sample]` section in the CosmoSIS `.ini` run file. The default value of this is 400, as

⁵Negative values can be chosen for N_{samples} but these correspond with an exit time before the instantaneous reheating exit time and a non-standard equation of state which gives an accelerating expansion during reheating.

this ensures that CLASS is using a high-fidelity power spectrum. For long running models, this can be reduced to improve performance at the cost of numerical accuracy. The value of `k_samples` should not be set below 80 for CLASS to function correctly. The two-point function task that `CppTSample` creates is integrated over a range of 13 time samples between $N_{\text{end}} - 11.0$ and N_{end} so that we can extract the observable values from the end of inflation to ensure the initial conditions are correct for post-inflationary history. These time samples are also used to measure the dispersion in the power spectrum to account for inflation models that are unstable in their super-horizon evolution and so reject them from any analysis.

The two-point function integration results are given to CLASS as a temporary data file which allows for the full precision of the numerical results to be used by CLASS. We use our modified CLASS module which utilises the `external_Pk` feature and is used to return the CMB predictions based on the sample processed. The results from this are passed on to the `Planck2015` module to calculate the likelihoods with the results returned for each sample in a text file by `CosmoSIS`. This set-up allows for both the inflation parameters and the cosmological parameters to be explored simultaneously by our module provided enough MCMC samples have been requested.

Then, if requested, `CppTSample` sets up and integrates any of the three-point function tasks that have been requested in the `CosmoSIS .ini` run file. All three-point function integrations are run over the same 13 e -fold range at the end of inflation so that the observables extracted are computed at the end of inflation. The equilateral three-point function `tk3e` is constructed from an equilateral configuration with $k_t = 3k_{\text{pivot}}$, and is used to obtain values for B^{eq} and $f_{\text{NL}}^{\text{eq}}$. The squeezed three-point function `tk3s` is constructed with configuration $k_t = 3k_{\text{pivot}}$, $\alpha = 0$ and $\beta = 0.98$, and is used to obtain values for B^{sq} and $f_{\text{NL}}^{\text{sq}}$. Finally, the folded three-point function `tk3f` is constructed with configuration $k_t = 3k_{\text{pivot}}$, $\alpha = 0$ and $\beta = 0.005$ which is used to obtain values for B^{fold} and $f_{\text{NL}}^{\text{fold}}$.

Error checking.—In an MCMC run over inflation parameters, there are many reasons why an integration could fail or for numerical instabilities to cause the results to be unreliable. In either of these scenarios, the sampler needs to fail gracefully without cancelling the current sampling run while keeping a record of the reason for the failure if possible. Thus, `CppTSample` does its calculations in a `try-catch` block with exceptions specifically chosen to catch various error states that a sample may encounter.

If any of the spectrum values are varying significantly near to the end of inflation then we should conclude that either the chosen scale hasn't exited the horizon yet or that the

power spectrum has strong scale-dependence with a significant running of the spectral index. Hence we chose the time sample near the end of inflation to allow us to perform a dispersion test on the spectra values which is implemented using the `dispersion` class and calculates the coefficient of variation [Fienberg, 1970]. This measures the variability of values compared to the mean and our test fails when this is larger than 5%

$$\left(1 + \frac{1}{4n}\right) \frac{\sigma_{\text{spec}}}{\mu_{\text{spec}}} \geq 0.05, \quad (3.29)$$

where n is the number of time samples used, σ_{spec} is the standard deviation of the spectrum values, μ_{spec} is the mean of the spectrum values and the pre-factor in brackets ensures the estimate isn't biased. If the test is failed, the `time_varying_spectrum` exception is used to log when the spectrum values are varying and sets the variable `time_var_pow_spec` equal to one in the returned results.

Additionally, we use `CppTransport` exceptions to check whether there has been a failed integration due to the following reasons

- `no_end_inflate`: no end-time found for inflation,
- `neg_Hsq`: negative H^2 value found,
- `integrate_nan`: integration yielded NaN,
- `zero_massless`: zero massless time found,
- `neg_epsilon`: negative ϵ value found,
- `large_epsilon`: a value $\epsilon \geq 3$ was found,
- `neg_V`: negative value of $V(\phi^I)$ was found,
- `ics_before_start`: sampler gave initial conditions starting before $N_{\text{init}} = 0$,
- `runtime_exception`: generic `CppTransport` runtime exception (see terminal output).

If any of these exceptions are thrown during a sample, `CppTSample` records that there is an issue with the current sample and immediately ceases the calculations, moving onto another sample. The reason for this failure is printed to the terminal to help debug models that frequently trigger these warnings.

3.4.3 Full pipeline

In summary, a user simply needs to create a `CppTransport` model file describing the fields and parameters of a model, with any values or priors for sampling over, and how they combine to create the model's potential and optional field-space metric. From this `CppTransport`

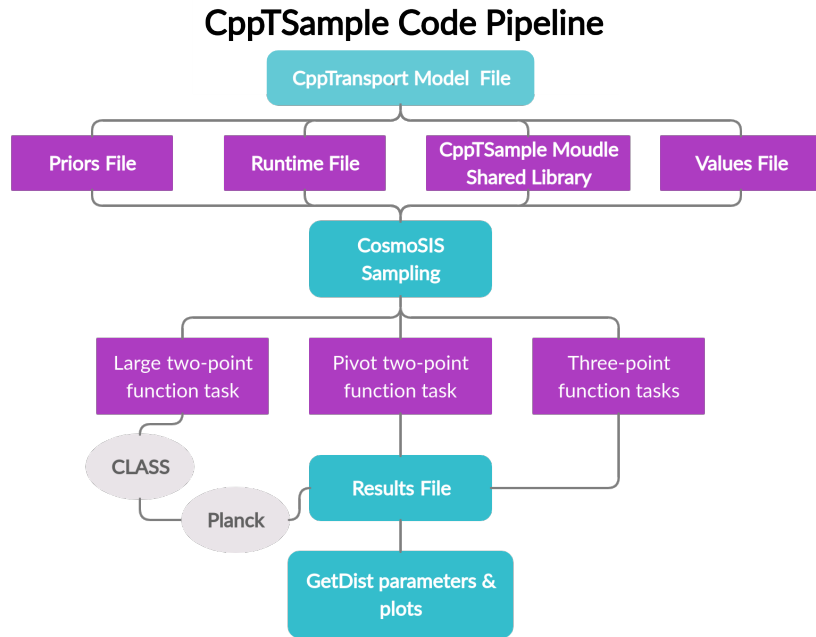


Figure 3.1: Diagram demonstrating the code pipeline used by CppTSample.

automatically generates all files needed for CosmoSIS sampling. Two 2-point function power spectra tasks and (optionally) three 3-point function bispectrum tasks are integrated. One of the power spectrum tasks solves over a wide range of wavenumbers which is used to compute the likelihoods based on Planck data whereas the other is used to measure r , n_s and n_t at a chosen pivot scale. The three bispectrum tasks are used to measure B and f_{NL} for equilateral, squeezed and folded triangle configurations all with perimeter $k_t = 3k_{\text{pivot}}$. The results for the MCMC chains are returned by CosmoSIS in a text file which can then be passed into our custom GetDist integration file which enables automatic generation of triangle covariance plots. The code pipeline can be seen diagrammatically in Figure 3.1.

3.5 Numerical results

In this section, we present results for several inflation models obtained with the CppTSample module. All plots and marginalised parameter constraints are found by passing results to the GetDist analysis program which is included as part of CosmoMC [Lewis & Bridle, 2002, Lewis, 2013]. All observable parameters are given for a pivot scale set to $k_{\text{pivot}} = 0.002 \text{ Mpc}^{-1}$ for comparison with Planck measurements and we set $M_{\text{P}} = 1$ throughout this section. Furthermore, we chose to only measure constraints on the equilateral bispectrum parameter ($f_{\text{NL}}^{\text{eq}}$) as the integration time is often long for squeezed and

Cosmological parameter	Planck 2015 values	Uniform prior ranges
$\Omega_c h^2$	0.1198 ± 0.0015	$0.095 \leq \Omega_c h^2 \leq 0.145$
$\Omega_b h^2$	0.02225 ± 0.00016	$0.019 \leq \Omega_b h^2 \leq 0.025$
h_0	0.6727 ± 0.0066	$0.6 \leq h_0 \leq 0.75$
τ	0.079 ± 0.017	$0.01 \leq \tau \leq 0.4$

Table 3.1: Planck 2015 cosmological parameters used for the cold dark matter density, baryon density, the reduced Hubble constant and the optical depth for CppTSample runs with the second column giving the values used when only inflation parameters are varied and the third column giving the uniform priors used for the full MCMC runs.

folded configurations⁶. The larger covariance plots that vary the cosmological parameters as well as the inflation model parameters are given in Appendix 3.7 to display them as clearly as possible.

MCMC runs.—We aimed to replicate the process of testing a new inflation model as much as possible despite using some well measured models. Initially, we use the `apriori` sampler [Foreman-Mackey et al., 2013] in CosmoSIS to explore the inflation model’s parameters with wide prior ranges whilst keeping the cosmological parameters ($\Omega_c h^2$, $\Omega_b h^2$, h_0 & τ as needed by CLASS) constant with the values given in the second column of Table 3.1. The values used are the best-fit Λ CDM Planck 2015 measurements [Aghanim et al., 2018] as their values are unlikely to differ significantly when sampling the cosmological parameters too. Typically the wide prior ranges will produce many samples with zero likelihood or give an integration error so we define *successful inflation* as a sample giving a likelihood above the CosmoSIS limit of $\ln(\mathcal{L}) = -1 \times 10^{30}$.

After finding the viable inflation model parameter ranges that give ‘successful’ inflation with a non-zero likelihood, we use each range to set the priors on a second run using the `Metropolis-Hastings` sampler [Metropolis et al., 1953] [Hastings, 1970] whilst also varying the cosmological parameters. This allows the inflation model to slightly vary the underlying cosmological model and hence ensure the maximum likelihood is found for that inflation model. The uniform priors used for the cosmological parameters are given in Table 3.1 where these are chosen to allow for a deviation from the corresponding Planck measurements without forcing them to be identical. We then cut 50% of the samples before giving covariance plots and marginalised constraints for all sampled and derived parameters in

⁶We demonstrate using squeezed and folded configurations in our forthcoming analysis of non-Gaussianities in D3-brane inflation [forthcoming].

each model and compare these with **Planck** constraints [Ade et al., 2016b] to determine the models that best describe CMB data.

Convergence criteria.—Evidently there is no requirement for convergence criteria for the parameter exploration runs with the apriori sampler because these are used to find viable parameter ranges for the Metropolis-Hastings data. For all MCMC runs using the Metropolis-Hastings sampler, we collect up to 200,000 samples/chain and require the Gelman-Rubin statistic [Gelman & Rubin, 1992] of the eigenvalues of the covariance matrix is $R \leq 1.01$ to declare convergence and in all models we use ≥ 10 chains/data-set with randomly assigned start positions for the single-field models and set start positions for the multi-field models. The R values returned by **CosmoSIS** for each sampled parameter are given for each model with the marginalised constraints and maximum likelihood values and we provide trace plots of $\ln(\mathcal{L})$ against sample number for each model in Appendix 3.8.

CMB data.—Every inflation model analysed uses the Planck 2015 likelihood codes⁷ [Aghanim et al., 2016] as it is packaged with **CosmoSIS** which returns the likelihood to the `likelihoods/planck2015_like` part of the datablock. For the initial run with the apriori sampler, we use the `commander` TT CMB data in the multipole range $2 \leq \ell < 30$ and the `plik_lite` TT data for the multipole range $30 \leq \ell \leq 2508$. The Metropolis-Hastings sampler run uses the full CMB polarisation data with the TT, EE, BB and TE likelihoods for the multipoles $2 \leq \ell < 30$ returned by the `bflike` library and the TT, TE, and EE likelihood for the multipoles $30 \leq \ell \leq 2508$ returned by the `plik_lite` library. We did not use the lensed power spectrum data or the Bicep-Keck-Planck (BKP) data [Ade et al., 2015]. Therefore our results will be most similar to the TT,TE,EE+lowP Planck 2015 results with less constraining power in the tensor to scalar ratio r due to the lack of BKP data.

3.5.1 Quartic inflation

Initially we analysed the single-field, quartic model of inflation [Linde, 1983] with the potential given by

$$V(\phi) = \frac{1}{4}\lambda\phi^4, \quad (3.30)$$

where the initial field value used was $\phi_i = 35.0$ which caused inflation to end after $N_{\text{end}} = 153.7$ e-folds.

⁷See the Planck PLA 2015 Wiki page for full details of all likelihood codes.

Initial parameter exploration.— In this model, the only sampled parameters are λ and N_{samples} because λ controls the amplitude of the scalar and tensor power spectra with some dependence on the pivot-scale exit-time. We therefore set a log-uniform prior on λ in the range $-14.4 \leq \log_{10}(\lambda) \leq -13.2$ and a uniform prior on N_{samples} in the range $0 \leq N_{\text{samples}} \leq 10$ to explore pivot exit-times after the instantaneous reheating (IRH) exit-time which is $N_{\text{piv}}^{(\text{IRH})} = 58.4$ e-folds before N_{end} . For each set of sample parameters, we find the power spectrum values at 200 log-spaced scales in the range $10^{-6} \text{ Mpc}^{-1} \leq k \leq 50 \text{ Mpc}^{-1}$ for CLASS to compute the CMB power spectrum from.

The CosmoSIS apriori sampler was then used to sample from the prior distributions where we were able to find 142,066 samples that gave successful inflation with a non-zero likelihood. These results can be seen in Figure 3.2 where we see the observables are determined using λ and the pivot exit-time N_{piv} where the power spectrum values A_s and A_t are both linearly dependent on λ and the n_s , n_t , r and $f_{\text{NL}}^{\text{eq}}$ observables depend linearly on N_{piv} . The central values $n_s \simeq 0.942$, $n_t \simeq -0.038$, $r \simeq 0.30$ and $f_{\text{NL}}^{\text{eq}} \simeq 0.038$ are all in good agreement with the slow-roll predictions for this well-tested model.

Marginalised constraints.—We used the constraints from the parameter exploration run to set the prior on λ as a log-uniform distribution in the range $-14.299 \leq \log_{10}(\lambda) \leq -13.4$ alongside the extra priors on the cosmological parameters given in Table 3.1. We then ran the Metropolis-Hastings sampler with 10 chains starting from randomly assigned starting positions which almost passed our convergence criteria with the worst Gelman-Rubin value being $R = 1.0102$ after 200,000 samples/chain to give a total of 2,000,000 samples. The marginalised constraints, best-fit values and Gelman-Rubin values are given in Table 3.2 with the covariance and convergence plots given in Figures 3.6 and 3.10 respectively.

Discussion.—From the marginalised parameters $n_s = 0.9454$ and $r = 0.2829$ in Table 3.2, we can see that the quartic model is incompatible with the Planck CMB constraints [Ade et al., 2016b] where n_s differs from $n_s = 0.968 \pm 0.006$ by -3.8σ and the r value is well above the limit $r_{0.002} < 0.11$. This model being disfavoured by CMB data has been well known since the WMAP releases but remains a valuable check on the results from our code. Moreover the constraints for n_s , n_t , r and $f_{\text{NL}}^{\text{eq}}$ are consistent with the slow-roll predictions for single-field models.

The incompatibilities with CMB data are also in the cosmological parameters $\Omega_c h^2 = 0.1257$, $\Omega_b h^2 = 0.02110$, $h_0 = 0.6458$ and $\tau = 0.051$ in Table 3.2 which differ from the Planck 2015 values given in Table 3.1 by $+3.9\sigma$, -7.2σ , -4.1σ and -1.6σ respectively. While it is unsurprising that these values differ because the cosmological parameters will

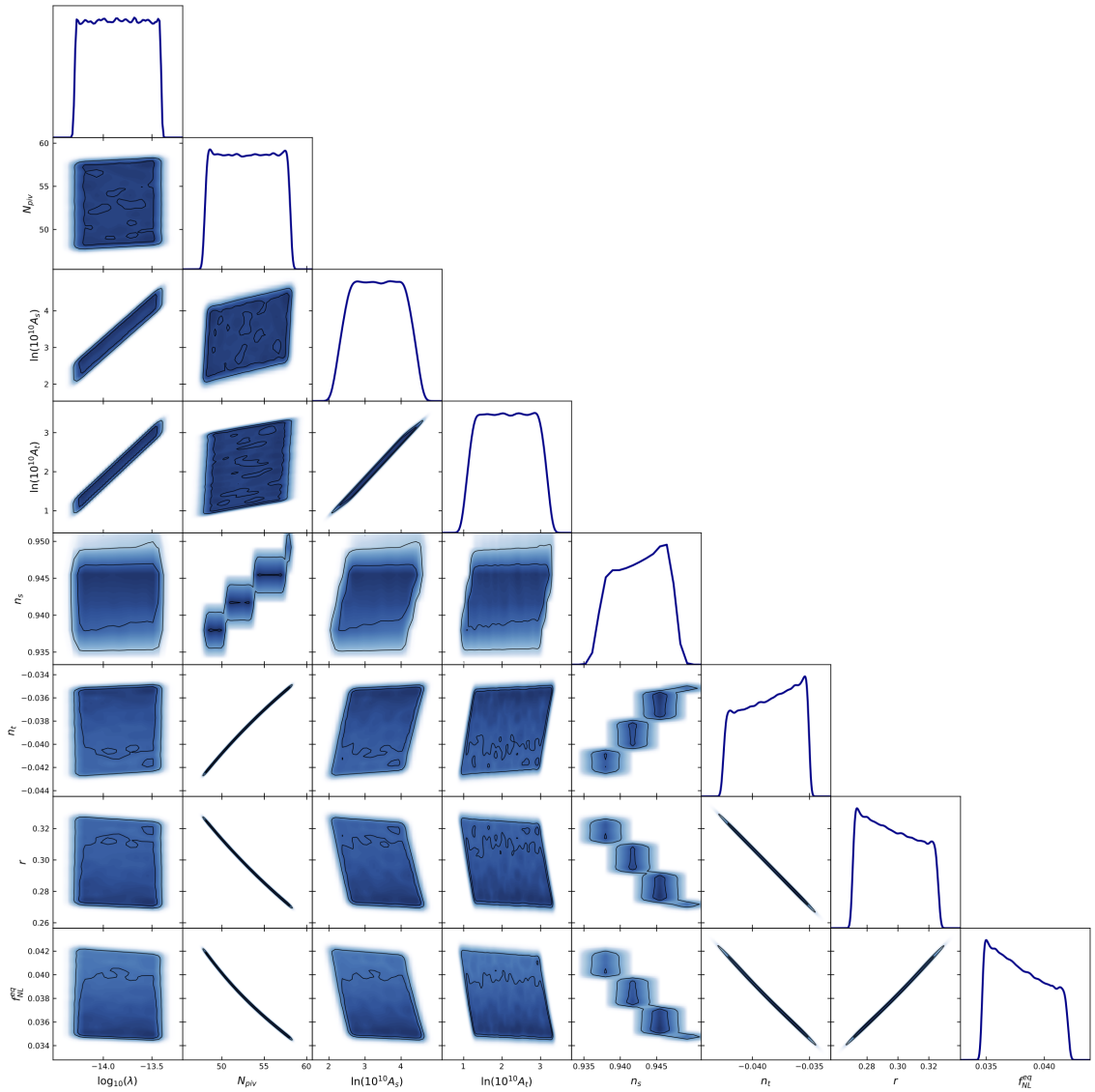


Figure 3.2: Covariance plots of $\log_{10}(\lambda)$, N_{piv} , $\ln(10^{10} A_s)$, $\ln(10^{10} A_t)$, n_s , n_t , r and $f_{\text{NL}}^{\text{eq}}$ for the chaotic quartic inflation model as returned by the apriori sampler on Planck 2015 TT data.

Parameter	68% limits	Best-fit values	R-values
$\log_{10}(\lambda)$	$-13.965^{+0.027}_{-0.062}$	-14.0226	1.0087
N_{piv}	$55.6^{+2.4}_{-0.68}$	57.9236	1.0102
$\Omega_c h^2$	$0.1257^{+0.0011}_{-0.0012}$	0.124987	1.0064
$\Omega_b h^2$	0.02110 ± 0.00013	0.0211662	1.0060
h_0	0.6458 ± 0.0050	0.648864	1.0079
τ	0.051 ± 0.019	0.051915	1.0008
$\ln(10^{10} A_s)$	3.223 ± 0.038	3.21556	–
$\ln(10^{10} A_t)$	$1.959^{+0.045}_{-0.062}$	1.91113	–
n_s	$0.9454^{+0.0024}_{-0.00060}$	0.947661	–
n_t	$-0.0367^{+0.0016}_{-0.00041}$	-0.0351432	–
r	$0.2829^{+0.0030}_{-0.012}$	0.271327	–
f_{NL}^{eq}	$0.03616^{+0.00036}_{-0.0015}$	0.0347216	–

Table 3.2: Marginalised 68% limits with best-fit values and Gelman-Rubin values for the quartic model returned by the Metropolis-Hastings sampler on the Planck 2015 TT+TE+EE+lowP likelihood with sampled parameters in bold.

adjust to compensate for the power spectrum produced by the inflation model, the deviations are the largest of any model making quartic inflation the least favourable model here.

3.5.2 Quadratic inflation

Next we analysed single-field, chaotic quadratic inflation [Linde, 1983] with the potential

$$V(\phi) = \frac{1}{2}m^2\phi^2, \quad (3.31)$$

where the initial field value used was $\phi_i = 25.0$ which causes inflation to end after $N_{\text{end}} = 157.3$ e-folds.

Initial parameter exploration.— In this model, the only parameters to sample are the parameter m in the potential and the exit-time N_{samples} because these determine the power spectrum amplitudes and observables similarly to the quartic model. We therefore set a log-uniform prior distribution on m in the range $-6.5 \leq \log_{10}(m) \leq -5$ and a uniform prior distribution on N_{samples} in the range $0 \leq N_{\text{samples}} \leq 10$ to explore the pivot exit-time after the IRH exit-time of $N_{\text{piv}}^{(\text{IRH})} = 57.2$ e-folds before N_{end} . For each set of sample parameters, we find the A_s and A_t values at 200 log-spaced scales in the range $10^{-6} \text{ Mpc}^{-1} \leq k \leq 50 \text{ Mpc}^{-1}$ for CLASS to compute the CMB power spectrum from.

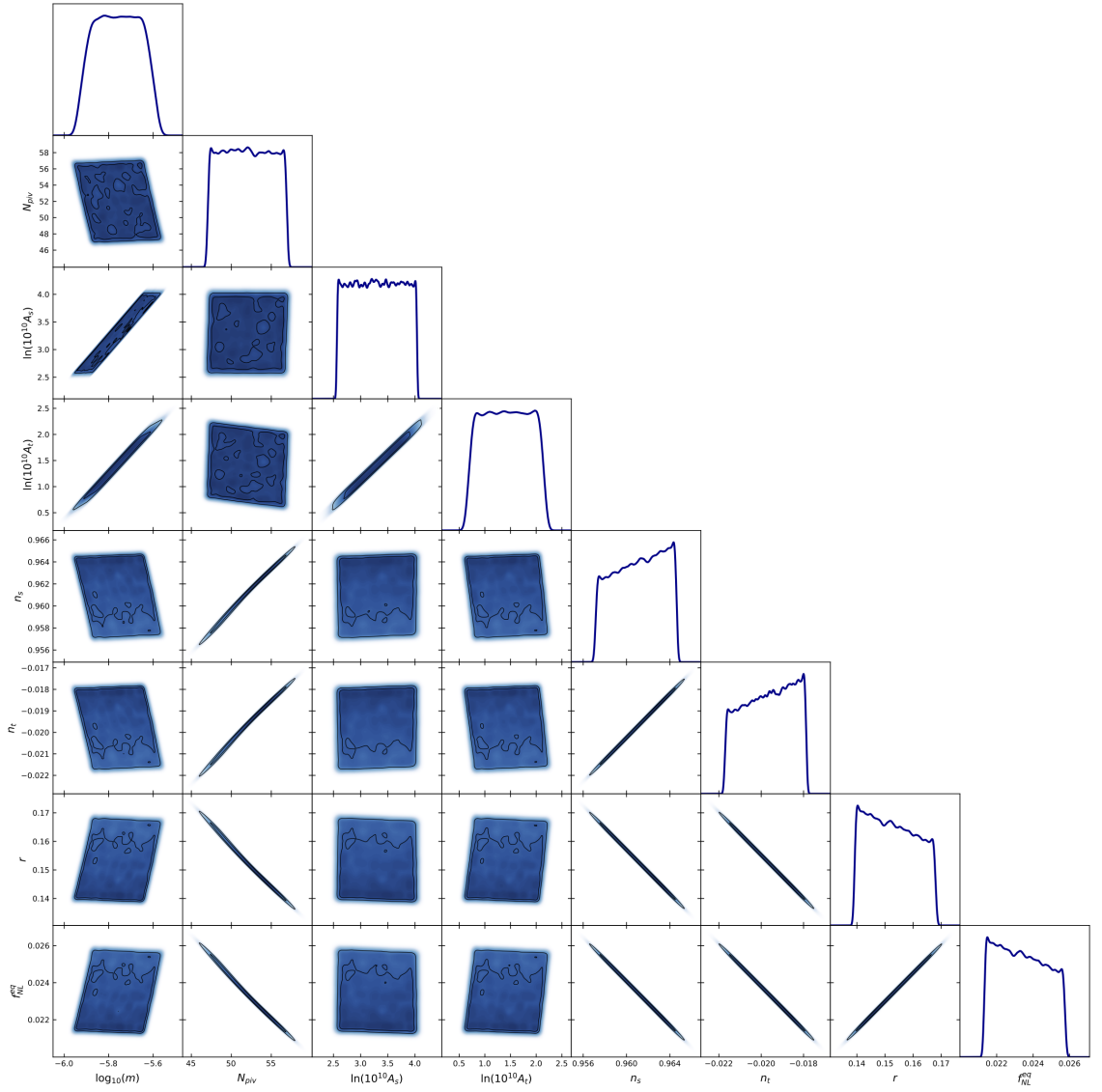


Figure 3.3: Covariance plots of $\log_{10}(m)$, N_{piv} , $\ln(10^{10} A_s)$, $\ln(10^{10} A_t)$, n_s , n_t , r and $f_{\text{NL}}^{\text{eq}}$ for the chaotic quadratic inflation model returned by the apriori sampler on Planck 2015 TT data.

Parameter	68% limits	Best-fit values	R-values
$\log_{10}(m)$	$-5.762^{+0.025}_{-0.012}$	-5.7414	1.009
N_{piv}	$49.29^{+0.51}_{-2.3}$	47.0134	1.010
$\Omega_c h^2$	0.1220 ± 0.0011	0.122289	1.006
$\Omega_b h^2$	0.02132 ± 0.00014	0.0212787	1.004
h_0	0.6613 ± 0.0049	0.659705	1.007
τ	0.059 ± 0.021	0.0561435	1.004
$\ln(10^{10} A_s)$	3.185 ± 0.041	3.18656	–
$\ln(10^{10} A_t)$	$1.356^{+0.068}_{-0.049}$	1.40357	–
n_s	$0.95904^{+0.00049}_{-0.0019}$	0.957114	–
n_t	$-0.02073^{+0.00025}_{-0.0010}$	-0.021725	–
r	$0.1607^{+0.0075}_{-0.0019}$	0.168134	–
f_{NL}^{eq}	$0.0246^{+0.0011}_{-0.00029}$	0.0257735	–

Table 3.3: Marginalised 68% limits with best-fit values and Gelman-Rubin values for the quadratic model returned by the Metropolis-Hastings sampler on the Planck 2015 TT+TE+EE+lowP likelihood with sampled parameters in bold.

The CosmoSIS apriori sampler was then used to obtain 200,000 samples where 91,381 successfully inflating samples were found with a non-zero likelihood. These results can be seen in Figure 3.3. Here we can see the mass of the field m determines the power spectrum amplitudes A_s and A_t with an increase in the viable values caused by later pivot exit-times with smaller values of N_{piv} . The pivot exit-time also determines the values of n_s , n_t , r and f_{NL}^{eq} where an earlier exit-time gives larger values of n_s and n_t and smaller values of r and f_{NL}^{eq} . As expected the central values $n_s \simeq 0.960$, $n_t \simeq -0.020$, $r \simeq 0.155$ and $f_{NL}^{eq} \simeq 0.024$ are all in good agreement with the slow-roll predictions for this well-tested model.

Marginalised constraints.—The results found from the parameter exploration run were used to set the prior on m as a log-uniform distribution from the previously found lower- and upper-limits in the range $-5.97 \leq \log_{10}(m) \leq -5.5$ with the priors on the cosmological parameters set using Table 3.1. We then ran the Metropolis-Hastings sampler with 15 chains starting from randomly assigned values which passed our convergence criteria after 177,080 samples per chain giving a total of 2,656,200 samples. The marginalised constraints, best-fit values and Gelman-Rubin values are given in Table 3.3 with the covariance and convergence plots given in Figures 3.7 and 3.11 respectively.

Discussion.—As seen from the marginalised parameters in Table 3.3, the quadratic model

gives results for $n_s = 0.95904$ and $r = 0.01607$ which disagree with the Planck 2015 constraints by -1.5σ for $n_s = 0.968 \pm 0.006$ and a value well above the limit $r_{0.002} < 0.11$. These values are closer than the quartic model seen in §3.5.1 so this model is favoured in comparison, the single-field quadratic potential is effectively ruled out based on Planck data. While both of these conclusions are well known for this model [Ade et al., 2016b] [Akrami et al., 2018], this is still a valuable test of our code. Moreover, our constraints on n_s and r match the slow-roll estimations based on the exit-time of the pivot scale and we are able to give constraints on the equilateral bispectrum based on an MCMC analysis.

Despite the incompatibility of the power spectrum observables with CMB data, we compare the cosmological constraints $\Omega_c h^2 = 0.1220$, $\Omega_b h^2 = 0.02132$, $h_0 = 0.6613$ and $\tau = 0.059$ in Table 3.3 with the Planck 2015 constraints in Table 3.1 which differ by $+1.5\sigma$, -5.8σ , -1.7σ and -1.2σ respectively. All of these parameters differ by at least 1.5σ which is because they would have been adjusted by the sampler to attempt to compensate for the incompatible power spectrum values. Although these results suggest that single-field inflation models with a monomial potential are not possible, there are smaller-order potentials [Silverstein & Westphal, 2008] and hilltop models [Boubekeur & Lyth, 2005] that are still compatible with data [Akrami et al., 2018].

3.5.3 α -attractor inflation

Achúcarro et al. proposed an α -attractor inflation model in [Achúcarro et al., 2017] where inflation is produced by a complex scalar field $Z = \rho e^{i\theta}$ which is decomposed into two fields with a radial component $\rho = \tanh(\phi/2)$ and an angular component θ . These fields are embedded on a hyperbolic manifold in field-space that originates from either a maximal $\mathcal{N} = 4$ superconformal symmetry or a $\mathcal{N} = 8$ supergravity. The hyperbolic field-space causes the multi-field model to give the same results for n_s and r as single-field α -attractors which means the cosmological predictions made from α -attractors have ‘universal’ predictions for n_s , r and f_{NL} which are given in terms of the pivot exit time N_* as

$$n_s \simeq 1 - \frac{2}{N_*}, \quad (3.32a)$$

$$r \simeq \frac{4}{N_*^2}, \quad (3.32b)$$

$$f_{\text{NL}} \simeq \frac{5}{6N_*}. \quad (3.32c)$$

Therefore this is an ideal candidate model to demonstrate the capacity for `CppTSample` to apply MCMC sampling to non-canonical inflation models and extract the optimal inflation parameters with the corresponding best-fit CMB observables that should correspond with

the universal predictions in equation (3.32). The potential is defined as

$$V(\phi, \theta) = V_0 \tanh^2\left(\frac{\phi}{\sqrt{2}}\right) \left[1 + 2A \cos(2\theta) \tanh^2\left(\frac{\phi}{\sqrt{2}}\right)\right], \quad (3.33)$$

and the field-metric is defined as

$$G_{IJ}(\phi, \theta) = \begin{pmatrix} 1 & 0 \\ 0 & \frac{1}{2} \sinh^2(\sqrt{2}\phi) \end{pmatrix}, \quad (3.34)$$

where the rows and columns are in the order (ϕ, θ) . The initial field values used were $\phi_i = 5.0$ and $\theta_i = 0.4$ which caused inflation to last for approximately $N_{\text{end}} \simeq 156$ e-folds where the inclusion of multiple fields now causes N_{end} to vary via the extra parameter in the potential (3.33) and the field-metric (3.34).

Initial parameter exploration.—The sampled parameters in this model are the Lagrangian parameters V_0 and A as well as the pivot exit-time via N_{samples} . We therefore set a log-uniform prior on V_0 in the range $-13 \leq V_0 \leq -11$ and a uniform prior on A in the range $0.1 \leq A \leq 0.3$ as well as a uniform prior on N_{samples} in the range $0 \leq N_{\text{samples}} \leq 10$ to explore the pivot exit-times after the IRH time of $N_{\text{piv}}^{(\text{IRH})} = 55.0$ e-folds before N_{end} . For each sample, we found the A_s and A_t values at 125 log-spaced scales in the range $10^{-6} \text{ Mpc}^{-1} \leq k \leq 50 \text{ Mpc}^{-1}$ for CLASS to compute the CMB power spectrum from.

The CosmoSIS apriori sampler was then used to sample from these prior distributions where 63,927 samples gave successful with a non-zero likelihood. These results can be seen in Figure 3.4 where we can see that V_0 modulates the amplitudes of the two spectra A_s & A_t whereas the parameter A controls the observable values n_s , n_t , r and $f_{\text{NL}}^{\text{eq}}$. The central values $n_s \simeq 0.963$, $n_t \simeq -3 \times 10^{-4}$, $r \simeq 0.0014$ and $f_{\text{NL}}^{\text{eq}} \simeq 0.0155$ are all in excellent agreement with the corresponding Planck parameter constraints.

Marginalised constraints.—The results from the apriori sampler were used to reduce the log-uniform prior range on V_0 to $-12.0 \leq V_0 \leq -11.0$ and to expands the uniform prior range on A as $0.01 \leq A \leq 0.3$. The Metropolis-Hastings sampler was then ran with 15 chains with the starting values set as $\log_{10}(V_0) = -11.5$, $A = 0.15$, $N_{\text{samples}} = 0$ and the cosmological parameter values in Table 3.1. We obtained 200,000 samples per chain giving a total of 3,000,000 samples which almost passed our convergence criteria where the marginalised constraints, best-fit values and Gelman-Rubin values are given in Table 3.4 with the covariance and convergence plots given in Figures 3.8 and 3.12 respectively.

Discussion.—From the marginalised parameters in Table 3.4, we can see that the alpha-attractor model gave values for n_s and r that are well within the constraints $n_s = 0.968 \pm 0.006$ and $r_{0.002} < 0.11$. Moreover the constraint on $f_{\text{NL}}^{\text{eq}}$ is well within 1σ of the Planck

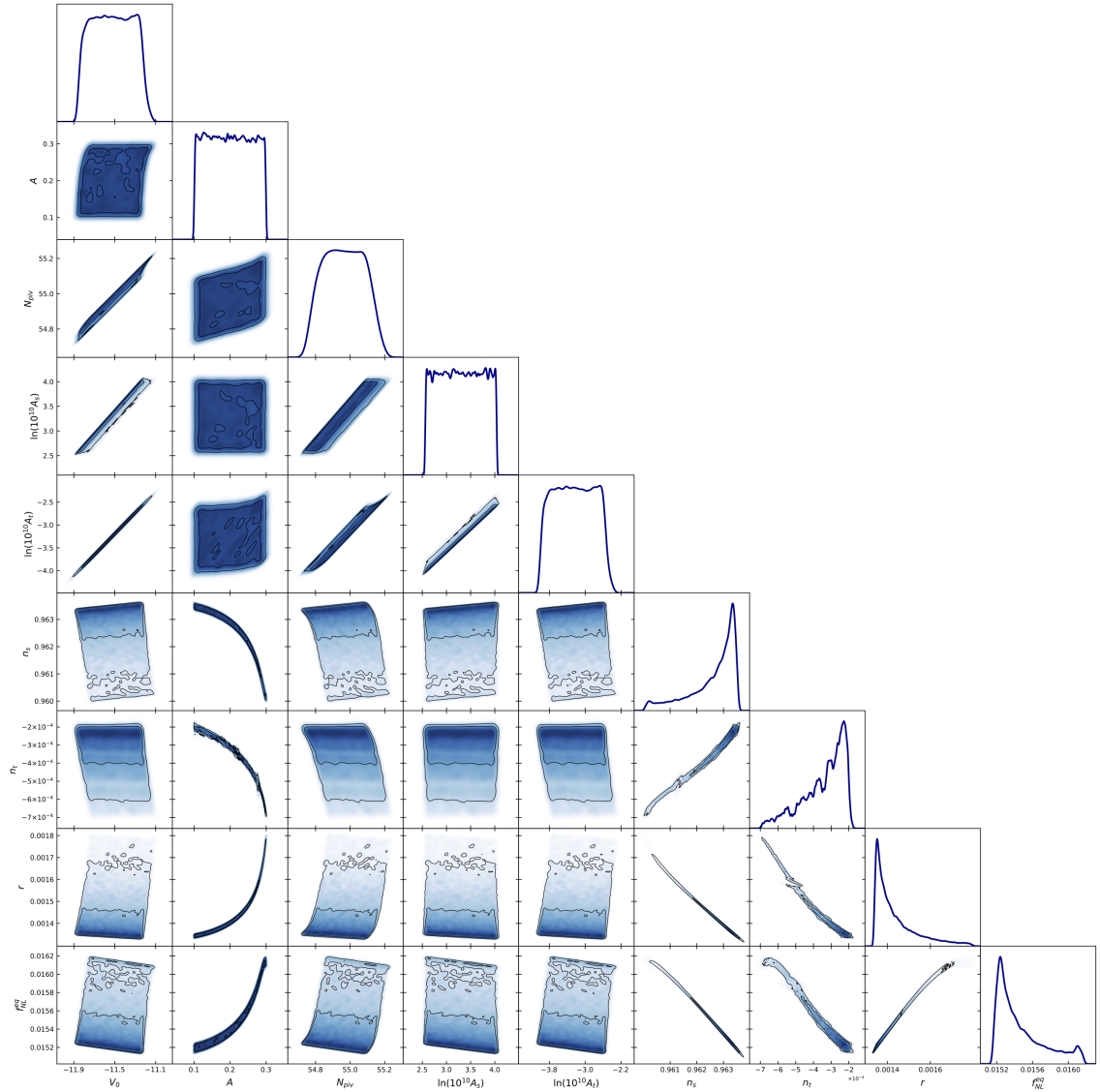


Figure 3.4: Covariance plots for the parameters $\log_{10}(V_0)$, A , N_{piv} , $\ln(10^{10} A_s)$, $\ln(10^{10} A_t)$, n_s , n_t , r and $f_{\text{NL}}^{\text{eq}}$ in the alpha-attraction inflation model as returned by the apriori sampler on Planck 2015 TT data.

Parameter	68% limits	Best-fit values	R-values
$\log_{10}(\mathbf{V}_0)$	$-11.573^{+0.032}_{-0.054}$	-11.4831	1.016
\mathbf{A}	$0.194^{+0.11}_{-0.043}$	0.296911	1.014
N_{piv}	54.932 ± 0.050	55.0137	1.005
$\Omega_c h^2$	0.1210 ± 0.0010	0.121904	1.003
$\Omega_b h^2$	0.02138 ± 0.00013	0.0213269	1.001
h_0	0.6656 ± 0.0045	0.661804	1.002
τ	0.061 ± 0.021	0.0595623	1.001
$\ln(10^{10} A_s)$	3.175 ± 0.042	3.18031	–
$\ln(10^{10} A_t)$	$-3.360^{+0.066}_{-0.11}$	-3.16871	–
n_s	0.9624 ± 0.0010	0.960202	–
n_t	$-0.00036^{+0.00019}_{-0.00010}$	-0.000643348	–
r	0.00146 ± 0.00012	0.00174845	–
f_{NL}^{eq}	$0.01552^{+0.00063}_{-0.00037}$	0.0161446	–

Table 3.4: Marginalised 68% limits with best-fit values and Gelman-Rubin values on the parameters in the alpha-attractor model as returned by the Metropolis-Hastings sampler on the Planck 2015 TT+TE+EE+lowP likelihood (sampled parameters in bold).

equilateral bispectrum constraint $f_{NL}^{eq} = -4 \pm 43$. We also compare the cosmological parameters with the constraints given in Table 3 of the Planck 2015 inflation constraints paper [Ade et al., 2016b] where our values for $\Omega_c h^2$, $\Omega_b h^2$, h_0 and τ differ by 0.8σ , -5.4σ , -1.1σ and -1.1σ respectively. Most of these are within approximately 1.1σ of the Planck data apart from $\Omega_b h^2$ but it is typical for the inflation model to have some effect on the cosmological parameters.

We now use the marginalised values in Table 3.4 to compare our data with the estimations given in equation (3.32). The estimations at the pivot exit-time $N_{piv} = 54.932$ give $n_s \simeq 0.9636$, $r \simeq 0.00133$ and $f_{NL} \simeq 0.001517$ which differ from the corresponding values in Table 3.4 by +0.12%, -8.90% and -2.25% respectively. The equivalent differences between the best-fit values in Table 3.4 are +0.35%, -24.4% and -6.17% respectively. Clearly the best predictions are for n_s and f_{NL} where we can consistently expect the predictions to be within 2 significant figure of the calculated values but the r value can differ by more than 10%. This is the first time the universality prediction [Achúcarro et al., 2017] for the bispectrum of α -attractors has been checked using an MCMC analysis as we have done. We also note that the equilateral bispectrum f_{NL}^{eq} has a very sharply defined constraint which potentially makes it an excellent candidate model to search for in future surveys if

it will ever be possible to measure $f_{\text{NL}} \simeq \mathcal{O}(10^{-1})$.

These conclusions were found despite not reaching the $R < 1.01$ convergence criteria with the worst values given as 1.016 for the $\log_{10}(V_0)$ parameter and 1.014 for the A parameter. The failure to converge was due to the strong dependence on the V_0 and A parameters in the potential (3.33) which meant that after 160,000 samples we initially reached $R \simeq 1.01$ for all parameters. Subsequently a change in the R value for one of these parameters was then countered by a change in R for the other parameter which could mean the $R < 1.01$ test is too strict for some multi-field models. Despite this our trace plot in Figure 3.12 and the R values being so close to 1.01 suggests we still have good convergence in this model.

3.5.4 Gelaton/QSFI inflation

Next, we studied a gelaton-like scenario [Tolley & Wyman, 2010] with the model defined in [Dias et al., 2016] where there is a light adiabatic field rotating on a circular trajectory. This field is dressed by the fluctuations of a heavier orthogonal field whose value tracks the minimum of the effective potential resulting in the two-field model behaving as if it has one field similarly to quasi-single field inflation [Chen & Wang, 2010]. The model is difficult to perform an MCMC analysis with since it has a large number of sampled parameters as well as an integration time that is typically longer than the other models seen here. Therefore it is an excellent example to demonstrate `CpptSample`'s parameter estimation capabilities on a complex model with a non-trivial field space metric.

In this model, the angular field θ is the adiabatic, light mode and the radial field R is the heavier mode with a potential defined as

$$V(R, \theta) = V_0 \left(1 + \alpha\theta + \frac{1}{2}\eta_R(R - R_0)^2 + \frac{1}{3!}g_R(R - R_0)^3 + \frac{1}{4!}\lambda_R(R - R_0)^4 \right), \quad (3.35)$$

and a field-metric given as

$$G_{IJ}(R, \theta) = \begin{pmatrix} 1 & 0 \\ 0 & R^2 \end{pmatrix}, \quad (3.36)$$

with the rows and the columns given in the order (R, θ) . The initial field values were set to be $R_i = 2.325$ and $\theta_i = 4.3$ which typically caused inflation to last for $N_{\text{end}} \simeq 101$ e-folds where there is a small variation due to including multiple fields similarly to the α -attractor model.

MCMC analysis and marginalised constraints.—In order to account for the slow integration time, we didn't do the parameter exploration run and instead perform the Metropolis-Hastings using 15 chains with start values based on our previous work with this model

Parameter	Start values	Uniform prior range
V_0	-10	$-11 \leq \log_{10}(V_0) \leq -9$
R_0	2.325	$2.25 \leq R_0 \leq 2.4$
η_R	0.6	$0.5 \leq \eta_R \leq 0.7$
g_R	100000	$99900 \leq g_R \leq 100100$
λ_R	5.6×10^7	$5.5 \times 10^7 \leq \lambda_R \leq 5.7 \times 10^7$
α	0.55	$0.5 \leq \alpha \leq 0.6$

Table 3.5: The start-values and priors used for the Gelaton/QSF1 model described in Equations (3.35) & (3.36).

[Butchers & Seery, 2018]. The priors and starting values are given for the Lagrangian parameters in Table 3.5 and for the cosmological parameters in Table 3.1. A uniform prior was set on N_{samples} in the range $0 \leq N_{\text{samples}} \leq 10$ with a starting value of $N_{\text{samples}} = 10$ to explore the pivot exit-times after the IRH time of $N_{\text{piv}}^{(\text{IRH})} = 56.2$ e-folds before N_{end} .

The power spectrum amplitudes A_s and A_t were computed over 80 log-spaced k values between 10^{-6} Mpc^{-1} and 50 Mpc^{-1} and we did not compute the 3-point function for this model. Instead we will use the optimal values given from the Planck likelihood by `CppTSample` to calculate the bispectrum separately using `CppTransport`. Our convergence criteria was passed after 60,320 samples per chain to give a total of 904,800 samples with the marginalised constraints, best-fit values and Gelman-Rubin values given in Table 3.6 as well as the covariance and convergence plots given in Figures 3.9 and 3.13 respectively.

Discussion.—In this model, we have found constraints by sampling 11 different parameters to produce the constraints on the power spectrum observables A_s , A_t , n_s , n_t and r . This further demonstrates that `CppTSample` can perform an MCMC analysis on models with a non-canonical field space and a potential with a large number of free parameters. The covariance plot in Figure 3.13 shows that the power spectrum observables are almost entirely determined by the values of V_0 and the pivot scale exit-time N_{piv} which implies the fit to power spectrum data is controlled by the leading terms of the potential (3.35). The constraints $n_s = 0.96847$ and $r = 0.0832$ in Table 3.6 are well within 1σ of the Planck 2015 constraints $n_s = 0.968 \pm 0.006$ and $r_{0.002} < 0.11$.

The cosmological parameter constraints $\Omega_c h^2 = 0.1195$, $\Omega_b h^2 = 0.02147$, $h_0 = 0.6723$ and $\tau = 0.066$ deviate from the Planck 2015 values given in Table 3.1 by -0.2σ , -4.9σ , -0.1σ and -0.8σ respectively. Again most of these with the exception of $\Omega_b h^2$ lie com-

Parameter	68% limits	Best-fit values	R-values
$\log_{10}(V_0)$	$-10.201^{+0.031}_{-0.023}$	-10.1905	1.004
R_0	2.325 ± 0.014	2.304	1.008
η_R	0.570 ± 0.029	0.550855	1.008
g_R	$(1.00001 \pm 0.00058) \cdot 10^5$	99972.1	1.010
λ_R	$(5.600 \pm 0.057) \cdot 10^7$	$5.56927 \cdot 10^7$	1.006
α	$0.5594^{+0.0081}_{-0.018}$	0.570577	1.010
N_{piv}	$47.78^{+0.27}_{-1.5}$	46.3132	1.007
$\Omega_c h^2$	0.1195 ± 0.0010	0.119695	1.004
$\Omega_b h^2$	0.02147 ± 0.00014	0.0214656	1.002
h_0	0.6723 ± 0.0045	0.671279	1.004
τ	0.066 ± 0.022	0.0671299	1.006
$\ln(10^{10} A_s)$	3.159 ± 0.044	3.16649	–
$\ln(10^{10} A_t)$	$0.673^{+0.057}_{-0.047}$	0.710462	–
n_s	$0.96847^{+0.00021}_{-0.00098}$	0.967507	–
n_t	$-0.010684^{+0.000075}_{-0.00034}$	-0.0110162	–
r	$0.0832^{+0.0026}_{-0.00054}$	0.0857748	–

Table 3.6: Marginalised 68% limits with best-fit values and Gelman-Rubin values on the parameters in the Gelaton/QSFI model as returned by the Metropolis-Hastings sampler with the Planck 2015 TT+TE+EE+lowP likelihood (sampled parameters in bold).

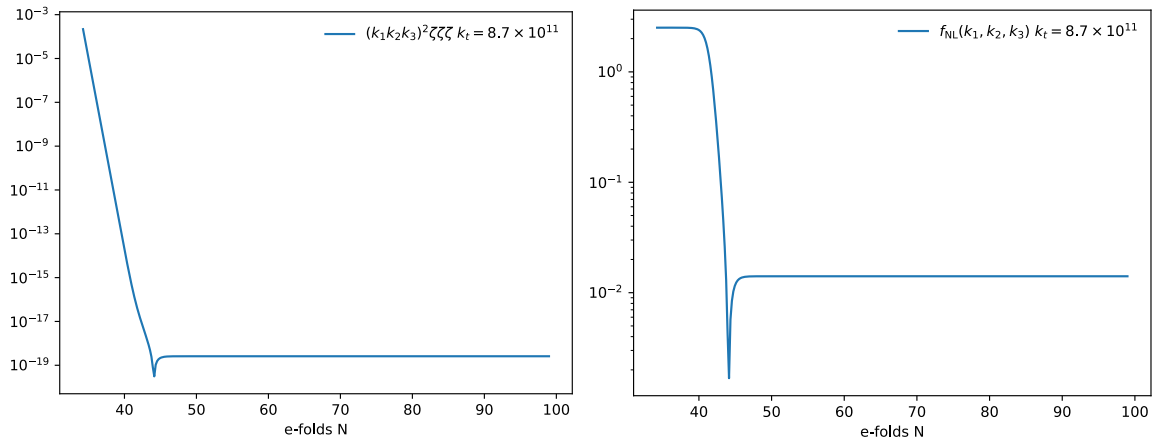


Figure 3.5: Two plots showing the bispectrum given by the Gelaton/QSFI model with parameters set from the values in Table 3.6. Left: dimensionless bispectrum (3.22) and right: reduced bispectrum (3.24) both for an equilateral configuration with $k_t = 3 \times 0.002 \text{ Mpc}^{-1}$.

fortably within 1σ of the Planck values which implies this model requires less adjustment of the cosmological parameters compared with other shown here.

Overall this model produces constraints that are highly compatible with current Planck constraints which means that Gelaton/QSFI inflation is favourable based on CMB data. We can further test the compatibility with CMB data by computing the bispectrum observables given by the best-fit parameters given in Table 3.6 with CppTransport. These parameters give the bispectrum plots seen in Figure 3.5 where the bispectrum values can be found from the `sqlite` databases stored by CppTransport which are $B^{\text{eq}} = 2.58 \times 10^{-19}$ and $f_{\text{NL}}^{\text{eq}} = 0.0141$ respectively in Figure 3.5. This demonstrates that estimations of the bispectrum can be found from MCMC results given by CppTSample despite using a model with a long integration time.

3.6 Conclusions

We have presented CppTSample, a new C++ module implemented using CosmoSIS, CppTransport and CLASS which applies MCMC sampling to find inflation parameter constraints based on the agreement with CMB data for models with a non-trivial field-space. Furthermore, these constraints are found by passing the *numerical* form of the primordial power spectrum with the `external_Pk` feature of CLASS so that all features of the power spectrum produced by an inflation model are accounted for when computing the likelihood. Additionally, the module uses CppTransport to compute the bispectrum observables, B and f_{NL} , for equilateral, squeezed and folded configurations allowing for an inflation paradigm to be

constrained based on the three-point statistics given from the best-fit to the CMB power spectrum.

This functionality is demonstrated with four different inflation models of varying complexity. We successfully reproduced all of the slow-roll predictions for the well constrained quartic and quadratic single-field models in Sections 3.5.1 & 3.5.2 where we gave equilateral bispectrum constraints produced by the Planck likelihood codes. These results reproduced established results for two well-known models and therefore demonstrates that the new framework gives reliable estimations of the observable parameters n_s , r and $f_{\text{NL}}^{\text{eq}}$.

We also applied the module to two multi-field inflation models which both have a non-trivial field-space metric. The first of these was an α -attractor model in Section 3.5.3 which demonstrates the full functionality of `CppTSample`. This model gave n_s and r values in good agreement with the CMB constraints given in the Planck releases [Akrami et al., 2018]. In addition, we were able to reproduce the ‘universality’ of attractor models found in [Achúcarro et al., 2017] using our module results as well as finding tight constraints on $f_{\text{NL}}^{\text{eq}}$ which shows the bispectrum could potentially be used for model selection in a future survey.

The second multi-field model in Section 3.5.4 was a Gelaton/QSFI model which showed that our module can still be used on a complex model with 11 MCMC parameters to sample and a long integration time. This model gave n_s and r values that are very compatible with Planck constraints which makes this model favourable compared with the others presented here. Despite the long integration time, we are still able to find the bispectrum observables given from the best-fit parameters found in an MCMC run by using the results of `CppTSample` to compute the bispectrum in `CppTransport`.

Acknowledgments The work reported in this paper has been supported by the European Research Council under the European Union’s Seventh Framework Agreement (FP7/2007-2013) and ERC Grant Agreement No. 308082. AM acknowledges support from the University of Sussex Junior Research Associate scheme and a Royal Astronomical Society Undergraduate Fellowship.

3.7 Appendix: Full covariance plots

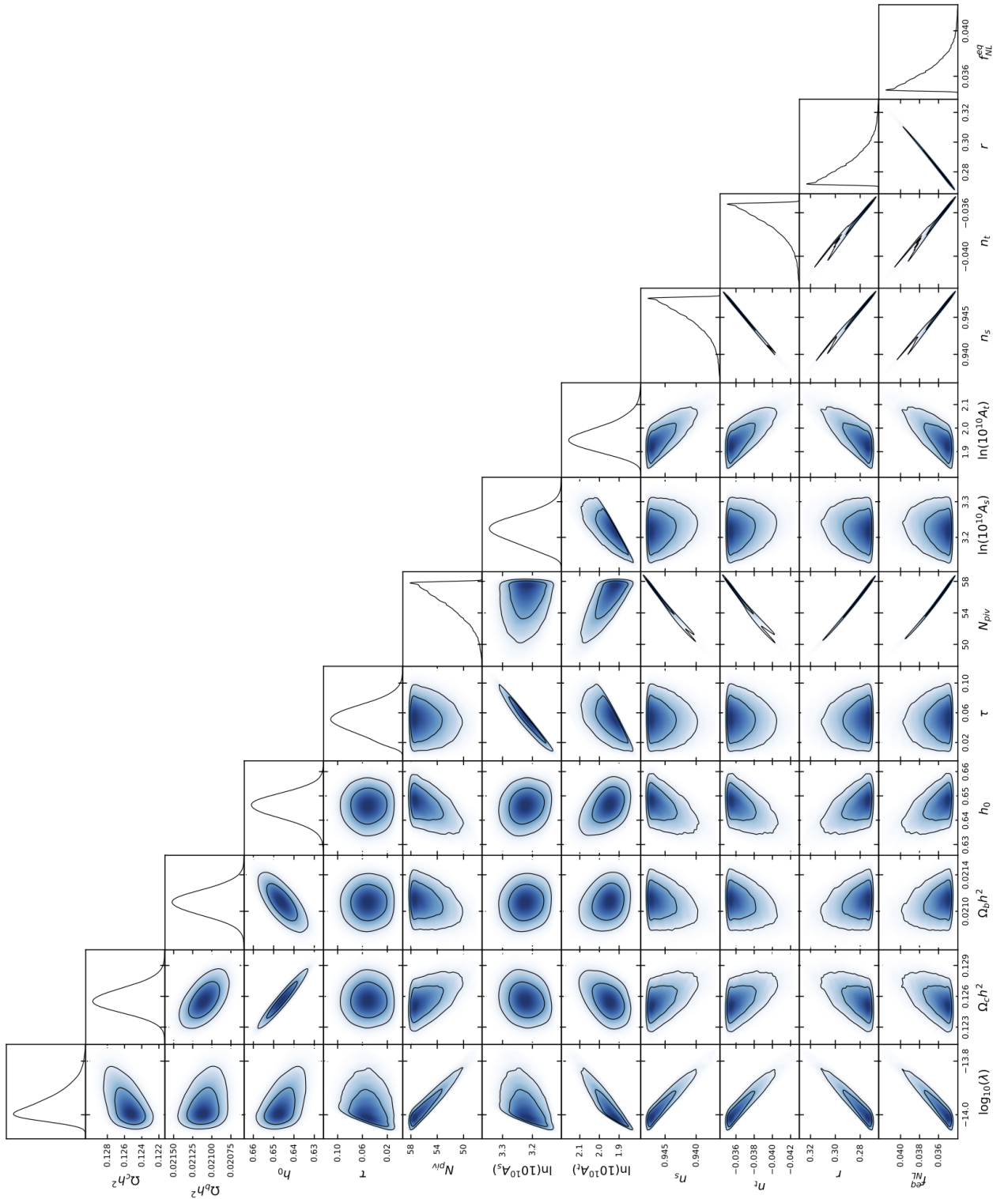


Figure 3.6: Covariance and distribution plots for the parameters $\log_{10}(\lambda)$, N_{piv} , $\Omega_c h^2$, $\Omega_b h^2$, h_0 , τ , $\ln(10^{10} A_s)$, $\ln(10^{10} A_t)$, n_s , n_t , r & $f_{\text{NL}}^{\text{eq}}$ in the quartic inflation model and based on Planck 2015 TT+TE+EE+lowP data.

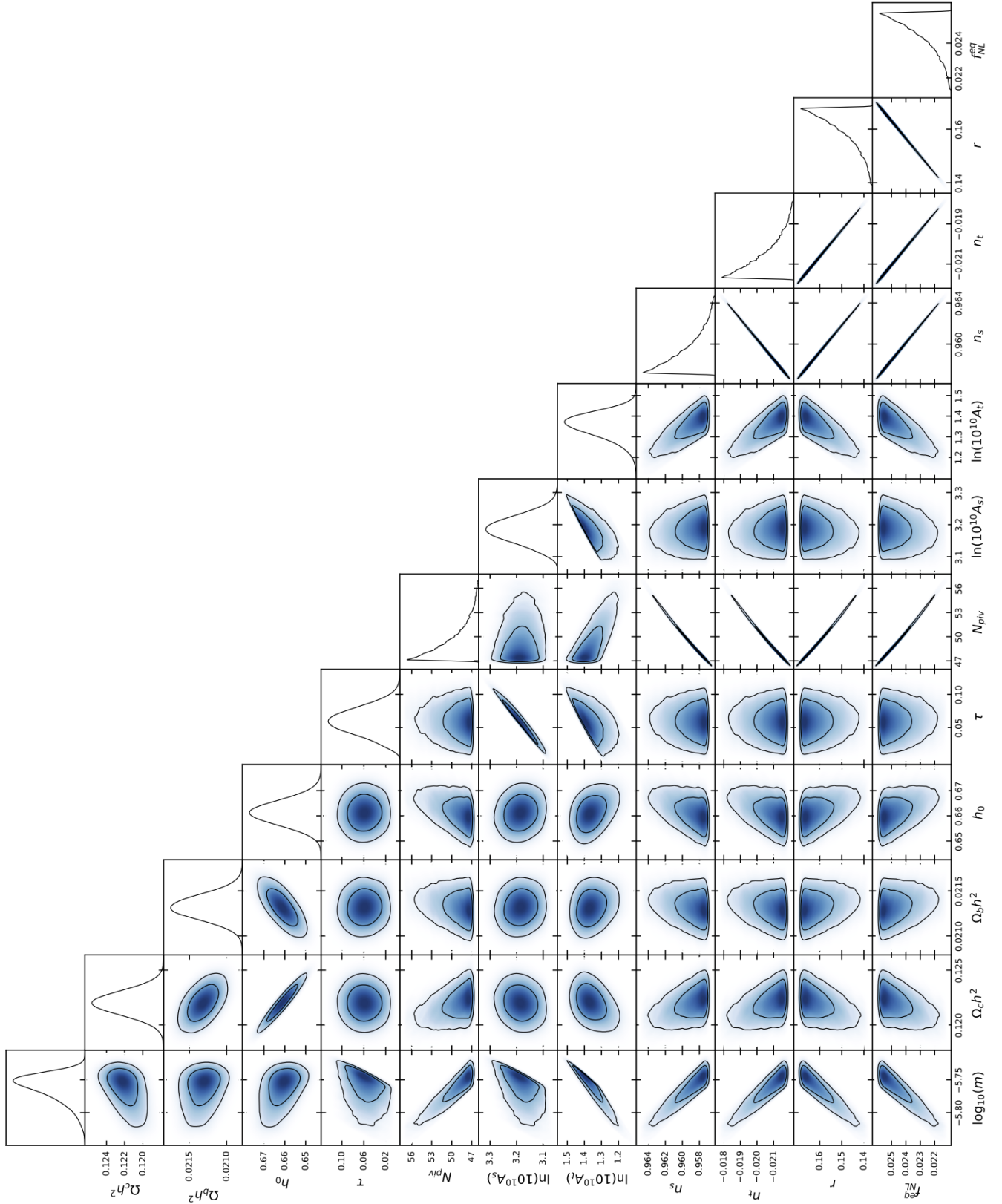


Figure 3.7: Covariance and distribution plots for the parameters $\log_{10}(m)$, N_{piv} , $\Omega_c h^2$, $\Omega_b h^2$, h_0 , τ , $\ln(10^{10} A_s)$, $\ln(10^{10} A_t)$, n_s , n_t , r & $f_{\text{NL}}^{\text{eq}}$ in the quadratic inflation model and based on Planck 2015 TT+TE+EE+lowP data.

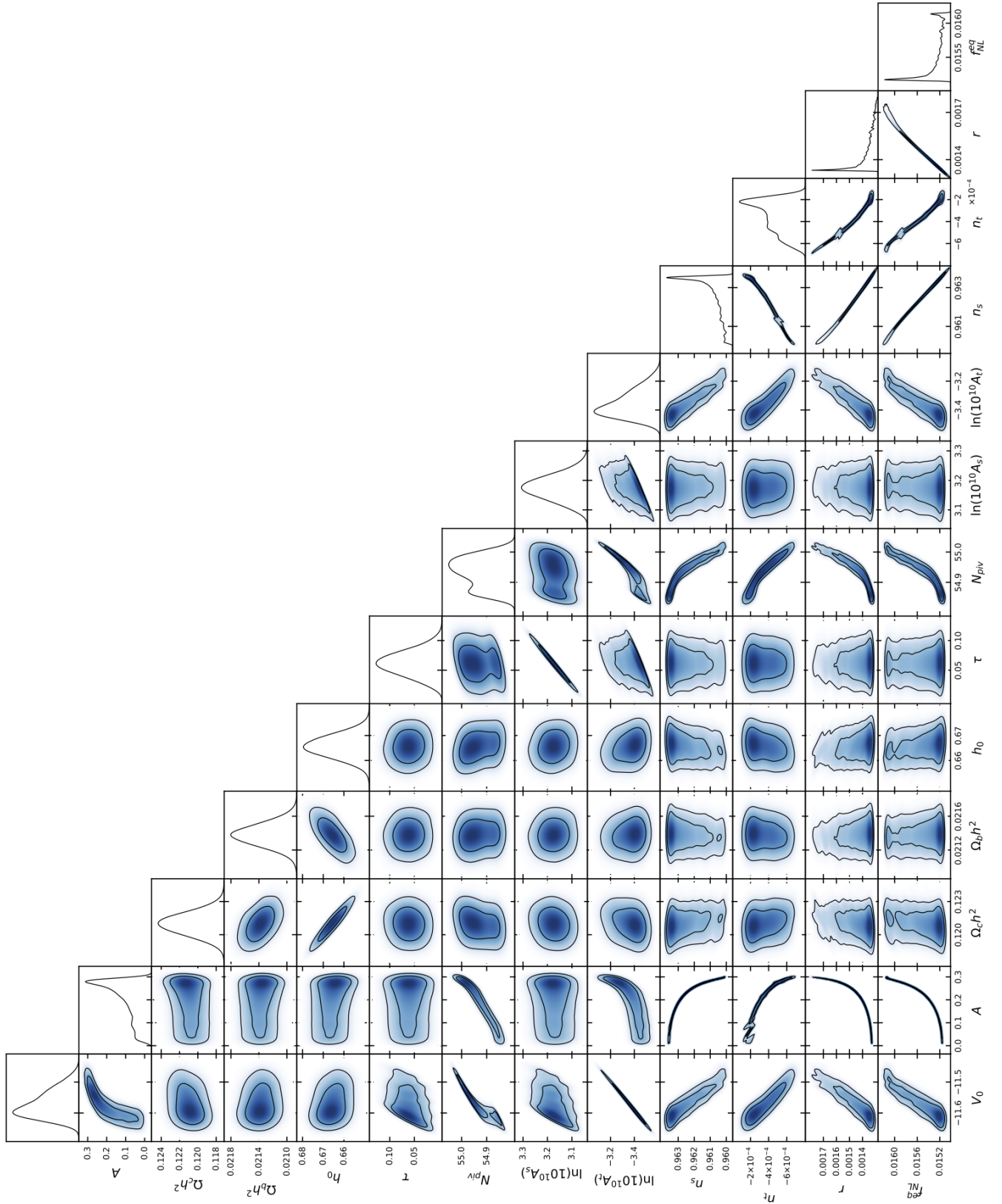


Figure 3.8: Covariance and distribution plots for the parameters $\log_{10}(V_0)$, A , N_{piv} , $\Omega_c h^2$, $\Omega_b h^2$, h_0 , τ , $\ln(10^{10} A_s)$, $\ln(10^{10} A_t)$, n_s , n_t , r & $f_{\text{NL}}^{\text{eq}}$ in the α -attractor model and based on Planck 2015 TT+TE+EE+lowP data.

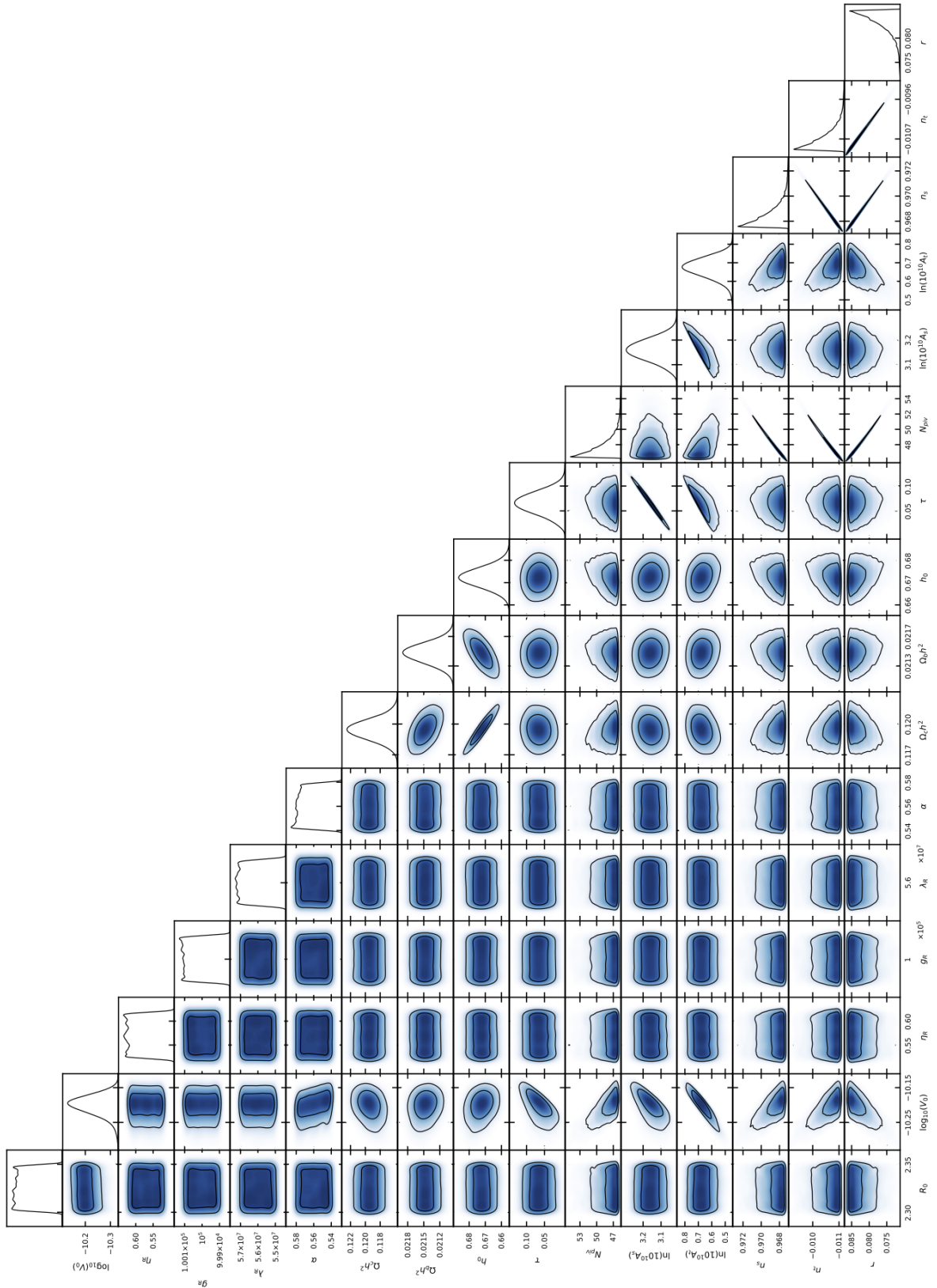


Figure 3.9: Covariance and distribution plots for the parameters R_0 , $\log_{10}(V_0)$, η_R , g_R , λ_R , α , $\Omega_c h^2$, $\Omega_b h^2$, h_0 , τ , $\ln(10^{10} A_s)$, $\ln(10^{10} A_t)$, n_s , n_t & r in the Gelaton/QSFI model and based on Planck 2015 TT+TE+EE+lowP data.

3.8 Appendix: Convergence plots

3.8.1 Quartic model

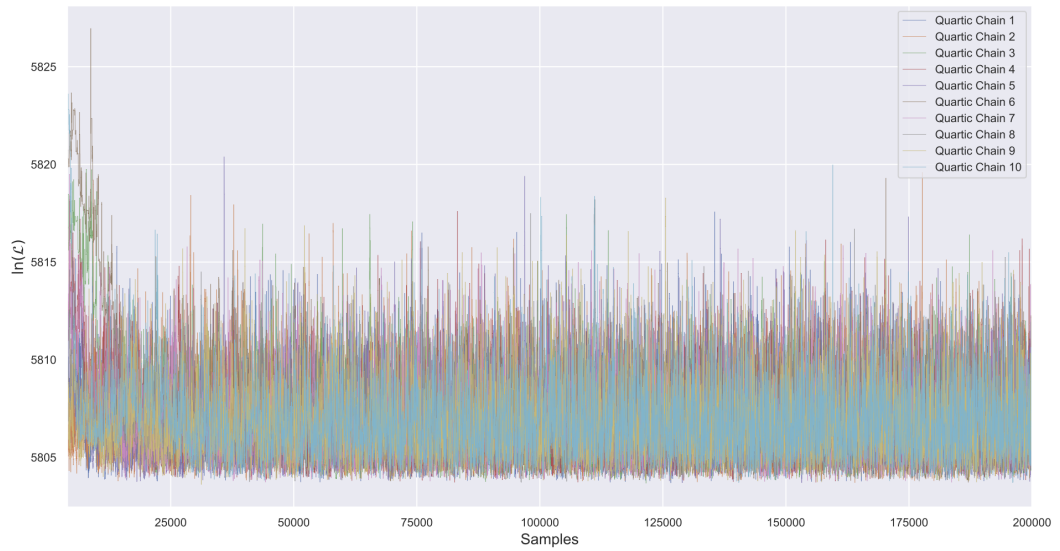


Figure 3.10: A trace plot of $\ln(\mathcal{L})$ vs. sample number for the 15 chains used in the quartic model MCMC data with the first 4000 samples removed.

3.8.2 Quadratic model

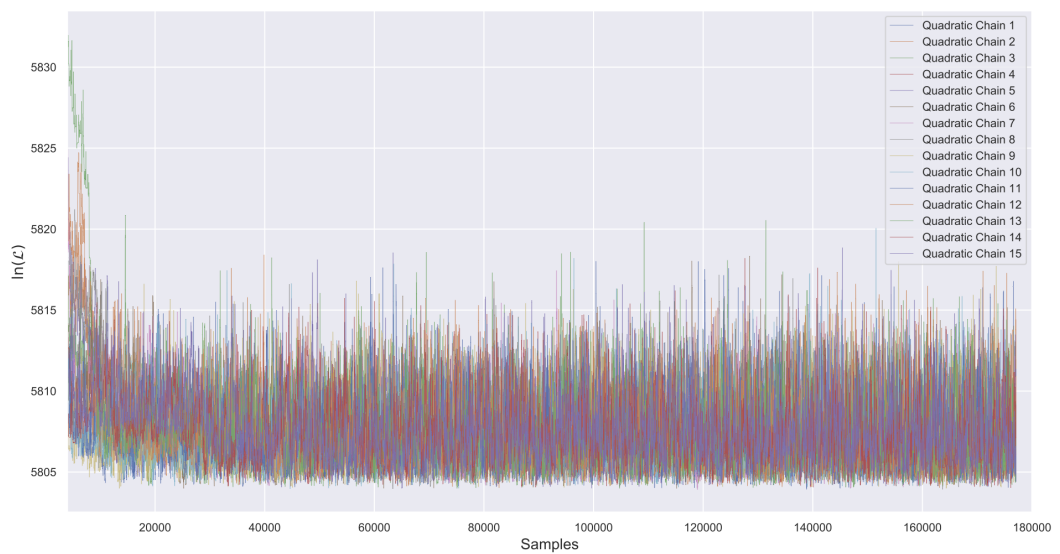


Figure 3.11: A trace plot of $\ln(\mathcal{L})$ vs. sample number for the 15 chains used in the quadratic model MCMC data with the first 4000 samples removed.

3.8.3 Alpha-attractor model

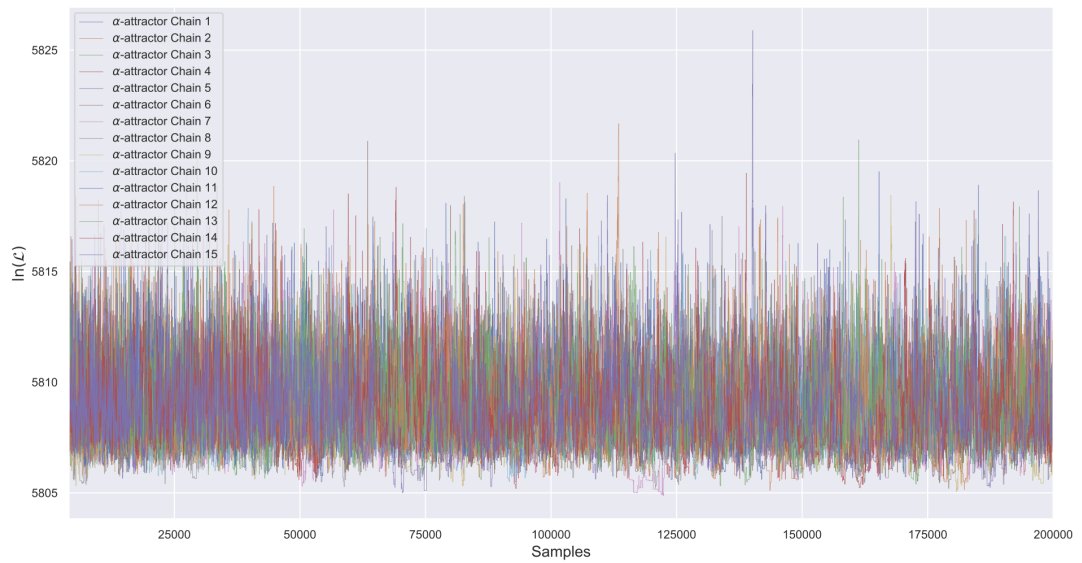


Figure 3.12: A trace plot of $\ln(\mathcal{L})$ vs. sample number for the 15 chains used in the alpha-attractor model MCMC data with the first 4000 samples removed.

3.8.4 Gelaton/QSFI model

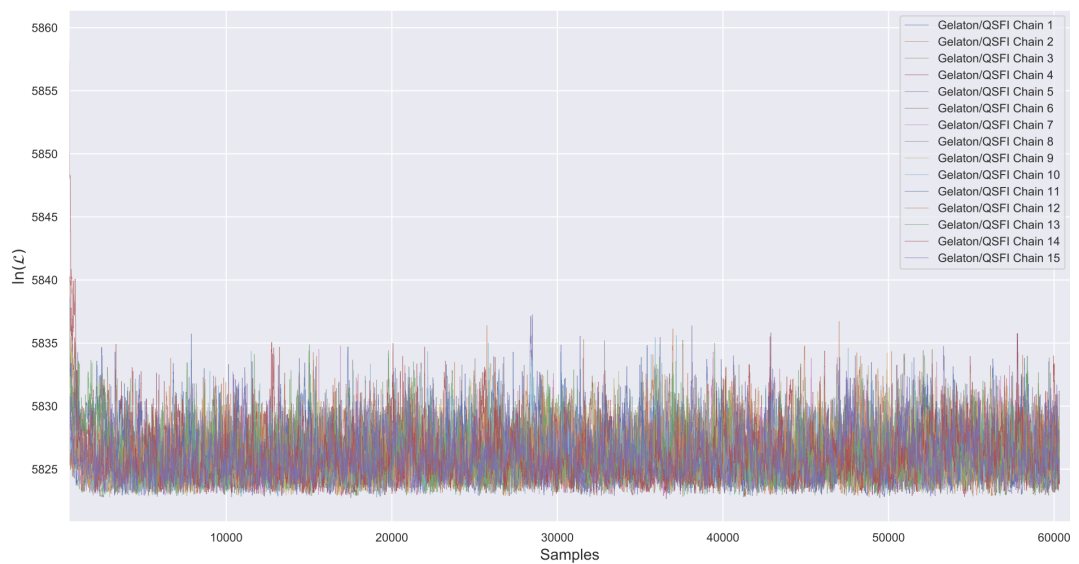


Figure 3.13: A trace plot of $\ln(\mathcal{L})$ vs. sample number for the 15 chains used in the Gelaton/QSFI model MCMC data with the first 500 samples removed.

Chapter 4

Conclusions

Constraining the theory of inflation requires solving substantial theoretical and experimental problems where the precise interplay between the underlying microphysics of the theories and the observed CMB signatures is well understood yet frustratingly incomplete. This problem is exacerbated when there are numerous candidate models for inflation, with many consistent with the two-point observables, that need to be systematically tested using higher-order observables such as the bispectrum and other non-Gaussian quantities. Furthermore, there is an increasing number of inflation paradigms originating from exotic beyond the Standard Model theories such as string theory which include multiple fields that are frequently embedded on a non-canonical field space.

My research presented in this thesis represents my contribution towards solving these problems where in chapter 2 we have seen how I have used the transport method approach to perturbation theory to build a numerical framework for computing the bispectrum in a non-trivial field space. In chapter 3, we have seen how I have developed an additional numerical package for performing a Bayesian analysis of these non-canonical models and therefore enable cosmologists to find constraints on *both* the power spectrum and the bispectrum. In the following section, I will list the key outcomes of each project.

4.1 Summary of the research

Project I: Numerical evaluation of inflationary 3-point functions on curved field space

In Chapter 2, we applied the formalism of covariant perturbations suggested by Gong & Tanaka [Gong & Tanaka, 2011] to the transport method which allowed us to find a field-covariant Hamiltonian with third-order perturbations of the field metric G_{IJ} . This

meant we could use the interaction picture of quantum mechanics and the “in-in” formalism [Schwinger, 1960] [Calzetta & Hu, 1987] [Weinberg, 2005] [Adshead et al., 2009] to compute the bispectrum produced by models with non-canonical field-spaces. Our approach meant that the majority of terms in the Hamiltonian covariantize naïvely where the only requirement is to track field index placement as well as the space-time indices. The only new terms appearing with this method are curvature quantities, such as R^I_{JKL} , that only appear in the m_{IJ} , A_{IJK} and B_{IJK} species tensors which describe the interactions between 2 fields, 3 fields and 2 fields + 1 momenta respectively. The evolution of these interaction-picture fields was then found using the Heisenberg equations of motion to obtain the covariant transport equations which are the differential equations that give the correlation function values throughout both the sub- and super-horizon eras of inflation.

As this formalism ensures extra terms from the field-metric are packaged into Christoffel and Riemann quantities, we found that the initial conditions for the two- and three-point functions and the gauge transformation to ζ also covariantize naïvely. This is a highlight of our approach since it means we are adding the minimal amount of extra terms needed to describe interactions in a non-trivial field space. Moreover, this simplicity meant that the enabling CppTransport to find correlation functions on a curved field-space mainly required adding code to calculate the curvature quantities and add these to the corresponding species tensors. Additionally, we used the index symmetries in the Riemann tensor to ensure the minimum number of unique components are computed by CppTransport.

We then tested the accuracy of the additions made to our code by using the Gelaton/QSFI model [Chen & Wang, 2010] [Tolley & Wyman, 2010] which has a Lagrangian that can be written using either canonical or non-canonical field coordinates. CppTransport was used to compute the power spectrum and bispectrum in both of these coordinates and the results were compared by measuring the residuals between their results. This comparison showed that the *worst* residual was just 0.07% with values typically around $10^{-5}\%$ for bispectrum values which demonstrated that both our calculations and the additions made to the code are successful.

Furthermore, we tested our implementation on the ‘quasi-two-field’ model [Dias et al., 2015b] against two other codes: mTransport and PyTransport. Although these both use the transport method, the comparison was valid as each code uses an entirely different numerical implementation. For mTransport, the residuals on the power spectrum remained below 0.1% throughout apart from on subhorizon scales where the two codes have different definitions of the gauge transformation to ζ . Nonetheless, the solutions converge to

the same values on super-horizon scales indicating strong agreement on the scales where observables are computed. The bispectrum residuals from PyTransport were typically less than 0.3% throughout for time evolutions of the 3-point function despite the model having super-horizon features in the spectrum. We made residuals of the reduced bispectrum as a function of k_t where agreement is usually $\leq 1\%$ apart from a small region after a section with extremely rapid oscillations.

Finally, we tested the code on a two-field gelaton model suggested in [Tolley & Wyman, 2010] which has a DBI potential defined on a hyperbolic manifold specifically chosen to give an enhanced equilateral bispectrum by adjusting the speed of sound for the inflaton perturbations. Our work showed that for monomial and hilltop potentials, a boost is found on equilateral configurations with a magnitude $|f_{\text{NL}}| \simeq 0.1$ but the effect is suppressed due to the competing requirements that the gelaton mass is larger than H whilst giving a reduction in c_s . Despite this, our work successfully demonstrated there is a boost in the equilateral bispectrum which could be observable with future measurements potentially making it a candidate model to search for.

Project II: CpptSample: sampling the primordial perturbation using CppTransport

In Chapter 3, we used the results discussed previously in Chapter 2 to build a cosmological code called CpptSample which is designed to add MCMC sampling functionality to CppTransport specifically so that we may find constraints on the non-trivial, multi-field models. The C++ code is implemented as a CosmoSIS module [Zuntz et al., 2015] so that we can pass the results from our framework to the numerous other modules available. This means a full Bayesian analysis can now be performed on multi-field models that require accurate tracking of the non-canonical field effects for the first time.

When computing the predicted CMB power spectrum from a model of inflation, the code uses the `external_Pk` feature of the CLASS module to pass the numerical form of the power spectrum so that all features of the primordial spectrum are included in the likelihood calculated from Planck 2015 data. Furthermore, our implementation of the matching equation defining the physical scales is rewritten in terms of the Hubble parameter H to account for non-trivial field interactions that wouldn't affect the value of the potential $V(\phi)$. This means we can use our module to accurately extract the values of the bispectrum and the reduced bispectrum for equilateral and squeezed configurations where the optimal model parameters come from the best-fit to the CMB data.

We tested the accuracy of our code on two well-known, single field models: the chaotic quadratic and quartic potentials. For these models, our MCMC analysis reproduced the slow-roll predictions of n_s , r and f_{NL} as expected for these simple inflation paradigms. Furthermore this confirmed that these models are disfavoured based on the values of n_s and r produced by them as well as a corresponding shift in the cosmological parameters to compensate for the ill-fitting power spectrum values. We were also able to give a constraint on the equilateral bispectrum value as expected for single-field inflation models.

We also applied the module to two multi-field models: an α -attractor model suggested by [Achúcarro et al., 2017] and the Gelaton/QSF1 model. The α -attractor model gave n_s and r values that agreed well with the Planck constraints and we were able to show that the ‘universality’ predictions for n_s , r and f_{NL} made in the original paper are accurate to within 10% in most cases. Furthermore, we found that the marginalised equilateral bispectrum values are tightly constrained which would make it an excellent candidate to search for in future surveys if it didn’t have a small value of $f_{\text{NL}}^{\text{eq}} \simeq 0.015$ which is unlikely to be observable.

The Gelaton/QSF1 results demonstrated that we could apply our framework to a model with 11 MCMC parameters to sample over with each having a long integration time. In this case, we used the best-fit model parameters given from the samples to compute the bispectrum values separately in CppTransport. We consider this an advantage of our method as it allows for bispectrum constraints to be easily found if the model has a long time per sample. The n_s and r values are also consistent with Planck constraints on these which makes it a favourable model compared to the other models analysed.

In all of the models analysed, we sampled the cosmological parameters $\Omega_c h^2$, $\Omega_b h^2$, h_0 and τ as well as the inflation parameters to compare these to the Λ CDM Planck constraints and determine how much they were changed by the underlying inflation model. As expected, we found that inflation models with poorer n_s and r values needed much larger changes in their cosmological parameters to compensate for their poor power spectrum observables.

4.2 Prospects for the future

Clearly, there remains many important questions to be answered on inflation. At the level of the power spectrum, there is still a lot to be learned about the exact form of the potential where we are really hoping to detect the elusive B-modes associated with the primordial gravitational waves from inflation. Moreover, detecting these would tell us the precise

energy scale of inflation and allow us to provide a lower bound on the tensor to scalar ratio which could instantly rule out many models. Furthermore, we are finding more evidence that the ‘running’ of the scalar spectral index, $\alpha_s \equiv dn_s/d \ln k$ is consistent with slow-roll predictions implying it should also be used to constrain inflation. This would also be supplemented with a tensor spectral index measurement with the detection of gravitational waves.

Thankfully, there is good reason to be optimistic about the potential detection of the B-mode polarisations as there are many CMB experiments (eg. CMB-S4 [Abazajian et al., 2016], CoRE [Di Valentino et al., 2018], LiteBIRD [Hazumi et al., 2019], Pico [Hanany et al., 2019], PIXIE [Kogut et al., 2011], Simons Observatory [Aguirre et al., 2019]) planned within the next decade that are designed specifically for their detection. Many of these S3 and S4 CMB experiments hope to measure an uncertainty in r that is potentially as small as $\sigma_r \sim 1 \times 10^{-4}$ which could rule out many of the models of inflation being discussed presently.

However, what if the B-modes are too small to be measured? Would that mean inflation should be abandoned? Even if we do measure the primordial gravitational waves and r , will we still have multiple models consistent with the two-point statistics of the CMB? In all of these cases, we have to find further constraints from non-Gaussianities to confront the inflation models with observation. Moreover, many of the new physics beyond the standard model theories promise to give inflation a theoretical understanding from particle physics but need their predictions to be calculated in a curved field-space. Evidently, there is a plethora of information to still be found about the early universe and my hope is that this thesis contributes towards achieving that goal.

Bibliography

- [Abazajian et al., 2016] Abazajian, K. N. et al. (2016). CMB-S4 Science Book, First Edition. Cited on 144
- [Achucarro et al., 2014] Achucarro, A., Atal, V., Hu, B., Ortiz, P., & Torrado, J. (2014). Inflation with moderately sharp features in the speed of sound: Generalized slow roll and in-in formalism for power spectrum and bispectrum. *Phys. Rev.*, D90(2), 023511. Cited on 107
- [Achúcarro et al., 2014] Achúcarro, A., Atal, V., Ortiz, P., & Torrado, J. (2014). Localized correlated features in the CMB power spectrum and primordial bispectrum from a transient reduction in the speed of sound. *Phys. Rev.*, D89(10), 103006. Cited on 64, 107
- [Achúcarro et al., 2011] Achúcarro, A., Gong, J.-O., Hardeman, S., Palma, G. A., & Patil, S. P. (2011). Features of heavy physics in the CMB power spectrum. *JCAP*, 1101, 030. Cited on 64
- [Achúcarro et al., 2017] Achúcarro, A., Kallosh, R., Linde, A., Wang, D.-G., & Welling, Y. (2017). Universality of multi-field α -attractors. Cited on 46, 101, 125, 128, 133, 143
- [Adam et al., 2016] Adam, R. et al. (2016). Planck 2015 results. I. Overview of products and scientific results. *Astron. Astrophys.*, 594, A1. Cited on 99
- [Ade et al., 2014a] Ade, P. A. R. et al. (2014a). BICEP2 II: Experiment and Three-Year Data Set. *Astrophys. J.*, 792(1), 62. Cited on 107
- [Ade et al., 2014b] Ade, P. A. R. et al. (2014b). Detection of B -Mode Polarization at Degree Angular Scales by BICEP2. *Phys. Rev. Lett.*, 112(24), 241101. Cited on 107
- [Ade et al., 2014c] Ade, P. A. R. et al. (2014c). Planck 2013 Results. XXIV. Constraints on primordial non-Gaussianity. *Astron. Astrophys.*, 571, A24. Cited on 27

- [Ade et al., 2015] Ade, P. A. R. et al. (2015). Joint Analysis of BICEP2/*Keck Array* and *Planck* Data. *Phys. Rev. Lett.*, 114, 101301. Cited on 24, 119
- [Ade et al., 2016a] Ade, P. A. R. et al. (2016a). Planck 2015 results. XVII. Constraints on primordial non-Gaussianity. *Astron. Astrophys.*, 594, A17. Cited on viii, 26, 27, 99
- [Ade et al., 2016b] Ade, P. A. R. et al. (2016b). Planck 2015 results. XX. Constraints on inflation. *Astron. Astrophys.*, 594, A20. Cited on 99, 107, 119, 120, 125, 128
- [Adshead et al., 2009] Adshead, P., Easther, R., & Lim, E. A. (2009). The 'in-in' Formalism and Cosmological Perturbations. *Phys. Rev.*, D80, 083521. Cited on 84, 141
- [Adshead et al., 2011] Adshead, P., Easther, R., Pritchard, J., & Loeb, A. (2011). Inflation and the Scale Dependent Spectral Index: Prospects and Strategies. *JCAP*, 1102, 021. Cited on 113, 114
- [Adshead et al., 2013] Adshead, P., Hu, W., & Miranda, V. (2013). Bispectrum in Single-Field Inflation Beyond Slow-Roll. *Phys. Rev.*, D88(2), 023507. Cited on 64
- [Aghanim et al., 2016] Aghanim, N. et al. (2016). Planck 2015 results. XI. CMB power spectra, likelihoods, and robustness of parameters. *Astron. Astrophys.*, 594, A11. Cited on 42, 100, 107, 119
- [Aghanim et al., 2018] Aghanim, N. et al. (2018). Planck 2018 results. VI. Cosmological parameters. Cited on viii, x, 7, 9, 40, 99, 118
- [Aguirre et al., 2019] Aguirre, J. et al. (2019). The Simons Observatory: Science goals and forecasts. *JCAP*, 1902, 056. Cited on 144
- [Akrami et al., 2018] Akrami, Y. et al. (2018). Planck 2018 results. X. Constraints on inflation. Cited on viii, 24, 29, 99, 100, 125, 133
- [Albrecht & Steinhardt, 1982] Albrecht, A. & Steinhardt, P. J. (1982). Cosmology for Grand Unified Theories with Radiatively Induced Symmetry Breaking. *Phys. Rev. Lett.*, 48, 1220–1223. Cited on 11, 45, 98
- [Alishahiha et al., 2004] Alishahiha, M., Silverstein, E., & Tong, D. (2004). DBI in the sky. *Phys. Rev.*, D70, 123505. Cited on 69
- [Allen et al., 1987] Allen, T. J., Grinstein, B., & Wise, M. B. (1987). Nongaussian Density Perturbations in Inflationary Cosmologies. *Phys. Lett.*, B197, 66–70. Cited on 25

- [Anderson et al., 2012] Anderson, G. J., Mulryne, D. J., & Seery, D. (2012). Transport equations for the inflationary trispectrum. *JCAP*, 1210, 019. Cited on 38
- [Arkani-Hamed et al., 2004] Arkani-Hamed, N., Creminelli, P., Mukohyama, S., & Zaldarriaga, M. (2004). Ghost inflation. *JCAP*, 0404, 001. Cited on 27
- [Arnowitt et al., 2008] Arnowitt, R. L., Deser, S., & Misner, C. W. (2008). The Dynamics of general relativity. *Gen. Rel. Grav.*, 40, 1997–2027. Cited on 29, 79
- [Audren et al., 2013] Audren, B., Lesgourgues, J., Benabed, K., & Prunet, S. (2013). Conservative Constraints on Early Cosmology: an illustration of the Monte Python cosmological parameter inference code. *JCAP*, 1302, 001. Cited on 100
- [Babich et al., 2004] Babich, D., Creminelli, P., & Zaldarriaga, M. (2004). The Shape of non-Gaussianities. *JCAP*, 0408, 009. Cited on 27
- [Bardeen, 1980] Bardeen, J. M. (1980). Gauge Invariant Cosmological Perturbations. *Phys. Rev.*, D22, 1882–1905. Cited on 20
- [Bardeen et al., 1983] Bardeen, J. M., Steinhardt, P. J., & Turner, M. S. (1983). Spontaneous Creation of Almost Scale - Free Density Perturbations in an Inflationary Universe. *Phys. Rev.*, D28, 679. Cited on 16
- [Bartolo et al., 2004] Bartolo, N., Komatsu, E., Matarrese, S., & Riotto, A. (2004). Non-Gaussianity from inflation: Theory and observations. *Phys. Rept.*, 402, 103–266. Cited on 25
- [Baumann, 2011] Baumann, D. (2011). Inflation. In *Physics of the large and the small, TASI 09, proceedings of the Theoretical Advanced Study Institute in Elementary Particle Physics, Boulder, Colorado, USA, 1-26 June 2009* (pp. 523–686). Cited on 20
- [Baumann & McAllister, 2015] Baumann, D. & McAllister, L. (2015). *Inflation and String Theory*. Cambridge University Press. Cited on 36, 46, 99
- [Bertschinger, 2001] Bertschinger, E. (2001). Cosmological perturbation theory and structure formation. In *Cosmology 2000: Proceedings, Conference, Lisbon, Portugal, 12-15 Jul 2000* (pp. 1–25). Cited on 21
- [Bielleman et al., 2016] Bielleman, S., Ibanez, L. E., Pedro, F. G., & Valenzuela, I. (2016). Multifield Dynamics in Higgs-otic Inflation. *JHEP*, 01, 128. Cited on 77

- [Blas et al., 2011] Blas, D., Lesgourgues, J., & Tram, T. (2011). The Cosmic Linear Anisotropy Solving System (CLASS) II: Approximation schemes. *JCAP*, 1107, 034. Cited on 40, 100, 107
- [Boubekeur & Lyth, 2005] Boubekeur, L. & Lyth, D. H. (2005). Hilltop inflation. *JCAP*, 07, 010. Cited on 125
- [Bridges et al., 2007] Bridges, M., Lasenby, A. N., & Hobson, M. P. (2007). WMAP 3-year primordial power spectrum. *Mon. Not. Roy. Astron. Soc.*, 381, 68–74. Cited on 100
- [Bunch & Davies, 1978] Bunch, T. S. & Davies, P. C. W. (1978). Quantum Field Theory in de Sitter Space: Renormalization by Point Splitting. *Proc. Roy. Soc. Lond.*, A360, 117–134. Cited on 18
- [Burrage et al., 2011] Burrage, C., de Rham, C., Seery, D., & Tolley, A. J. (2011). Galileon inflation. *JCAP*, 1101, 014. Cited on 27
- [Butchers & Seery, 2018] Butchers, S. & Seery, D. (2018). Numerical evaluation of inflationary 3-point functions on curved field space—with the transport method & CppTransport. *JCAP*, 1807(07), 031. Cited on 2, 37, 38, 99, 102, 103, 104, 130
- [Byrnes & Choi, 2010] Byrnes, C. T. & Choi, K.-Y. (2010). Review of local non-Gaussianity from multi-field inflation. *Adv. Astron.*, 2010, 724525. Cited on 27, 38
- [Byrnes et al., 2006] Byrnes, C. T., Sasaki, M., & Wands, D. (2006). The primordial trispectrum from inflation. *Phys. Rev.*, D74, 123519. Cited on 38
- [Calzetta & Hu, 1987] Calzetta, E. & Hu, B. (1987). Closed Time Path Functional Formalism in Curved Space-Time: Application to Cosmological Back Reaction Problems. *Phys. Rev. D*, 35, 495. Cited on 141
- [Chen et al., 2007] Chen, X., Huang, M.-x., Kachru, S., & Shiu, G. (2007). Observational signatures and non-Gaussianities of general single field inflation. *JCAP*, 0701, 002. Cited on 27, 69
- [Chen & Wang, 2010] Chen, X. & Wang, Y. (2010). Large non-Gaussianities with Intermediate Shapes from Quasi-Single Field Inflation. *Phys. Rev.*, D81, 063511. Cited on 36, 46, 61, 99, 129, 141
- [Chernikov & Tagirov, 1968] Chernikov, N. A. & Tagirov, E. A. (1968). Quantum theory of scalar fields in de Sitter space-time. *Ann. Inst. H. Poincaré Phys. Theor.*, A9, 109. Cited on 18

- [Christensen & Meyer, 2000] Christensen, N. & Meyer, R. (2000). Bayesian methods for cosmological parameter estimation from cosmic microwave background measurements. Cited on 42, 100
- [Christensen et al., 2001] Christensen, N., Meyer, R., Knox, L., & Luey, B. (2001). II. Bayesian methods for cosmological parameter estimation from cosmic microwave background measurements. *Class. Quant. Grav.*, 18, 2677. Cited on 42, 100
- [Chuang et al., 2013] Chuang, C.-H. et al. (2013). The clustering of galaxies in the SDSS-III Baryon Oscillation Spectroscopic Survey: single-probe measurements and the strong power of normalized growth rate on constraining dark energy. *Mon. Not. Roy. Astron. Soc.*, 433, 3559. Cited on 107
- [Creminelli, 2003] Creminelli, P. (2003). On non-Gaussianities in single-field inflation. *JCAP*, 0310, 003. Cited on 25
- [Creminelli & Zaldarriaga, 2004] Creminelli, P. & Zaldarriaga, M. (2004). Single field consistency relation for the 3-point function. *JCAP*, 10, 006. Cited on 27
- [de la Bella et al., 2018] de la Bella, L. F., Regan, D., Seery, D., & Parkinson, D. (2018). Impact of bias and redshift-space modelling for the halo power spectrum: Testing the effective field theory of large-scale structure. Cited on 101
- [Di Valentino et al., 2018] Di Valentino, E. et al. (2018). Exploring cosmic origins with CORE: Cosmological parameters. *JCAP*, 1804, 017. Cited on 144
- [Dias et al., 2015a] Dias, M., Elliston, J., Frazer, J., Mulryne, D., & Seery, D. (2015a). The curvature perturbation at second order. *JCAP*, 1502(02), 040. Cited on 38, 57, 58, 65, 94, 95, 96, 104
- [Dias et al., 2016] Dias, M., Frazer, J., Mulryne, D. J., & Seery, D. (2016). Numerical evaluation of the bispectrum in multiple field inflation—the transport approach with code. *JCAP*, 1612(12), 033. Cited on 38, 47, 48, 49, 50, 53, 54, 55, 56, 57, 60, 61, 77, 83, 85, 99, 102, 103, 104, 129
- [Dias et al., 2015b] Dias, M., Frazer, J., & Seery, D. (2015b). Computing observables in curved multifield models of inflation—A guide (with code) to the transport method. *JCAP*, 1512(12), 030. Cited on 34, 38, 47, 48, 49, 53, 55, 57, 64, 99, 102, 104, 141
- [Dias & Seery, 2012] Dias, M. & Seery, D. (2012). Transport equations for the inflationary spectral index. *Phys. Rev.*, D85, 043519. Cited on 37

- [Dodelson & Hui, 2003] Dodelson, S. & Hui, L. (2003). A Horizon ratio bound for inflationary fluctuations. *Phys. Rev. Lett.*, 91, 131301. Cited on 13
- [Dunkley et al., 2005] Dunkley, J., Bucher, M., Ferreira, P. G., Moodley, K., & Skordis, C. (2005). Fast and reliable mcmc for cosmological parameter estimation. *Mon. Not. Roy. Astron. Soc.*, 356, 925–936. Cited on 99, 100
- [Dunkley et al., 2009] Dunkley, J. et al. (2009). Five-Year Wilkinson Microwave Anisotropy Probe (WMAP) Observations: Likelihoods and Parameters from the WMAP data. *Astrophys. J. Suppl.*, 180, 306–329. Cited on 100
- [Durrer, 2008] Durrer, R. (2008). *The Cosmic Microwave Background*. Cambridge: Cambridge University Press. Cited on 38
- [Easther et al., 2006] Easther, R., Kinney, W. H., & Powell, B. A. (2006). The Lyth bound and the end of inflation. *JCAP*, 08, 004. Cited on 23
- [Easther & Peiris, 2012] Easther, R. & Peiris, H. V. (2012). Bayesian Analysis of Inflation II: Model Selection and Constraints on Reheating. *Phys. Rev.*, D85, 103533. Cited on 46, 77, 100
- [Efstathiou & Mack, 2005] Efstathiou, G. & Mack, K. J. (2005). The Lyth bound revisited. *JCAP*, 05, 008. Cited on 23
- [Einstein, 1916] Einstein, A. (1916). The Foundation of the General Theory of Relativity. *Annalen Phys.*, 49(7), 769–822. [,65(1916)]. Cited on 4
- [Eisenstein et al., 2005] Eisenstein, D. J. et al. (2005). Detection of the Baryon Acoustic Peak in the Large-Scale Correlation Function of SDSS Luminous Red Galaxies. *Astrophys. J.*, 633, 560–574. Cited on 6
- [Elliston et al., 2011] Elliston, J., Mulryne, D. J., Seery, D., & Tavakol, R. (2011). Evolution of fNL to the adiabatic limit. *JCAP*, 1111, 005. Cited on 29, 75, 112
- [Elliston et al., 2012] Elliston, J., Seery, D., & Tavakol, R. (2012). The inflationary bispectrum with curved field-space. *JCAP*, 1211, 060. Cited on 37, 38, 49, 51, 53, 55, 80, 89, 102, 104
- [Falk et al., 1993] Falk, T., Rangarajan, R., & Srednicki, M. (1993). The Angular dependence of the three point correlation function of the cosmic microwave background

- radiation as predicted by inflationary cosmologies. *Astrophys. J.*, 403, L1. Cited on 25, 26
- [Fergusson & Shellard, 2007] Fergusson, J. R. & Shellard, E. P. S. (2007). Primordial non-Gaussianity and the CMB bispectrum. *Phys. Rev.*, D76, 083523. Cited on 27, 59, 67, 105
- [Feroz et al., 2009] Feroz, F., Hobson, M. P., & Bridges, M. (2009). MultiNest: an efficient and robust Bayesian inference tool for cosmology and particle physics. *Mon. Not. Roy. Astron. Soc.*, 398, 1601–1614. Cited on 100, 107
- [Feroz et al., 2013] Feroz, F., Hobson, M. P., Cameron, E., & Pettitt, A. N. (2013). Importance Nested Sampling and the MultiNest Algorithm. Cited on 100, 107
- [Ferrara et al., 2013] Ferrara, S., Kallosh, R., Linde, A., & Porrati, M. (2013). Minimal Supergravity Models of Inflation. *Phys. Rev.*, D88(8), 085038. Cited on 36, 46
- [Fienberg, 1970] Fienberg, S. E. (1970). *Biometrics*, 26(2), 351–355. Cited on 116
- [Fixsen, 2009] Fixsen, D. J. (2009). The Temperature of the Cosmic Microwave Background. *Astrophys. J.*, 707, 916–920. Cited on 10
- [Flauger et al., 2017] Flauger, R., Mirbabayi, M., Senatore, L., & Silverstein, E. (2017). Productive Interactions: heavy particles and non-Gaussianity. *JCAP*, 1710(10), 058. Cited on 64
- [Foreman-Mackey et al., 2013] Foreman-Mackey, D., Hogg, D. W., Lang, D., & Goodman, J. (2013). emcee: The MCMC Hammer. *Publ. Astron. Soc. Pac.*, 125, 306–312. Cited on 107, 118
- [Friedman, 1922] Friedman, A. (1922). On the Curvature of space. *Z. Phys.*, 10, 377–386. [Gen. Rel. Grav.31,1991(1999)]. Cited on 5
- [Friedmann, 1924] Friedmann, A. (1924). On the Possibility of a world with constant negative curvature of space. *Z. Phys.*, 21, 326–332. [Gen. Rel. Grav.31,2001(1999)]. Cited on 3
- [Gangui et al., 1994] Gangui, A., Lucchin, F., Matarrese, S., & Mollerach, S. (1994). The Three point correlation function of the cosmic microwave background in inflationary models. *Astrophys. J.*, 430, 447–457. Cited on 25, 26

- [Gao et al., 2012] Gao, X., Langlois, D., & Mizuno, S. (2012). Influence of heavy modes on perturbations in multiple field inflation. *JCAP*, 1210, 040. Cited on 64
- [Garcia-Bellido & Wands, 1995] Garcia-Bellido, J. & Wands, D. (1995). Constraints from inflation on scalar - tensor gravity theories. *Phys. Rev.*, D52, 6739–6749. Cited on 28
- [Garcia-Bellido & Wands, 1996] Garcia-Bellido, J. & Wands, D. (1996). Metric perturbations in two field inflation. *Phys. Rev.*, D53, 5437–5445. Cited on 28, 75
- [Gell-Mann & Low, 1951] Gell-Mann, M. & Low, F. (1951). Bound states in quantum field theory. *Phys. Rev.*, 84, 350–354. Cited on 50, 84
- [Gelman & Rubin, 1992] Gelman, A. & Rubin, D. B. (1992). Inference from Iterative Simulation Using Multiple Sequences. *Statist. Sci.*, 7, 457–472. Cited on 119
- [Gibbons & Hawking, 1977] Gibbons, G. W. & Hawking, S. W. (1977). Action Integrals and Partition Functions in Quantum Gravity. *Phys. Rev.*, D15, 2752–2756. Cited on 33, 79
- [Gong & Tanaka, 2011] Gong, J.-O. & Tanaka, T. (2011). A covariant approach to general field space metric in multi-field inflation. *JCAP*, 1103, 015. [Erratum: *JCAP*1202,E01(2012)]. Cited on 36, 49, 75, 78, 102, 140
- [Gordon & Trota, 2007] Gordon, C. & Trota, R. (2007). Bayesian Calibrated Significance Levels Applied to the Spectral Tilt and Hemispherical Asymmetry. *Mon. Not. Roy. Astron. Soc.*, 382, 1859–1863. Cited on 100
- [Gordon et al., 2001] Gordon, C., Wands, D., Bassett, B. A., & Maartens, R. (2001). Adiabatic and entropy perturbations from inflation. *Phys. Rev.*, D63, 023506. Cited on 28, 75
- [Greenwood et al., 2013] Greenwood, R. N., Kaiser, D. I., & Sfakianakis, E. I. (2013). Multifield Dynamics of Higgs Inflation. *Phys. Rev.*, D87, 064021. Cited on 46
- [Guth, 1981] Guth, A. H. (1981). The Inflationary Universe: A Possible Solution to the Horizon and Flatness Problems. *Phys. Rev.*, D23, 347–356. Cited on 11, 45, 98
- [Guth & Pi, 1982] Guth, A. H. & Pi, S. Y. (1982). Fluctuations in the New Inflationary Universe. *Phys. Rev. Lett.*, 49, 1110–1113. Cited on 16

- [Hamazaki & Kodama, 1996] Hamazaki, T. & Kodama, H. (1996). Evolution of cosmological perturbations during reheating. *Prog. Theor. Phys.*, 96, 1123–1146. Cited on 28
- [Hanany et al., 2019] Hanany, S. et al. (2019). PICO: Probe of Inflation and Cosmic Origins. Cited on 144
- [Handley et al., 2015] Handley, W. J., Hobson, M. P., & Lasenby, A. N. (2015). PolyChord: nested sampling for cosmology. *Mon. Not. Roy. Astron. Soc.*, 450(1), L61–L65. Cited on 100
- [Hastings, 1970] Hastings, W. (1970). Monte Carlo Sampling Methods Using Markov Chains and Their Applications. *Biometrika*, 57, 97–109. Cited on 118
- [Hazra et al., 2013] Hazra, D. K., Sriramkumar, L., & Martin, J. (2013). BINGO: A code for the efficient computation of the scalar bi-spectrum. *JCAP*, 1305, 026. Cited on 46
- [Hazumi et al., 2019] Hazumi, M. et al. (2019). LiteBIRD: A Satellite for the Studies of B-Mode Polarization and Inflation from Cosmic Background Radiation Detection. *J. Low. Temp. Phys.*, 194(5-6), 443–452. Cited on 144
- [Hilbert, 1915] Hilbert, D. (1915). Die Grundlagen der Physik. 1. *Gott. Nachr.*, 27, 395–407. [120(1915)]. Cited on 3
- [Hinshaw et al., 2013] Hinshaw, G. et al. (2013). Nine-Year Wilkinson Microwave Anisotropy Probe (WMAP) Observations: Cosmological Parameter Results. *Astrophys. J. Suppl.*, 208, 19. Cited on 9, 99, 100, 107
- [Hobson et al., 2010] Hobson, M. P., Jaffe, A. H., Liddle, A. R., Mukherjee, P., & Parkinson, D. (2010). *Bayesian methods in cosmology*. Cambridge University Press. Cited on 100
- [Hojjati et al., 2011] Hojjati, A., Pogosian, L., & Zhao, G.-B. (2011). Testing gravity with CAMB and CosmoMC. *JCAP*, 1108, 005. Cited on 107
- [Hu & Sugiyama, 1995a] Hu, W. & Sugiyama, N. (1995a). Anisotropies in the cosmic microwave background: An Analytic approach. *Astrophys. J.*, 444, 489–506. Cited on 39
- [Hu & Sugiyama, 1995b] Hu, W. & Sugiyama, N. (1995b). Toward understanding CMB anisotropies and their implications. *Phys. Rev.*, D51, 2599–2630. Cited on 39

- [Hu & Sugiyama, 1996] Hu, W. & Sugiyama, N. (1996). Small scale cosmological perturbations: An Analytic approach. *Astrophys. J.*, 471, 542–570. Cited on 39
- [Hubble, 1929] Hubble, E. (1929). A relation between distance and radial velocity among extra-galactic nebulae. *Proc. Nat. Acad. Sci.*, 15, 168–173. Cited on 3
- [Huston & Christopherson, 2012] Huston, I. & Christopherson, A. J. (2012). Calculating Non-adiabatic Pressure Perturbations during Multi-field Inflation. *Phys.Rev.*, D85, 063507. Cited on 46
- [Huston & Malik, 2009] Huston, I. & Malik, K. A. (2009). Numerical calculation of second order perturbations. *JCAP*, 0909, 019. Cited on 46
- [Huston & Malik, 2011] Huston, I. & Malik, K. A. (2011). Second Order Perturbations During Inflation Beyond Slow-roll. *JCAP*, 1110, 029. Cited on 46
- [Ibanez et al., 2015] Ibanez, L. E., Marchesano, F., & Valenzuela, I. (2015). Higgs-otic Inflation and String Theory. *JHEP*, 01, 128. Cited on 77
- [Kallosh & Linde, 2013a] Kallosh, R. & Linde, A. (2013a). Non-minimal Inflationary Attractors. *JCAP*, 10, 033. Cited on 36
- [Kallosh & Linde, 2013b] Kallosh, R. & Linde, A. (2013b). Universality Class in Conformal Inflation. *JCAP*, 1307, 002. Cited on 46, 77
- [Kallosh et al., 2013] Kallosh, R., Linde, A., & Roest, D. (2013). Superconformal Inflationary α -Attractors. *JHEP*, 11, 198. Cited on 36, 46, 77
- [Kazin et al., 2014] Kazin, E. A. et al. (2014). The WiggleZ Dark Energy Survey: improved distance measurements to $z = 1$ with reconstruction of the baryonic acoustic feature. *Mon. Not. Roy. Astron. Soc.*, 441(4), 3524–3542. Cited on 107
- [Knox et al., 2001] Knox, L., Christensen, N., & Skordis, C. (2001). The age of the universe and the cosmological constant determined from cosmic microwave background anisotropy measurements. *Astrophys. J.*, 563, L95–L98. Cited on 42, 100
- [Kodama & Hamazaki, 1996] Kodama, H. & Hamazaki, T. (1996). Evolution of cosmological perturbations in a stage dominated by an oscillatory scalar field. *Prog. Theor. Phys.*, 96, 949–970. Cited on 28

- [Kogut et al., 2011] Kogut, A. et al. (2011). The Primordial Inflation Explorer (PIXIE): A Nulling Polarimeter for Cosmic Microwave Background Observations. *JCAP*, 1107, 025. Cited on 144
- [Komatsu et al., 2011] Komatsu, E. et al. (2011). Seven-Year Wilkinson Microwave Anisotropy Probe (WMAP) Observations: Cosmological Interpretation. *Astrophys. J. Suppl.*, 192, 18. Cited on 99, 107
- [Komatsu & Spergel, 2001] Komatsu, E. & Spergel, D. N. (2001). Acoustic signatures in the primary microwave background bispectrum. *Phys. Rev.*, D63, 063002. Cited on 25
- [Kosowsky et al., 2002] Kosowsky, A., Milosavljevic, M., & Jimenez, R. (2002). Efficient cosmological parameter estimation from microwave background anisotropies. *Phys. Rev.*, D66, 063007. Cited on 42, 100
- [Lahav & Liddle, 2014] Lahav, O. & Liddle, A. R. (2014). The Cosmological Parameters 2014. Cited on 9
- [Larson et al., 2011] Larson, D. et al. (2011). Seven-Year Wilkinson Microwave Anisotropy Probe (WMAP) Observations: Power Spectra and WMAP-Derived Parameters. *Astrophys. J. Suppl.*, 192, 16. Cited on 99, 107
- [Lee et al., 2005] Lee, H.-C., Sasaki, M., Stewart, E. D., Tanaka, T., & Yokoyama, S. (2005). A New delta N formalism for multi-component inflation. *JCAP*, 0510, 004. Cited on 78
- [Lesgourgues, 2011] Lesgourgues, J. (2011). The Cosmic Linear Anisotropy Solving System (CLASS) I: Overview. Cited on 2, 40, 100, 107
- [Lewis, 2013] Lewis, A. (2013). Efficient sampling of fast and slow cosmological parameters. *Phys. Rev.*, D87(10), 103529. Cited on 112, 117
- [Lewis & Bridle, 2002] Lewis, A. & Bridle, S. (2002). Cosmological parameters from CMB and other data: A Monte Carlo approach. *Phys. Rev.*, D66, 103511. Cited on 42, 100, 112, 117
- [Lewis et al., 2000] Lewis, A., Challinor, A., & Lasenby, A. (2000). Efficient computation of CMB anisotropies in closed FRW models. *Astrophys. J.*, 538, 473–476. Cited on 40, 100, 107
- [Liddle, 1998] Liddle, A. R. (1998). *An introduction to modern cosmology*. Cited on 11

- [Liddle & Leach, 2003] Liddle, A. R. & Leach, S. M. (2003). How long before the end of inflation were observable perturbations produced? *Phys. Rev.*, D68, 103503. Cited on 13, 113
- [Liddle et al., 2006] Liddle, A. R., Mukherjee, P., & Parkinson, D. (2006). Cosmological model selection. Cited on 100
- [Linde, 1982] Linde, A. D. (1982). A New Inflationary Universe Scenario: A Possible Solution of the Horizon, Flatness, Homogeneity, Isotropy and Primordial Monopole Problems. *Phys. Lett.*, 108B, 389–393. Cited on 11, 45, 98
- [Linde, 1983] Linde, A. D. (1983). Chaotic Inflation. *Phys. Lett.*, 129B, 177–181. Cited on 16, 119, 122
- [Lukash, 1980] Lukash, V. N. (1980). Production of phonons in an isotropic universe. *Sov. Phys. JETP*, 52, 807–814. [*Zh. Eksp. Teor. Fiz.*79,1601(1980)]. Cited on 20
- [Lyth, 1985] Lyth, D. H. (1985). Large Scale Energy Density Perturbations and Inflation. *Phys. Rev.*, D31, 1792–1798. Cited on 16, 20, 29
- [Lyth, 1997] Lyth, D. H. (1997). What would we learn by detecting a gravitational wave signal in the cosmic microwave background anisotropy? *Phys. Rev. Lett.*, 78, 1861–1863. Cited on 23, 24
- [Lyth & Liddle, 2009] Lyth, D. H. & Liddle, A. R. (2009). *The primordial density perturbation: Cosmology, inflation and the origin of structure*. Cited on 15, 38
- [Lyth et al., 2005] Lyth, D. H., Malik, K. A., & Sasaki, M. (2005). A General proof of the conservation of the curvature perturbation. *JCAP*, 0505, 004. Cited on 29, 31, 94, 95
- [Lyth & Riotto, 1999] Lyth, D. H. & Riotto, A. (1999). Particle physics models of inflation and the cosmological density perturbation. *Phys. Rept.*, 314, 1–146. Cited on 46, 99
- [Lyth & Rodriguez, 2005] Lyth, D. H. & Rodriguez, Y. (2005). The Inflationary prediction for primordial non-Gaussianity. *Phys. Rev. Lett.*, 95, 121302. Cited on 31
- [Lyth & Seery, 2008] Lyth, D. H. & Seery, D. (2008). Classicality of the primordial perturbations. *Phys. Lett.*, B662, 309–313. Cited on 19
- [Lyth & Wands, 2002] Lyth, D. H. & Wands, D. (2002). Generating the curvature perturbation without an inflaton. *Phys. Lett.*, B524, 5–14. Cited on 27

- [Lyth & Wands, 2003] Lyth, D. H. & Wands, D. (2003). The CDM isocurvature perturbation in the curvaton scenario. *Phys. Rev.*, D68, 103516. Cited on 75
- [Maldacena, 2003] Maldacena, J. M. (2003). Non-Gaussian features of primordial fluctuations in single field inflationary models. *JHEP*, 05, 013. Cited on 25, 27, 32, 33, 34, 51, 79
- [Malik & Wands, 2004] Malik, K. A. & Wands, D. (2004). Evolution of second-order cosmological perturbations. *Class. Quant. Grav.*, 21, L65–L72. Cited on 94
- [Martin & Ringeval, 2006] Martin, J. & Ringeval, C. (2006). Inflation after WMAP3: Confronting the Slow-Roll and Exact Power Spectra to CMB Data. *JCAP*, 0608, 009. Cited on 46
- [Martin et al., 2014] Martin, J., Ringeval, C., & Vennin, V. (2014). Encyclopædia Inflationaris. *Phys. Dark Univ.*, 5-6, 75–235. Cited on 100
- [Mather et al., 1994] Mather, J. C. et al. (1994). Measurement of the Cosmic Microwave Background spectrum, by the COBE FIRAS instrument. *Astrophys. J.*, 420, 439–444. Cited on 9
- [Metropolis et al., 1953] Metropolis, N., Rosenbluth, A. W., Rosenbluth, M. N., Teller, A. H., & Teller, E. (1953). Equation of state calculations by fast computing machines. *The Journal of Chemical Physics*, 21(6), 1087–1092. Cited on 107, 118
- [Mollerach, 1990] Mollerach, S. (1990). Isocurvature Baryon Perturbations and Inflation. *Phys. Rev.*, D42, 313–325. Cited on 27
- [Mortonson et al., 2011] Mortonson, M. J., Peiris, H. V., & Easther, R. (2011). Bayesian Analysis of Inflation: Parameter Estimation for Single Field Models. *Phys. Rev.*, D83, 043505. Cited on 46, 77, 100, 113, 114
- [Mukhanov, 2005] Mukhanov, V. (2005). *Physical Foundations of Cosmology*. Oxford: Cambridge University Press. Cited on x, 16, 21
- [Mukhanov, 1985] Mukhanov, V. F. (1985). Gravitational Instability of the Universe Filled with a Scalar Field. *JETP Lett.*, 41, 493–496. [Pisma Zh. Eksp. Teor. Fiz.41,402(1985)]. Cited on 16
- [Mulryne, 2013] Mulryne, D. J. (2013). Transporting non-Gaussianity from sub to super-horizon scales. *JCAP*, 1309, 010. Cited on 38, 47, 48, 55, 83

- [Mulryne & Ronayne, 2016] Mulryne, D. J. & Ronayne, J. W. (2016). PyTransport: A Python package for the calculation of inflationary correlation functions. Cited on 38, 47, 99
- [Mulryne et al., 2010] Mulryne, D. J., Seery, D., & Wesley, D. (2010). Moment transport equations for non-Gaussianity. *JCAP*, 1001, 024. Cited on 37, 47, 55, 83, 99, 102
- [Mulryne et al., 2011] Mulryne, D. J., Seery, D., & Wesley, D. (2011). Moment transport equations for the primordial curvature perturbation. *JCAP*, 1104, 030. Cited on 37, 47, 55, 83, 99, 102
- [Norena et al., 2012] Norena, J., Wagner, C., Verde, L., Peiris, H. V., & Easther, R. (2012). Bayesian Analysis of Inflation III: Slow Roll Reconstruction Using Model Selection. *Phys. Rev.*, D86, 023505. Cited on 46, 77, 100
- [Parkinson et al., 2006] Parkinson, D., Mukherjee, P., & Liddle, A. R. (2006). A Bayesian model selection analysis of WMAP3. *Phys. Rev.*, D73, 123523. Cited on 100
- [Peebles, 1966] Peebles, P. (1966). Primeval Helium Abundance and the Primeval Fireball. *Phys. Rev. Lett.*, 16(10), 410–413. Cited on 8
- [Peebles & Yu, 1970] Peebles, P. J. E. & Yu, J. T. (1970). Primeval adiabatic perturbation in an expanding universe. *Astrophys. J.*, 162, 815–836. Cited on 39
- [Perlmutter et al., 1999] Perlmutter, S. et al. (1999). Measurements of Omega and Lambda from 42 high redshift supernovae. *Astrophys. J.*, 517, 565–586. Cited on 7
- [Polarski & Starobinsky, 1996] Polarski, D. & Starobinsky, A. A. (1996). Semiclassicality and decoherence of cosmological perturbations. *Class. Quant. Grav.*, 13, 377–392. Cited on 19
- [Polyakov, 1974] Polyakov, A. M. (1974). Particle Spectrum in the Quantum Field Theory. *JETP Lett.*, 20, 194–195. [300(1974)]. Cited on 11
- [Price et al., 2015] Price, L. C., Frazer, J., Xu, J., Peiris, H. V., & Easther, R. (2015). MultiModeCode: An efficient numerical solver for multifield inflation. *JCAP*, 1503(03), 005. Cited on 46, 77, 100
- [Rees & Sciama, 1968] Rees, M. J. & Sciama, D. W. (1968). Large scale Density Inhomogeneities in the Universe. *Nature*, 217, 511–516. Cited on 39

- [Remmen & Carroll, 2014] Remmen, G. N. & Carroll, S. M. (2014). How Many e -Folds Should We Expect from High-Scale Inflation? *Phys. Rev.*, D90(6), 063517. Cited on 13
- [Renaux-Petel & Turzynski, 2015] Renaux-Petel, S. & Turzynski, K. (2015). On reaching the adiabatic limit in multi-field inflation. *JCAP*, 06, 010. Cited on 29
- [Riess et al., 1998] Riess, A. G. et al. (1998). Observational evidence from supernovae for an accelerating universe and a cosmological constant. *Astron. J.*, 116, 1009–1038. Cited on 7
- [Riess et al., 2011] Riess, A. G., Macri, L., Casertano, S., Lampeitl, H., Ferguson, H. C., Filippenko, A. V., Jha, S. W., Li, W., & Chornock, R. (2011). A 3% Solution: Determination of the Hubble Constant with the Hubble Space Telescope and Wide Field Camera 3. *Astrophys. J.*, 730, 119. [Erratum: *Astrophys. J.* 732,129(2011)]. Cited on 107
- [Ringeval, 2008] Ringeval, C. (2008). The exact numerical treatment of inflationary models. *Lect. Notes Phys.*, 738, 243–273. Cited on 46
- [Ringeval et al., 2006] Ringeval, C., Brax, P., van de Bruck, C., & Davis, A.-C. (2006). Boundary inflation and the WMAP data. *Phys. Rev.*, D73, 064035. Cited on 46
- [Roest et al., 2013] Roest, D., Scalisi, M., & Zavala, I. (2013). Kähler potentials for Planck inflation. *JCAP*, 1311, 007. Cited on 36
- [Ronayne & Mulryne, 2017] Ronayne, J. W. & Mulryne, D. J. (2017). Numerically evaluating the bispectrum in curved field-space – with PyTransport 2.0. Cited on 38, 47, 48, 64, 66, 99, 102
- [Sachs & Wolfe, 1967] Sachs, R. K. & Wolfe, A. M. (1967). Perturbations of a cosmological model and angular variations of the microwave background. *Astrophys. J.*, 147, 73–90. [Gen. Rel. Grav.39,1929(2007)]. Cited on 39
- [Salopek & Bond, 1990] Salopek, D. S. & Bond, J. R. (1990). Nonlinear evolution of long wavelength metric fluctuations in inflationary models. *Phys. Rev.*, D42, 3936–3962. Cited on 25
- [Sasaki, 1986] Sasaki, M. (1986). Large Scale Quantum Fluctuations in the Inflationary Universe. *Prog. Theor. Phys.*, 76, 1036. Cited on 16

- [Sasaki & Stewart, 1996] Sasaki, M. & Stewart, E. D. (1996). A General analytic formula for the spectral index of the density perturbations produced during inflation. *Prog. Theor. Phys.*, 95, 71–78. Cited on 29, 100
- [Sasaki et al., 2006] Sasaki, M., Valiviita, J., & Wands, D. (2006). Non-Gaussianity of the primordial perturbation in the curvaton model. *Phys. Rev.*, D74, 103003. Cited on 38
- [Schomblond & Spindel, 1976] Schomblond, C. & Spindel, P. (1976). Unicity Conditions of the Scalar Field Propagator $\Delta(1)(x,y)$ in de Sitter Universe. *Ann. Inst. H. Poincaré Phys. Theor.*, 25, 67–78. Cited on 18
- [Schwinger, 1960] Schwinger, J. (1960). The special canonical group. *Proceedings of the national academy of sciences of the United States of America*, 46(10), 1401. Cited on 141
- [Seery, 2016] Seery, D. (2016). CppTransport: a platform to automate calculation of inflationary correlation functions. Cited on 38, 47, 60, 99, 101, 109, 110
- [Seery & Lidsey, 2005a] Seery, D. & Lidsey, J. E. (2005a). Primordial non-Gaussianities from multiple-field inflation. *JCAP*, 0509, 011. Cited on 33, 34, 51, 79
- [Seery & Lidsey, 2005b] Seery, D. & Lidsey, J. E. (2005b). Primordial non-Gaussianities in single field inflation. *JCAP*, 0506, 003. Cited on 33, 51, 69, 79
- [Seery et al., 2007] Seery, D., Lidsey, J. E., & Sloth, M. S. (2007). The inflationary trispectrum. *JCAP*, 0701, 027. Cited on 38
- [Seery et al., 2012] Seery, D., Mulryne, D. J., Frazer, J., & Ribeiro, R. H. (2012). Inflationary perturbation theory is geometrical optics in phase space. *JCAP*, 1209, 010. Cited on 29, 37, 47, 75, 83, 99, 102
- [Senatore et al., 2010] Senatore, L., Smith, K. M., & Zaldarriaga, M. (2010). Non-Gaussianities in Single Field Inflation and their Optimal Limits from the WMAP 5-year Data. *JCAP*, 1001, 028. Cited on 27
- [Silk, 1968] Silk, J. (1968). Cosmic black body radiation and galaxy formation. *Astrophys. J.*, 151, 459–471. Cited on 40
- [Silverstein & Tong, 2004] Silverstein, E. & Tong, D. (2004). Scalar speed limits and cosmology: Acceleration from D-acceleration. *Phys. Rev.*, D70, 103505. Cited on 27, 69

- [Silverstein & Westphal, 2008] Silverstein, E. & Westphal, A. (2008). Monodromy in the CMB: Gravity Waves and String Inflation. *Phys. Rev. D*, 78, 106003. Cited on 125
- [Smith et al., 2003] Smith, R. E., Peacock, J. A., Jenkins, A., White, S. D. M., Frenk, C. S., Pearce, F. R., Thomas, P. A., Efstathiou, G., & Couchmann, H. M. P. (2003). Stable clustering, the halo model and nonlinear cosmological power spectra. *Mon. Not. Roy. Astron. Soc.*, 341, 1311. Cited on 107
- [Sreenath et al., 2015] Sreenath, V., Hazra, D. K., & Sriramkumar, L. (2015). On the scalar consistency relation away from slow roll. *JCAP*, 1502(02), 029. Cited on 46
- [Starobinsky, 1982] Starobinsky, A. A. (1982). Dynamics of Phase Transition in the New Inflationary Universe Scenario and Generation of Perturbations. *Phys. Lett.*, 117B, 175–178. Cited on 19, 29
- [Starobinsky, 1985] Starobinsky, A. A. (1985). Multicomponent de Sitter (Inflationary) Stages and the Generation of Perturbations. *JETP Lett.*, 42, 152–155. [Pisma Zh. Eksp. Teor. Fiz.42,124(1985)]. Cited on 29
- [Sunyaev & Zeldovich, 1970] Sunyaev, R. A. & Zeldovich, Ya. B. (1970). Small scale fluctuations of relic radiation. *Astrophys. Space Sci.*, 7, 3–19. Cited on 39
- [’t Hooft, 1974] ’t Hooft, G. (1974). Magnetic Monopoles in Unified Gauge Theories. *Nucl. Phys.*, B79, 276–284. [,291(1974)]. Cited on 11
- [Takahashi et al., 2012] Takahashi, R., Sato, M., Nishimichi, T., Taruya, A., & Oguri, M. (2012). Revising the Halofit Model for the Nonlinear Matter Power Spectrum. *Astrophys. J.*, 761, 152. Cited on 107
- [Tolley & Wyman, 2010] Tolley, A. J. & Wyman, M. (2010). The Gelaton Scenario: Equilateral non-Gaussianity from multi-field dynamics. *Phys. Rev.*, D81, 043502. Cited on 46, 48, 61, 67, 68, 99, 129, 141, 142
- [Tsujikawa & Yajima, 2000] Tsujikawa, S. & Yajima, H. (2000). New constraints on multifield inflation with nonminimal coupling. *Phys. Rev.*, D62, 123512. Cited on 28
- [Verde et al., 2003] Verde, L. et al. (2003). First year Wilkinson Microwave Anisotropy Probe (WMAP) observations: Parameter estimation methodology. *Astrophys. J. Suppl.*, 148, 195. Cited on 100

- [Vernizzi & Wands, 2006] Vernizzi, F. & Wands, D. (2006). Non-gaussianities in two-field inflation. *JCAP*, 0605, 019. Cited on 25
- [Visser & Barcelo, 2000] Visser, M. & Barcelo, C. (2000). Energy conditions and their cosmological implications. In *Proceedings, 3rd International Conference on Particle Physics and the Early Universe (COSMO 1999): Trieste, Italy, September 27-October 3, 1999* (pp. 98–112). Cited on 12
- [Wands et al., 2000] Wands, D., Malik, K. A., Lyth, D. H., & Liddle, A. R. (2000). A New approach to the evolution of cosmological perturbations on large scales. *Phys. Rev.*, D62, 043527. Cited on 20, 100
- [Weinberg, 2005] Weinberg, S. (2005). Quantum contributions to cosmological correlations. *Phys. Rev.*, D72, 043514. Cited on 50, 88, 89, 141
- [Wu et al., 1999] Wu, K. K. S., Lahav, O., & Rees, M. J. (1999). The large-scale smoothness of the Universe. *Nature*, 397, 225–230. [,19(1998)]. Cited on 3
- [York, 1972] York, Jr., J. W. (1972). Role of conformal three geometry in the dynamics of gravitation. *Phys. Rev. Lett.*, 28, 1082–1085. Cited on 79
- [Zhao et al., 2009] Zhao, G.-B., Pogosian, L., Silvestri, A., & Zylberberg, J. (2009). Searching for modified growth patterns with tomographic surveys. *Phys. Rev.*, D79, 083513. Cited on 107
- [Zuntz et al., 2015] Zuntz, J., Paterno, M., Jennings, E., Rudd, D., Manzotti, A., Dodelson, S., Bridle, S., Sehrish, S., & Kowalkowski, J. (2015). CosmoSIS: modular cosmological parameter estimation. *Astron. Comput.*, 12, 45–59. Cited on 2, 100, 106, 142